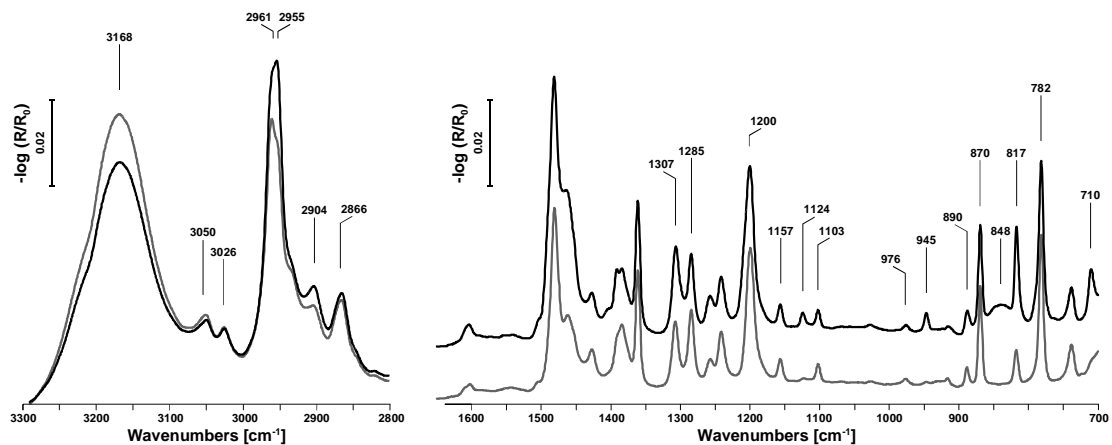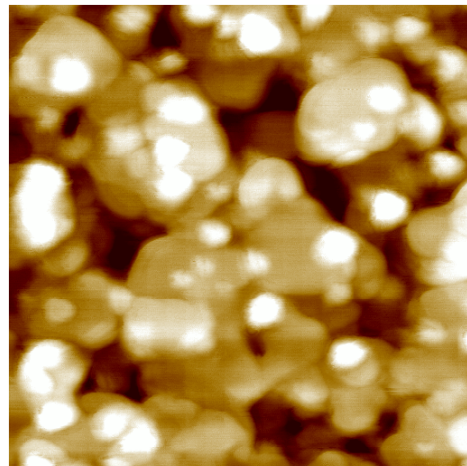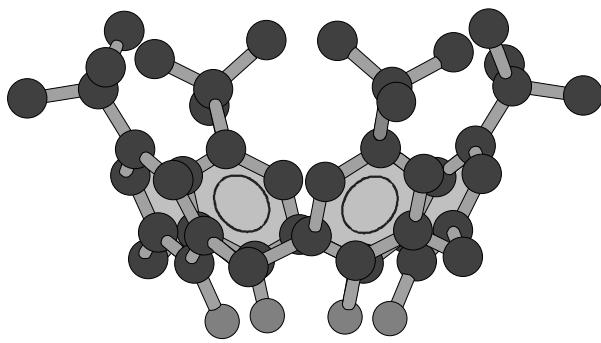# Oliver Maute

Preparation of Ordered *tert*-Butylcalix[4]arene Layers on Modified Surfaces: Comparative FTIR, SFM, TPD, and Contact Angle Studies

Preparation of Ordered *tert*-Butylcalix[4]arene Layers on Modified Surfaces: Comparative FTIR, SFM, TPD, and Contact Angle Studies

---

Präparation orientierter *tert*-Butylcalix[4]aren-Schichten auf modifizierten Gold- und Silizium-Substraten: Vergleichende Untersuchungen mit FTIR-Spektroskopie, AFM, TDS und Kontaktwinkel-Messungen

DISSERTATION

der Fakultät für Chemie und Pharmazie
der Eberhard Karls Universität Tübingen

zur Erlangung des Grades eines Doktors
der Naturwissenschaften

1999

vorgelegt von

Oliver Maute

To My Family

Preparation of Ordered *tert*-Butylcalix[4]arene Layers on Modified Surfaces: Comparative FTIR, SFM, TPD, and Contact Angle Studies

Table of Contents

Chemistry is a science of interactions,
of transformations and of models.
Jean Marie Lehn

1 Introduction and Motivation

1.1 Supramolecular Chemistry and Molecular Recognition

Supramolecular chemistry [1, 2] is based on specific intermolecular, non-covalent, and multiple binding interactions between a molecular receptor ('*host*') and a smaller substrate or analyte molecule ('*guest*'). The resulting *supermolecules* are highly organized, stoichiometric associates of two or more molecules or ions with well defined thermodynamic, kinetic, structural, and conformational properties. They are characterized both by their architecture or superstructure, and the nature of the intermolecular interactions. In solution, entropically driven repulsive forces between solvent and guest molecules (i. e. hydrophobic in water or lipophobic forces in organic solvents) may contribute to the host-guest attraction [3]. The latter are distinguished in metal-ion coordination, COLUMBIC or electrostatic forces, hydrogen bond interactions, VAN DER WAALS attractions, donor-acceptor or cation-π interactions [4]. Since the intermolecular forces generally are weaker than covalent bonds, supramolecular species are thermodynamically less stable and dynamically more flexible than molecules. Polymolecular association of receptors, carriers or catalysts in one specific phase like films, layers, or membranes lead to *supramolecular assemblies* as sketched out in Fig. 1.1. For their work on the topic of supramolecular chemistry, *J. M. LEHN*, *D. J. CRAM* and *C. J. PEDERSEN* were awarded the *NOBEL* Prize in 1987 [1, 5, 6].

In retrospective, supramolecular chemistry originates from several interaction models, partly established more than a century ago. The *concept of biological receptors and substrates* by *P. EHRLICH* [7], 'corpore non agunt nisi fixata' says that molecules do not act if they do not bind. Since complementarity of host and guest molecules in pairs with respect to size, geometry and relative orientation of binding sites (expressed e. g. by their functional groups) results in selective attraction, *E. FISCHER*'s *lock and key principle* [8] marks the basis of molecular recognition. The required selective affinity between receptors and substrates makes supramolecular chemistry a generalization of *coordination chemistry*, introduced by *A. WERNER* [9]. Finally, the *hand-in-glove*

model by *D. E. KOSHLAND* [10] takes into account the flexibile structures of both receptor and substrate molecules.
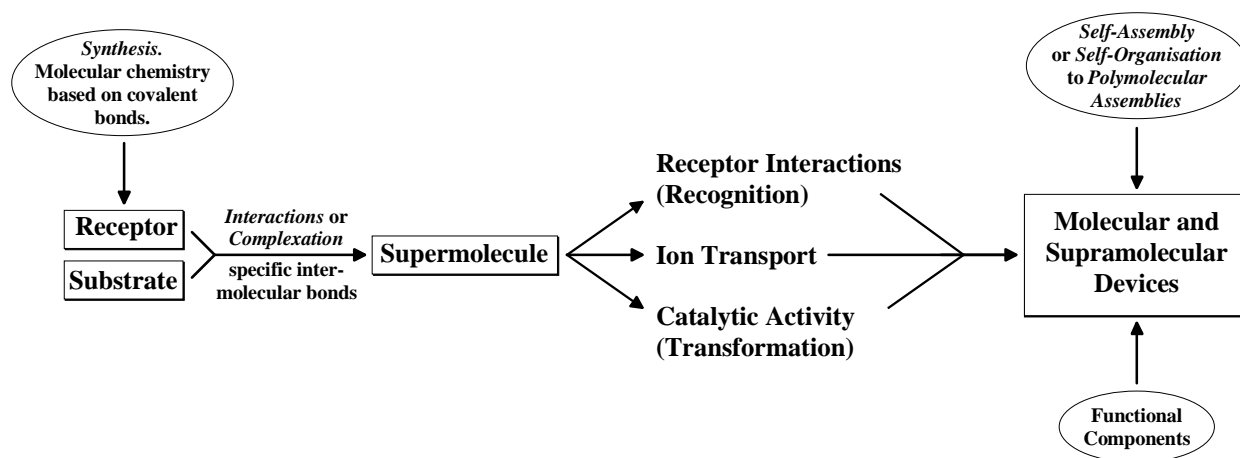
Figure 1.1:   *From molecular to supramolecular chemistry. While molecular chemistry is based on the covalent bond, supramolecular chemistry describes the chemistry of molecular assemblies and intermolecular bonds. Atoms, molecules, supermolecules, and supramolecular assemblies represent the letters, words, sentences, and books in the language of chemistry [2].*

Supramolecular chemistry rests on transport processes, catalysis and molecular recognition that will briefly be described in the following [2].

Molecular recognition deals with the selective binding of a specific substrate or analyte to a receptor molecule. This concept imitates biological interactions like antigen-antibody association or enzymatic reactions, and shows a very promising pathway to obtain highly sensitive and selective chemical sensors that are required for a continuous analysis of our environment or of production processes. A wide variety of receptors model compounds with different shape and size have been synthesized. *Endo-receptors* like crown ethers, cyclodextrins, and calixarenes are macrocyclic structures that mimic the active center of enzymes, where convergent interactions bind the substrate in a cavity of suitable architecture. Mainly in the realm of pharmacy, receptor design calculations are performed to optimize size, shape, and binding site geometry balancing rigid and flexible properties of the host. While high selectivity can be achieved with a rigid host molecule, dynamic processes like exchange and catalysis demand more flexibility in the recognition structure. Therefore, molecular modeling and molecular docking calculations are used to test and specify a receptor even before being synthesized. Assemblies with neutral organic molecules (e. g. toluene, chloroform, and perchlorethylene), cations (such as Na^+, Ca^{2+}, and organic ammonium ions) and anions as *guest* molecules are formed.

On the other hand, divergent interactions bind substrates to the outer surfaces of *exo-receptors*. For a highly selective exo-supramolecular recognition, a large-scale contact area with sufficient binding sites and a suitable geometrical and electronic complementarity of receptor and substrate are

necessary. Biological events like protein-protein interactions and antigene-antibody reactions correspond to the recognition of huge molecules of similar size or at interfaces like monolayers, films, and membranes.

In *chemical sensor systems* [11], the reading-out of supramolecular information is performed with convenient microelectronic devices (*transducers*) that monitor changes in physical properties of the sensitive films such as changes of mass Δm, capacity ΔC, conductivity $\Delta\sigma$, or temperature ΔT. In order to transform these signals, the recognition structures have to be connected to the devices by means of self assembly or evaporation techniques. Suitable transducers are quartz microbalances (QMB, Δm), interdigital structures ($\Delta\sigma$), interdigital capacitors (ΔC), and amperometric sensors (ΔI). Examples for commercially available chemical sensors are the lambda probe (a solid state electrolyte of ZrO_2 stabilized with Y_2O_3 to measure the partial pressure of oxygen in exhaust gases of cars) and the *TAGUSHI* sensor (determination of combustible or explosive gases by redox reactions at a SnO_2 surface). One of the most interesting topics is the development of an electronic nose by *W. GÖPEL* et al. (i. e. Modular Sensor System MOSES II) with a combination of metal oxide and organic polymer sensors [12].
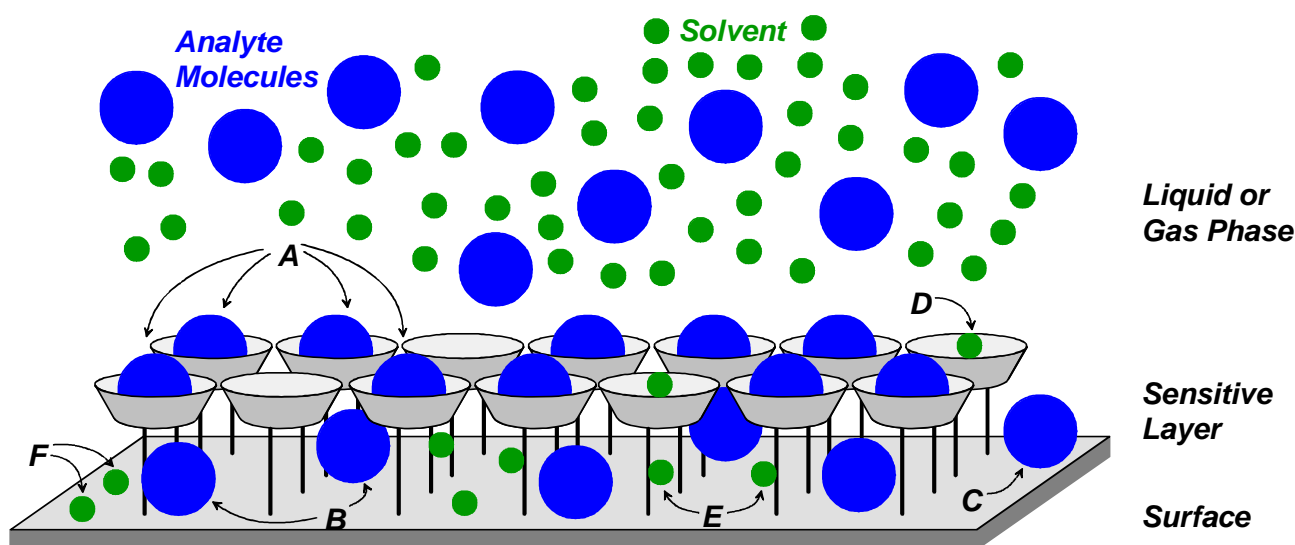
Figure 1.2:   *Schematic representation of a sensitive layer of receptor molecules in the vicinity of the liquid or vapor phase of the analyte. Due to different interactions, various adsorption positions are accessible: Supramolecular inclusion of analyte (A) or solvent (D), adsorption at the surface (C, and F), or interaction with the aliphatic spacer that links the recognition structure to the transducer surface (B, and E for analyte and solvent, respectively).*

1.2   Motivation and Purpose of this Thesis

Development and optimization of a sensor system, as outlined above, marks an extensive and interdisciplinary challenge, whereas a dissertation can deal only with several aspects of this goal. A suitable chemical sensor is expected to meet all requirements of high sensitivity towards the analyte, high selectivity and sufficient stability. For the case of strong interactions, the recognition of organic

molecules resembles the highly selective antigene-antibody interactions. For a wider field of applications, recognition structures have to be designed that interact reversibly and highly selective with any desired analyte. In this context, figure 1.2 shows a monolayer architecture of a recognition structure that is able to interact with analytes both in the liquid and the vapor phase. For this purpose, the monolayer system is quite convenient since both the layer formation and the recognition event are characterized by means of spectroscopy or microscopy. Host-guest interactions that are due to bulk effects can be neglected.

Aiming at the preparation of covalently bond, ordered monolayers of recognition structures, the first step has to be a general proof whether the chosen model substance forms ordered layers. This easily is probed by infrared spectroscopy in ATR mode (see details below). Since the use of ATR substrates as transducers, however, is rather limited, the acquired knowledge will be transferred in order to generate ordered films on more suitable substrates such as silicon and gold that can be modified in various ways to fit the properties of the recognition molecule. Finally, a covalent binding of the recognition structure to the substrates has to be performed.

1.3   Introduction to Calixarene Chemistry

Calix[n]arenes [13, 14] are cyclic oligomers consisting of *n* phenol units bridged by methylene groups in *ortho*-position to the phenolic hydroxyl group. For $n = 4\text{-}20$, these cavity compounds are easily accessible from a base-induced condensation as initiated by *A. ZINKE* [15] or a stepwise synthesis dating back to *B. T. HAYES* and *R. F. HUNTER* [16]. In 1975, *C. D. GUTSCHE* coined their name [17] considering that the most stable conformation of the tetramer resembles a greek *calix* crater, whereas *aren* indicates the presence of aryl residues in the macrocyclic array. A rapidly increasing number of studies and publications dealing with calixarenes published every year, demonstrates the growing interest in the properties and benefit of this family of $[1_n]$meta-cyclophanes [18].
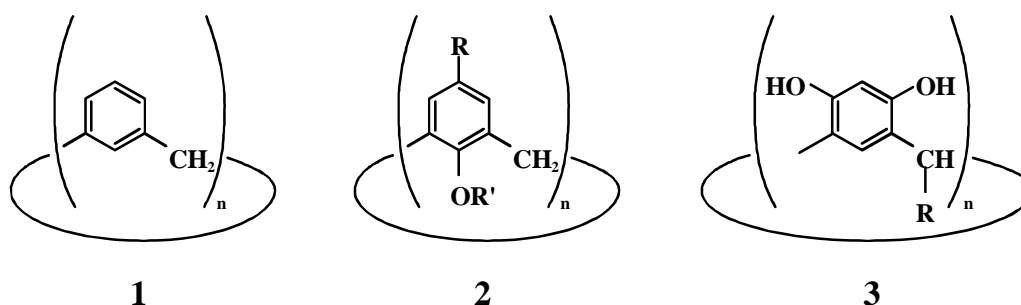

Figure 1.3:   ***Family of [1ₙ]metacyclophanes.*** *Structure **1** shows the skeleton of [1ₙ]metacyclophanes, **2** scetches the backbone of the calix[n]arenes with the hydroxyl groups in endo position. A base-induced condensation of resorcin and aldehydes yields resorcin[n]arenes with exocyclic OH groups, **3** [18].*

Properties. The π-basic cavity with aromatic rings and aliphatic side chains at the upper rim (*para*-position to the hydroxyl groups, *R* in figure 1.3) marks the hydrophobic part of the molecule, while the hydrophilic behaviour results of the phenolic OH groups at the lower rim. Compared to the most organic compounds, calix[*n*]arenes have an extremely high melting point, and a high thermal and chemical stability. Chemical modifications are possible both at the upper and the lower rim in order to introduce functional groups or to change solubility of the molecule or the size of the cavity. This makes calix[*n*]arenes versatile molecular platforms and suitable precursors for the building of supramolecular structures. Due to the selective inclusion of neutral molecules, cations, and anions confirmed by numerous X-ray structural and NMR studies [19-21], they serve as model substances for polar receptors and represent the third generation of supermolecules, after crown ethers and cyclodextrines [22].

Possible applications reach from highly specific ligands for analytical purpose or medical diagnosis to the construction of artificial enyzmes, and from the synthesis of new materials for non-linear optics to catalysis. Further applications concern the area of decontamination of waste water, recovery of cesium and uranium, separation of neutral organic molecules, stabilizers for organic polymers, and the preparation of ultrathin films and sieve membranes with pores in molecular size [18, 23].

Sensor application. While in the past much scientific effort has been spent on the characterization of the different conformations and the inclusion properties of calix[*n*]arenes, only a few publications deal with calixarene layers. In most cases, Langmuir-Blodgett films [24] of soluble calix[*n*]arene derivatives at the water-air interface are studied with focus on complexation properties [25-27]. On the other hand, reversible inclusion into the cavity makes calixarenes an appropriate mass sensitive coating material on quartz micro balances (QMB) for the detection of gaseous and volatile molecules, as has been shown for thick *tert*-butylcalix[4]arene layers [28]. In order to achieve, improve, and explain a high selectivity in terms of supramolecular chemistry, systems with an neglectable bulk effect have to be produced where only supramolecular host-guest interaction occur. Suitable for this purpose are thin films of organic receptor molecules - or even better closed monolayers - with a preferred orientation of the molecules i. e. with all cavities aligned towards the phase of the analyte. For that reason, this thesis closes the gap between thick layers on solid substrates and Langmuir-Blodgett monolayers on water by presenting methods to prepare and characterize thin layers (i. e. multi- and monolayers) of *tert*-butylcalix[4]arene on silicon and gold surfaces with different wettability properties and surface modifications.

Chiral recognition is an important principle both in biology and pharmacology [29]. Often one of the enantiomers is more effective than the other (e. g. in the case of inhalation anesthetics [30]) or they show opposite effect (as observed for several barbiturates [31]). The human sense of smell is also capable of chiral recognition as demonstrated for carvone, $\Delta^{1,8(9)}$ *p*-menthadien-2-one, a double unsaturated terpenoid ketone [32]. The S-(+)-enantiomer appears in cumin and anethum oil and smells of cumin, whereas the R-(-)-carvone has the fragrance of peppermint.

1.4   Structure of This Thesis

Chapter 2 surveys the literature dealing with calixarenes with respect to the most characteristic features and the layer forming properties of this family of molecules.

The layers are characterized by surface sensitive methods like various techniques of Fourier-transform infrared (FT-IR) spectroscopy in ATR (attenuated total reflection) mode or IRAS (infrared reflection absorption spectroscopy), temperature programmed desorption (TPD), scanning force microscopy (SFM), ellipsometry, contact angle measurements, UV and X-ray photoelectron spectroscopy (UPS, XPS) that are described in chapter 3.

The layers are prepared by PVD (physical vapor deposition) and SAM (self-assembled monolayer) techniques that will be outlined in chapter 4. Additionally, the UHV systems used for PVD and spectroscopy are displayed. A synthetic pathway to a monolayer forming calixarene amino acid derivative is demonstrated.

The results are presented and discussed in chapter 5, which is divided between the used substrates and their modifications. Thin layers of *tert*-butylcalix[4]arene were prepared on the native oxid adlayer of silicon surfaces or after modification with a siloxan layer carrying an oxiran ring as reactive group for a covalent link to the calixarene. Because of the hydrophobic cavity and hydrophilic hydroxyl groups at the lower rim, the formation of films with a preferred orientation of the *tert*-butylcalix[4]arene molecules is expected to be influenced by the wettability properties of the surface and possible interactions with the substrate. While IRAS probes the orientation, TPD experiments give a measure of the binding strength of *tert*-butylcalix[4]arene layers deposited on self assembled monolayers (SAMs) of thiols $HS-(CH_2)_n-X$ on gold where the wettability properties are defined by terminal groups, X, such as $-CH_3$, $-OH$ and $-CO-C_6H_5$.

2   Recent Studies on Calixarenes

Their shape of a molecular bowl predestines calixarenes as easy to prepare recognition structures in host-guest chemistry that bind cations and organic guests in their cavity, as outlined in chapter 1. The diversity of calixarene chemistry is reviewed by *C. D. Gutsche* [13], *V. Böhmer* [14, 18], and *S. Shinkai* [22, 33, 34].

This chapter summarizes recent results of calixarene chemistry with a focus on the characterization of calixarenes and the formation of thin layers that are relevant to the experimental part of this thesis. After glancing the synthesis of calixarenes and their relatives, the identification of the different conformations, the detection of host-guest complexes by spectroscopic means, and the topic of chiral calixarenes are illuminated.

2.1   Synthesis and Nomenclature

One-step synthesis, figure 2.1, either as base-induced condensation of *para* alkyl phenols with formaldehyde or as acid-catalyzed reactions produces calix[*n*]arenes, *n* = 4...20, with identical *para*-substituents, whereas fragment condensation leads to calix[*n*]arenes with different groups at the upper rim.

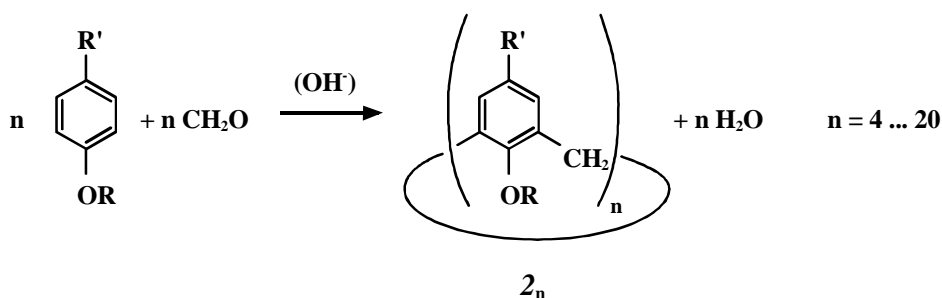*Figure 2.1:   Classical base-induced one step synthesis of calix[n]arenes as condensation of para alkyl phenols with formaldehyde.*

In non-convergent fragment synthesis, *one* linear oligomer is formed and cyclized in *one* final step, while in convergent synthesis intermolecular condensation of *two (or more)* fragments (mono-, di- or oligomer units) is followed by intramolecular cyclization, as designed by '2+2', '3+1', or

'2+1+1' synthesis for 2_4 [18]. The latter is more flexible concerning the *para* substituents, and also offers a suitable pathway to bridged calixarenes [15, 16, 35, 36]. Replacement of the methylene bridge by sulfur leads to thiacalix[4]arenes that can also be synthesized by reaction of *p-tert*-butyl-phenol and elemental sulfur [37, 38].

Ionophoric and chromophoric host molecules, and derivatives like calixcrowns, bridged calixarenes, dimers, calixspherands, and calixcryptands are synthesized using the calixarene backbone as a rigid platform for a vide variety of modifications both at the upper and lower rim [18]. In contrast to this, carcerandes and hemicarcerandes are derivatives of the resorcinarenes. Homocalixarene, oxacalix-arene, azacalixarene, and heterocalixarenes contribute to the calixarene related compounds [13].

Originally 'calixarene' considers the shape of the cyclic tetramer 2_4 (figures 1.3 and 2.1) in *cone* conformation, but nowadays, 'calixarene' is applied only to the basic structure for the cyclic oligomers 1_n (figure 1.3). With the number *n* of aryl groups given in brackets and the *para* substituenet designated by name, the key component of this thesis, the cyclic tetramer obtained from *p-tert*-butylphenol, 2_4 (*R* = H, and *R' = tert*-butyl), is consequently called *p-tert*-butylcalix[4]arene-25,26,27,28-tetrol or - indicating all substituents by their position - 5,11,17,23-tetra-*tert*-butyl-25,26,27,28-tetrahydroxycalix[4]arene [13]. For convenience, it will be referred to as '*tert*-butyl-calix[4]arene' in the following.

2.2   Conformations of Calixarenes

In 1955, *J. W. CRONWORTH* [39] discovered the four rotational diastereomers of the cyclic tetramer, today known as *conformations*. The different conformations result from the nearly free rotation of the phenol rings around the σ(C-C) bonds that link the methylene group with the aromatic rings. Potential rotational modes for the phenol units are ① '*para*-substituent-through-the-annulus' and ② 'oxygen-through-the-annulus' rotation, fig. 2.2 a) [34].
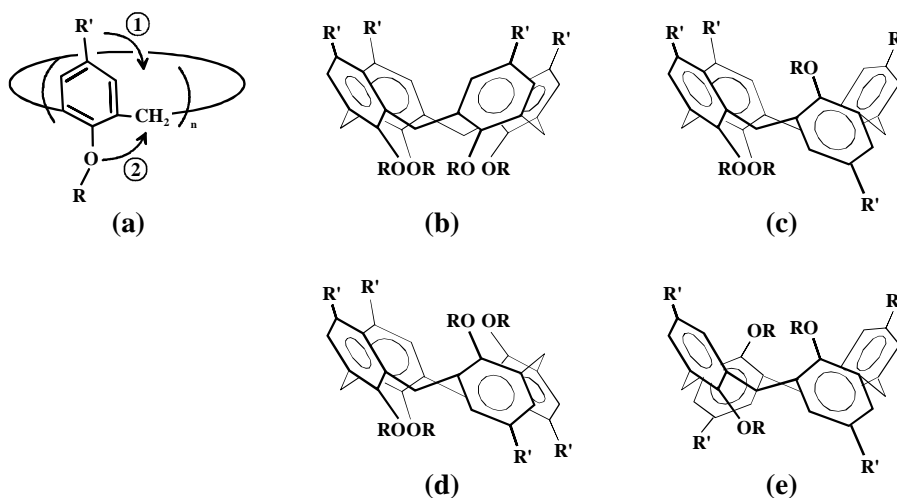

Figure 2.2:   Conformations. a) Inversion modes of the phenol units in calix[n]arenes. The conformations of calix[4]-arenes $2_4RR'$ are denoted as b) cone, c) partial cone, d) 1,2- and e) 1,3-alternate conformation [13].

The conformations of calix[*4*]arenes assigned as '*cone*', '*partial cone*', '*1,2-*', and '*1,3-alternate*', figure 2.2 b–e), are distinguished by the [1]*H-NMR* pattern of their methylene protons [13, 19]. Since their cavities differ in size, shape, polarity and inclusion properties, numerous publications deal with the various influences affecting their equilibrium, such as template effects during the synthesis, size or charge of the guest molecules.

Often, due to steric properties of the substituents *R* ($R \neq$ H) and *R'*, the more flexible *partial-cone* conformation is favored, compared to the relatively rigid *cone* or *alternate* structures, especially for bulky substituents *R'*. Bridging at the upper or lower rim, or bulky substituents ($R >$ ethyl) at the lower rim prevent the interconversion (will be described below) and the different conformations can be isolated. Since *cone* with four dipole moments oriented in the same direction is the most polar conformation, it is favored to *partial-cone* with one inverted dipole, in polar solvents [22, 34, 36, 40]. Several force field or semi-empirical calculations deal with the relative stability of the conformers [40-46] and the influences on their appearance in infrared spectra [47-49].

The easiest case, however, is realized for the tetrahydroxycalix[4]arenes like the *tert*-butylcalix[4]-arene. Due to strong intramolecular hydrogen bonding between the four phenolic OH groups, the *cone* conformation is energetically favored for all of these calix[4]arenes, and the molecules adopt C_{4v} symmetry with a π-basic cavity located at the upper rim.

Depending on the number *n* of aromatic units of the calixarenes $2_\mathbf{n}$ with $R =$ H, the hydroxyl groups at the lower rim play an important role for physical and chemical properties, such as reactivity, acidity, preferred conformation, and rigidity of the cavity.

The dislocation of the OH stretching vibration, ν(OH), and a low field displacement of the chemical shift, δ_{OH}, in *IR* and [1]*H-NMR* spectroscopy, respectively, give a measure for the strength of the hydrogen bond. Compared to $\tilde{\nu}$ [ν(OH)] ≈ 3600 cm^{-1} for free phenolic hydroxyl groups, a significant shift of ν(OH) towards lower wavenumbers and $\delta_{OH} > 10$ monitors the hydrogen bonds that are strong in calix[4]- and -[6]arenes and weaker in calix[5]arenes (table 2.1).

Table 2.1:   *Stretching frequencies (IR), chemical shifts (^{1}H-NMR), and free energies of activation (in CDCl$_3$) for conformational inversion of p-tert-butylcalix[n]arenes [13].*

	ν_{OH} [cm^{-1}]	δ_{OH}	ΔG [kJ mole^{-1}]
calix[4]arene	3138	10.2	65.6
calix[5]arene	3290	8.0	55.2
calix[6]arene	3152	10.5	55.6
calix[7]arene	3149	10.3	56.0
calix[8]arene	3190	9.6	65.6

Consequently, a deformation of the cone conformation by an included guest molecule or in bridged calix[4]arenes [36] diminishes the hydrogen bonds and leads to higher values of $\tilde{\nu}$ [ν(OH)]. From the position of the OH stretching vibration mode, $\tilde{\nu}$ [ν(OH)] $\approx 3140\,cm^{-1}$, and dipole moment measurements, *S. W. KELLER* et al. [50] concluded that *all* of the four hydroxyl groups at the lower rim of the *tert*-butylcalix[4]arene contribute to *one* hydrogen bonded ring. In infrared analysis, the 1,2,3,5-substittion pattern on the aromatic rings was detected by an absorption band at $854\,cm^{-1}$ [16].

The *cone* conformer is identified by one characteristic pair of doublets of the Ar-CH$_2$-Ar methylene protons (AB system, a coupling constant $^2J = 12 \ldots 14\,Hz$ is characteristic for geminal protons). At temperatures higher than $T_c \approx 50...60°C$, interconversion between two mirror-image *cone* conformations occurs at a rate comparable to the *NMR* time scale, and the doublets coalesce to give rise to a sharp singlet. The activation energy of the interconversion ΔG depends on the solvent, table 2.1 [3, 19, 22].

As confirmed by computational studies, even symmetric tetra-*O*-alkylated *cone* calix[4]arenes do not adopt regular C_{4v} symmetry. Rather results the C_{4v} symmetry, observed in ^1H-*NMR* spectra from a fast interconversion between two C_{2v} symmetric structures assigned as '*pinched-cone*' conformation, where two opposite aromatic rings are almost parallel and the other two adopt a flattened position. In the solid state most calixarene derivatives adopt a *pinched-cone* conformation, fig. 2.3. [51].
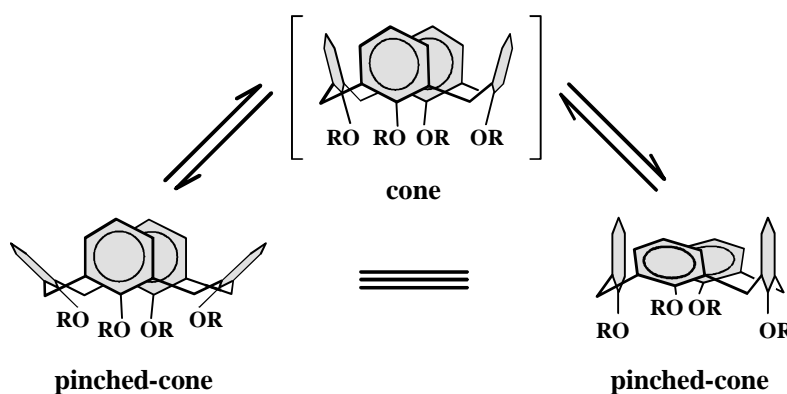
Figure 2.3: C_{2v}-C_{2v} *interconversion of tetraalkoxycalix[4]arene in cone conformation* [51]

2.3 Complex Formation and Detection of Guest Molecules

X-ray structural analysis was the early proof of host-guest interactions that lead to an inclusion into the cavity, as demonstrated first by *R. UNGARO* and coworkers for the 1:1 complex of *tert*-butyl-calix[4]arene with toluene [20]. Most of the small organic molecules like chloroform, benzene, xylene, and pyridine [21, 52] form 1:1 inclusion complexes with *tert*-butylcalix[4]arene, whereas two *tert*-butylcalix[4]arenes include one anisole molecule [21]. Simultaneous inclusion of neutral

organic and cationic guests is reported for K^+ / methanol and Na^+/toluene, with the organic molecule located in the hydrophobic cavity and the cation complexed by ionophoric functionalities like ester or amid groups at the lower rim [21, 53]. Force field calculations [28], molecular mechanics simulations [54], and ab initio MO calculations [55] provide correlating theoretical data concerning the relative orientation of host and guest molecule, conformational changes during complex formation, and contribution of dispersion interaction to the complexation energy.

C. D. GUTSCHE et al. [3] classified the non-covalent intermolecular forces responsible for the formation of strong complexes as "entropically (type I)" or "enthalpically driven (type II)". Repulsive interactions between the guest molecule and the solvent, e. g. hydrophobic forces in the case of water soluble hosts, contribute to type I forces, while attractive forces (type II) between host and guest arise from *COULOMBIC* (charge-charge or dipole-dipole) interactions, hydrogen bond interactions, *VAN DER WAALS* interactions, and cation-π or CH-π interactions [56]. Generally, complexation is not attributed to one single interaction but to combinations of them [4, 57].

The selectivity of analyte-binding events usually is estimated either by two-phase solvent extraction or by *^1H NMR* measurements in liquids, e. g. by employing the aromatic solvent induced shift (*ASIS*) [3]. Interactions between calixarenes and alkali metal cations, ammonium ions or onium salts are detected by mass spectrometry (fast atom bombardment, *FAB*, or secondary ion mass spectrometry, *SIMS* [58-61]). Guest inclusion may also lead to a spectral shift in absorption spectra of chromogenic calixarenes, or an increase of fluorescence of calix[4]arenes that bear a fluorophore functionality and a fluorescence quenching moiety near the cavity. Conformational changes of redox-switched calixarenes during the inclusion step can be tracked by cyclic voltammetry. [34].

2.4   Layer Formation of Calixarenes and Their Derivatives

Recent publications describe three main pathways to generate calixarene layers of different thickness. The *LANGMUIR BLODGETT* technique dates back to the 1920's, and yields two-dimensional molecular films at the gas-liquid interface. In several cases, the calixarene monolayers produced in this way are transferred to a solid substrate. For self-assembled monolayers (SAMs) on metal surfaces, sulfur containing side groups are introduced to the molecular backbone as often reported for resorcin[*n*]arenes, while only rather few calix[4]arene SAMs yet have been prepared. In contrast to this, the thickness of calixarene layers that are produced by thermal evaporation on various substrates is in the range of 100 Å to 2 μm [28, 62], i. e. far away from the monolayer range.

2.4.1   *LANGMUIR BLODGETT* Layers

The *LANGMUIR BODGETT* (LB) method rests on the amphiphilic structure of the used molecules. It was the first technique to construct ordered molecular assemblies. Molecules with a hydrophilic head and a hydrophobic tail are spread on a liquid subphase, in most cases water, compressed to

form a closed monolayer and finally transferred on hydrophilic substrates such as glass, quartz, chromium, and, most commonly, silicon wafers [24]. *S. SHINKAI*'s group were among the first who generated LB films of calixarenes bearing sulphonate or ester groups at the lower rim. The surface pressure (π) - area (A) isotherms of the latter selectively respond to alkali metal ions ($Li^+ < Na^+ > K^+ > Rb^+$ for the calix[4]arenetetraester) in the subphase, figure 2.4a) [33, 63].
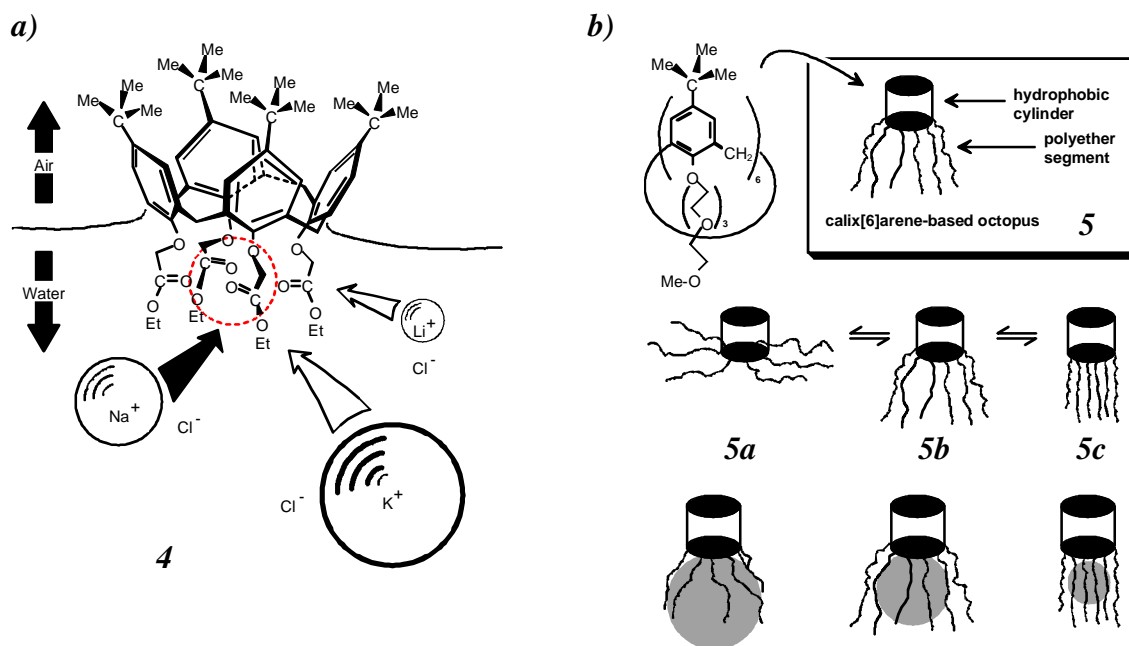
Figure 2.4:   Examples for LANGMUIR BLODGETT films at the water-air interface. a) tert-butylcalix[4]arene tetraethyl-ester, **4**, selectively includes alkali metal ions into the polar cavity immersed in the liquid subphase. b) 'tentacles' of the amphiphilic tert-butylcalix[6]arene poly(ethyleneglycol) monomethyl ether, **5**, lie at the air-water interface or are immersed into the subphase for a compressed film.

Stable monolayers of chromophoric calix[*n*]arenes, *n* = 4, 6, were prepared by *J. C. THYSON* et al. The π-*A* isotherms show sensitivity to changes in pH and interactions with ammonium guests in the subphase [27]. *L. DEI* et al. produced LB films of *tert*-butylcalix[6]arenes at the air-water interface with a high selectivity for cesium [25] or guanidinium cations [64]. Upon compression, the initial parallel orientation of the molecules, i. e. with the hydroxyl groups fully immersed in the water, collapses and forms a perpendicular orientation of closely packed molecules where the phenolic OH are only partially immersed.

S. L. REGEN and coworkers [65] generated octopus molecules with a *tert*-butylcalix[6]arene backbone. Their polyether 'tentacles' lie on the water-air interface at low surface pressures and are reversibly forced into the subphase when the film is compressed. The idea of 'fine-tuning' the interaction with a guest molecule by adjusting the tentacles is depicted in figure 2.4b). Molecular sieves fabricated by the same group on the basis of LB multilayers of calix[6]arene derivatives using poly[1-(trimethylsilyl)-1-propyne] as supporting material showed a selective permeation for He and N_2, whereas SF_6 could not pass the composite membrane [66].

LB monolayers of *tert*-octylcalix[8]arene and its tetraester derivatives show a high selectivity for I^- > F^- > Br^- > Cl^-, and Cs^+ > Rb^+ > Na^+ >> K^+, respectively. *J. C. M. STIRLING* and coworkers transferred these LB films on the hydrophobic surface of *n*-type silicon surfaces [26] and also discovered a pyroelectric effect of Calix[8]arenes with carboxyl and amino groups at the lower rim alternating in Langmuir-Blodgett multilayers [67].

The first molecular resolution SFM images of a calixarene result from *LANGMUIR-BLODGETT* films of *tert*-butylcalix[6]arenes that were transferred on modified mica. In order to stabilize the LB monolayer, both amphiphilic octadecanol and the calixarene were spread at the air-water interface. Since the calixarene films cannot withstand the lateral forces exerted on them by the scanning SFM cantilever, *M. NAMBA* et al. immobilized the mixed monolayer on FTS (1*H*,1*H*,2*H*,2*H*-perfluoro-decyltrichlorosilane) treated mica [68].

For additional examples for stable monolayers at the air-water interface based on calix[*n*]arenes alkylated or acylated at the upper or lower rim that selectively recognize metal ions, ammonium cations or even sugars the interested reader is referred to [69].

2.4.2 Self-Assembled Monolayers (SAM)

The self-assembly of molecules such as alkylsiloxanes, amines, carboxylic acids, and alkane-thiolates on oxidic and metallic substrates, e. g. gold, silver, copper, and platinum, occurs spontaneously by the immersion of an appropriate substrate into a solution of an surface active agent in an organic solvent [24]. Research in the area of SAMs of alkanethiols, $HS\text{-}(CH_2)_n\text{-}X$, on gold dates back to *R. G. NUZZO* and *D. L. ALLARA* [70], and bases on the very strong covalent binding of sulfur to the metal surface, while the tail group provides the functionality. As reviewed in several articles [71], the surface properties, e. g. wetting and reactivity, of the SAM are varied by use of a wide variety of different tail groups, $X = \text{-}CH_3$, -OH, -(C=O)OCH_3, -O-(C=O)CH_3 and -O(C=O)C_5H_6 during adsorption or by modification of the SAM after formation. Mixed monolayers, i. e. SAMs with two or more functionalities at the surface, are obtained by mixing two differently terminated thiols in the preparation solution [72] or by the formation of two-component molecular gradients, as described first by *B. LIEDBERG* and *P. TENGVALL* [73].

Formally, the adsorption of alkanethiols may be considered as an oxidative addition of the S-H bond to the gold surface, followed by a reductive elimination of the hydrogen, according to

$$\text{R-S-H} + \text{Au}_n^0 \rightarrow \text{R-S}^-\text{Au}^+ \cdot \text{Au}_n^0 + \tfrac{1}{2}\,\text{H}_2 \tag{2.1}$$
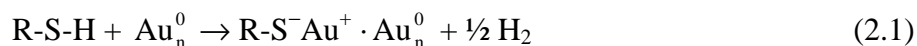
The bonding of the thiolate group to the gold surface is very strong (approximately 150 kcal mol^{-1}) and the overall energy for adsorption of alkanethiolates on gold was determined to $\approx$ -20 kcal mol^{-1}. In the SAM, the symmetry if the sulfur atom is hexagonal with a S$\cdots$S spacing of 4.97 Å and a calculated area per molecule of 21.4 Å. Since the *VAN DER WAALS* diameter of the alkane chain, $\approx$ 4.6 Å, is too small to completely cover that area, the alkyl chains in the SAMs usually are tilted

≈ 26-28° from the surface normal, and display ≈ 52-55° rotation about the molecular axis. Thiols of sufficient chain length, i. e. eight or more CH_2 groups, form densely packed SAMs with a c(4x2) superlattice of a $\sqrt{3} \times \sqrt{3}$ R30° lattice [74]. Further information about this area is provided in [75].

While many publications deal with the formation of resorcin[*n*]arene SAMs [76], only a few papers describe the preparation of calixarene SAMs. As outlined in figure 2.5, *D. L. DERMONDY* et al. prepared polydiacetylene / calix[*n*]arene bilayers on gold surfaces. After formation and two-dimensional cross-linking of a COOH-terminated SAM, the carboxylic acid group is converted to the more reactive acid chloride. Finally, the calix[*n*]arene, *n* = 4, 6, is linked through ester reaction. The authors found a 58% and 61% coverage for the calix[4]arene and calix[6]arene, respectively [77].
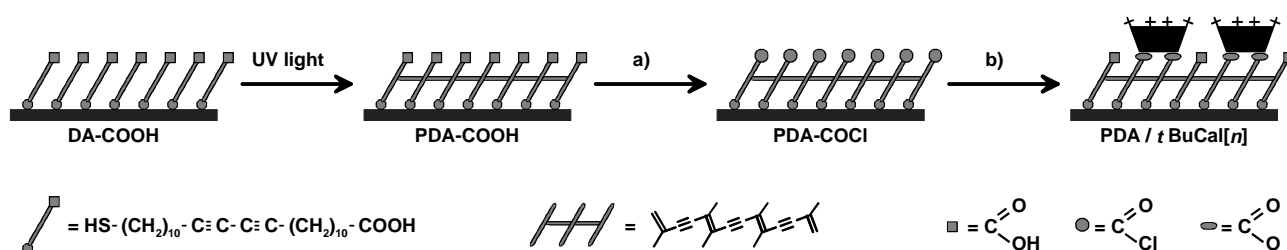
Figure 2.5: *Self assembly of polydiacetylene / calix[n]arene bilayers on gold. After UV light induced polymerization of the SAM, the terminal carboxyl groups of PDA-COOH were converted into carboxylic acid chlorides, PDA-COCl by exposition to SOCl₂ vapor (a). The calix[n]arenes, n = 4, 6, are covalently bound (b) to form the PDA / tBuCal[n] bilayer.*

X. YANG et al performed the covalent binding of an organic NLO (non-linear optic) chromophore to a quartz glass via *p*-chlormethylphenyltrichlorsilane and quarternized pyridyl groups, figure 2.6 [78].
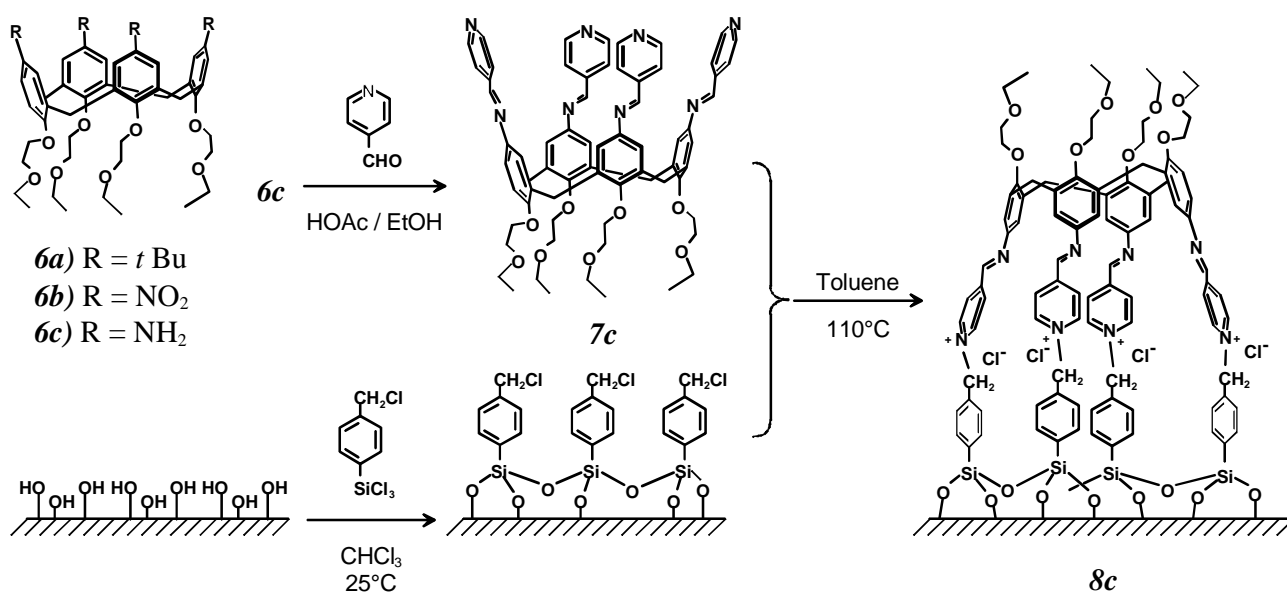
Figure 2.6: *p-chlormethylphenyltrichlorsilane coated quartz glass covalently binds calix[4]arene derivatives.*

Similar to the procedures for resorcin[4]arenes, *D. N. REINHOUDT* and his workgroup produce SAMs of calixarene based tetrasulfides carrying four -$(CH_2)_{11}$-S-$(CH_2)_{10}$-CH_3 segments at the lower rim. The tilt angles of the alkane segments agrees with the values determined for alkane thiols, but also depends on the rigidity of the cavity [79].

C. D. GUTSCHE, D. L. ALLARA et al. report the formation of *tert*-butylcalix[4]arenetetrathiolate (BCAT) SAMs on gold surfaces [80]. The BCAT molecule was transformed from *tert*-butyl-calix[4]arene by the *NEWMAN-KVART* method and shows a 1,3-alternate conformation both in solid and liquid phase. In the monolayers, the molecules adopt cone conformation with their phenyl rings preferentially oriented parallel to the surface normal axis. *X. DELAIGUE* et al. [81] characterized the BCAT mercury complex.

2.4.3   Physical Vapor Deposition (PVD)

The least frequently used way to generate thin calixarene layers follows PVD techniques performed under ultra high vacuum (UHV) conditions. In this context, *R. B. CHAÂBANE* et al. prepared, annealed and characterized 'thin' layers ($1000\,\text{Å} \le d \le 2\,\mu\text{m}$, i. e. nominally 100-2000 monolayers) of *p*-isopropylcalix[6]arene by means of FT-IR and X-ray diffraction [62].

Systematic studies by *SCHIERBAUM* et al. [28, 82] reveal the qualification of modified calix[*n*]arenes, $n = 4$, 6, and 8, as coating material for mass sensitive chemical sensors and as model compounds for the molecular recognition of organic molecules. For this purpose, thin films with a thickness in the range of $50\,\text{Å} \le d \le 1500\,\text{Å}$ were prepared by *KNUDSEN* sublimation. Quartz microbalance measurements clearly indicate mass changes of the calixarene layers that result from interactions with solvent molecules from the ambient gas phase, while temperature programmed desorption yielded information about frequency factors, desorption rates and the activation energy for desorption. The results correlate with data that arise from force field calculations using TRIPOS that established a correlation of the observed inclusion behaviour with theoretical data.

2.5   *Chiral Calixarenes*

The introduction of optically active residues at the upper or lower rim generates chiral calixarenes like *9* or *10*, figure 2.7. Asymmetrical calix[4]arenes carry three (AABC type) or four different *para*-substituents at the upper rim, or have one single *meta*-substituted phenyl unit. Dissymmetric calix[*n*]arenes, *11* and *12*, with C_4 and C_5 symmetry, are prepared by the condensation of derivatives of 3,4-disubstituted phenols [18, 83].

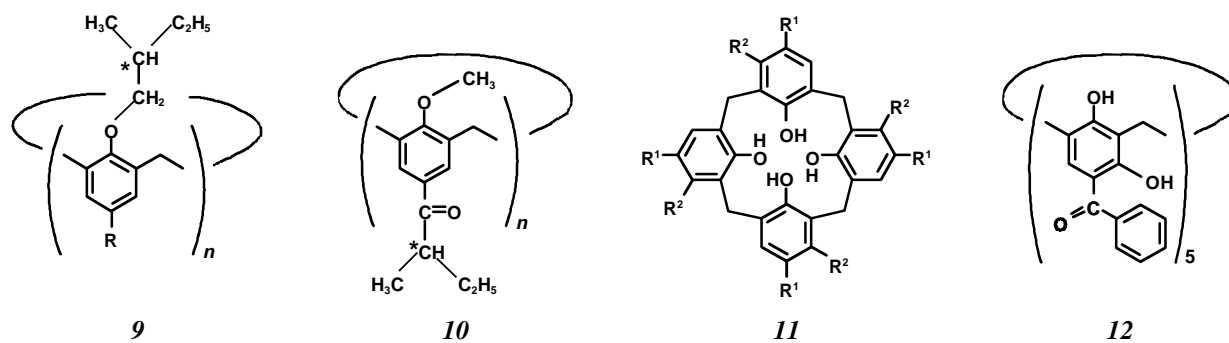*Figure 2.7: Calixarenes with chiral substituents (9, 10), and dissymetric (11, 12) calixarenes show chirality.*

In this thesis, the synthesis and characterization of a new type of layer forming chiral calix[4]arenes will be described. This calixarene combines chirality applied by amino acids and the recognition by the calixarene platform with the technique of self assembled monolayers known from alkane thiols.

3   Theoretical Section

This chapter describes the theoretical background of the measurement techniques that were used for the characterization of the *tert*-butylcalix[4]arene films. The most important method is infrared spectroscopy, especially internal reflection spectroscopy in attenuated total reflection (ATR) mode and external reflection-absorption spectroscopy (IRAS). Additional surface characterizations were performed using scanning force microscopy (SFM), single wavelength ellipsometry, and contact angle measurements. Methods carried out in the UHV, such as temperature programmed desorption (TPD), ultraviolet and X-ray photoelectron spectroscopy (UPS and XPS) provide complementary information.

3.1   Fourier Transform Infrared Spectroscopy

3.1.1   Introduction

Infrared radiation interacts with the sample, excites molecular vibrations and rotations, and thereby loses intensity at energies that are characteristic for the functional groups of the molecule or the investigated film. The basic principles of infrared spectroscopy (e. g. experimental setup, quantum mechanical models, degrees of freedom, symmetry considerations, normal modes, etc.) are described in textbooks such as [84-94].

Selection Rules and Molecular Symmetry. Different selection rules in infrared and Raman spectroscopy determine whether a certain vibration mode can interact with the incident radiation. Infrared activity requires a permanent dipole moment of the molecule, and in order to absorb infrared radiation, a molecular vibration mode must cause a change in the dipole moment, $\underline{\mu}$, of the molecule. Raman activity correlates to dipole moments induced by the electric field $\underline{E}$, i. e. the deformability of the electron cloud of the molecule as indicated by the polarizability $\underline{\alpha}$. Therefore, molecular vibrations that are accompanied by a change in the polarizability of the molecule are Raman active. The selection rules for infrared and Raman activity of vibration modes of the *tert*-butylcalix[4]arene molecule (point group C_{4v}) are summarized in the character table 3.1.

Table 3.1:   Character table for the point group C_{4v} in Schoenflies notation [85, 95].

C_{4v}	I	$2\,C_4\,(z)$	C_2	$2\,\sigma_v$	$2\,\sigma_d$	IR activity	Raman activity
A_1	1	1	1	1	1	T_c	$\alpha_{aa} + \alpha_{bb},\ \alpha_{cc}$
A_2	1	1	1	-1	-1		
B_1	1	-1	1	1	-1		$\alpha_{aa} - \alpha_{bb}$
B_2	1	-1	1	-1	1		α_{ab}
E	2	0	-2	0	0	(T_a, T_b)	$(\alpha_{ac}, \alpha_{bc})$

The symmetry elements are denoted as identity (I), four- and twofold rotation axes of symmetry (C_4, and C_2), and the planes of symmetry parallel to C_4 (σ_v, and σ_d). A_1, A_2, B_1, B_2, and E denote the various symmetry types (or species). Since T_a, T_b, and T_c show the transformation properties of translation of the electric dipole moment, they are infrared active, giving rise to total symmetric A_1 and in (a, b) plane degenerated E-type vibrations. In Raman spectra, A_1, B_1, B_2, and E-type vibrations appear whereas totally symmetric vibrations are distinguished from the rest by measurements of the depolarization ratio.

By means of group theory [85, 95], the number of vibration modes of the various symmetry species for the *tert*-butylcalix[4]arene molecule ($C_{44}H_{56}O_4$), with $N_R = 104$ atoms is calculated to result in $\Gamma = 42\,A_1 + 34\,A_2 + 40\,B_1 + 38\,B_2 + 76\,E = 306$ vibration modes.

Absorption Intensity. In terms of quantum mechanics [90], infrared activity of a molecular vibration requires that the transition dipole moment, $\underline{R}_{fi}$, has a nonzero component for at least one direction in space. The absorption intensity, I, of a vibration band in the spectrum is proportional to the square of the scalar product of the transition dipole moment $\underline{R}_{fi}$ and the electric field $\underline{E}$

$$I \propto \left[\underline{E} \cdot \underline{R}_{fi}\right]^2 \quad \text{with} \quad \underline{R}_{fi} = \int \Psi_f^* \, \underline{\mu} \, \Psi_i \, d\tau \quad \text{and} \quad \underline{\mu} = \begin{pmatrix} \mu_x \\ \mu_y \\ \mu_z \end{pmatrix} \tag{3.1}$$

Ψ_f^* and Ψ_i denote the conjugate complex wavefunctions of the final and initial state. Consequently, the intensity depends on the magnitude of $\underline{\mu}$ and $\underline{E}$ and their relative orientation.

$$I \propto \left|\underline{\mu}\right|^2 \cdot \left|\underline{E}\right|^2 \cdot \cos^2(\underline{\mu}, \underline{E}) \tag{3.2}$$

Maximum intensity occurs if the dipole moment is aligned parallel to the exciting electric field, whereas zero intensity is observed when they are perpendicular with respect to each other. For an ordered film, i. e. if the molecules have a preferred orientation in the layer, $\mu_x \neq \mu_y \neq \mu_z$ leads to different intensities (dichroism) of transitions polarized in x-, y-, or z-direction. The latter can selectively be excited by separation of the corresponding components of the electric field. For

example, in ATR mode, the electric field is split up by a polarizer to generate a transverse magnetic (*TM*, $E_{//,0}$) and a transverse electric (*TE*, $E_{\perp,0}$) wave, parallel and perpendicular to the plane of incidence, i. e. the (x, z)-plane in figure 3.1b) [96]. Boundary conditions for metallic surfaces have the effect that in IRAS, only vibrational modes which oscillate perpendicular to the surface ($E_{||}$) are excited (*surface selection rule*), figure 3.1c) [97].

Coordinate Systems. Depending on their orientation in the film, the dipole moments, $\underline{\mu}$, of the molecules contribute to the total dipole moment, $\underline{M}$, of the overlayer. For convenience, two different coordinate systems are introduced, figure 3.1 [98]:

1. Molecular system (a, b, c), with c aligned parallel to the principal axis of the molecule, C_4, and a and b in the symmetry planes σ_v of the *tert*-butylcalix[4]arene molecule. The molecular dipole moments are denoted as $\underline{\mu}_c$ and $\underline{\mu}_{a,b}$.

2. Spectrometer system (x, y, z), with the organic layer on the surface, i. e. in the (x, y)-plane, z as the direction of the surface normal, x as the direction of propagation of the infrared radiation, and the plane of incidence in the (x, z)-plane.

a)   *b)*

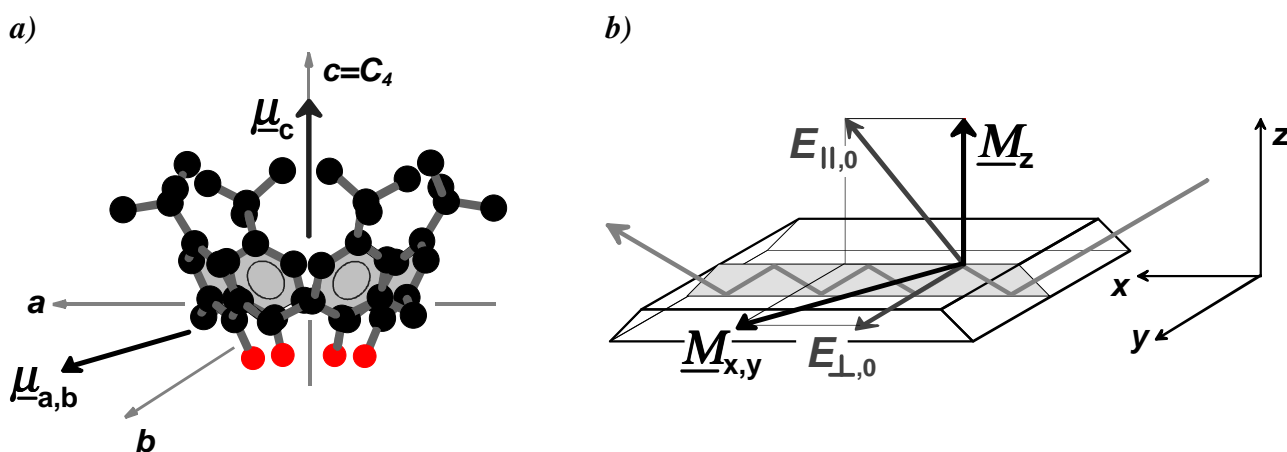Figure 3.1:   *For the tert-butylcalix[4]arene molecule, the three axes of the molecular coordinate system, a, b, and c, coincide with the axes and planes of symmetry, i. e. 2 x σ_v, and C_4. For comparison, the spectrometer systems (x, y, z) used in ATR and IRAS are displayed. The plane of incidence is defined as the (x, z)-plane, with x as the direction of the propagating radiation and z as surface normal.*
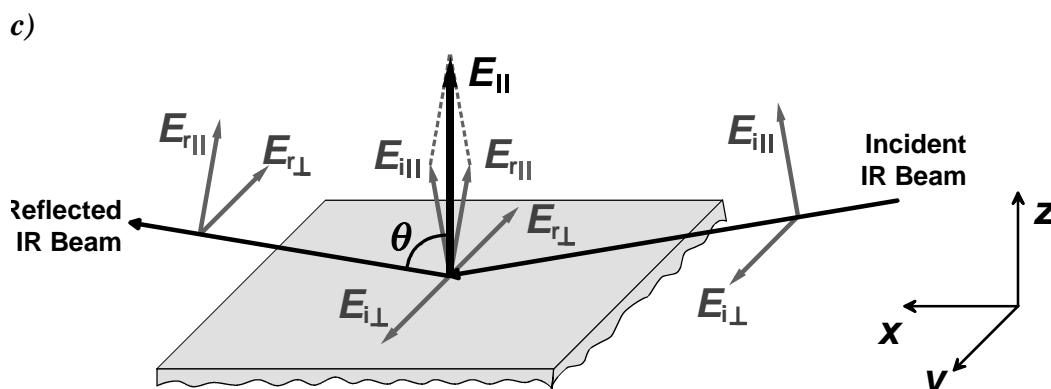
c)

Figure 3.1:   The spectrometer coordinate system (x, y, z) used in IRAS (continued). The plane of incidence is defined as the (x, z)-plane, with x as the direction of the propagating radiation and z as surface normal

3.1.2   Attenuated Total Reflection (ATR)

This paragraph reveals details of the theory of FT-IR spectroscopy in ATR mode. The evanescent field results from interference at the interface between the ATR crystal and the ambient medium, e. g. an organic film of sufficient thickness ($d_f > d_p$, two-phase system). It gives rise to three spatial components, E_x, E_y, and E_z, that contribute to the *TM* (E_x, E_z) and *TE* (E_y) waves mentioned above. The interactions of the IR radiation with thin organic film deposited on the ATR crystal will be explained in terms of a three-phase model.

Evanescent Field. Total internal reflection of infrared radiation occurs at the interface between an infrared-transparent, optically denser crystal with the refractive index n_i, and the ambient medium with $n_t < n_i$. The boundary condition for solving *MAXWELL'S* equations requires the tangential components of the electric and magnetic fields and the normal displacement to be continuous at the interface between the two media. This leads to *FRESNEL'S* equations that describe the reflected ($\underline{r}$) and transmitted ($\underline{t}$) field [89, 96]. Total reflection, i. e. the vanishing of the transmitted beam, takes place for angles of incidence, θ_i, greater than the so-called critical angle θ_c. The critical angle is calculated according to *SNELL'S* law [94].

$$\theta_t \geq 90° \Leftrightarrow \theta_i > \theta_c \text{ with } \sin\theta_c = \frac{n_t}{n_i} \tag{3.3}$$

Interference of the incident and reflected electric field at the totally reflecting interface generates a standing wave, i. e. the evanescent field, aligned perpendicular to the surface with a sinusoidal shape in the ATR-crystal, figure 3.2b). The amplitude decreases exponentially in the optically rarer medium according to equation (3.5). At the interface, electric fields exist in all spatial directions with anisotropic amplitudes E_0, as given in equation (3.4) and displayed in figure 3.2a) [96].
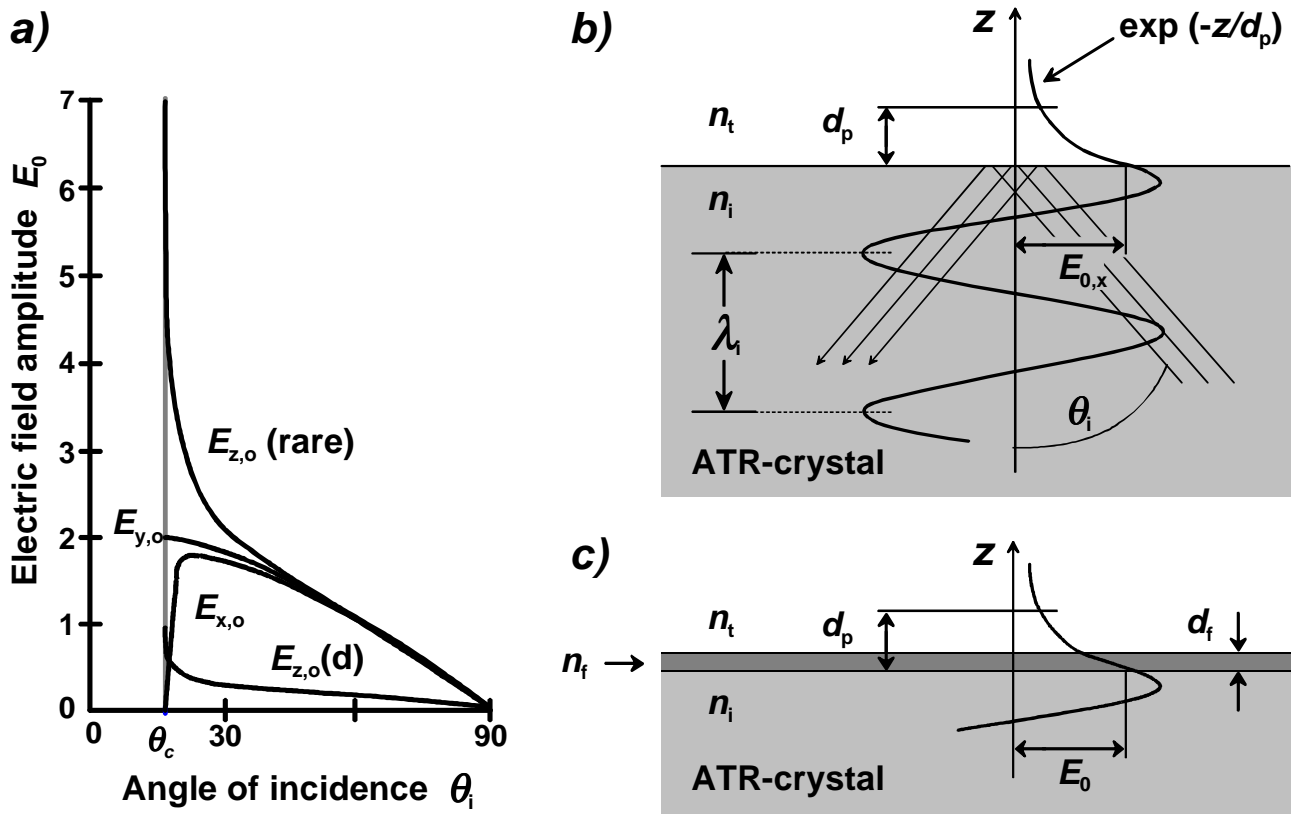
Figure 3.2:   a) Electric field amplitudes for unit incident amplitude versus angle of incidence at a total reflecting interface for $n_{ti} = 0.285$. E_y is the field for polarization perpendicular to the plane of incidence, whereas E_x and E_z are components of the field for parallel polarization. $E_{z,0}$ (rare) and $E_{z,0}$ (d)denote E_z for the optically rarer and denser medium, respectively [96].

b) Evanescent field established as standing wave at the interface between the ATR crystal (n_i) and the ambient phase (n_t), e. g. air or a film with a thickness of $d_f > d_p$.

c) This three-phase system describes the situation for very thin films, $d_f < d_p$.

$$E_{xo} = \frac{2\cos\theta_i \sqrt{\sin^2\theta_i - n_{ti}^2}}{\sqrt{1-n_{ti}^2}\sqrt{(1+n_{ti}^2)\sin^2\theta_i - n_{ti}^2}} \ ,$$

$$E_{\perp 0} = E_{yo} = \frac{2\cos\theta_i}{\sqrt{1-n_{ti}^2}} \ , \tag{3.4}$$

$$E_{zo} = \frac{2\sin\theta_i \cos\theta_i}{\sqrt{1-n_{ti}^2}\sqrt{(1+n_{ti}^2)\sin^2\theta_i - n_{ti}^2}}$$

In the ambient medium, the amplitude of the evanescent field decreases exponentially with the distance from the interface, z (figure 3.2b):

$$E = E_0 \exp(-z/d_p) \ . \tag{3.5}$$

At the distance $z = d_p$, the amplitude of the electric field drops to e^{-1} of its value E_0 at the surface; d_p is called depth of penetration, and given by

$$d_p = \frac{\lambda_i}{2\pi\sqrt{\sin^2\theta_i - n_{ti}^2}} \quad , \quad \text{with } n_{ti} = \frac{n_t}{n_i} \quad \text{and} \quad \lambda_i = \frac{\lambda_0}{n_i} \quad , \tag{3.6}$$

where λ_i is the wavelength of the light in the incident medium (in this case, the ATR crystal), and λ_0 denotes its wavelength in the vacuum. The depth of penetration depends on the angle of incidence and the relative refractive index n_{ti}, and is proportional to the wavelength λ_i [96, 99].

***TM* and *TE* Wave.** The spatial components of the evanescent field are distinguished with respect to the plane of polarization. The infrared beam polarized parallel to the plane of incidence gives rise to the transverse magnetic (*TM*) wave with an amplitude $E_{\parallel,0}$ given by

$$E_{\parallel,0} = \sqrt{\left|E_{zo}\right|^2 + \left|E_{xo}\right|^2} \tag{3.7}$$

that can interact with the *x*- and *z*-components of the transition dipole moment of the sample, i. e. $\underline{M}_x$ and $\underline{M}_z$. $E_{yo} = E_{\perp,0}$ represents the electric field for perpendicular polarized radiation generating the transverse electric (*TE*) wave that only excites the *y*-component of the dipole moment, $\underline{M}_y$ (equation 3.4). *TM* and *TE* wave are displayed in figure 3.3.
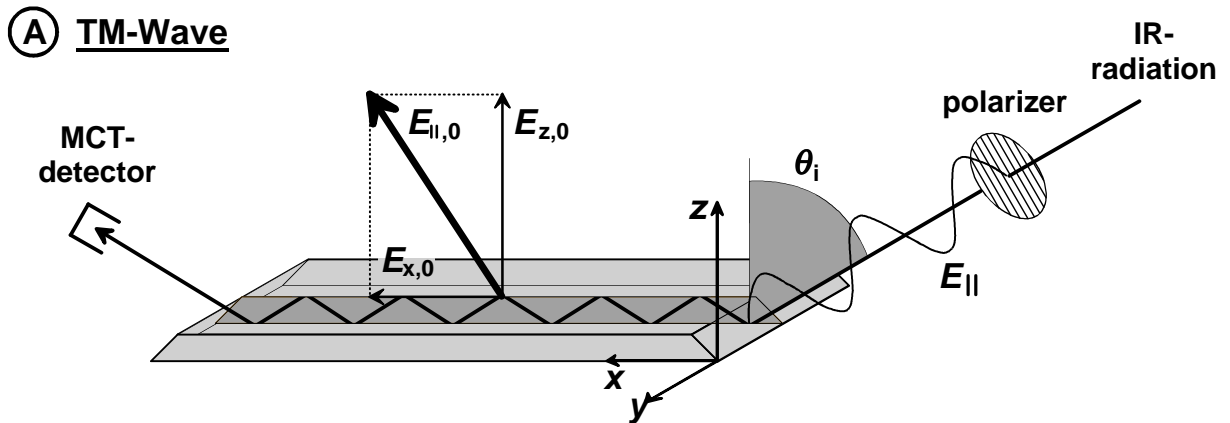

Figure 3.3:   Schematic presentation of attenuated total reflection (ATR) in multiple reflection mode. For easier recognition, the plane of incidence is drawn in a darker grey than the rest of the ATR crystal. Infrared light polarized parallel to the plane of incidence contributes (A) to the TM wave.
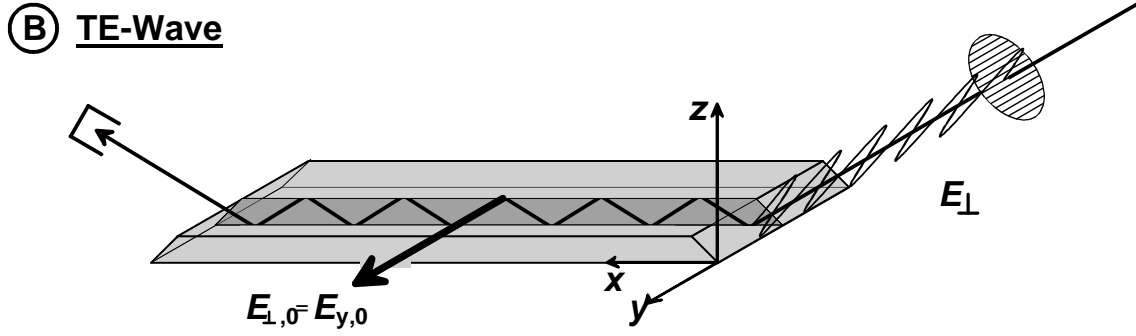
Figure 3.3   Attenuated total reflection (ATR) in multiple reflection mode (schematic presentation continued). (B) The TE wave consists of infrared light polarized perpendicular to the plane of incidence.

When the film thickness is much larger than the penetration depth d_p, only molecules within the so-called effective thickness, d_e, interact with the infrared radiation. For a weakly absorbing sample medium, d_e is proportional to the square of the intensity of the oscillating standing wave at the interface, E_{xo}^2, E_{yo}^2, and E_{zo}^2 as given in equation 3.4, while the factor $\cos^{-1}\theta_i$ corresponds to the change in area sampled by the IR beam. The effective thickness for the *TM* and *TE* waves, $d_{e,\parallel}$ and $d_{e,\perp}$, respectively, is determined by $E_{\parallel,0}^2 = E_{xo}^2 + E_{zo}^2$, $E_{\perp,0}^2 = E_{yo}^2$ and equation 3.8.

$$d_e = \frac{n_{ti} \cdot E_0^2 \cdot d_p}{2\cos\theta_i} \tag{3.8}$$

$$d_{e,\parallel} = \frac{n_{ti} \cdot \cos\theta_i \cdot (2\sin^2\theta_i - n_{ti}^2)\lambda_i}{\pi \cdot (1-n_{ti}^2) \cdot [(1+n_{ti}^2)\cdot \sin^2\theta_i - n_{ti}^2]\cdot \sqrt{\sin^2\theta_i - n_{ti}^2}}, \text{ and } d_{e,\perp} = \frac{n_{ti} \cdot \cos\theta_i \cdot \lambda_i}{\pi \cdot (1-n_{ti}^2)\cdot \sqrt{\sin^2\theta_i - n_{ti}^2}} \tag{3.9}$$

Three-phase system. For thin films deposited on the ATR crystal, the evanescent field has a sizeable intensity even outside of the film, i. e. in the upper medium in figure 3.2. Since the thickness d_f of the film is small compared to d_p, the electric field is considered constant throughout the film, and the intensities of the electric field, $E_\parallel^2$ and $E_\perp^2$, and the effective thickness are given by

$$E_\parallel^2 = \frac{4\cos^2\theta_i \cdot [(1+n_{tf}^2)\sin^2\theta_i - n_{ti}^2]}{(1-n_{ti}^2)\cdot [(1+n_{ti}^2)\sin^2\theta_i - n_{ti}^2]} \quad \text{and} \quad E_\perp^2 = \frac{4\cos^2\theta_i}{1-n_{ti}^2}, \quad \text{and} \tag{3.10}$$

$$d_{e,\parallel} = \frac{4n_{if}\cos^2\theta_i \cdot [(1+n_{tf}^2)\sin^2\theta_i - n_{ti}^2]\cdot d_f}{(1-n_{ti}^2)\cdot [(1+n_{ti}^2)\sin^2\theta_i - n_{ti}^2]} \quad \text{and} \quad d_{e,\perp} = \frac{4n_{if}d_f\cos\theta_i}{1-n_{ti}^2} \quad . \tag{3.11}$$

3.1.3   Dichroism and Orientation of the Molecules

Dichroic Ratio. A preferred spatial orientation (anisotropic growth) of the molecules in the film with respect to the surface and the evanescent field leads to different absorption intensities in the *TM* and *TE* wave for the same vibration mode. Type and degree of orientation in the layer can be

estimated by the fraction of the reflectivities R_{TM} and R_{TE}, i. e. the dichroic ratio, $D_{TE/TM}$, as defined by

$$D_{TE/TM} = \frac{\ln R_{TE}}{\ln R_{TM}} \qquad (3.12)$$

Assuming the two-phase system for thick films (figure 3.2b) and using the complex refractive index for the absorbing medium, $n_j^* = n_j(1+i\kappa_j)$, where $j = x$, y, and z, instead of n_t, *FLOURNOY* and *SCHAFFERS* [96, 100] demonstrated that R_{TM} and R_{TE} result from *FRESNEL'S* equations to give

$$\ln R_{TE} = -\frac{4n_y^2 \kappa_y}{n_i^2 \tan\theta_i \sqrt{\left(1-\left(\frac{n_y^2}{n_i^2 \sin^2\theta_i}\right)\right)\cdot\left(1-\left(\frac{n_y^2}{n_i^2}\right)\right)}} \qquad (3.13)$$

$$\ln R_{TM} = -\frac{4n_x n_z\left(\kappa_z + \kappa_x\left(1-\left(\frac{n_z^2}{n_i^2 \sin^2\theta_i}\right)\right)\right)}{n_i^2 \tan\theta_i \sqrt{\left(1-\left(\frac{n_z^2}{n_i^2 \sin^2\theta_i}\right)\right)\cdot\left(1-\left(\frac{n_z^2}{n_i^2\sin^2\theta_i}\right)+\left(\frac{n_x^2 n_z^2 \cot^2\theta_i}{n_i^4}\right)\right)}} \qquad (3.14)$$

For an isotropic refractive index, i. e. if $n_x = n_y = n_z$, these equations can be written as

$$\ln R_{TE} = -\alpha\cdot\kappa_y \qquad (3.15)$$

$$\ln R_{TM} = -\beta\cdot\kappa_x - \gamma\cdot\kappa_z \qquad (3.16)$$

At an angle of incidence of $\theta_i = 45°$, and for a uniaxial organic film, i. e. $\kappa_x = \kappa_y$, with an estimated refractive index of $n_f = 1.50$ on KRS-5, $n_i = 2.37$ (or ZnSe, $n_i = 2.40$), the values of the constants are $\alpha = 5.99$ (5.48), $\beta = 1.99$ (1.97), and $\gamma = 10.00$ (9.00), respectively. For isotropic films, i. e. if the molecules show no preferred orientation, holds $\ln R_{TM} = 2\cdot\ln R_{TE}$ [100].

Molecular Orientation. The correlation between the orientation of the molecules in the film and the detected dichroism of the absorption bands in ATR spectra is described in terms of the two coordinate systems, figure 3.1. This is due to the fact that infrared and raman activity are understood on a molecular level, whereas the spectra display the behaviour of a film of molecules with respect to the spectrometer coordinate system. As suggested by *ZBINDEN* [98], the transition moment $\underline{\mu}_{abc}$ in molecular coordinates is transformed to $\underline{\mu}_{xyz}$ in spectrometer coordinates by use of the transformation matrix $\underline{T}$ as illustrated in figure 3.4a) and given by $\underline{\mu}_{xyz} = \underline{T}\cdot\underline{\mu}_{abc}$, where

$$(\mu_x,\mu_y,\mu_z) = \begin{pmatrix} T_{11} & T_{12} & T_{13} \\ T_{21} & T_{22} & T_{23} \\ T_{31} & T_{32} & T_{33} \end{pmatrix}\cdot\begin{pmatrix} \mu_a \\ \mu_b \\ \mu_c \end{pmatrix}. \qquad (3.17)$$

The number of transition moments that point in the segment υ, $\upsilon+\delta\upsilon$; $\zeta+\delta\zeta$ is denoted by the distribution function $a(\upsilon, \zeta)$. This gives rise to the absorption intensity, $I_{x,y,z}$, of the entire film, for example I_x, as given by an integration of the form

$$I_x = \int_{\upsilon=0}^{\pi} \int_{\zeta=0}^{2\pi} a(\upsilon,\zeta) \cdot \sin\upsilon \cdot \mu_x^2 \, d\zeta d\upsilon \tag{3.18}$$

In this way, models for molecular orientation such as axial, uniaxial, or planar, can be formulated in terms of equation 3.17 and compared to the observed dichroism. For the case of *tert*-butylcalix[4]-arene spectra measured in ATR mode with polarized radiation, this equation is simplified, since M_x and M_z correlate with the *TM* wave, while M_y coincides with *TE*. The degeneration of the *E*-type vibrations in the (a, b)-plane, leads to a combined excitation of $\underline{\mu}_a$ and $\underline{\mu}_b$.
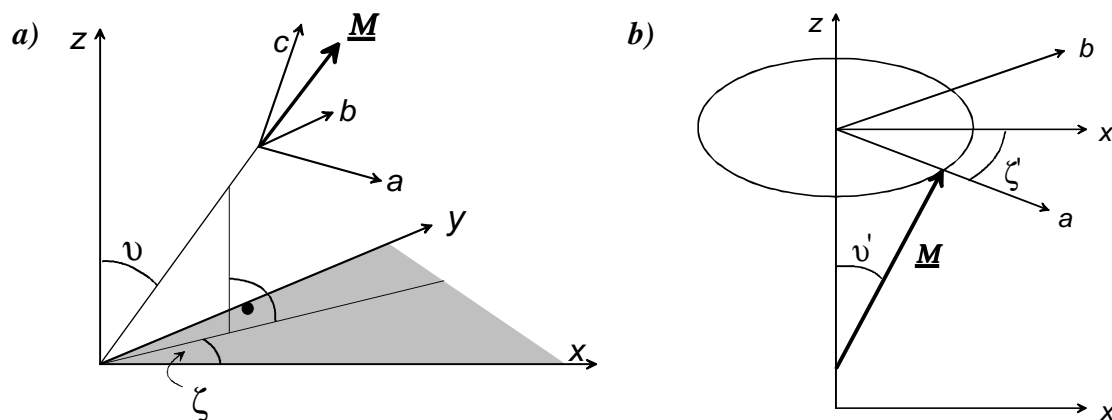
Figure 3.4: *a) Orientation of the dipole moment $\underline{\mu}$ in the molecular, (a, b, c), and the spectrometer coordinate system, (x, y, z). b) Perfect axial orientation, the principal axis ($C_4 = c$) is parallel to the z-axis. The transition moment $\underline{\mu}$ forms an angle υ' with the c-axis [98].*

The dichroic behaviour for a perfect axial orientation of the molecules in the film will be deduced in the following, figure 3.4b). In this type of orientation, the molecules are aligned parallel, but slightly tilted with respect to the $z = c$ axis. For an individual molecule, the transition moment $\underline{\mu}$ forms an angle of υ' with the c axis, and, consequently, the components of $\underline{\mu}$ in coordinates of the molecule result in $\mu_a = |\underline{\mu}| \sin \upsilon'$, $\mu_b = 0$, and $\mu_c = |\underline{\mu}| \cos \upsilon'$, and the components in the spectrometer system are given by the transformation equation

$$(\mu_x, \mu_y, \mu_z) = \begin{pmatrix} \cos\zeta' & \sin\zeta' & 0 \\ -\sin\zeta' & \cos\zeta' & 0 \\ 0 & 0 & 1 \end{pmatrix} \cdot \begin{pmatrix} \mu_a \\ \mu_b \\ \mu_c \end{pmatrix} \tag{3.19}$$

The absorption intensity for an individual molecule, for example, in the *x*-direction, is proportional to the square of the component of the transition moment μ_x. The expected band intensity, I_x, for the

whole film is obtained by integrating μ_x^2 over all possible molecular orientations. For the specific case of perfect axial orientation, the integration has to be carried out over the angle ζ' only.

$$I_x = \frac{1}{2\pi} \int\limits_{\zeta'=0}^{2\pi} (\cos\zeta'\cdot\mu_a + \sin\zeta'\cdot\mu_b)^2 d\zeta' = \frac{1}{2\pi}\mu^2 \sin^2 \upsilon' \int\limits_{0}^{2\pi} \cos^2 \zeta' d\zeta' = \frac{1}{2}\mu^2 \sin^2 \upsilon' \qquad (3.20)$$

$$I_z = \frac{1}{2\pi} \int\limits_{\zeta'=0}^{2\pi} \mu_c^2 d\zeta' = \mu^2 \cos^2 \upsilon' \qquad (3.21)$$

with the normalization factor $1/2\pi$. Symmetry considerations show that $I_y = I_x$. Consequently, the expected dichroic ratio concerning the three main axes results in

$$D_{x/y} = 1 , \quad \text{and} \quad D_{x/z} = D_{y/z} = \frac{1}{2}\tan^2 \upsilon' \qquad (3.22)$$

For a transition moment that is parallel to $c = z$ ($\upsilon' = 0°$), $D_{y/z}$ becomes 0, and for a perpendicular band ($\upsilon' = 0°$) $D_{y/z}$ is equal to infinity. If a film is known to have perfect axial orientation, the angle υ' for various transition moments can be calculated from the observed dichroic ratio of the corresponding vibration bands [98].

3.1.4   Infrared Reflection Absorption Spectroscopy (IRAS)

General Purpose. Since IRAS provides information about the direction of transition dipoles in a sample, it is a useful characterization method to study the molecular structure or the orientation of molecules in thin organic films and the binding at chemically modified metallic surfaces. It originates from the work of *S. A. FRANCIS* and *A. H. ELLISON* [101], while important theoretical contributions were made by *R. G. GREENLER* [97, 102].

The incident electromagnetic radiation interacts with the sample layer, subsequently hits the reflective surface typically at 'grazing' angle of $\theta_i = 83°$ from the surface normal, and again interacts with the sample on its way to the detector, figure 3.5. The intensity of an absorption band in the spectrum depends on the amplitude of the electric field at the surface, the orientation of the transition dipole moment relative to the electric field, and the amount of molecules interacting with the radiation that is proportional to the secant of the angle of incidence. Since the beam area is larger for higher angles of incidence, the sensitivity of the reflection method is raised by a factor of approximately 25 as compared to transmission through the same film at normal incidence.
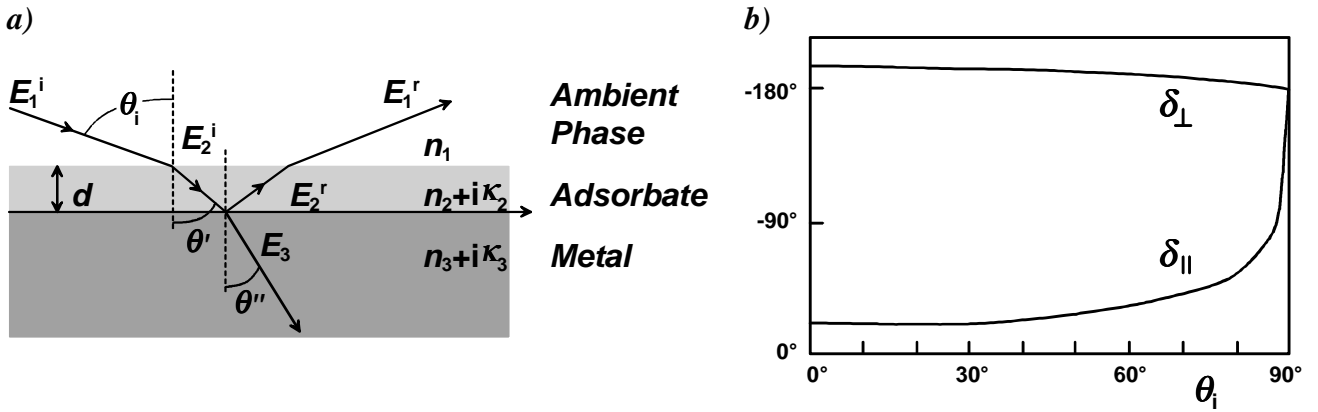
Figure 3.5: a) *Three-layer model of a plane metal surface covered by a thin, isotropic, and homogeneous layer. b) The parallel and perpendicular components of the infrared radiation experience a phase shift upon reflection at the metal surface. While $\delta_\perp \approx -180°$ for all angles of incidence, θ_i, $\delta_\parallel$ strongly depends on θ_i [97, 102].*

Electric Field [89, 97, 102, 103]. A model for the shape of the electric field at the metal surface is depicted in figure 3.1. Here, the incident beam is separated into two components parallel ($E_{i\parallel}$) and perpendicular ($E_{i\perp}$) with respect to the plane of incidence which is defined by the incident and reflected beam and the surface normal. *FRESNEL'S* equations provide amplitude r and phase δ of the reflected wave with respect to the incident wave in terms of the complex refractive index $n_j^* = n_j(1 + i\kappa_j)$. Since $n^2 + \kappa^2 \gg 1$ holds for metals in the infrared region, the reflectivities, $R_\parallel$ and $R_\perp$, and phase shifts on reflection, $\delta_\parallel$ and $\delta_\perp$ (figure 3.5 b), are given by

$$R_\parallel = r_\parallel^2 = \frac{(n - \sec\theta_i) + \kappa^2}{(n + \sec\theta_i) + \kappa^2} \quad \text{and} \quad R_\perp = r_\perp^2 = \frac{(n - \cos\theta_i) + \kappa^2}{(n + \cos\theta_i) + \kappa^2} \tag{3.23}$$

with the secant of the angle of incidence, $\sec\theta_i = 1/\cos\theta_i$. If the amplitude of the incident electric field is $E_i \sin\vartheta$ (where ϑ is an arbitrary phase), the reflected wave is described by $E_r = E_i\, r \sin(\vartheta + \delta)$, and, consequently, the resulting field at the surface is given by

$$E = E_i + E_r = E_i\, [\sin\vartheta + r \sin(\vartheta + \delta)] \tag{3.24}$$

both for $E \equiv E_\parallel$, i.e. the parallel, and $E \equiv E_\perp$, the perpendicular component. For all angles of incidence θ_i, $E_{i\perp}$ and $E_{r\perp}$ remain parallel to the surface and, consequently, the resulting electric field perpendicular to the plane of incidence results in

$$E_\perp = E_{i\perp}\, [\sin\vartheta + r_\perp \sin(\vartheta + \delta_\perp)]. \tag{3.25}$$

For $r_\perp \approx 1$ and $\delta_\perp \approx -180°$ at any angle of incidence, the phase change leads to destructive interference and an infinitesimal small electric field $E_\perp$ at the surface. Since nearly no interactions with the adsorbate occur, vibration modes with an electric dipole moment aligned perpendicular to the plane of incidence will not be excited.

In contrast to this, the phase shift of the parallel polarized electric field, $\delta_\parallel$, strongly varies with the angle of incidence. For a wide range of angles θ_i, small values of $\delta_\parallel$ result, while, at grazing incidence, $\theta_i \approx 90°$, the vector of the parallel polarized electric field, $\underline{E}_\parallel$, experiences a phase shift of $\delta_\parallel = -180°$, and $E_{i\parallel}$ and $E_{r\parallel}$ cancel each other out at the metal surface. For a reflection phase shift close to 90°, the vectors of the incident and reflected $\underline{E}_\parallel$ field add constructively and give rise to an elliptical standing wave with a sizable component normal to the surface. Consequently, maximum amplification of $E_\parallel$ occurs at a high but yet not grazing angle of incidence. The components of the $E_\parallel$ vector are parallel ($E_{\parallel,x}$) and normal ($E_{\parallel,z}$) to the surface, i. e. in the x- and z-directions, figure 3.1 and 3.6, with

$$E_{\parallel,x} = E_{i,\parallel,x} + E_{r,\parallel,x} = E_{i\parallel} \cos \theta_i \, [\sin \theta_i - r_\parallel \sin (\vartheta + \delta_\parallel)], \text{ and} \tag{3.26}$$

$$E_{\parallel,z} = E_{i,\parallel,z} + E_{r,\parallel,z} = E_{i\parallel} \sin \theta_i \, [\sin \vartheta + r_\parallel \sin (\vartheta + \delta_\parallel)]. \tag{3.27}$$

Since they are in opposite directions, the components $E_{i,\parallel,x}$ and $E_{r,\parallel,x}$ combine to result in only a very small $E_{\parallel,x}$ for all θ_i, (offset in figure 3.6). In contrast to this, $E_{\parallel,z}$ tremendously increases at high angles of incidence, yielding a maximum normal component of $\sim 2\,E_{i\parallel}$ at $\theta_i \approx 82$ - 84°. For the parallel polarized beam, the enhancement of $E_{\parallel,z}$ by a factor of $\frac{1}{3}$, and the small resulting field $E_{\parallel,x}$ are depicted in figure 3.6. For further mathematical formulation, the interested reader is referred to [89, 97, 102].
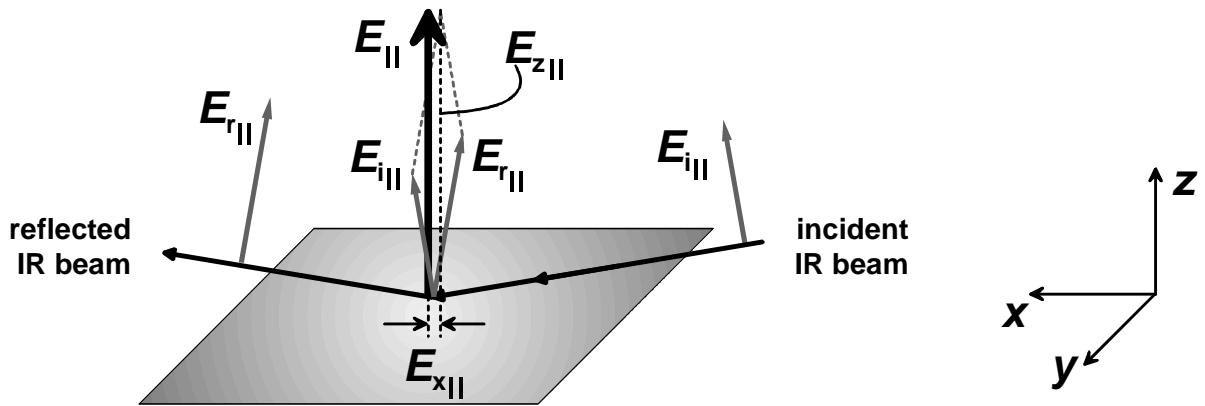
Figure 3.6:   Reflection geometry of the parallel component of the electric field $E_\parallel$ that impinges the metallic surface at a high angle of incidence. While $E_{i\parallel}$ and $E_{r\parallel}$ denote the incident and reflected $\underline{E}$ vectors, $E_{\parallel,x}$ and $E_{\parallel,z}$ result from constructive interference at the surface. The resulting total electric field $E_\parallel$ is aligned parallel to the plane of incidence.

As mentioned above, the number of molecules interacting with the radiation is proportional to $\sec \theta_i$. Thus, the total absorption intensity in IRAS experiments (figure 3.7) is given by

$$\Delta R = (E_{\parallel,z} / E_{i\parallel})^2 \sec \theta_i. \tag{3.28}$$

This function has the same shape for all metals reflecting in the infrared. Since the reflectivity of the clean metal, however, depends both upon the refractive index and the extinction coefficient (n_3 and k_3 in figure 3.5), the optimum angle of incidence is different for different metals [89, 92].

Figure 3.7:   *Electric field (broken line) at a clean gold surface as a function of the angle of incidence, θ_i. It results from constructive interference of incident and reflected radiation parallel to the plane of incidence. The solid line represents the tot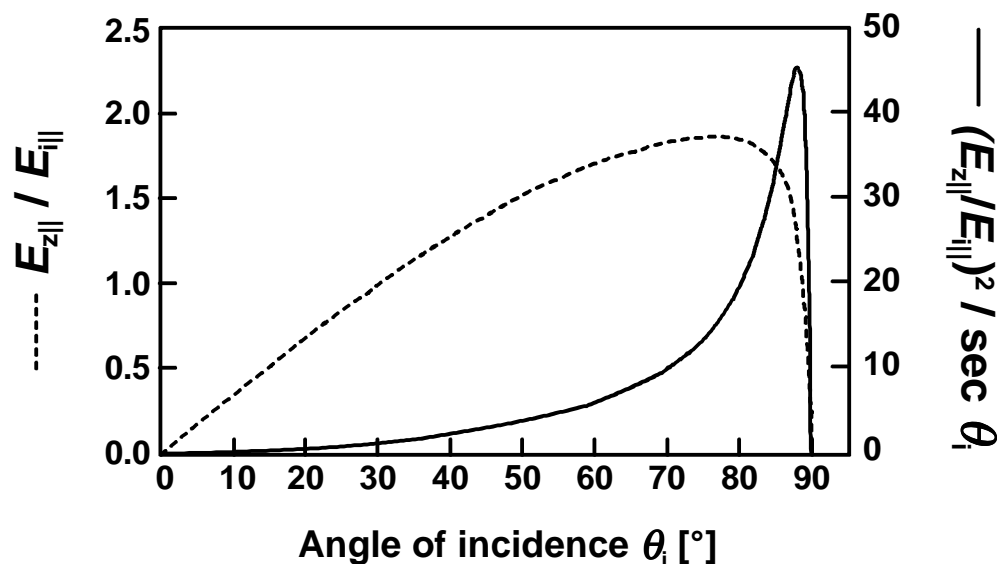al absorption intensity for vibrational excitation. In the calculations, the refractive index of gold, $n^* = 9.05 + 28.2\ i$, was used [89, 104a].*

It is a quite unique characteristic for IRAS spectroscopy that there exists no perpendicular field, $E_\perp$, at the metal surface, whereas enhanced sensitivity occurs for the parallel field, $E_\parallel$. This additional selection rule is called the *surface dipole selection rule*. Since only vibrational modes that are aligned parallel to the surface normal will appear with enhanced intensity, the orientation of the molecules or a particular chemical group can be determined from a comparison of the IRAS and the bulk (transmission) infrared spectra. For non-metallic substrates, e. g. semi-conductors, maximum sensitivity is obtained for angles of incidence $\theta_i = 60 - 80°$ for the parallel polarization, and close to normal, i. e. $\theta_i \approx 90$ for the components perpendicular with respect to the plane of incidence. In thsi case, vibrational modes in the sample layer are excited by all three directions of the electric field, and only the dipole selection rule (cf. table 3.1) determines the activity of a vibrational mode in the spectra.

Comparing the two variants of surface sensitive infrared spectroscopy, it becomes clear that the dichroism of particular absorption bands that indicates a preferred orientation of the molecules results from different interaction effects. While in ATR mode, the three components of the evanescent field are separated by the polarizer to generate the *TM* and *TE* waves, the *surface dipole selection rule* results in something similar in IRAS for metallic surfaces. The phase shift upon reflection reduces $E_\perp \equiv E_y$, and $E_{\parallel,x}$, and enhances only $E_{\parallel,z}$ for high but not grazing angles of incidence.

3.2   Ellipsometry

General Considerations. Ellipsometry is a common optical technique for the determination of the thickness and refractive index of thin films adsorbed or evaporated on a reflecting substrate, as initiated by *DRUDE* in 1889 [105]. For isotropic media, *FRESNEL'S* equations of reflection (r) and transmission (t) define the ellipsometric angles Δ and Ψ that describe the change in the state of polarization of light upon reflection at the surface [106].

Measurement principle. If linearly polarized light is reflected from a metallic surface, amplitude and phase of both parallel ($E_\parallel$) and perpendicular ($E_\perp$) components are changed, i. e. they experience a phase shift, $\delta_\parallel$ and $\delta_\perp$, as described for IRAS in the previous paragraph. Consequently, linearly polarized monochromatic light incident on a surface becomes elliptically polarized after reflection. This phenomenon is used to estimate the thickness of the considered film.

In the case of the PCSA (*P*olarizer, *C*ompensator, *S*ample, *A*nalyzer) ellipsometer setup, shown in figure 3.8, a compensator, *C*, counterbalances this phase shift prior to reflection in order to have linearly polarized radiation reflected from the surface.

Measuring changes in the state of polarization of the reflected light, the polarizer *P* and the analyzer *A* are adjusted to extinguish the light intensity, i. e. to become zero at the detector. Usually the measurement results are represented as ellipsometric angles Δ and Ψ which are related to the polarizer and analyzer angles in quenching position.
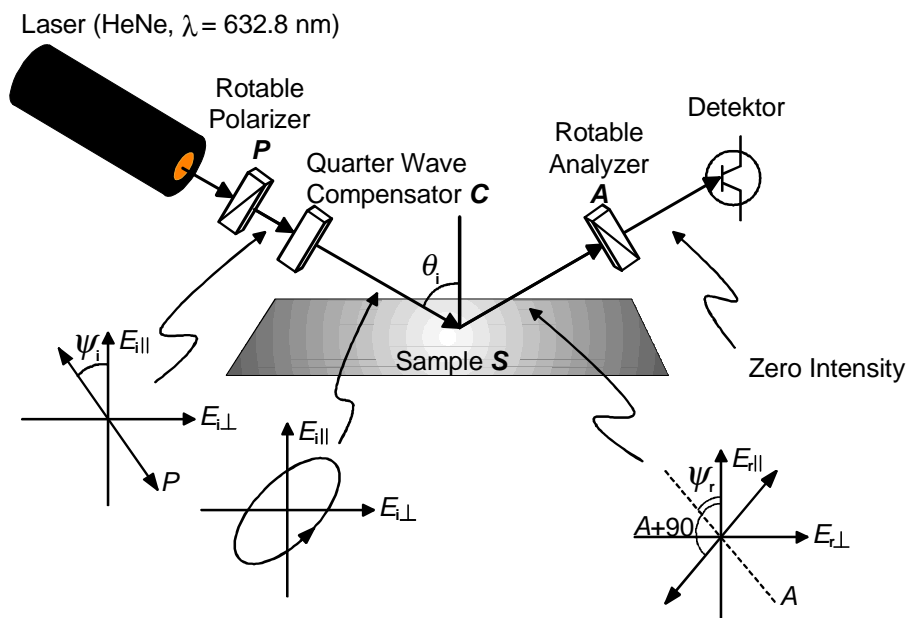
Figure 3.8:   *The principal setup and function of the PCSA null ellipsometer consisting of **P**olarizer, **C**ompensator, **S**ample and **A**nalyzer (redrawn from [104b]). By compensation the phase shift, initially linearly polarized monochromatic light becomes elliptically polarized prior to reflection, and turns out linearly polarized after reflection at the surface. The analyzer is adjusted to yield zero intensity at the detector.*

The thickness of the organic film is determined in two steps. For the clean substrate, *FRESNEL*'s equations are applied to calculate the refractive index, $n_s^* = n_s + i\kappa_s$ for the two phase system depicted in figure 3.9 a). After preparation of the film, the sample is measured again, and, with knowledge of n_s^* and n_f^*, Δ and Ψ are converted into an average thickness of the film, d_f, using the three-phase model in figure 3.9 b) and the method of McCrackin [107]. Δ and Ψ can be obtained experimentally, i. e. $\Delta = 270° - 2\,P$ and $\Psi = A$.
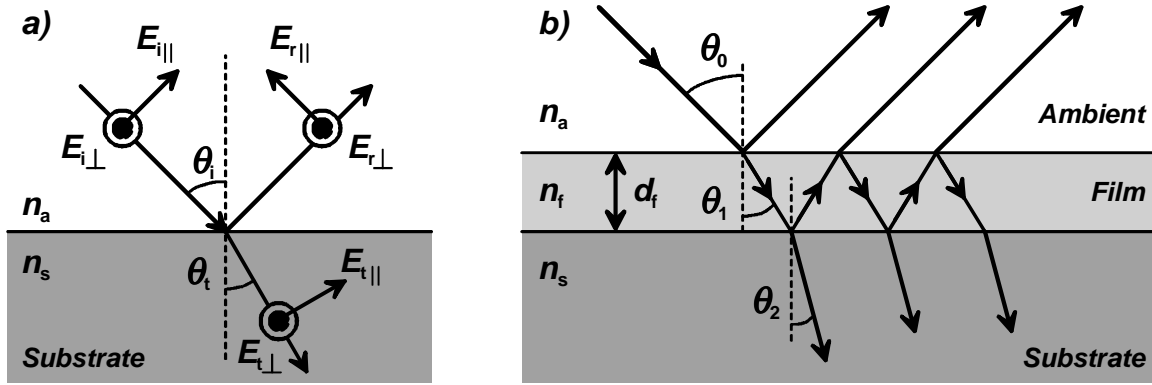

Figure 3.9:   Reflection and transmission of a plane polarized wave. a) Two-phase system with parallel (E∥) and perpendicular (E⊥) components of the electric field. b) A three-phase model is used to determine the thickness of the layer, d_f, on a substrate. n_a, n_f, and n_s are the (complex) refractive indices of the ambient, the film and the substrate respectively, while θ_i denotes the angle of incidence, i = 0,1,2 [106].

FRESNEL equations. The reflected and transmitted parts of the incident light are evaluated in terms of the complex *FRESNEL* coefficients $r_\parallel = |r_\parallel|\exp(i\delta_\parallel)$ and $r_\perp = |r_\perp|\exp(i\delta_\perp)$, where $\delta_\parallel$ and $\delta_\perp$ denote the phase differences after reflection for the parallel and perpendicular components. The complex ratio of the reflection coefficients, ρ, can be calculated from

$$\rho = \frac{r_\parallel}{r_\perp} = \left|\frac{r_\parallel}{r_\perp}\right| \exp\left[i(\delta_\parallel - \delta_\perp)\right] = \tan\psi \exp(i\Delta) \,. \tag{3.29}$$

Ψ and Δ determine the differential changes in amplitude and phase, with $\tan\Psi = |r_\parallel| / |r_\perp|$. By substitution of $r_\parallel$ and $r_\perp$ from *FRESNEL*'s equations, and using of *SNELL*'s law, the refractive index of the substrate, n_s, is given by

$$n_s = n_a \sin\theta_i \sqrt{1 + \frac{1-\rho}{1+\rho}\tan^2\theta_i} \tag{3.30}$$

The ellipsometric measurements of an organic layer on a gold substrate is described by the three-phase system with multiple reflections, as displayed in figure 3.9b). With the *FRESNEL* reflection coefficients of the parallel-plane interfaces between ambient (*a*) and film (*f*), and between film and substrate (*s*) for the parallel and perpendicular light, $r_{\parallel,af}$, $r_{\parallel,fs}$, $r_{\perp,af}$, and $r_{\perp,fs}$, respectively, the summation of all the reflected partial waves leads to the total reflection amplitudes

$$r_{\|,\mathrm{afs}} = \frac{r_{\|,\mathrm{af}} + r_{\|,\mathrm{fs}} \cdot \exp(-2\,i\beta)}{1 + r_{\|,\mathrm{af}} \cdot r_{\|,\mathrm{fs}} \cdot \exp(-2\,i\beta)} \quad , \;\mathrm{and} \quad r_{\perp,\mathrm{afs}} = \frac{r_{\perp,\mathrm{af}} + r_{\perp,\mathrm{fs}} \cdot \exp(-2\,i\beta)}{1 + r_{\perp,\mathrm{af}} \cdot r_{\perp,\mathrm{fs}} \cdot \exp(-2\,i\beta)} \tag{3.31}$$

Equation 3.31 is known as *DRUDE* equation. Finally with equation 3.29, the complex reflectance ratio, ρ, can be calculated from

$$\tan\psi\, e^{i\Delta} = \rho = \frac{r_{\|}}{r_{\perp}} = \frac{r_{\|,\mathrm{af}} + r_{\|,\mathrm{fs}} \cdot \exp(-2\,i\beta)}{1 + r_{\|,\mathrm{af}} \cdot r_{\|,\mathrm{fs}} \cdot \exp(-2\,i\beta)} \cdot \frac{1 + r_{\perp,\mathrm{af}} \cdot r_{\perp,\mathrm{fs}} \cdot \exp(-2\,i\beta)}{r_{\perp,\mathrm{af}} + r_{\perp,\mathrm{fs}} \cdot \exp(-2\,i\beta)} \tag{3.32}$$

$$\mathrm{with} \quad \beta = 2\pi \left(\frac{d_{\mathrm{f}}}{\lambda}\right)\sqrt{n_{\mathrm{f}}^2 - n_{\mathrm{a}}^2 \sin^2\theta_{\mathrm{i}}} \tag{3.33}$$

The film thickness d_{f} can be calculated from the phase angle β (film phase thickness), whereas λ is the wavelength of the light in vacuum. In this way, ρ can be understood as a function of n_{a}, n_{f}, n_{s}, d_{f}, θ_0, and λ. In order not to end up in an underdetermined system for the calculation of d_{f}, n_{a}, is determined in the first measurement step mentioned above, and n_{f}, is pre-set to an appropriate value for organic layers. For further details, the interested reader is suggested to consult [106].

3.3   *Contact Angle Measurements*

Contact angle measurements characterize the surface with respect to wetting properties and surface tension. Surface and interfacial energies determine how macroscopic liquid droplets deform when they adhere to a surface. Thus the liquid drop contact angle θ, measured at the triple point where vapor, liquid and solid phase are in contact, probes microscopic properties of the surface, such as hydrophilicity, surface roughness or heterogeneity and characteristics of the interface, e. g. work of adhesion and interfacial energy. Since equilibrium conditions correlate to a minimum of *GIBBS* free energy, solids and liquids always take the shape with the lowest amount of free surface at a maximum of volume, like curved surfaces or drops. On a hydrophilic surface, for example, a drop of water is favorable spread out over the surface, whereas it exposes minimal area to a hydrophobic surface [108-112].

The case of a sessile drop on a solid substrate is illustrated in figure 3.10. The *surface energies* of the solid-vapor and liquid-vapor interface are denoted as γ_{sv} and γ_{lv}, whereas γ_{sl} is the solid-liquid *interfacial surface energy*. The relation between the contact angle θ and the interfacial energies are described by *YOUNG'S* equation $\gamma_{\mathrm{lv}}\cos\theta = \gamma_{\mathrm{sv}} - \gamma_{\mathrm{sl}}$ that will be deduced in the following.
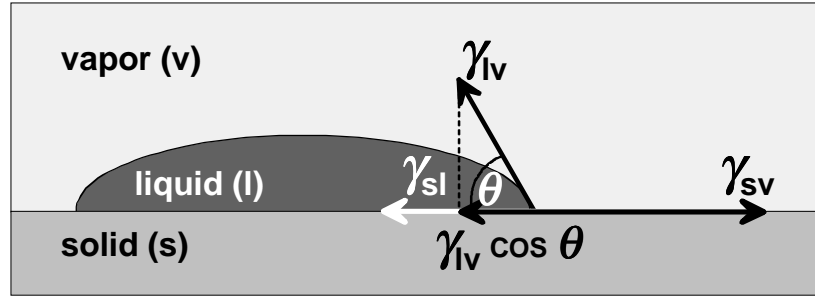
Figure 3.10: Schematic setup of static contact angle measurements. A liquid drop (l) on a solid surface (s) is in equilibrium with the ambient gas (vapor, v) saturated with respect to the vapor pressure of the liquid. θ defines the static contact angle at the solid-liquid interface, γ_{ij} are the surface tensions for the interfaces, and the subscripts s, l and v refer to the solid, liquid and vapor phases, respectively.

Interface Energies and *YOUNG'S* Equation. To increase the surface of a liquid or a solid by an area of $dA_\Diamond$, one has to surmount intermolecular forces, to break chemical bonds of the bulk and to remove neighbour atoms. Driving force for the formation of a new interface is a decrease in free energy dG. The reversible work of adhesion W_{ad} is defined as difference in free energy needed to separate the solid-liquid interface from the solid-vacuum and the liquid-vacuum interfaces. Consequently, it derives from the *GIBBS* free energy G for constant temperature T, pressure p and amount of substance N_i.

$$dG = -SdT + Vdp + \gamma\, dA_\Diamond + \sum \mu_i dN_i$$

$$(dW_{ad})_{T,p} = \left(\frac{\partial G}{\partial A_\Diamond}\right)_{T,p,N} \cdot dA_\Diamond = \gamma_{ij} \cdot dA_\Diamond,\ \text{with}\ \gamma_{ij} = \left(\frac{\partial G}{\partial A_{\Diamond,ij}}\right)_{T,p,N} \tag{3.34}$$

The measurement setup of contact angles θ consists of a liquid drop on a solid surface that is in equilibrium with the ambient vapor, as described by a three-phase system displayed in fig 3.10. The free interfacial energy is given by the *DUPRÉ* equation

$$W_{slv} = \gamma_{sv} + \gamma_{lv} - \gamma_{sl} \tag{3.35}$$

Since each interfacial energy exerts a pressure tangentially along the interface, the surface forces acting in different directions have to balance out in the triple point under equilibrium conditions. Vector addition of γ_{ij} in figure 3.10 gives the *YOUNG* equation

$$\gamma_{lv}(1+\cos\theta) = W_{slv} = \gamma_{sl} + \gamma_{lv} - \gamma_{sv}$$

$$\Rightarrow\ \gamma_{sv} = \gamma_{sl} + \gamma_{lv}\cos\theta\ \Leftrightarrow\ \cos\theta = \frac{\gamma_{sv} - \gamma_{sl}}{\gamma_{lv}} \tag{3.36}$$

A combination of equations (3.35) and (3.36) leads to the *YOUNG-DUPRÉ* equation

$$W_{ad} = \gamma_{lv}(1+\cos\theta) \tag{3.37}$$

Equation (3.37) provides a relation between the work of adsorption, the contact angle θ and γ_{lv}. The maximum of W_{ad} results for θ approaching 0°.

The contact angle θ and cos θ, respectively, characterizes the wetting behaviour of a surface towards a liquid phase. cos θ varies from 1 for complete wetting to -1 for complete non-wetting. Since wetting or partial wetting occurs for cos $\theta > 0$ and $\gamma_{sv} - \gamma_{sl} > 0$, it is favoured for high-energy surfaces like metals or oxides rather than for organic surfaces with low interfacial energy, or when solid and liquid are similar and a small γ_{sl} results.

Typical contact angles are listed in table 3.2. The most common liquids in contact angle characterization of SAMs are water and hexadecane (HD). While water probes the hydrophilicity, i. e. the polar characteristics of the surface known, HD probes the apolar characteristics and provides information on the surface composition. For example, in probing the molecular order in -CH$_3$ terminated SAMs with HD, a contact angle $\theta < 47°$ means that CH$_2$ groups are exposed to HD, and, hence, indicates disorder of the aliphatic chains in the SAM [104a].

Table 3.2:   Typical contact angles for various interfaces [104b, 113].

liquid / solid system	static contact angle
H_2O / HS-C_nH_{2n}-CH$_3$ (SAM on gold)	110-112°
H_2O / HS-C_nH_{2n}-OH (SAM on gold)	< 20°
H_2O / wool	160°
mercury / glass or steel	140° / 154°
hexadecane / OH- or -CH$_2$ terminated SAM	< 10°
hexadecane / -CH$_3$ terminated SAM	47°

Several methods are applied to measure the contact angle. Often the amount of liquid in the drop on the surface is increased or decreased, thus measuring the two meta stable states of the advancing θ_a and receding contact angle θ_r, figure 3.11 a) and b). Another way is to move the surface relative to a drop with constant volume. Here, θ_a measures the advancing contact angle when the drop moves over the virgin surface, and θ_r is the angle of the drop retracted from the previously wetted surface, figure 3.11 c).

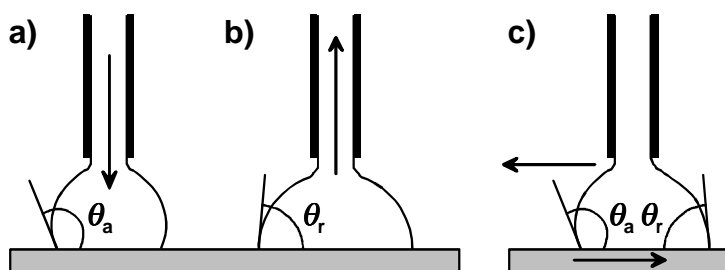*Figure 3.11: Contact angle measurements by the sessile drop method. Increasing (a) and decreasing (b) of the drop size measures the advancing (θ_a) and receding (θ_r) contact angle. (c) By moving the substrate, both contact angles are measured simultaneously.*

The difference of the two angles $\Delta\theta = \theta_a - \theta_r$ is called contact angle *hysteresis* and provides information about the roughness and chemical heterogeneity of the surface. Different chemical or structural components on a surface, i.e. microscopic domains of two different species having different contact angle, produce a heterogeneous surface. The resulting contact angle can be calculated as suggested by Cassie [114]

$$\cos\theta = \sum_i f_i \cos\theta_i \tag{3.38}$$

where f_i is the fraction of the ith component on the surface and θ_i is the contact angle of i on a homogene surface. So, different works of adhesion and cohesion are summarized to give a total work of adhesion and cohesion via Young's equation.

3.4   *Adsorption and Growing Modes*

Particles impinging on the surface are either adsorbed or reflected. The adsorption rate, R_{ads}, is defined by equation 3.39, with the sticking coefficient, S, i. e. the proportion of collisions with the surface that lead to adsorption, and the collision rate, $Z_{(s)}$,

$$R_{ads} = \frac{dN^{ads}_{(s)}}{dt} = S \cdot Z_{(s)}, \text{ with } Z_{(s)} = \frac{p}{\sqrt{2\pi \, mkT}} \tag{3.39}$$

$N^{ads}_{(s)} = \varphi \cdot N^{ads}_{tot}$ represents the density of adsorbed particles per unit area, defined by the total number of adsorption sites available, N^{ad}_{tot}, and surface coverage, φ. The collision rate depends on the partial pressure p, the mass m, and the temperature, T, of the adsorbing gas, while k_B is the *BOLTZMANN* constant. The sticking coefficient, S, is affected by the condensation coefficient $\sigma_{(s)}$, an activation barrier E_{act} (e. g. for chemisorption), and the amount of suitable vacant adsorption sites, $f(\varphi) = 1 - \varphi$ for non-dissociative adsorption (Langmuir conditions)

$$S(\varphi) = \sigma_{(s)} \cdot f(\varphi) \cdot \exp\left(-\frac{E_{act}}{kT}\right) \tag{3.40}$$

The ability of the substrate to dissipate the energy of impinging molecules, orientational and steric effects of the molecules relative to the binding sites of the surface contribute to $\sigma_{(s)}$ [90, 130, 131].

The adsorption of molecules frequently proceeds through a two-step process that leads to a chemisorbed state via a precursor physisorbed phase, according to the scheme

$$Y_{2 \text{ (gas)}} \underset{k_d}{\overset{k_c}{\rightleftarrows}} Y_{2 \text{ (phys)}} \xrightarrow{k_a f(\varphi)} 2 \, Y_{\text{(chem)}} \tag{3.41}$$
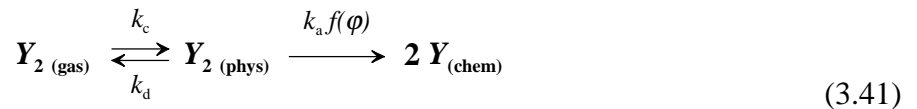
$Y_{2\,(gas)}$, $Y_{2\,(phys)}$, and $Y_{(chem)}$ represent the adsorbat in the gaseous, physisorbed and chemisorbed state. The rate constants k_c and k_d apply to condensation and desorption of the precursor state, and $k_a{\cdot}f(\varphi)$ is the rate constant for conversion from the precursor to the chemisorbed state [115].

Figure 3.12 depicts the interaction potential of the surfaces for a Y_2 molecule that perpendicularly approaches the surface. In the case of $E_a > E_{dp}$, molecules in the physisorbed state have to overcome an energy barrier ΔE, before they are subsequently chemisorbed at the surface [115, 130].
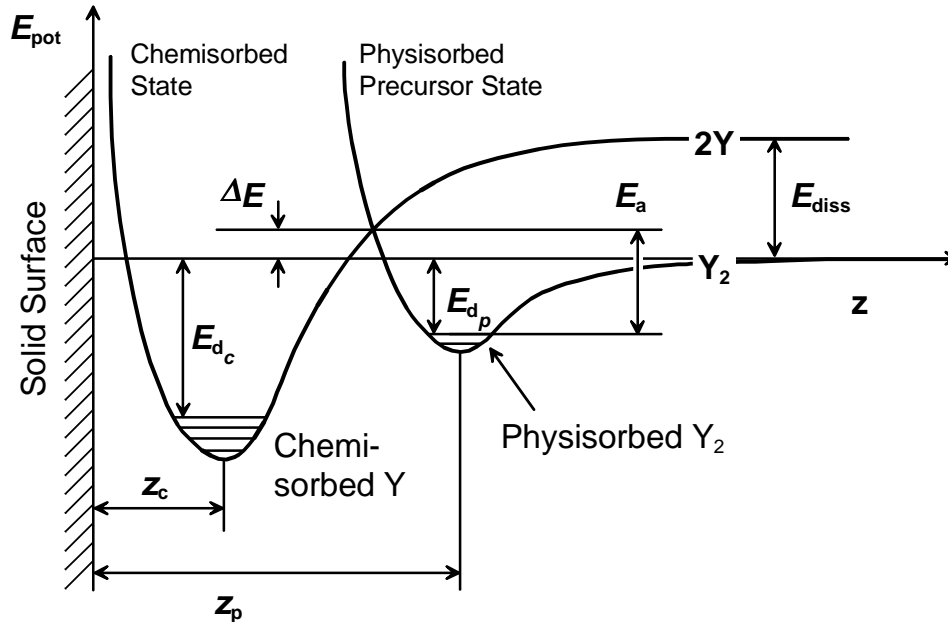
Figure 3.12: Interaction potential for chemisorption and physisorption of a molecule that impinges the surface perpendicular, i. e. in z-direction [115, 130].

For the growth of films on a substrate, three possible modes are distinguished. They are illustrated schematically in figure 3.13 [115, 116]. In the *'island growth'*, or *VOLMER-WEBER* mode, small clusters are nucleated directly on the substrate surface and then grow and form islands of the condensed phase. This happens when the deposited molecules are more strongly bound to each other than to the substrate. Therefore, this mode is displayed by many systems of metals growing on insulators, including many metals on alkali halides, graphite or compounds like mica.

$\varphi < 1$ ML

$1 < \varphi < 2$

$\varphi > 2$

(a)   (b)   (c)

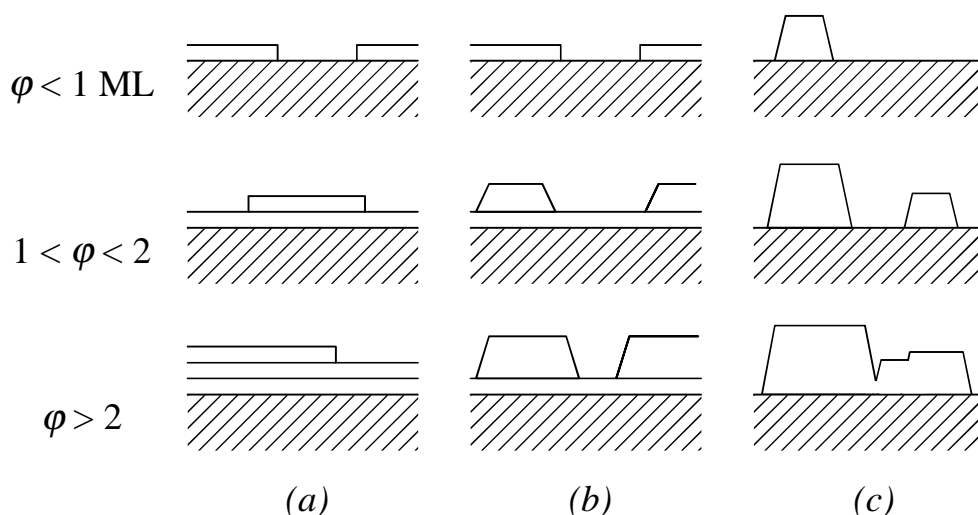*Figure 3.13: Schematic presentation of the three growth modes (a) Layer-by-layer (FRANK-VAN DER MERVE), (b) layer plus island (STRANSKI-KASTRANOV), or (c) isalnd (VOLMER-WEBER) mode. φ represents the coverage of monolayers [116].*

The *'layer-by-layer'*, or *FRANK-VAN DER MERVE* mode, displays the opposite characteristics. Since the molecules are more strongly bound to the substrate than to each other, the first molecules that condense form a complete monolayer on the surface. Subsequently, this first layer is covered by a somewhat less tightly bound second layer. Providing that the decrease in binding is monotonic toward the value for a bulk crystal of the deposit, the layer growth mode is obtained. This growth mode is observed in the case of adsorbed gases, such as several rare gases on graphite and on several metals in some metal-metal systems, and in semiconductor growth on semiconductors.

The *'layer plus island'* or *STRANSKI-KRASTANOV*, growth mode is an intermediate case. After forming the first monolayer, or a few monolayers, subsequent layer growth is unfavourable and islands are formed on top of the 'intermediate' layer. There are many possible reasons for this mode to occur and almost any factor which disturbs the monotonic decrease in binding energy charateristics may be the cause [115, 116].
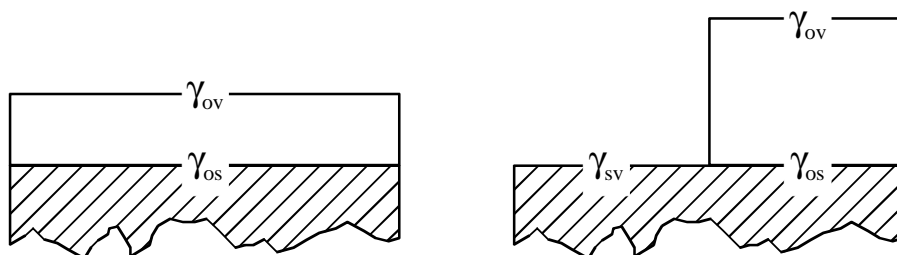

Figure 3.14: Two epitaxial growth alternatives, FRANK-VAN DER MERVE and VOLMER-WEBER [117].

For an estimation which one of the three growth modes is likely to occur, the energy difference, ΔE, between the two epitaxial overlayer arrangements is considered. According to the surface tension

that gives rise to contact angles as described by the *YOUNG* equation, γ_{ov}, γ_{os}, and γ_{sv}, denote the free energy at the overlayer-vacuum interface, the overlayer-substrate interface, and the substrate-vacuum interface, respectively, as illustrated in figure 3.14. Assuming that the *VOLMER-WEBER* cluster occupies half of the available surface, the energy difference ΔE is given by

$$\Delta E = E_{FV} - E_{VW}$$
$$\Delta E = (\gamma_{ov} + \gamma_{os}) \cdot A - \tfrac{1}{2}\,(\gamma_{ov} + \gamma_{os} + \gamma_{sv}) \cdot A \qquad (3.42)$$

Consequently, a complete wetting, i. e. *FRANK-VAN DER MERVE* growth, is expected when $\Delta\gamma = \gamma_{ov} + \gamma_{os} - \gamma_{sv} < 0$, *VOLMER WEBER* growth when $\Delta\gamma > 0$, and *STRANSKI-KRASTANOV* growth when $\Delta\gamma \approx 0$, always keeping in mind, that this estimation is only qualitatively useful since any effects that might arise from the anisotropy of the surface tension are completely neglected. However, methods to determine γ_{os} are rather limited [117]

The influence of thin film morphology can be estimated on basis of electron attenuation in XPS or Auger electron spectra [118]. Figure 3.15 displays extinction curves for characteristic substrate electrons as a function of average coverage of an overlayer. In these examples, the mean free path, λ, is taken as two monolayers, close to the minimum mean free path achievable. In the case of the uniform overlayer, the growth is assumed to be layer-by-layer, and the extinction curve is a series of straight lines with the envelope of points at integral coverage corresponding to an exponential decay. The other curves correspond to a 'single layer plus islanding' growth mode and a case of pure islanding. For the curves involving islanding it is assumed that 50% of the surface is covered.
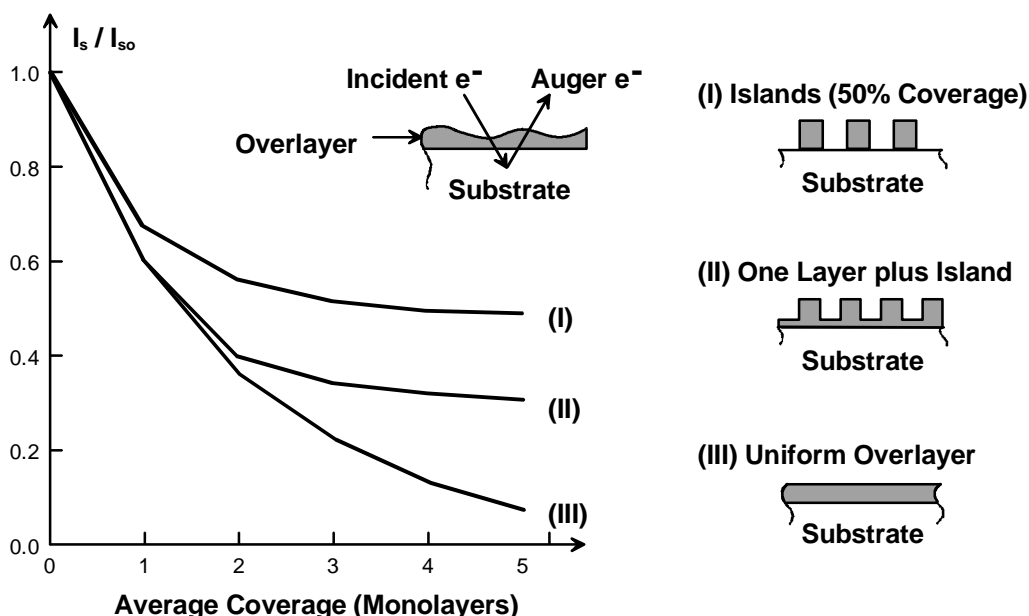

Figure 3.15: Extinction curves for characteristic substrate electrons as a function of average coverage of an overlayer [118].

3.5 Temperature Programmed Desorption (TPD)

TPD (also known as thermal desorption spectroscopy, *TDS*) provides useful information about thermodynamics of chemical reactions and energies of molecules adsorbed at a surface. The method dates back to the early work of *F. URBACH*, *J. B. TAYLOR* and *I. LANGMUIR*, and *L. R. APKER* [119-121], followed by additional pioneering by *G. J. EHRLICH* [122], while *P. A. REDHEAD* [123] developed the theoretical background. Several analytical techniques to determine kinetic parameters are reviewed in literature [124-129].

As outlined in figure 3.16, first a well-defined amount of molecules is adsorbed on a convenient substrate in the UHV at low temperatures. Subsequent desorption of the adsorbate layer is performed by rising the temperature of the surface or by irradiation with light or energetic particles. The desorbing species are monitored with a mass spectrometer counting molecules and molecular fragments in the UHV chamber as a function of the sample temperature.
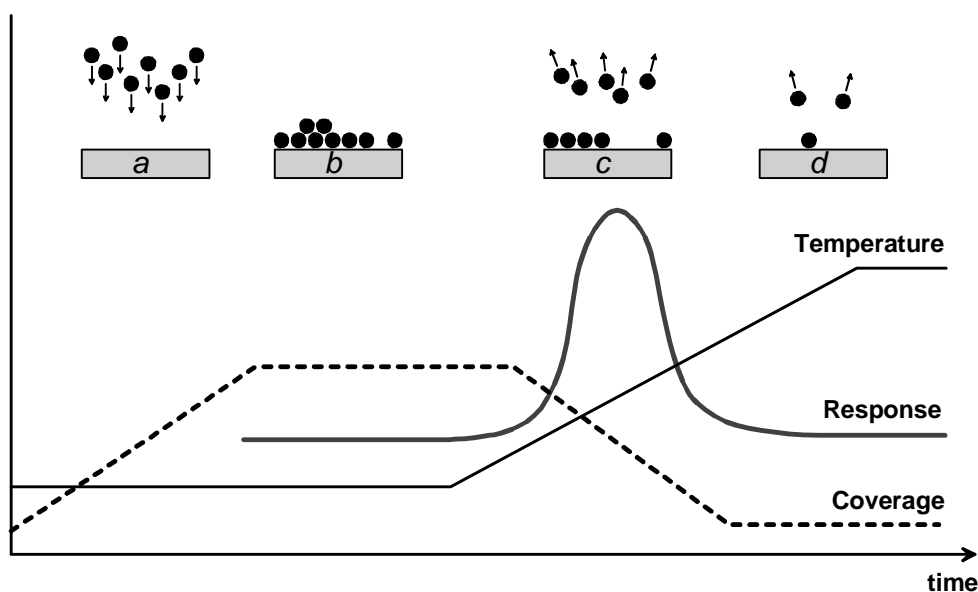
Figure 3.16: The experimental principle of TPD experiments: (a) Deposition of the molecules, (b) adsorbed molecules, (c) heating leads to desorption as detected by mass spectrometery, (d) the response decreases to zero as the last molecules desorb [104a].

The desorption [90, 130, 131] process is described by the desorption rate, R_{des}, i. e. the number of desorbing particles per unit time and surface area. The activation barrier mentioned above and the binding energy E_B contribute to the desorption activation energy, $E_{A,des} = E_B + E_{act}$. Since only molecules that surmount $E_{A,des}$ can desorb from the surface, R_{des} follows an *ARRHENIUS* formalism based on the *BOLTZMANN* distribution (*POLANYI-WIGNER* equation [132])

$$R_{des} = -\frac{dN_{(s)}^{ads}}{dt} = k_m \cdot \left(N_{(s)}^{ads}\right)^m = k_m^0 \cdot \exp\left(-\frac{E_{A,des}}{RT}\right) \cdot \left(N_{(s)}^{ads}\right)^m \qquad (3.43)$$

with the reaction order denoted as m, and the frequency (or pre-exponential) factor, k_m^0. For a first order kinetic, k_1 is the reciprocal of the mean surface lifetime, τ, for adsorbed particles (*FRENKEL* relation):

$$k_1 = k_1^0 \cdot \exp\left(-\frac{E_{A,des}}{RT}\right) = \frac{1}{\tau} \quad \Leftrightarrow \quad \tau = \tau_0 \cdot \exp\left(\frac{E_{A,des}}{RT}\right) \tag{3.44}$$

Consequently, τ depends on the depth $\Delta E_{A,des}$ of the potential wall, whereas τ_0 lies within the time domain of lattice vibrations, $\tau_0 \approx 10^{-13}$ s.
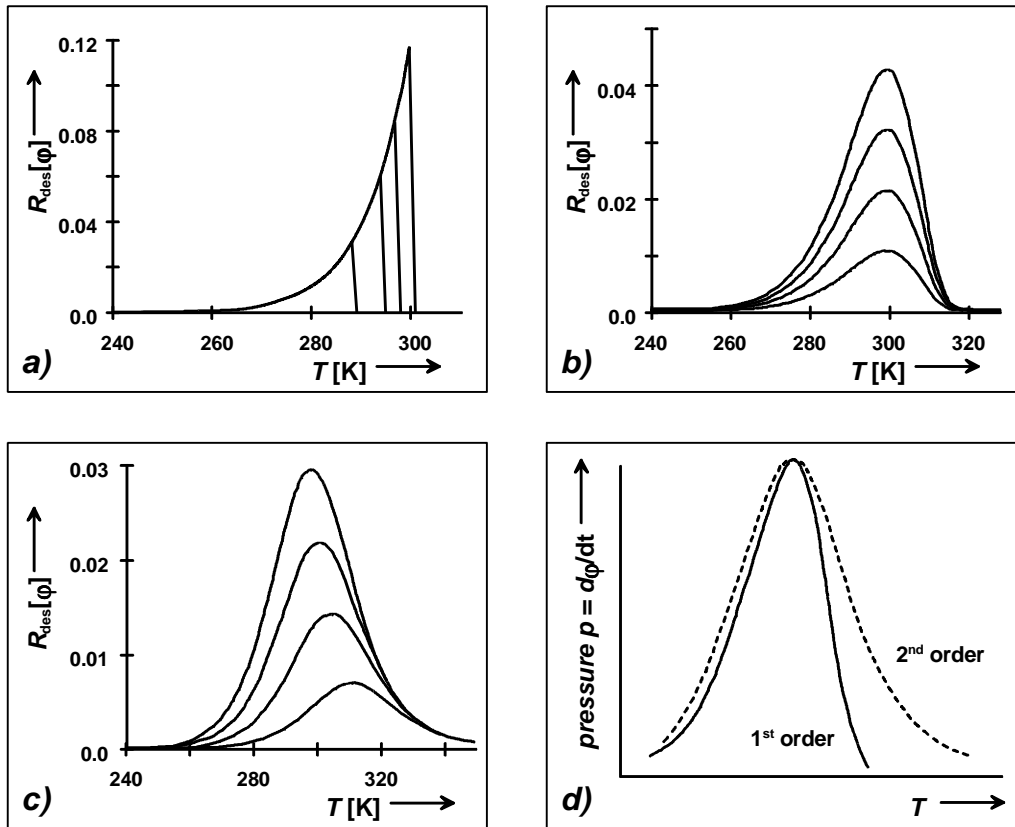
Figure 3.17: Simulated TPD spectra for initial coverages $\varphi = 0.25, 0.50, 0.75$, and 1.00, respectively, calculated for $E_{A,des} = 80$ kJ/mol and $k_m^0 = 10^{13}$ mol/sec [123, 133].

  (a) Zero-order desorption.
  (b) First-order desorption process. The peak temperature is invariant with various coverages.
  (c) Second-order desorption kinetic. T_{peak} increases with decreasing coverages φ.
  (d) Normalized desorption rate for a first-order and second-order kinetic. While $m \geq 2$ leads to a symmetric curve relative to T_{peak}, first-order desorption causes a less symmetric TPD trace.

In thermal desorption experiments, the surface temperature may increase linearly with time t, $T = T_0 + \beta t$, with $T_0 = T(t=0)$, or in a hyperbolic way (i. e. as linear decrease of the reciprocal temperature), $1/T = 1/T_0 - \beta' t$.

A characteristic property of the TPD traces is the desorption peak temperature, T_p, that results from the derivative (dR_{des}/dt) of the desorption rate with respect to time t.

$$\left(\frac{d^2 N_{(s)}^{ads}}{dt^2}\right)_{T=T_p} = -k_m^0 \cdot \frac{dN_{(s)}^{ads}}{dt} \cdot \exp\left(-\frac{E_{A,des}}{R(T_0 + \beta t)}\right) + k_m^0 \cdot N_{(s)}^{ads} \cdot \frac{\beta E_{A,des}}{RT^2} \cdot \exp\left(-\frac{E_{A,des}}{R(T_0 + \beta t)}\right) = 0 \ (3.45)$$

The maximum desorption rate is found for (dR_{des}/dt) = 0, and with equation 3.43 follows [104c]

$$\left(k_m^0\right)^2 \cdot m \cdot \left(N_{(s)}^{ads}\right)^m \cdot \exp\left(-\frac{2E_{A,des}}{R(T_0 + \beta t)}\right) = k_m^0 \cdot N_{(s)}^{ads} \cdot \frac{\beta E_{A,des}}{RT^2} \cdot \exp\left(-\frac{E_{A,des}}{R(T_0 + \beta t)}\right)$$

$$\frac{k_m^0 \cdot m \cdot \left(N_{(s)}^{ads}\right)^{m-1}}{\beta} \cdot \exp\left(-\frac{E_{A,des}}{RT_{peak}}\right) = \frac{E_{A,des}}{RT_{peak}^2} \tag{3.46}$$

While for a first-order kinetic, ($m = 1$), the peak temperature, T_p, is independent of the initial coverage, T_p shifts for higher desorption order ($m \geq 2$) if $N_{(s)}^{ads}$ is varied. Additional information about m results from the shape of the desorption curve. Second and higher order curves are symmetric with respect to T_p, whereas first-order desorption causes less symmetric TPD traces, figure 3.17d).

Order of desorption. *Zero-order desorption kinetics*, $m = 0$, is expected, when the desorption rate is independent of coverage, e. g. for the condensation of particles at a surface, or desorption from multilayers, where each molecule desorbs from a site where it is surrounded by similar molecules. TPD traces simulated for an ideal zero-order desorption process and for different initial coverages are shown in figure 3.17a). Note the common leading edge and the characteristic shift to higher peak temperatures with increasing coverage.

Providing a non-dissociative adsorption and molecules that do not interact with each other, the desorption follows *first-order kinetics*, where the rate of desorption is proportional to the surface coverage φ, figure 3.17b).

For particles that dissociate on the surface during adsorption (e. g. for chemisorption), a higher order desorption kinetic ($m \geq 2$) is observed, if m fragments first have to recombine in a rate-determining step before desorption. For $m = 2$, a simulated TPD trace is displayed in figure 3.17c) for various initial coverages, φ. The peak temperature, T_p, depends on φ, as given in equation 3.46.

Analysis Techniques. Several methods to determine kinetic parameters like the pre-exponential factor k_m^0, the order of desorption, m, and the activation energy for desorption, $E_{A,des}$, from the measured TPD curves are described in literature [125]. While analysis of the *peak width* or *shape* provides information about the desorption order, a variation of the *heating rate* or the evaluation according to *Redhead* are useful methods to determine k_m^0 or $E_{A,des}$.

The historical *Redhead method* [123] is based on equation 3.47, and yields the pre-exponential factor k_m^0, when the activation energy, $E_{A,des}$, has already been determined and *vice versa* by measuring the desorption peak temperature for a particular initial coverage φ. For an order $m > 0$, k_m^0 can be calculated from

$$k_m^0 = \frac{\beta \cdot E_{A,des}}{R \cdot T_{peak}^2 \cdot \left(N_{(s)}^{ads}\right)^{m-1}} \cdot \exp\left(\frac{E_{A,des}}{RT_{peak}}\right), \ m > 0 \tag{3.47}$$

Equation 3.47 shows that T_{peak} is independent of coverage for a first order desorption with constant $E_{A,des}$. Thus, $E_{A,des}$ can be found directly from the measurement of T_{peak} provided a value of k_m^0 is assumed. For $10^{13} > k_m^0 / \beta > 10^8$ [K^{-1}], equation 3.47 can be approximated by

$$\frac{E_{A,des}}{RT_{peak}} = \ln \frac{k_m^0 \cdot T_{peak}}{\beta} - 3.64 \tag{3.48}$$

3.6   *X-Ray Photoelectron Spectroscopy (XPS)*

XPS was used to determine the composition of the deposited films and to give insight into the chemical environment of the surface constituents. XPS is surface sensitive since the mean free path of electrons in the solid state is in the range of nanometers. High-energy photons (either monochromatic Al K$_\alpha$ radiation, $h\nu = 1486.6$ eV, or Mg K$_\alpha$, $h\nu = 1253.6$ eV) incident on a sample in the UHV cause a photoelectric effect, thus emitting electrons from the core levels of the sample. The binding energy of the electron, E_B, depends on the atomic charge distribution and can be determined by measurement of the kinetic energy, E_{kin}, of the photoelectron

$$E_{kin} = h\nu - IE \tag{3.49}$$

where $h\nu$ is the energy of the exciting X-ray, and IE is the ionization energy of the sample, i. e. the difference in energy between the emitting orbital and the vacuum level. Therefore, IE correlates to the binding energy with respect to vacuum level, E_B^{vac}. Using E_F, the Fermi level, instead of E_{vac} as reference of the energy, equation 3.49 results in

$$E_B = h\nu - E_{kin} - \phi \tag{3.50}$$

where ϕ is the working function of the sample, i. e. $\phi = E_{vac} - E_F$, and E_B is the binding energy of the emitted photoelectron with respect to the Fermi level [90, 92, 134].

3.7   Scanning Force Microscopy (SFM)

Scanning Force Microscopy was invented by *G. BINNIG, C. F. QUADE*, and *C. GERBER* in 1986 [135] and traces back to the concept of scanning tunneling microscopy (STM) found by *G. BINNIG* et al four years before [136]. By measuring the distance dependent forces between the surface and a molecular-sized tip as a sensor, one probes the topography of both conducting and isolating samples on an atomic scale, as displayed in figure 3.18.
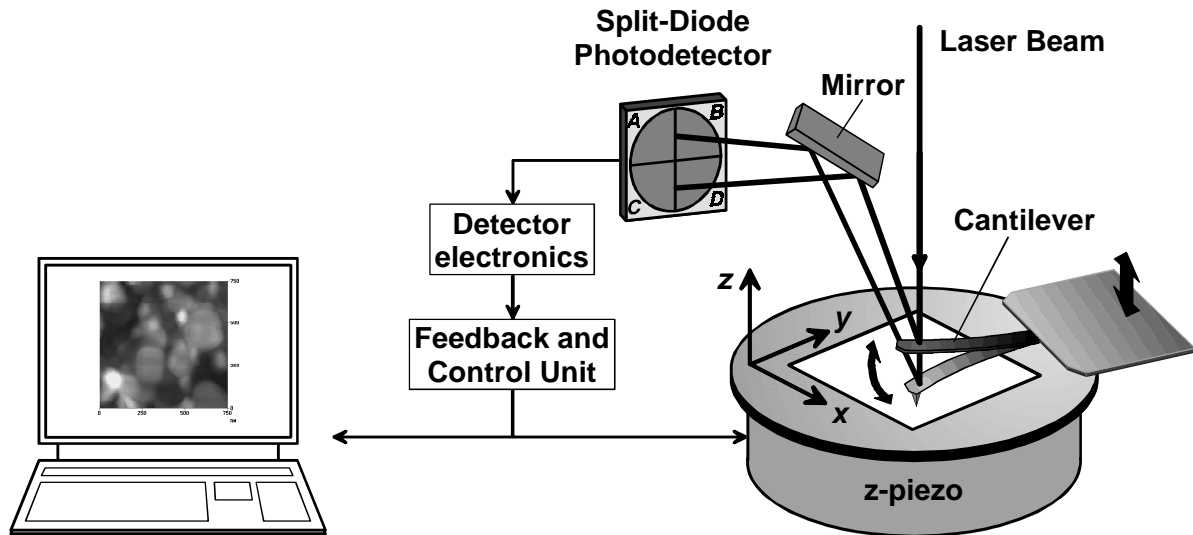

Figure 3.18: Principle of scanning force microscopy (SFM). The tip interacts with the surface during image acquisition. The feedback circuit regulates the z-control (piezo) in order to achieve a constant deflection signal from the photodetector while the sample is raster scanned. In SFM modes, the differential voltage signal Δ=(A+B)-(C+D) is measured, whereas LFM is focussed on the lateral difference Δ=(A+C)-(B+D).

The tip, located at the end of a flexible cantilever, is placed very close to the sample surface. So short-range attractive and repulsive forces ($< 10^{-9}$ N) lead to a vertical deflection of the cantilever from its equilibrium position. A laser beam is reflected from the cantilever to a four segment photodetector, and the deflection (in the sub-ångstrom range) is measured by changes in the differential voltage signal *Δ=(A+B)-(C+D)*. By scanning the tip parallel to the surface, either the local variation of the tip-surface repulsive force or the *z*-scanner position required for maintaining a constant force is converted into an atomic-scale height or deflection (force) image [137].

LENNARD-JONES **Potential.** Beside electrostatic interactions between charges and dipoles (i. e. *COULOMB* energy), there is a wide variety of attractive and repulsive forces, such as friction, dispersion, adhesive, and *VAN DER WAALS*'s forces. Since the latter are not of simple nature, they are best described as interaction pair potentials by the *LENNARD-JONES* equation [90, 109]

$$E_{\text{pot}}(r) = 4E_0 \left[\frac{A}{r^{12}} - \frac{B}{r^6} \right] \qquad (3.51)$$

wherein r denotes the distance between interacting atoms or molecules, E_0 is the potential energy at the minimum (equilibrium), and A and B are constant factors characteristic for the concerned atoms or molecules.
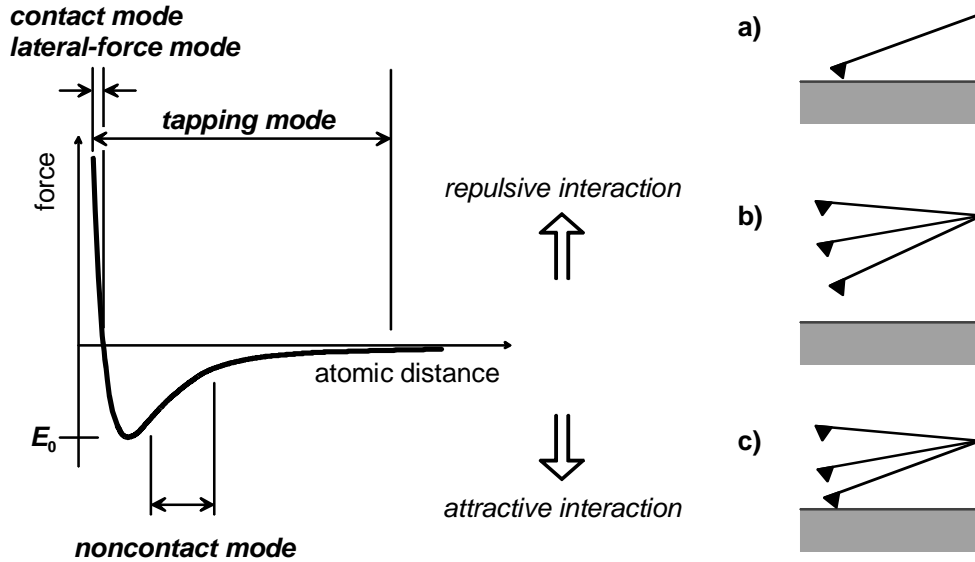

Figure 3.19: LENNARD-JONES *potential. As the atoms are gradually brought together, they weakly attract each other. First, the attraction increases with a decreasing interatomic distance, until electrostatic repulsion between the electron clouds occurs and finally the atoms are in contact. The region for contact (a), non-contact (b) and tapping mode (c) SFM are shown to the right [137, 138].*

The first term in equation (3.51) describes the repulsive force. The second term marks the attractive VAN DER WAALS interaction that combines the *orientation* force between two permanently polarized molecules *(KEESOM)*, the *induction* force as dipole-induced dipole interaction *(DEBYE)*, and the LONDON *dispersion* force between fluctuating dipole moments of neutral molecules, respectively. Thus B can be calculated using atomic or molecular properties [109].

$$B = \left(\frac{1}{4\pi\varepsilon_0}\right)^2 \left(\frac{\mu_1^2 \mu_2^2}{3 k_B T} + \left(\mu_1^2 \alpha_2 + \mu_2^2 \alpha_1\right) + \frac{3}{2}\alpha_1 \alpha_2 \frac{I_1 I_2}{I_1 + I_2}\right) \qquad (3.52)$$

ε_0 denotes the dielectric permittivity, μ_1 and μ_2 the electric dipole moment, α_1 and α_2 the electric polarizability, and I_1 and I_2 the ionization potential of two interacting particles. T is the absolute temperature and k_B the BOLTZMAN constant. Often, the third term in equation (3.52) dominates, since generally dispersion forces exceed the dipole-dependent induction and orientation forces, except for small highly polar molecules, such as water.

In real SFM measurements, several atoms of the tip interact with several molecules on top of the sample surface. Therefore, the VAN DER WAALS energy of the two macroscopic bodies, w, is calculated by summarizing the interaction energies of all atoms of the tip with all the atoms of the sample according to the HAMAKER summation method [109, 139]. Depending on the tip geometry, w

follows various interaction laws as displayed in figure 3.20 in terms of the *HAMAKER* constant H that is defined as

$$H = \pi^2 C \rho_1 \rho_2 \tag{3.53}$$

where ρ_1 and ρ_2 are the number of atoms per unit volume in the two bodies, and C is the coefficient in the atom-atom pair potential. In this context, w stands for the interaction of atoms and molecules or macroscopic bodies, respectively, at a distance of r, and with radius or diameter R_i.
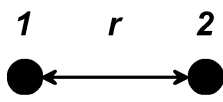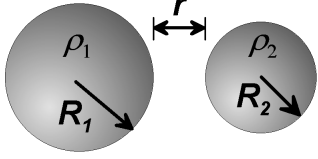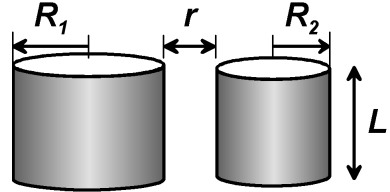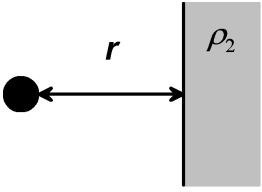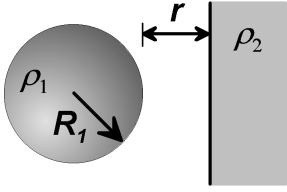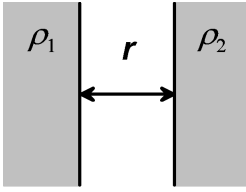
Two atoms	*Two spheres*	*Two cylinders*
$w = -\dfrac{C}{r^6}$	$w = -\dfrac{H}{6r}\dfrac{R_1 R_2}{R_1 + R_2}$	$w = \dfrac{HL}{12\sqrt{2}r^{3/2}}\left(\dfrac{R_1 R_2}{R_1 + R_2}\right)^{1/2}$
Atom-surface	*Sphere-surface*	*Two surfaces*
$w = -\dfrac{C\pi\rho_2}{6r^3}$	$w = -\dfrac{HR_1}{6r}$	$w = -\dfrac{H}{12\pi r^2}$

Figure 3.20: Non-retarded VAN DER WAALS interaction free energies between atoms, molecules or bodies of different geometries as calculated by the HAMAKER summation method [109, 139].

Typical values for the *HAMAKER* constant of condensed phases are about 10^{-9} J for interactions across vacuum. Further details are provided by *ISRAELACHVILI* [109]. Since the exact tip geometry remains unknown, the sphere-surface model is used in most of the theoretical considerations.

SFM Modes. Contact, non-contact and tapping mode SFM differ in the force between tip and surface, the vibration amplitude of the cantilever and in detection principle (figure 3.19) [137, 138].

Contact mode means that the tip comes through the fluid layer on the sample surface, and, thus, directly contacts the surface. Under ambient air conditions, most surfaces are covered by a layer of

adsorbed gases (condensed water vapor and other contaminants) which is typically several nanometers thick. When touching this layer, the tip meets two additional forces pulling it down into the layer, thus increasing the overall force on the sample: A higher surface tension results from capillary actions that cause a meniscus to form, and trapped electrostatic charges both on the tip and the sample contribute to additional adhesive forces, that lead to hysteresis in the force-*vs*-distance curve. Consequently, the scanning tip can exert strong vertical and lateral shear forces on the sample. The latter may cause inelastic or elastic surface deformations or the removal of weakly bounded and defective layers, thus probing mechanical properties (e. g. indentation, adhesion or friction) of the sample. During imaging in contact mode, changes in cantilever deflection are monitored. Maintaining a constant deflection, i. e. a constant repulsive force between tip and sample, the height profile displays the vertical movement of the *z*-scanner at each (x, y) data point.

In non-contact mode, the surface is tracked with a tip oscillating above the fluid layer with an amplitude a few nanometers (>10 nm). In this way, neither tip nor sample can be contaminated during scanning, and no force is exerted to the surface. The height profile results of the spatial variation of the attractive long-range VAN DER WAALS forces as measured by a decrease of the resonance frequency of the cantilever. Usually, non-contact mode only works with low scan rates (1-2 Hz) on very flat, extremely hydrophobic surfaces, where the adsorbed fluid layer is at a minimum.

In tapping mode SFM, the cantilever is vertically oscillating at or near its resonance frequency ($v \approx 300 \dots 400$ kHz) with an amplitude ranging from 20 nm to 100 nm. During scanning, the tip lightly 'taps' on the surface, and, in this way, gets in intermittent contact with the sample penetrating through the adsorbed fluid overlayer without being trapped by adhesive meniscus forces. In tapping mode, soft surfaces are less modified than during imaging in contact mode. Compared to the 'free' cantilever, the oscillation amplitude is lowered by interactions with the surface, and this amplitude drop is used for the feedback loop. Operation also can take place in a liquid environment.

For samples with flat surfaces, regions with different friction can be distinguished by lateral force microscopy (LFM, cf. figure 3.18), i. e. a variation of contact-mode SFM. Here, the lateral force applied to the tip is detected by a differential signal from the horizontal segments of the photodetector.

For further details including considerations about artefacts (e. g. multiple tips or tip convolution) the reader is referred to [137, 140, 141].

4   Experimental Section

This chapter summarizes the different preparation procedures that generated *tert*-butylcalix[4]arene films either on pure or modified silicon or gold surfaces, and lists the technical equipment used for their characterization. The *tert*-butylcalix[4]arene was preparared according to [142].

4.1   Preparation of the Samples

Substrates. The amorphous native oxide layer of Si (001) wafers (Aurel, n-doped (P), specific resistivity of 3 ... 5 Ω·cm, wafer thickness $d = 483 \dots 533$ μm) was used as SiO_2 substrate (①). Gold substrates (②) used for IRAS were prepared by coating cleaned Si (001) wafers by a 25 Å titanium adhesive layer, and, subsequently, by 2000 Å gold by means of electron beam evaporation in a Balzers UMS 500 P system. The evaporation rate was 1 Å s^{-1} for titanium, and 7 Å s^{-1} for gold, while a base pressure of at least 10^{-9} mbar and a pressure below $3 \cdot 10^{-7}$ mbar were maintained during the evaporation. Gold substrates on silicon (③) and mica (④) for SFM were prepared in a UHV system designed and built at our laboratory [133]. Cleaned Si wafer or freshly split mica (Goodfellow, pure ruby, $d = 0.15$ mm) in a size of $10 \cdot 10$ mm^2 were transferred inward the recipient and thermally cleaned for 12-15 h at a temperature $T_s \approx 725$ K while a base pressure in the range of 10^{-10} mbar was maintained. The deposition of an adhesive layer of $d = 50$ Å Ti (only for the Si substrate) occurred at an evaporation rate of 10 Å min^{-1}, whereas the gold film, $d = 2000$ Å, was deposited at a rate of 100 Å min^{-1}. A pressure below 10^{-7} mbar was maintained during the evaporation. Subsequent annealing at $T_s \approx 500$ K for 1 h improved the smoothness of the gold films.

Cleaning procedures. Prior to incubation, the gold surfaces (②, ③) were washed in a 5 : 1 : 1 mixture of MillyQ water (18.2 MΩ cm^{-1}, Millipore Milly-Q plus 185), 30 % hydrogen peroxide, and 25 % ammonia for 7 min at 350 K (TL 1 procedure). Silicon substrates were cleaned either by the TL 1 recipe or in a freshly prepared 3 : 1 mixture of 97 % sulfuric acid and 30 % hydrogen peroxide (piraña) for 15 min.

Preparation of the BC4MA and thiol monolayers (SAM). The gold substrates were incubated for at least 17 h in ethanolic 2 mM solution of the corresponding thiol, HS-C$_n$H$_{2n}$-X, in a plastic beaker at room temperature. After incubation, the samples were rinsed in ethanol, ultrasonicated in ethanol

for 10 minutes, then rinsed again, finally blown dry in nitrogen gas and immediately analyzed or transferred into the recipient of the UHV system. The same procedure holds for the self-assembly of the bis(*tert*-butylcalix[4]arene) methionine acylamide, BC4MA with the exception that 1 mM solution of BC4MA was used for incubation.

The phenyl terminated Au / S-(CH$_2$)$_{18}$-O-CO-C$_6$H$_5$ monolayer was prepared according to the procedure by *ENQUIST* [143] by use of Au / S-(CH$_2$)$_{18}$-OH surface as substrate for modification.

Preparation of the GOPTS monolayer. In a glass beaker with a lid, droplets of 3-glycidyl<u>o</u>xy<u>p</u>ropyl-<u>t</u>rimethoxy<u>s</u>ilane, abbreviated as 'GOPTS' in the following, were spread on piraña cleaned silicon surfaces until a complete coverage was achieved. After 30 min the samples were rinsed and ultrasonicated in acetone for 5 min and rinsed again to remove supernatant GOPTS. After drying in nitrogen gas, they were transferred into the UHV as fast as possible. Both the acidity of at least one of the phenyl groups of the *tert*-butylcalix[4]arene molecule and the reactivity of the tight three-membered oxirane ring were expected to lead to a chemical reaction on the surface.

3-glycidyl<u>o</u>xy<u>p</u>ropyl-<u>t</u>rimethoxy<u>s</u>ilane

'GOPTS'
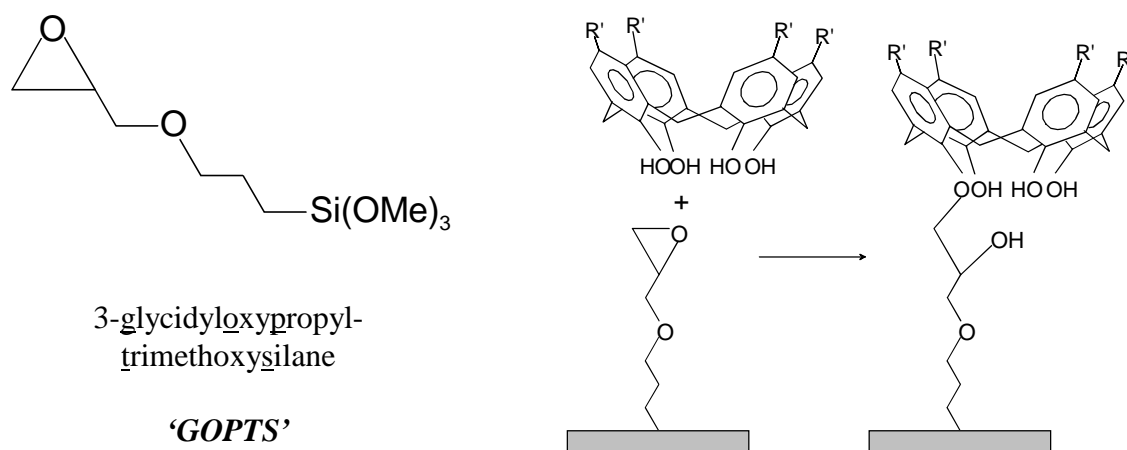
4.2   Technical Equipment

Infrared spectroscopy. Transmission infrared spectroscopy of the compounds dispersed in KBr at a concentration $x \approx 5 \cdot 10^{-3}$, was performed on a Bruker IFS 48 and a Bruker IFS 66v system both equipped with a liquid nitrogen cooled MCT detector. *tert*-Butylcalix[4]arene films deposited on ZnSe and KRS-5 were measured in ATR mode at an angle of incidence $\theta_i = 45°$ using a KRS-5 polarizer on the Bruker IFS 48. At 2 cm^{-1} (IFS 48) and 1 cm^{-1} (IFS 66v) resolution, 1000 interferograms were recorded within $\approx$ 10 min. During the measurements, the chamber of the IFS 48 was permanently purged with dried air to remove water and CO$_2$ from the chamber. The reflection-absorption (RA) spectra were recorded either on a Bruker IFS 66 system equipped with a grazing angle (85°) infrared reflection accessory or on a Bruker Vector 22 system connected to the UHV system depicted in figure 4.2. Both systems use a liquid nitrogen cooled MCT detector. Again, 1000 interferograms were averaged at a resolution of 2 cm^{-1}. Gold surfaces covered with a monolayer of

HS-$(CD_2)_{15}$-CD_3 (IFS 66) or freshly sputtered and annealed gold surfaces (Vector 22) were taken as references. In all cases, a three-term Blackmann-Harris apodization function was applied to the interferograms before Fourier transformation. While ATR spectra were carefully baseline corrected (in order not to manipulate the dichroic ratio of the absorption bands), transmission and RA spectra are presented as measured, i. e. without any correction.

Scanning force microscopy. The SFM images presented in this thesis were recorded in contact mode on a Park Scientific Instrument Universal SPM system using 2.5 µm or 10 µm scanners and Si_3N_4 cantilevers supplied by Park Scientific Instruments. Upon imaging, the scanning tip exerts forces on the sample in the range 10^{-8}-10^{-7} N. Tapping mode scanning force microscopy was performed on the Nanoscope III by Digital Instruments, DI, using Nanoprobe^{TM} SPM tips of TESP type, $l = 125$ µm in length with an drive frequency on $\nu \approx 300$ kHz. In all cases, it was scanned at low rates of 1-2 Hz.

Ellipsometery. Single-wavelength ellipsometry was performed using an automatic Rudolf Research AutoEL ellipsometer equipped a with He-Ne laser light source, $\lambda = 632.8$ nm at an angle of incidence of 70°. Prior to their incubation, the gold substrates were measured as reference. The film thickness was averaged from seven different spots on the sample.

Contact Angle Goniometry. Contact angles were measured with a Ramé-Hart NRL 100 goniometer in air. Water taken freshly from the Milli-Q and hexadecane were used to probe hydrophilicity and homogeneity of the samples.

4.3   *bis(tert-Butylcalix[4]arene) Methionine Methyl Ester Acylamide*
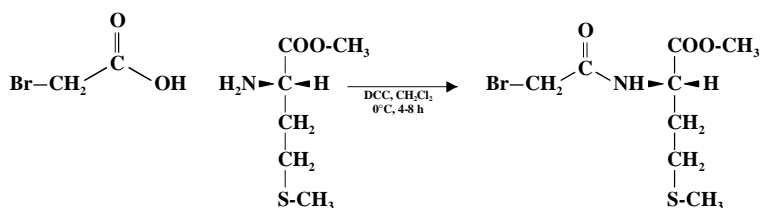
Preparation of the acylamide bromide. A three-necked flask (100 mL) was loaded with 4.0 g (20 mmol) of methionine methyl ester hydrochloride in 50 mL methylene chloride and cooled to -15°C. By dropwise addition of 2.8 mL (2.03 g, 20 mmol) of triethylamine, the hydrochloride was converted into the free base. During a continuous cooling of the reaction mixture, 4.55 g (22 mmol, i. e. 1.1 equiv.) of dicyclohexylcarbodiimid (DCC) in 10 mL dry methylene chloride and subsequently 2.78 g (20 mmol) bromoacetic acid in 5 mL methylene chloride were added dropwise to keep the temperature of the reaction mixture below -5°C. Additional stirring was performed for 1 h at 0°C and subsequently for two hours at room temperature to complete the reaction.

The resulting salts were filtered off and washed twice with 25 mL of methylene chloride. The solvent was removed under reduced pressure on a rotary evaporator, and the crude product was

dissolved in ethyl acetate. The remaining urea was filtered off, and the product was kept in a refrigerator for crystallization.
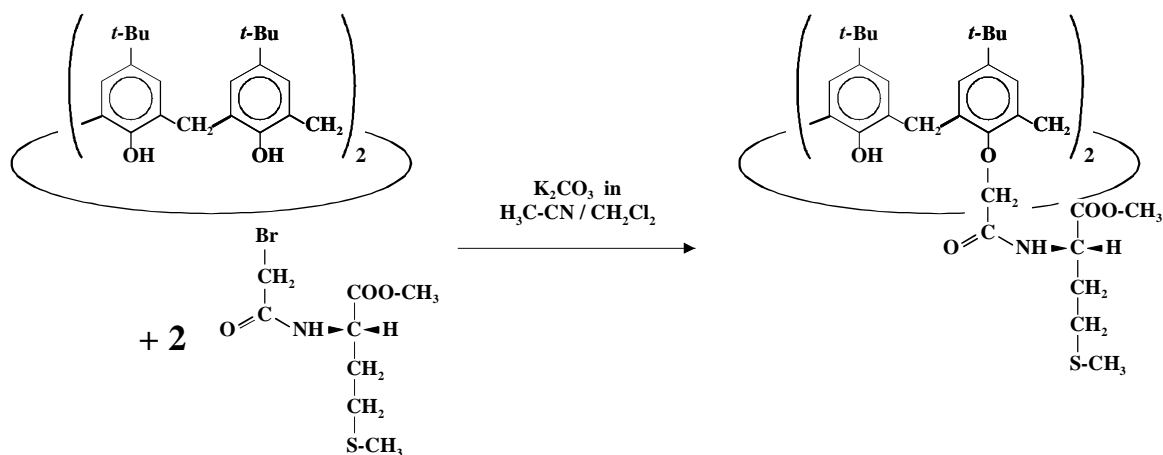
Reaction to bis(*tert*-butylcalix[4]arene) methionine methyl ester acylamide. A three-necked flask equipped with stirrer, calcium chloride drying tube and condenser was loaded with 1.9 g (3 mmol) of *tert*-butylcalix[4]arene in 50 mL acetonitrile, 2 g (14.3 mmol), potassium carbonate, and 1.7 g (6 mmol) acylamide bromide. The mixture was stirred under reflux for 48 h, while the progress of the reaction was monitored by thin-layer chromatography, TLC (Merck silica gel 60, F_{254}: hexane / ethyl acetate 4 : 1).

After the completion of the reaction, the acetonitrile was distilled off under reduced pressure. The residue was taken up in 50 mL diethyl ether and 30 mL water, and was transferred to a separating funnel. The organic phase was separated and washed twice with water, while the water phase was washed with diethyl ether, 50 mL each. The united organic phases were dried over anhydrous magnesium sulfate for 3 h, and the filtrate was concentrated under reduced pressure to a volume of approximately 15 mL. Finally, the product was stored in the refrigerator order to let it crystallize.
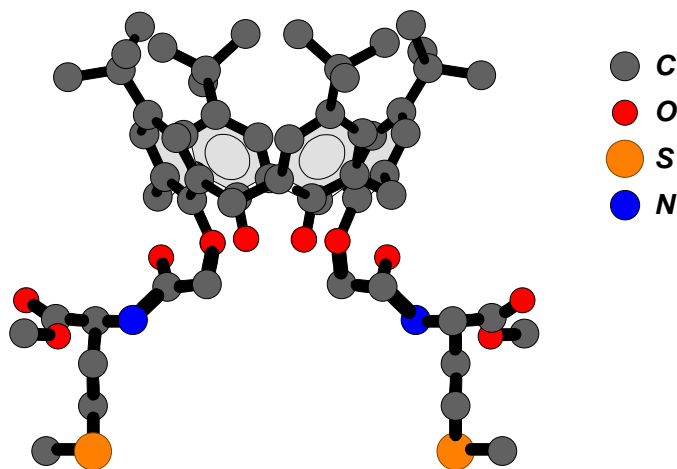
Figure 4.1:   The bis(tert-butylcalix[4]arene) methionine acylamide molecule.

4.4 Ultrahigh Vacuum systems

4.4.1 Combination of IRAS and TPD

The deposition of *tert*-butylcalix[4]arene films on thiol SAMs on gold and studies of the inclusion behaviour both of *tert*-butylcalix[4]arene and BC4MA were carried out on the ultra high vacuum system depicted in figure 4.2. The system consists of three chambers, i. e. a load lock, a preparation chamber (with mass spectrometer, sputter gun and evaporation cell) and a measurement chamber (for IRAS and mass spectrometery) as described elsewhere [144].

Front view (to the left):

a) sample holder, b) LL - load lock, c) PC - preparation chamber, d) MC - measurement chamber, e) FTIR spectrometer, f) IR detector chamber, g) dosing valve or evaporation cell, h) mass spectrometer port.

Top top view of the measurement position (below):

a) sample stage, e) FT-IR spectrometer with transfer optics, f) IR detector chamber with i) MCT IR detector, k) polarizer, l) mass spectrometer.

Figure 4.2: : Experimental setup for combined evaporation, temperature programmed desorption (TPD) and IRAS measurements of thiol and calix[4]arene layers on gold surfaces [144].

4.4.2 Großgerät

tert-Butylcalix[4]arene films on silicon and the 'GOPTS' modified silicon substrates were prepared by *KNUDSEN* evaporation and characterized by XPS and UPS in the UHV system sketched out in figure 4.3.

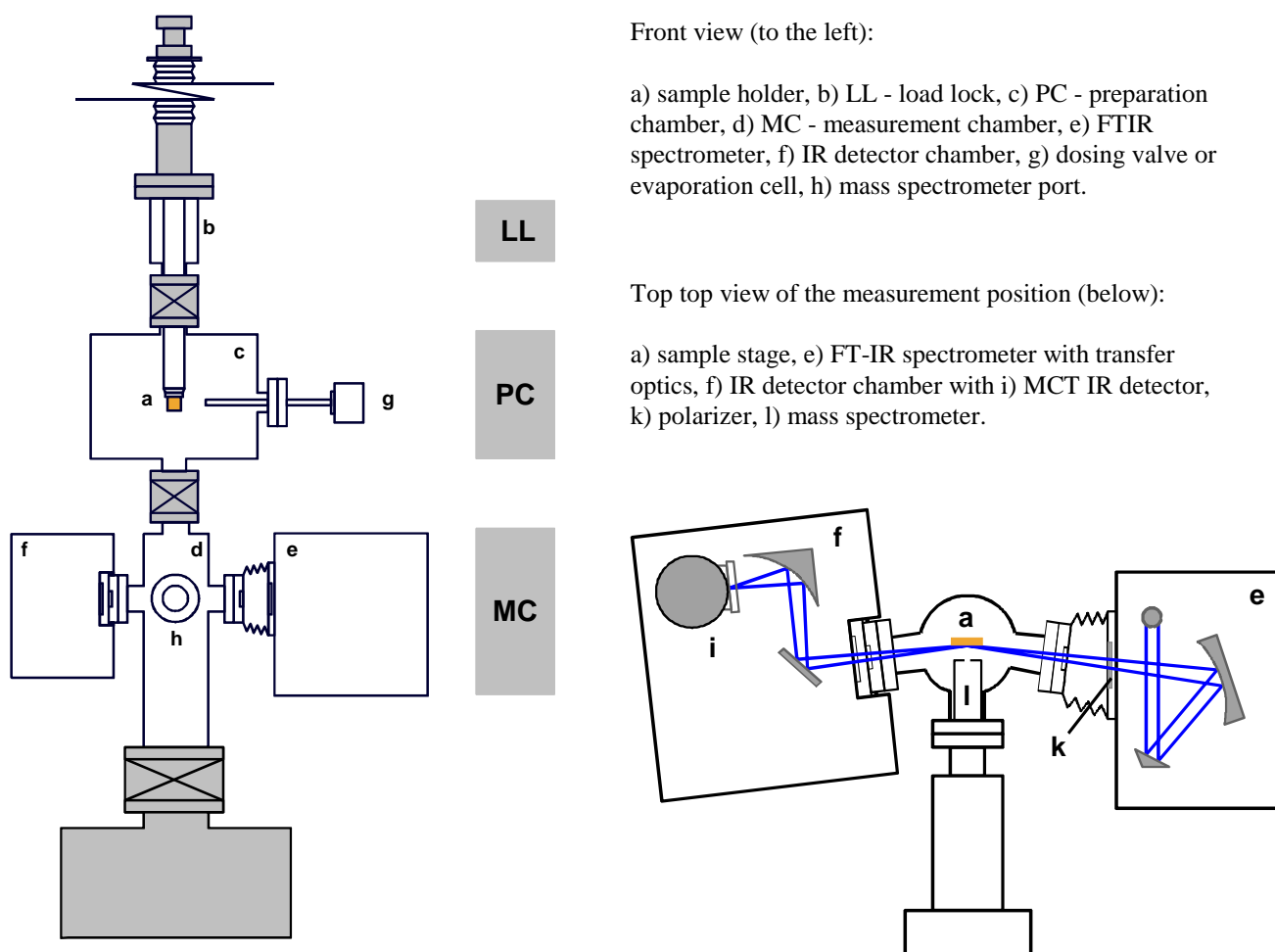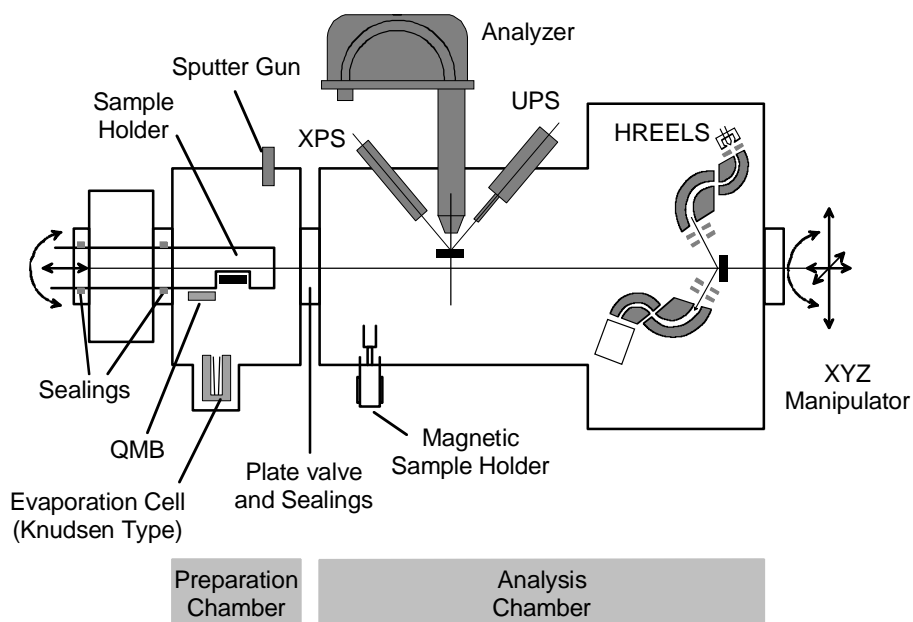*Figure 4.3:*   *Großgerät, redrawn from [146]. The preparation chamber is equipped with an evaporation cell of KNUDSEN type and a quartz micro balance to monitor the film thickness via a Leybold-Heraeus deposition monitor Inficon XTM. A X-ray source (Mg K_α, 1253.6 eV), the UV lamp (He^I, p $\approx$ 1·10^{-8} mbar, He^{II}, p $\approx$ 7·10^{-9} mbar) and the analyzer are located in the analysis chamber.*

Evaporation of *tert*-butylcalix[4]aren in the UHV. Prior to deposition from a *KNUDSEN* evaporation cell, the *tert*-butylcalix[4]arene molecules were thermally cleaned in UHV at temperatures slightly below their sublimation temperature to ensure their purity. The calixarenes were evaporated at a cell temperature of $T_{cell} \approx$ 475-500 K and a pressure of approx. 3·10^{-8} mbar in the preparation chamber (base pressure below 10^{-9} mbar) on an unheated substrate, i. e. T_s = 298 K. Deposition rates of 0.1 ... 0.5 Å s^{-1} were maintained for at least 1 h before and after the evaporation to establish a constant rate of *tert*-butylcalix[4]arene. The results are smooth and homogeneous films as checked with scanning force microscopy and confirmed by XPS and UPS for layers of a different thickness, d = 20 ... 500 Å

5   Results and Discussion

The growing behaviour of molecular films on a particular substrate strongly depends on the relative strength of the forces between the molecules of the growing film and the interactions between the substrate and the film, that are influenced by chemical properties of the surface, such as wetting and reactivity. In this context, the results of the preparation of *tert*-butylcalix[4]arene layers will be presented with respect to the different substrates and the corresponding characterization methods.

Transmission Fourier transform infrared spectroscopy (FT-IR) characterizes the *tert*-butylcalix[4]-arene molecule prior to and after the inclusion of suitable organic guest molecules [145]. Information about the growth of calixarene layers prepared by thermal deposition on semiconducting substrates like zinc selenide, ZnSe, thallium bromide-iodide Tl(BrI), 'KRS 5', or the native oxide surface of silicon, SiO_2, is obtained from FT-IR spectroscopy in attenuated total reflection mode (ATR). The orientation of the molecules in the layer can be estimated from the dichroism observed for the *TM* and *TE* waves ATR spectra (cf. chapter 3) by use of linearly polarized radiation. Infrared reflection-absorption spectroscopy (IRAS) is suitable for metallic surfaces with different wetting properties that, for instance, are defined by the terminal groups of adsorbed alkane thiols, $HS-(CH_2)_n-X$, as outlined in chapter 2.

Scanning force microscopy (SFM) images show the growing mode of calixarenes on the substrates. They indicate whether the 'layer-plus-island (*STRANSKI-KASTRANOV*)', 'layer-by-layer (*FRANK-VAN DER MERVE*)', or 'island growth (*VOLLMER-WEBER*)' mode is preferred. Additional characterization of the layers is performed by contact angle measurements, temperature programmed desorption (TPD) and photoelectron spectroscopy (XPS, UPS).

5.1   *The tert-Butylcalix[4]arene Host Molecule*

The *tert*-butylcalix[4]arene molecule consists of a cavity shaped by four phenyl moieties that are bridged by methylene groups. It bears *tert*-butyl groups at the upper, and hydroxyl groups at the lower rim. The characteristic vibration modes of these functionalities and skeletal vibrations contribute to the spectrum. Figure 5.1 shows a typical FT-IR transmission spectrum of the *tert*-butylcalix[4]arene host with an empty cavity and indicates the characteristic IR absorption bands.
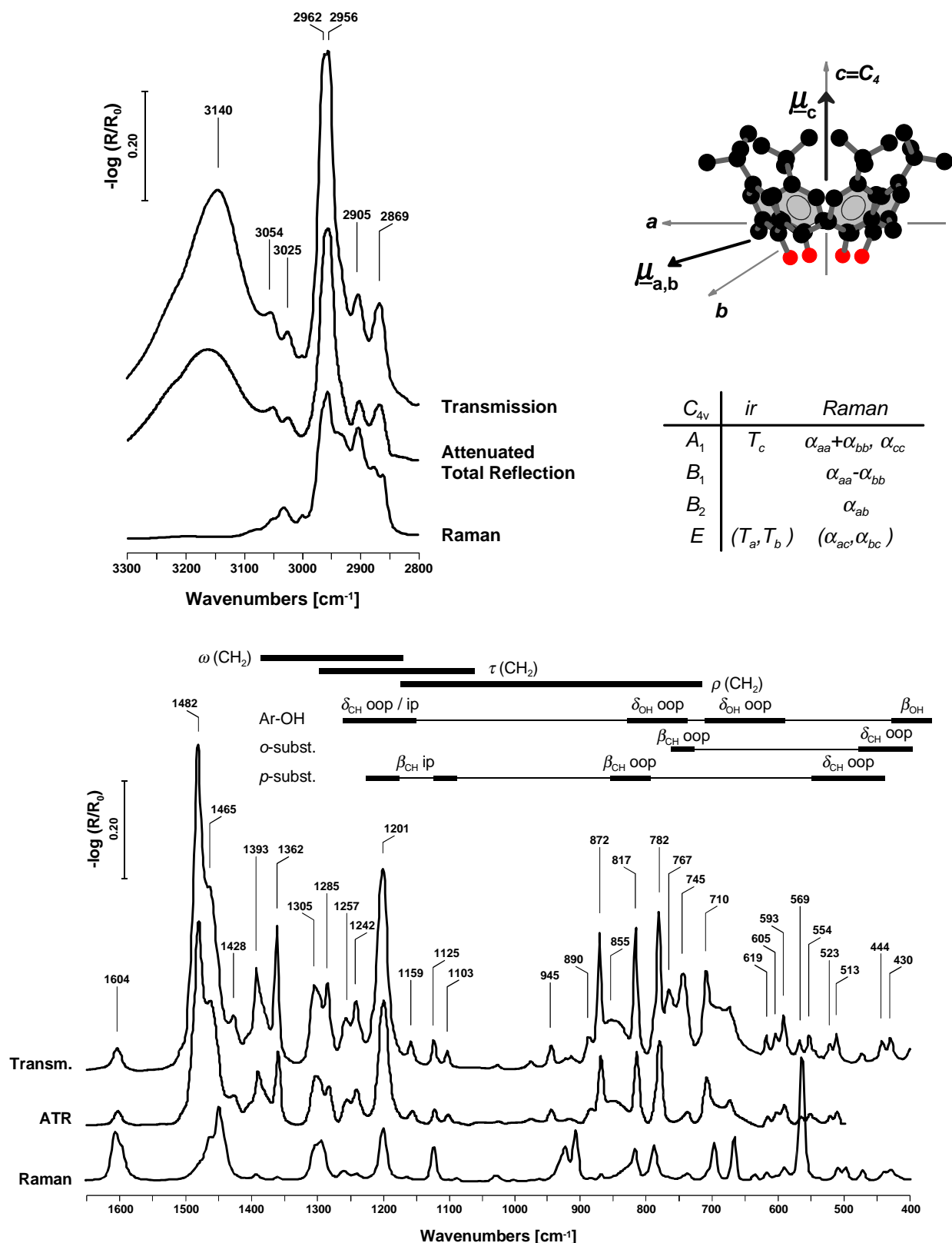
Figure 5.1: FT-IR transmission, ATR and Raman spectra of the tert-butylcalix[4]arene molecule. The regions for wagging (ω), twisting (τ), rocking (ρ), deformation (δ), bending (β), and combination vibration modes are depicted. The calixarene molecule and the orientation of the dipole moments $\mu_{a,b}$ and μ_c are shown in the top right-hand corner. The table indicates the activity and polarization (direction) of the A_1, B_1, B_2 and E type vibration modes.

In table 5.1, the vibration modes are assigned both with respect to their infrared and Raman activity as well as taking into account their behaviour in the ordered films, as will be illustrated in chapter 5.2.

Table 5.1:   Assignment of IR modes [cm^{-1}] for the tert-butylcalix[4]arene molecule [147-149].

wavenumber [cm^{-1}]		mode assignment [a]
3140	ν_{ar}(OH)	stretching vibration of the aromatic OH group (A_1)
3054, 3025	ν_{ar}(CH)	stretching vibration of the aromatic CH group, 7 & 20 [b]
2962, 2956	ν_{as}(CH$_3$)	asymmetric CH$_3$ stretching vibration [e]
2905	ν_{as}(CH$_2$)	asymmetric CH$_2$ stretching vibration, oop
2869	ν_s(CH$_3$)	symmetric CH$_3$ stretching vibration, in-plane (ip)
1604, 1482	ν_{ar}(CC)	stretching vibration of the aromatic rings, 8A, 19A
1465, 1428	δ_{as}(CH$_3$) δ_{sc}(CH$_2$)	asymmetric CH$_3$ deformation band (oop) overlapped by the CH$_2$ scissor vibration
1393, 1362	δ(CH)	deformation vibration of the *tert*-butyl group (E)
1305	ω(CH$_2$)	CH$_2$ wagging, 19B
1285, 1257, 1201		skeletal vibration of *tert*-butyl bond to the aromatic ring (E)
1242	ν(CO)	CO stretching vibration
1159	δ(OH)	aromatic OH deformation vibration (ip), 9A (E)
1125	δ_{ar}(CH)	aromatic CH groups [c], characteristic for phenols (A_1)
945		skeletal vibration [c] or 7B (A_1)
890	ω(CH)	CH wagging, 17B
872, 855		1,2,3,5 tetrasubstituted benzene rings [d]
817	ν(C-CH$_3$)	*tert*-butyl group
782	β(CC)	in-plane deformation of aromatic rings, 12
745	δ(OH)	OH deformation out-of-plane
710	ρ(CH$_2$)	CH$_2$ rocking (A_1)

[a] ν_s / ν_{as}: symmetric / asymmetric stretching vibration; δ_s / δ_{as}: symmetric / asymmetric deformation vibration, δ_{sc}: scissoring mode; ω: wagging, τ: twisting, ρ: rocking, β: bending.

[b]   nomenclature of *WILSON* for the assignment of the C-H vibrations of the phenyl ring [150].

[c], [d]   assignment as suggested by *SODA* [149] or *HAYES* and *HUNTER* [16].

[e] ν_{as}(CH$_3$) splits into an in-plane mode [r$_a^-$] at $\tilde{\nu}$ = 2962 cm^{-1} (E) and an out-of-plane mode [r$_b^-$] at $\tilde{\nu}$ = 2956 cm^{-1} (A_1)

An ATR spectrum of a thin *tert*-butylcalix[4]arene film ($d = 175$ Å) evaporated on a KRS 5 crystal and the Raman spectrum of fine *tert*-butylcalix[4]arene powder are included in the figure 5.1. A comparison of the transmission and ATR spectra proves the high thermal stability of the *tert*-butyl-calix[4]arene molecule. Since the positions and the intensities of the characteristic vibration bands in the KBr pellet are equal to those in the film, it becomes evident that the molecules can be sublimated without decomposition.

Additional information is provided by the activity of several vibration modes in the *TM* but not in the *TE* waves of ATR spectra, cf. chapter 5.2. With respect of their absence in the *TE* wave spectra, the absorption modes at wavenumbers $\tilde{\nu} = 1125, 945, 855, 710, 604, 570,$ and 512 cm^{-1} are assigned as belonging to the A_1-type vibration modes.

As mentioned in chapter 2, the most important feature of calixarenes in IR spectra is the position of the aromatic OH stretching vibration mode, ν_{ar}(OH), that measures the strength of intramolecular hydrogen-bonding interactions among the OH groups at the lower rim. This interaction stabilizes the *cone* conformation of the cyclic tetramer (C_{4v} symmetry). In comparison to $\tilde{\nu} = 3607$ cm^{-1} for a free and unassociated aromatic hydroxyl group, the vibration band is significantly broadened and shifted toward lower wavenumbers. Due to a closed ring of hydrogen bonds at the lower rim of the *tert*-butylcalix[4]arene, i. e. a high degree of association, the stretching vibration of the aromatic OH group possesses a large dipole moment, and, hence, appears with a high intensity in the IR spectra. The opposite is observed in Raman spectra: nearly no polarizability of the ν_{ar}(OH) vibration leads to a minute absorption.

The assignment of the CH vibrations of the phenyl rings took into account both the position of the vibration bands as estimated from benzene, toluene, *m*-xylene, and mesitylene, and the activity in IR and Raman spectra [150].

In contrast to the characteristic stretching vibration modes, a defined assignment is impossible for several vibration modes that appear in the fingerprint area or in the region of the skeletal vibrations. For completeness, the vibration modes of the functional groups in the *tert*-butylcalix[4]arene molecule are summarized in the following and sketched out in figure 5.1.

Additional modes of the CH$_2$ groups are the wagging ($\tilde{\nu} = 1382$-1170 cm^{-1}), twisting ($\tilde{\nu} = 1295$-1063 cm^{-1}), and the rocking vibration ($\tilde{\nu} = 1174$-724 cm^{-1}). The substitution pattern of the aromatic rings is characterized by several in-plane (ip) or out-of-plane (oop) bending (β) or ring deformation (δ) vibrations, respectively. *p*-substitution leads to absorption at $\tilde{\nu} = 1225$-1175 cm^{-1} (β, ip), $\tilde{\nu} = 1125$-1090 cm^{-1} (β, ip), $\tilde{\nu} = 860$-800 cm^{-1} (β, oop) and $\tilde{\nu} = 560$-450 cm^{-1} (δ, oop). *o*-substi-tution gives rise to an absorption at $\tilde{\nu} = 770$-735 cm^{-1} (β, oop) and $\tilde{\nu} = 490$-410 cm^{-1} (δ, oop), whereas $\tilde{\nu} = 835$-745 cm^{-1} (δ_{OH}, oop), $\tilde{\nu} = 720$-600 cm^{-1} (δ, oop), $\tilde{\nu} = 440$-380 cm^{-1} (β, OH), and $\tilde{\nu} = 1260$-1150 cm^{-1} (δ_{CH}, ip and oop) result from the phenol group.

5.2   Layers on Semiconducting ATR Crystals KRS 5 and ZnSe

5.2.1   The Pure *tert*-Butylcalix[4]arene on ZnSe

FT-IR spectroscopy in attenuated total reflection mode is a suitable technique to characterize the growth of organic layers that are deposited on ATR crystals. It provides useful information about the orientation of the molecules in the film if linear polarized radiation is employed. Figure 5.2 shows the ATR spectra of a 'thick' *tert*-butylcalix[4]arene film ($d = 200$ Å) on a ZnSe crystal for the transverse magnetic (TM, $E_\parallel$ with respect to the plane of incidence) and the transverse electric wave (TE, $E_\perp$). The film was obtained by thermal evaporation of pure *tert*-butylcalix[4]arene powder. Differences in the reflectivities R_{TM} and R_{TE} of certain vibration modes are observed both in the region of the OH and CH stretching vibrations, as well as in the fingerprint area.

The perpendicular polarized infrared radiation is almost unaffected at the wavenumbers $\tilde{\nu} = 1124$, 947, 848, and 710 cm^{-1}, whereas parallel polarized radiation is absorbed by the *tert*-butylcalix[4]-arene layer at these wavenumbers. This pronounced dichroism of the reflectivities, R_{TM} and R_{TE}, indicates an ordered, i. e. anisotropic, growth of *tert*-butylcalix[4]arene on the ZnSe crystal. Two regions of deformation and skeletal vibrations with significant differences in the dichroic ratios, $D_{TE/TM}$, i. e. the fraction of R_{TE} and R_{TM} (cf. chapter 3), are displayed in figure 5.3.

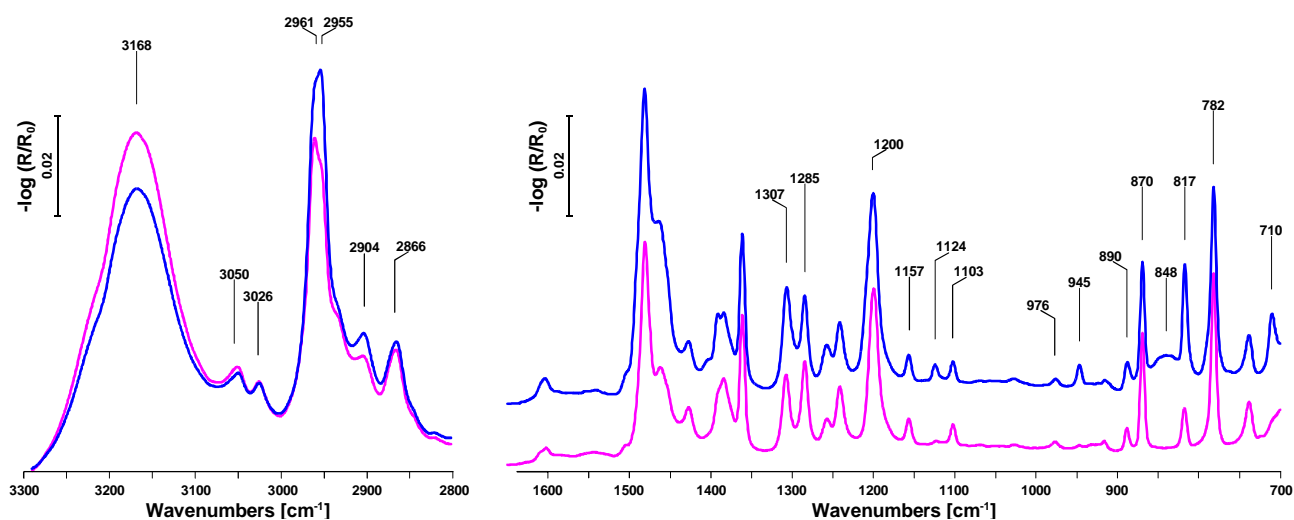*Figure 5.2:   FTIR-ATR spectra of tert-butylcalix[4]arene (d = 200 Å) on ZnSe. Transverse magnetic (TM) and transverse electric wave (TE), are the components of the polarized infrared radiation parallel or perpendicular with respect to the plane of incidence. Vibration bands with a significantly different dichroic ratio of TM and TE wave are magnified in figure 5.3.*
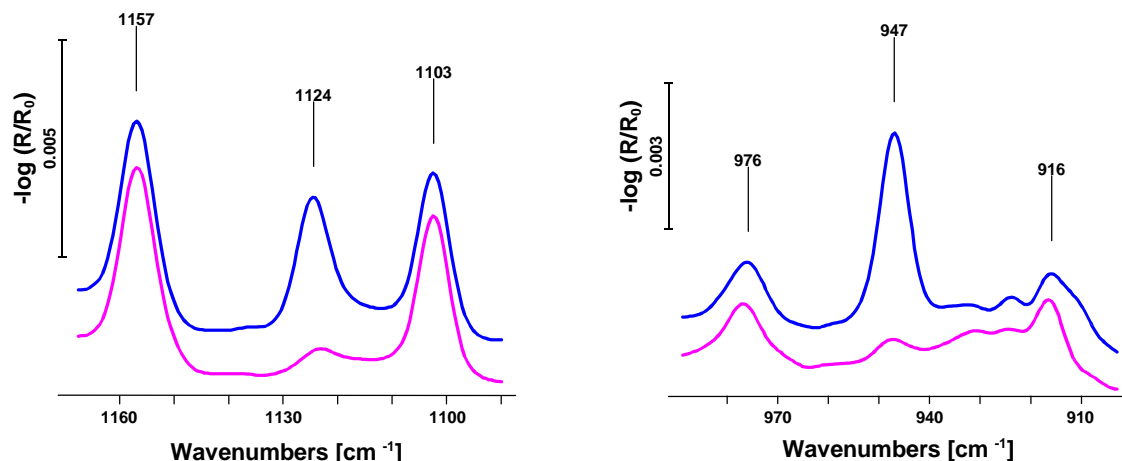
Figure 5.3:   FTIR-ATR spectra of tert-butylcalix[4]arene (d = 200 Å) on ZnSe, details of figure 5.2. A pronounced dichroism is observed for $\tilde{v}$ [δ(CH)] = 1124 cm^{-1} and for the skeletal vibration at $\tilde{v}$ = 947 cm^{-1}.

The dichroic ratio of selected infrared vibration bands of *tert*-butylcalix[4]arene films with a thickness of 20 Å ≤ d ≤ 7500 Å evaporated on ZnSe are listed in table 5.2. Note that the layer thickness does not significantly affect the dichroic behaviour of the infrared bands.

Table 5.2:   Dichroic ratio, $D_{TE/TM}$, of selected infrared bands for tert-butylcalix[4]arene films on ZnSe.

layer	wavenumbers $\tilde{v}$ [cm^{-1}]							
thickness	1124	976	947	870	848	780	710	675
50 Å	0.06	1.07	0.07	1.20	0.12	1.04	0.183	1.01
200 Å	0.10	1.16	0.10	1.23	0.01	0.91	0.10	0.87
7500 Å	0.08	0.84	0.03	1.03	0.14	0.80	0.09	0.99

Three additional features are worth mentioning: First, due to the orienting interaction with the substrate, the OH stretching vibration appears at $\tilde{v}$ [v(OH)] = 3168 cm^{-1}.

Also, on a closer examination of the asymmetric CH$_3$ stretching vibration, one finds the peak of the absorption band at $\tilde{v}$ = 2962 cm^{-1} for the *TE* wave, while it is centered at $\tilde{v}$ = 2956 cm^{-1} in the *TM* wave spectrum. This corresponds to the splitting of the vibration into an in-plane mode referred to in literature as an [r_a^-] branch at $\tilde{v}$ = 2962 cm^{-1} and an out-of-plane mode, i. e. [r_b^-], $\tilde{v}$ = 2956 cm^{-1} [151]. The fact that the in-plane mode is more strongly excited by the *TE* wave, while the out-of-plane mode shows a stronger interaction with *TM* is another conclusive piece of evidence for the preferred orientation of the *tert*-butylcalix[4]arene molecules in the film.

Finally, the significant deflection of the dichroic ratio from $D_{TE/TM}$ = 0 or 1 at $\tilde{v}$ = 817 cm^{-1} is explained by a local symmetry effect. Keeping in mind that, strictly speaking, only the calix[4]arene

backbone holds C_{4v} symmetry, it becomes clear that the local C_{3v} symmetry of the *tert*-butyl groups at the upper rim causes the mentioned deflection. Therefore, the absorption band located at $\tilde{v} = 817$ cm^{-1} is assigned as belonging to the v(C-CH$_3$) of *tert*-butyl group in table 5.1.

5.2.2   *tert*-Butylcalix[4]arene Layers on KRS 5

Under certain conditions, an anisotropic growth of *tert*-butylcalix[4]arene is also observed on KRS 5 crystals, as illustrated for the fingerprint area and lower frequency region in figure 5.4. This *tert*-butylcalix[4]arene layer ($d = 172$ Å) was produced by thermal deposition of crystalline inclusion complexes of *tert*-butylcalix[4]arene with toluene in the cavity.
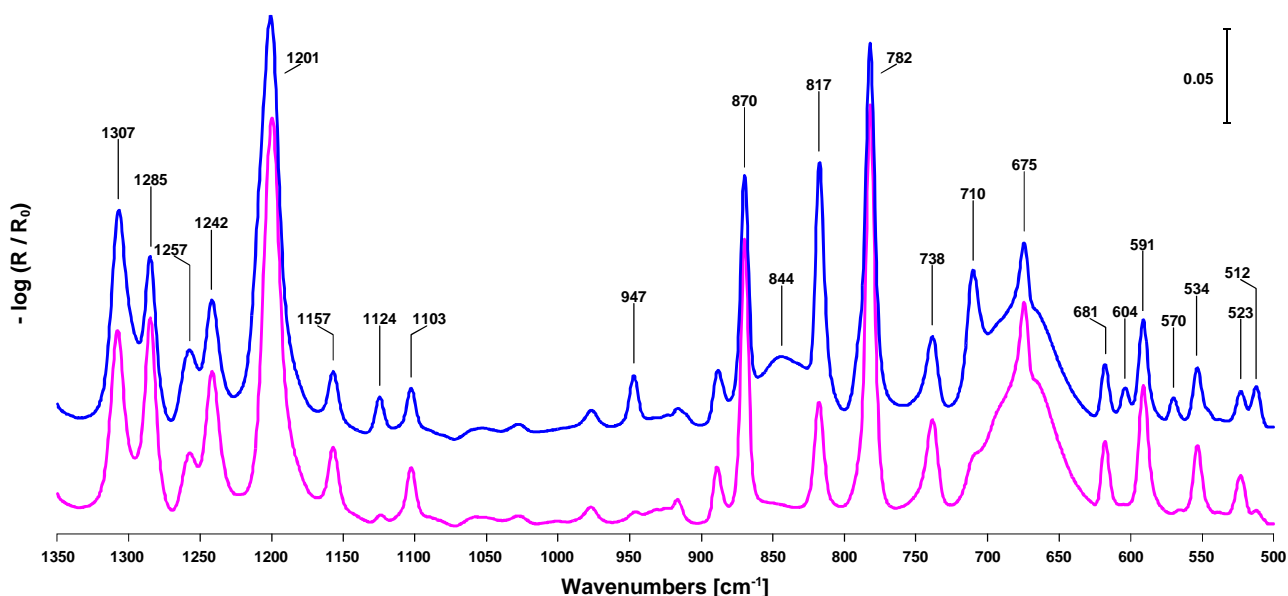

Figure 5.4:   FTIR-ATR spectra of a tert-butylcalix[4]arene layer (d = 172 Å) on KRS 5. Crystalline inclusion complexes of tert-butylcalix[4]arene with toluene were used as evaporation material.

The pronounced dichroism of R_{TM} and R_{TE} detected at wavenumbers $\tilde{v}$ = 1124, 947, 710, 604, 570 and 512 cm^{-1} in the ATR spectra proves the oriented growth of the *tert*-butylcalix[4]arene molecules. The presence of toluene in the cavity is indicated by the position of the OH stretching vibration band, $\tilde{v} = 3172$ cm^{-1}, and the shifting of the OH out-of-plane deformation vibration from $\tilde{v} = 745$cm^{-1} to $\tilde{v} = 738$ cm^{-1}. The solvent is found to play an important role in the orientation of the molecules. If the partial pressure of toluene is decreased by cooling the baffle of the vacuum system with liquid N$_2$ during the evaporation, isotropic growth is detected in the ATR spectra.

On the other hand, if an isotropically grown layer is stored in an atmosphere of chloroform vapor for several hours, anisotropy increases with the exposition time and leads to a growing dichroism of the particular vibration bands mentioned above. In this context, however, an ordering of the molecules in the film has to be distinguished from the growing of crystallites. Isotropic growth on the KRS 5 crystal is achieved by deposition of calixarene molecules that, prior to thermal evaporation, were

recrystallized from chloroform and dried at approximately 410 K in low vacuum to ensure that no solvent molecules are included in the cavity, figure 5.1.

5.2.3   Observed Dichroism and Suggested Growth Model

The theoretical background necessary to elucidate the relation between the detected dichroism of infrared absorption bands and the orientation of molecules in the film is outlined in chapter 3. In terms of the spectrometer coordinate system (x, y, z), the *TM* wave excites vibration modes with a transition moment aligned in the (x, z)-plane, i. e. the plane of incidence, whereas the *TE* wave interacts exclusively with vibrations that correlate to changes of the dipole moment in the y-direction. The character table of the point group C_{4v} lists the dipole-allowed and infrared active vibration modes of the *tert*-butylcalix[4]arene molecule that belong to the symmetry species A_1 or E. With respect to the molecular coordinate system (a, b, c), vibrations of the A_1-type are polarized in the c-direction that coincides with the principal axis, C_4, while the E type is degenerated in the (a, b)-plane. As suggested by ZBINDEN [98], and due to the common excitation of μ_a and μ_b, the following preferred orientations of the *tert*-butylcalix[4]arene molecules, sketched out in figure 5.5, may serve as models in order to explain the dichroic behaviour. Figure 5.5a) schematically shows the transition moments $\mu_{a,b}$ and μ_c of the *tert*-butylcalix[4]arene molecule, whereas the two-dimensional degeneration of $\mu_{a,b}$ is indicated by the bowl that symbilizes the *tert*-butylcalix[4]arene. Possible orientations of the principal axis and, hence, μ_c, parallel to one of the axes of the spectrometer coordinate system (x, y, z), are depicted in figure 5.5b-d). The calixarene molecules may also be tilted in the layer.

TM excitation (x,z)	$A_1 + E$	E	$A_1 + E$
TE excitation (y)	E	A_1	E
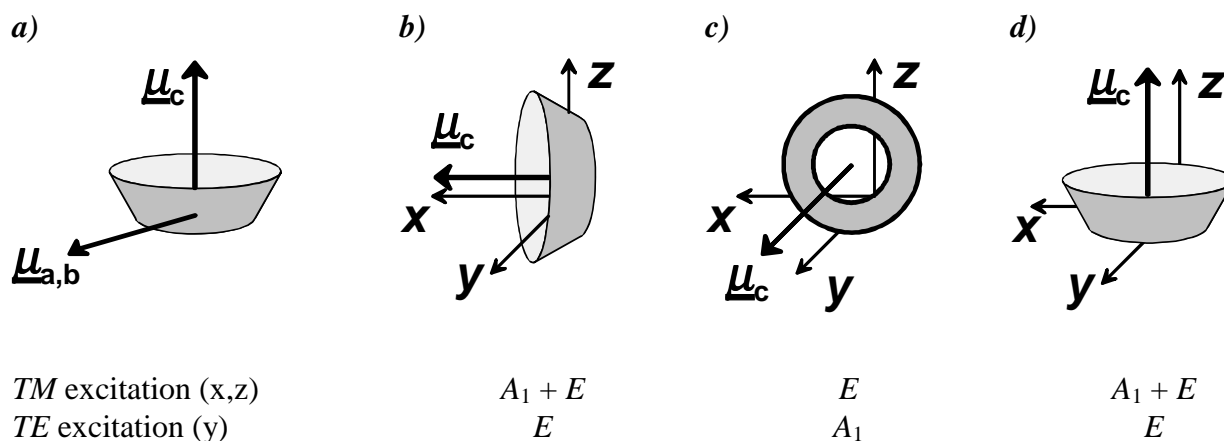
Figure 5.5:   *a) Transition moments for infrared active vibration modes of the tert-butylcalix[4]arene molecule. b), c), and d) Possible orientations of the tert-butylcalix[4]arene molecule in the layer with respect to the coordinate system (x, y, z) of the spectrometer.*

A preferred molecular orientation with the c axis arranged parallel to the y axis, i. e. parallel to the surface but perpendicular to the plane of incidence, figure 5.5c), exclusively leads to an excitation of either A_1 or E-type vibrations. Therefore, it can not explain vibrations with $D_{TE/TM} \approx 1$, and, consequently, does not concur with the observed dichroism. In contrast to this, a supposed

orientation of the molecules with their principal axis parallel to the *x*- or *z*-axis of the spectrometer correctly predicts the appearance of the dichroic ratios of $D_{TE/TM} \approx 0$ and $D_{TE/TM} \approx 1$. In their growth, however, the molecules can not discriminate between the *x*- and *y*-axis, since the latter are defined only by the way the sample is mounted in the spectrometer. From these considerations, it follows that only the orientation model depicted in figure 5.5d), i. e. $C_4 = c \parallel z$, meets all requirements to explain the observed dichroic behaviour and, consequently, indicates an uniaxial orientation of the molecules in the layer with the *c* and C_4 axis aligned nearly perfectly parallel to the surface normal, however, 'face-up' or 'face-down' orientation can not be distinguished.

The slight absorption of the *TE* wave at the wavenumbers $\tilde{v}$ = 1124, 947, 710, 604, 570 and 512 cm^{-1} is attributed to three effects. A lack of long range ordering in the entire layer and the degree of polarization, determined to > 98 %, are assumed to exhibit only a small influence. The main effect, however, is due to a deflection from the high symmetric *cone* conformation. The *cone-cone* interconversion and the *pinched-cone* conformation (C_{2v}) of the calixarene backbone, cf. chapter 2, as well as the local symmetry of the *tert*-butyl groups at the upper rim, lower the degree of symmetry of the *tert*-butylcalix[4]arene molecule.

In terms of the theory developed by *FLOURNOY*, *SCHAFFERS*, and *MIRABELLA* [99, 100], the relationship between the orientation of the molecules characterized by the spatial attenuation indices κ_x, κ_y, and κ_z, and the measured reflectivities for the transverse electric and transverse magnetic wave, R_{TE} and R_{TM}, is given by

$$\ln R_{TE} = - \alpha \, \kappa_y$$
$$\ln R_{TM} = - \beta \, \kappa_x - \gamma \, \kappa_z \qquad (5.1)$$

The constants α, β, and γ were calculated in chapter 3. For uniaxial layers ($\kappa_x = \kappa_y$) on a ZnSe crystal ($n_i = 2.40$) these equations are transformed to

$$\ln R_{TE} = - 5.48 \, \kappa_x$$
$$\ln R_{TM} = - 1.97 \, \kappa_x - 9.00 \, \kappa_z \qquad (5.2)$$

Consequently, *E*-type vibrations, with their transition moment aligned parallel to the (*x*, *y*)-plane, are expected to show a dichroic ratio of $D_{TE/TM} = 5.48 / 1.97$, i. e. $D_{TE/TM} \approx 2.80$ for a perfect uniaxial orientation of the *tert*-butylcalix[4]arene molecules, whereas no absorption should occur for A_1-type vibrations at these wavenumbers.

Since this is not the case, the method by *ZBINDEN* can be applied to estimate the actual orientation of the *tert*-butylcalix[4]arene molecules in the film, assuming a perfect axial orientation. The tilt angles, v', formed by the dipole moment μ of the molecules and the surface normal, i. e. the *z*-axis, are calculated according to equation (3.19), $D_{TE/TM} = \frac{1}{2} \tan^2 v'$, and listed in table 5.3.

Table 5.3: *Average dichroic ratio, $\overline{D}_{TE/TM}$, and calculated tilt angles, υ', for selected A_1-type vibration modes of tert-butylcalix[4]arene on ZnSe.*

	Wavenumbers $\tilde{v}$ [cm^{-1}]						
	1124	947	848	710	604	570	512
$\overline{D}_{TE/TM}$	0.08	0.07	0.09	0.10	0.06	0.07	0.05
υ'	21.8°	20.5°	23.0°	24.0°	19.1°	20.5°	17.5°

From these results, a perfect axial orientation of the *tert*-butylcalix[4]arene molecules on ZnSe is concluded whereas the principal axis (C_4) of the molecules forms an angle of υ' ≈ 21° with the *z*-axis of the spectrometer coordinate system.

Figure 5.6 summarizes the facts described above that lead to a dichroic behaviour in ATR spectra. According to their relative orientation, the molecular dipole moments, $\underline{\mu}$, of a certain vibration mode sum up to yield the dipole moment, $\underline{M}$, of the entire film. If $\underline{M}$ lies in the plane of incidence, only absorption of the *TM* wave takes place, giving rise to $D_{TE/TM} = 0$. An equal amount of infrared radiation of the *TE* and *TM* wave is absorbed by the overlayer, i. e. $D_{TE/TM} = 0$, if $\underline{M}$ is aligned parallel to the (*x*, *y*)-plane.
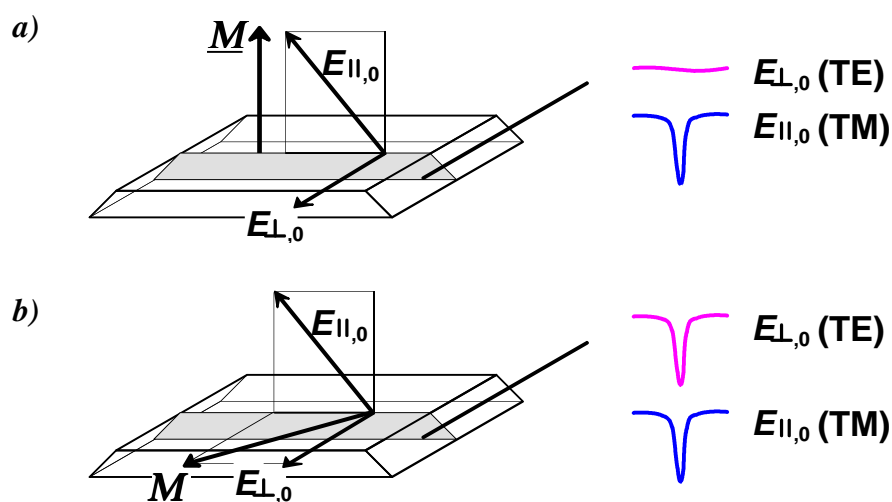
Figure 5.6: *The orientation of the dipole moment $\underline{M}$ of a certain vibration mode of the film, relative to the plane of incidence, determines the amount of absorbed radiation and the degree of the dichroism. This is demonstrated for an arrangement of $\underline{M}$ (a) parallel to the plane of incidence, and (b) parallel to the surface.*

5.3   *tert-Butylcalix[4]arene Layers on Silicon*

This chapter deals with the results of the preparation and characterization of *tert*-butylcalix[4]arene layers on the amorphous native oxide adlayer of Si (001) wafers. Surface sensitive characterization

is performed by X-ray and ultraviolet photoelectron spectroscopy (XPS and UPS [90]), whereas scanning force microscopy (SFM) yields information about the growing mechanism of the layers.

5.3.1   Characterization by XPS and UPS

Substrate. The comprehensive XP spectrum in figure 5.7a) and details for the O(1s), C(1s), and Si(2p) levels in figure 5.8 confirm that the washing of the substrate followed by thermal cleaning in the UHV generates a SiO_2 surface of sufficient purity and smoothness. No signal with an intensity above the noise level is detected in the XP spectrum of the C(1s) core level region. The SiO_2 is characterized by O(1s) with a binding energy, E_B, of 532.0 eV, Si(2p) peaks for the pure silicon centered at $E_B = 99.9$ eV, and a small amount of Si^{IV} ($E_B = 102.8$ eV) resulting from the oxide adlayer, $d \approx 5 ... 10$ Å [152].

Calixarene Films. *tert*-Butylcalix[4]arene films ($d = 20 ... 500$ Å) were deposited on SiO_2 by *KNUDSEN* sublimation, $T_{cell} \approx 475\text{-}500$ K at deposition rates of $0.1 ... 0.5$ Å s^{-1}. The XP spectra of three particular stages of the layer preparation are displayed in figure 5.7: the clean SiO_2 surface (trace *a*), a thin layer of *tert*-butylcalix[4]arene, $d = 30$ Å, i. e. 3 monolayers (trace *b*), and a thick calixarene layer of $d = 250$ Å (trace *c*).

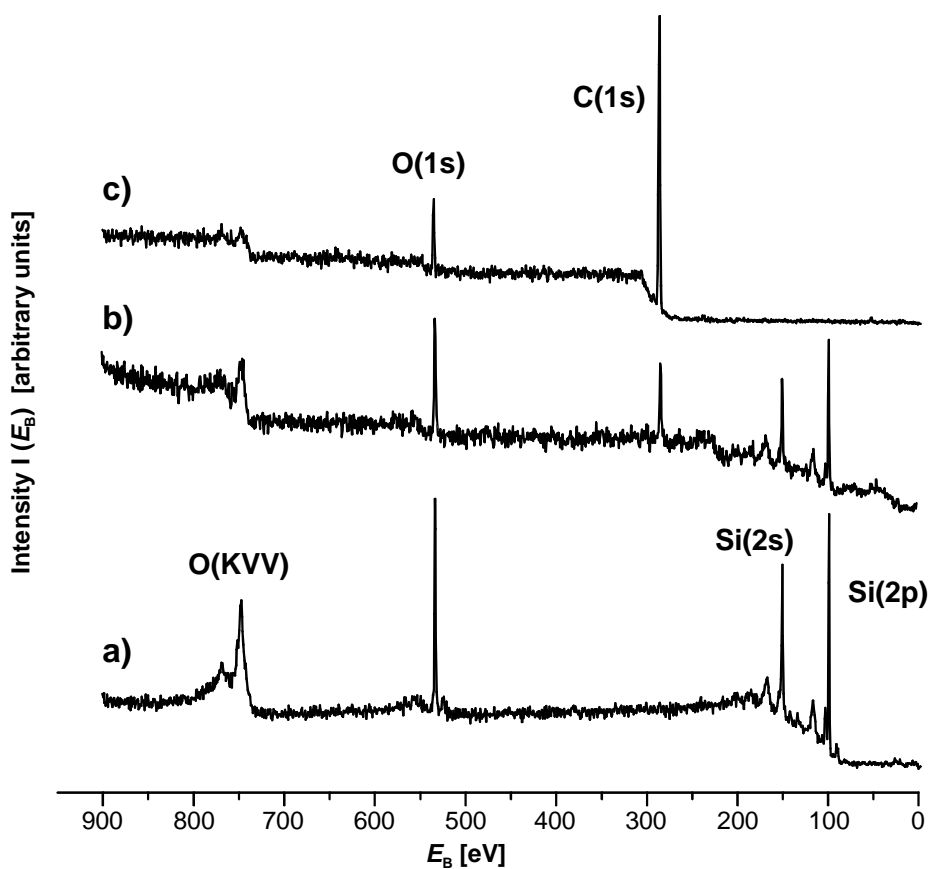*Figure 5.7:   X-ray photoelectron spectra. a) pure Si / SiO₂ (001) substrate. b) tert-butylcalix[4]arene layer, d = 30 Å, c) tert-butylcalix[4]arene layer, d = 250 Å, on Si / SiO₂ (001).*

The aliphatic and aromatic carbon atoms in the *tert*-butylcalix[4]arene molecules give rise to the C(1s) peak with binding energy $E_B = 284.5$ eV. The peak heights, both of the oxygen (1s) and the silicon (2s) and (2p) levels, decrease with increasing film thickness. Due to the phenol groups in the *tert*-butylcalix[4]arene, the O(1s) peak still appears in spectrum of the thick layer (trace *c* in figure 5.7), where the substrate peaks have vanished.
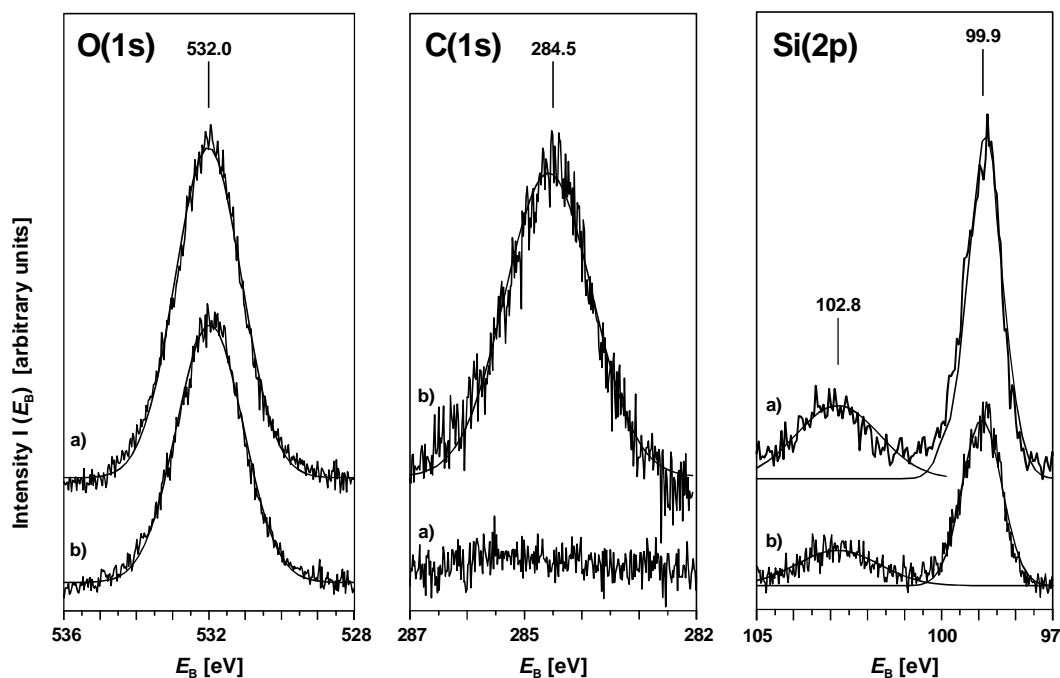

Figure 5.8:   MgK$_\alpha$ excited XP spectra of the core level region of O (1s), C (1s) and Si (2p) of a) the pure Si / SiO$_2$ substrate, and b) a tert-butylcalix[4]arene layer (d = 30 Å) on Si / SiO$_2$.

It is widely known that parameters like the evaporation rate and the substrate temperature have a strong influence on the growing behaviour of organic layers. Keeping this in mind, it is not surprising that moderate evaporation rates of 0.1 ... 0.5 Å s^{-1} generated homogeneous films, whereas higher rates (≥ 10 Å s^{-1}) caused the deposition of molecular clusters rather than well-defined layers.

The influence of the substrate temperature correlates with the diffusion of molecules in the condensed phase that follows an Arrhenius like law showing an exponential temperature dependence, i.e. $\sim \exp(-E_A/RT)$. Consequently, a higher substrate temperature during the evaporation or an annealing process afterwards may supply sufficient energy for a migration of the molecules on the surface, and films produced in this way are expected to be more homogeneous. The annealing effect of a slightly increased substrate temperature is demonstrated in figure 5.9a). The C(1s) peak of a *tert*-butylcalix[4]arene layer, $d = 50$ Å, is denoted as (II); for comparison, (I) shows the XPS trace of the pure silicon surface. After 30 min of annealing at $T_s \approx 325$ K in the UHV, the C(1s) peak of the calixarene layer has tremendously decreased, as depicted in trace (III). The result of the 'annealing' is best described by the peak area of (II) and (III). Immediately after evaporation, the C(1s) peak covers $A_p = 402$ aau. (arbitrary area units), whereas a peak area of

A_p = 174 aau. after annealing indicates the desorption of approximately more than half of the organic film. With figure 3.16, this decrease might also have been interpreted as result of an 'island' or 'layer plus island' modification of the film, the latter, however, could not be detected in SFM.
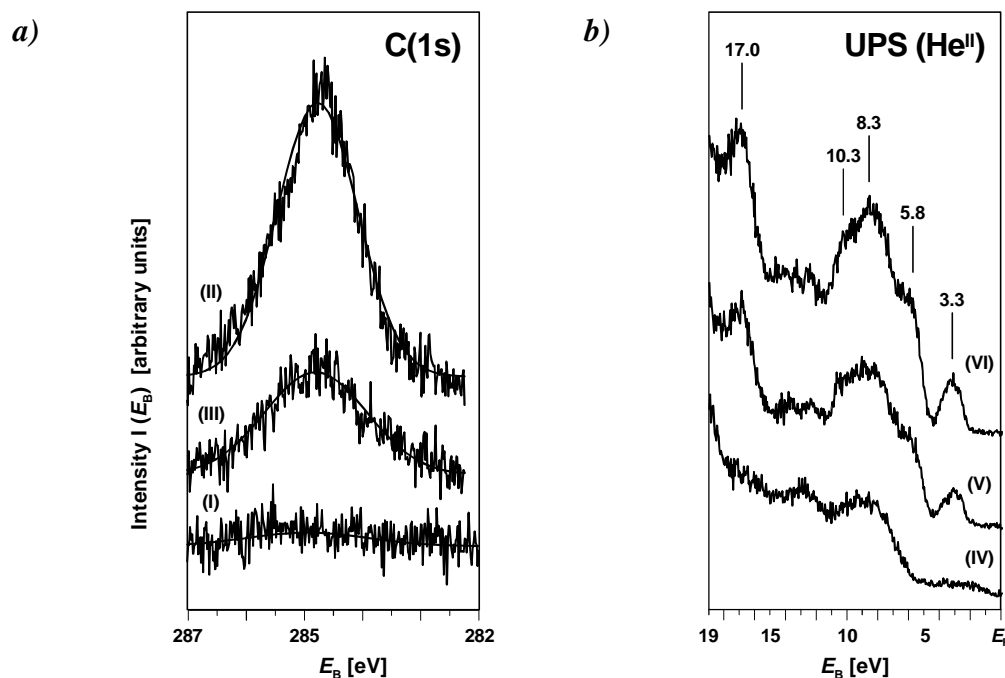

Figure 5.9:   a) XP spectra of the C(1s) peak during the annealing experiment. (I) clean SiO_2 surface, (II) tert-butyl-calix[4]arene layer (d = 50 Å) on SiO_2 immediately after evaporation, and (III) after 30 min of annealing at $T_s \approx$ 325 K.

b) He^{II} UV photoelectron spectra. (IV) clean SiO_2 surface, (V) tert-butylcalix[4]arene film, d = 20 Å ($\approx$ 2 monolayers), on SiO_2, and (VI) tert-butylcalix[4]arene film, d = 50 Å, on SiO_2.

Figure 5.9b) shows the He^{II} UV photoelectron spectra of a clean SiO_2 surface before (IV) and after coating with *tert*-butylcalix[4]arene, d = 20 Å (V) or d = 50 Å (VI). Evidently, the molecular orbitals of the physisorbed calixarene molecules contribute to the additional peaks in spectra (V) and (VI), centered at binding energies E_B = 17.0, 10.3, 8.3, 5.8, and 3.3 eV, respectively. Since the results of a molecular orbital calculation of the *tert*-butylcalix[4]arene are not available for an assignment, the peak positions were compared to an UPS spectrum of benzene on Ni (111) [90, 153]. The spectra of *tert*-butylcalix[4]arene on SiO_2 and benzene on Ni show the same shape, whereas the calixarene has lower binding energies. The π level with the smallest ionization potential is centered at E_B = 3.3 eV ($\approx$ 4 eV for benzene), while E_B = 10.3, 8.3, 5.8 eV and E_B = 17.0 eV of the calixarene correspond to E_B = 7.5 ... 6 eV and E_B = 10 ... 8.5 eV ($1e_{1g}$) in the benzene spectrum.

5.3.2   SFM Images of Thick *tert*-Butylcalix[4]arene Films

The quality of the *tert*-butylcalix[4]arene films prepared on SiO_2 surfaces was probed by scanning force microscopy. Typical SFM images of 'thick' *tert*-butylcalix[4]arene films, d = 200 Å, on the native SiO_2 / Si (001) surface are shown in the figures 5.10-5.12.

a)   *b)*
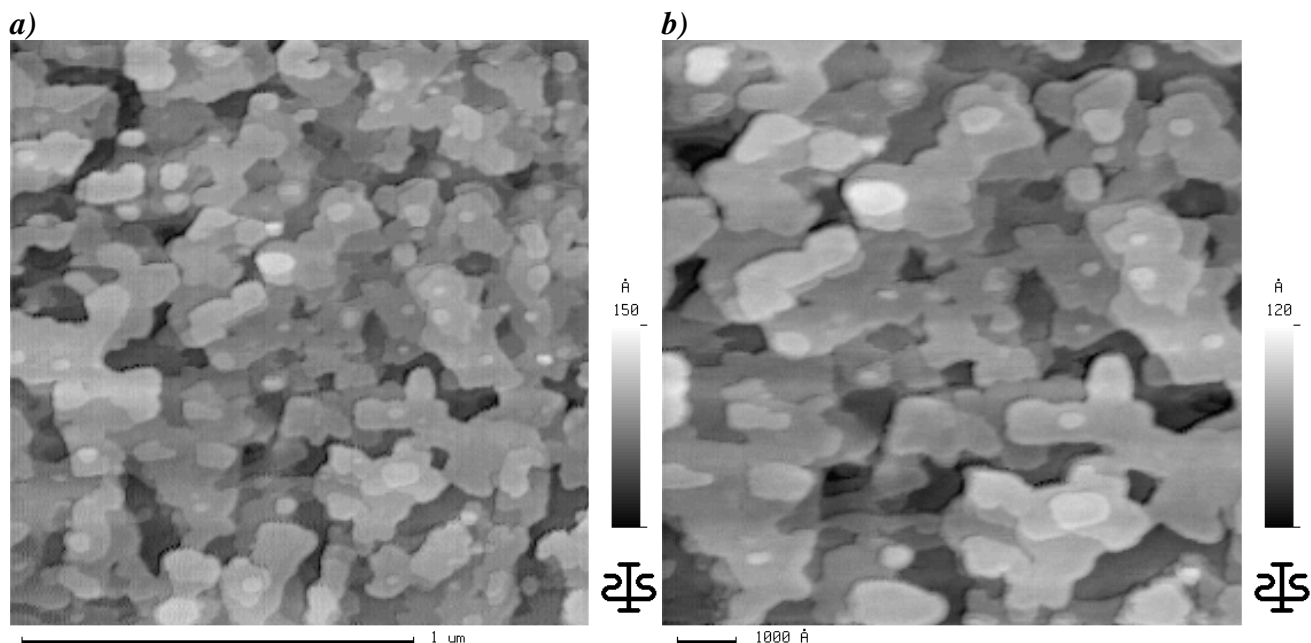
Figure 5.10: *Contact mode SFM images of a tert-butylcalix[4]arene (d = 200 Å) on SiO$_2$ / Si (001). The scanned area is a) (1.5µm)^2 and b) (1µm)^2.*
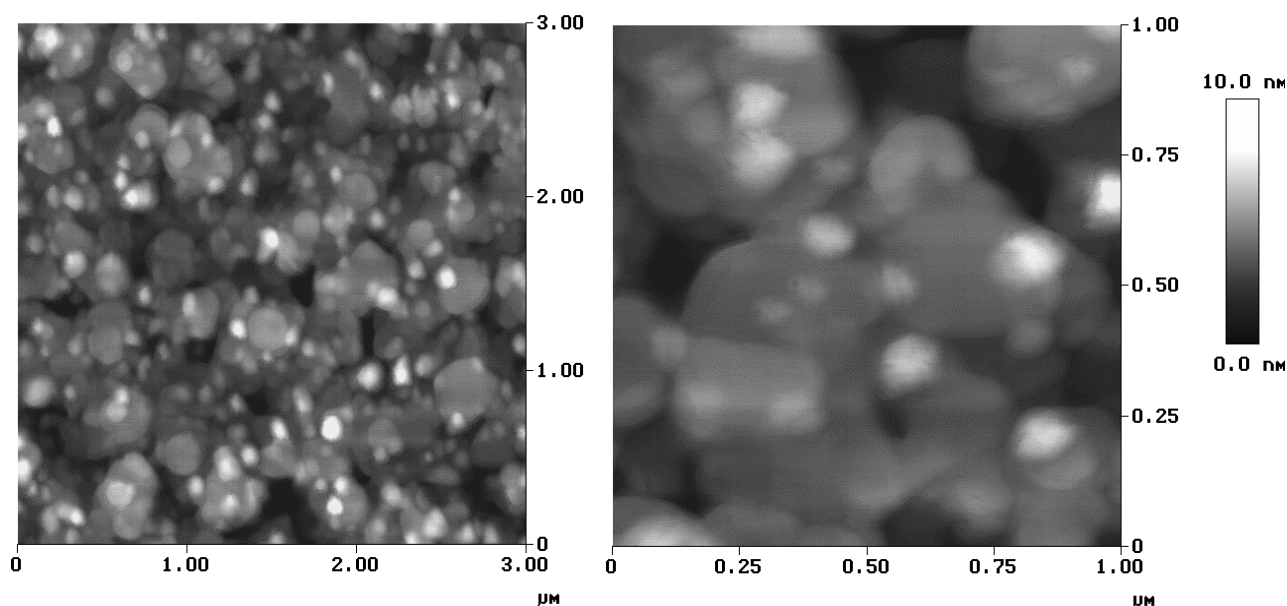
Figure 5.11: *Tapping mode SFM images of tert-butylcalix[4]arene (d = 200 Å) on native SiO$_2$ / Si (001).*

One recognizes large areas of the same gray scale value. They indicate that the top layers grow with high perfection, generating a two-dimensional 'island' arrangement of the molecules. Beside the terraced calixarene layers, areas of darker gray indicate that some inferior layers are not totally completed. This suggests a growth mechanism according to the *VOLMER-WEBER* model, i. e. a cluster and island growth: If the intermolecular interactions of the adsorbate molecules predominate over adsorbate-substrate attractions, first the formation of three-dimensional clusters is energetically

favoured over a two-dimensional growth of completed layers. With increasing coverage, the three-dimensional clusters grow together and form nearly completed inferior layers. Additional confirmation of the assumed growth mechanism is found in the contourline profiles, illustrated in figure 5.12. As marked by dashed lines in the image, the layer topography is determined parallel (horizontal line) and perpendicular (vertical line) to the scan direction of the tapping cantilever, and depicted below or on the right hand side of the SFM image, respectively.
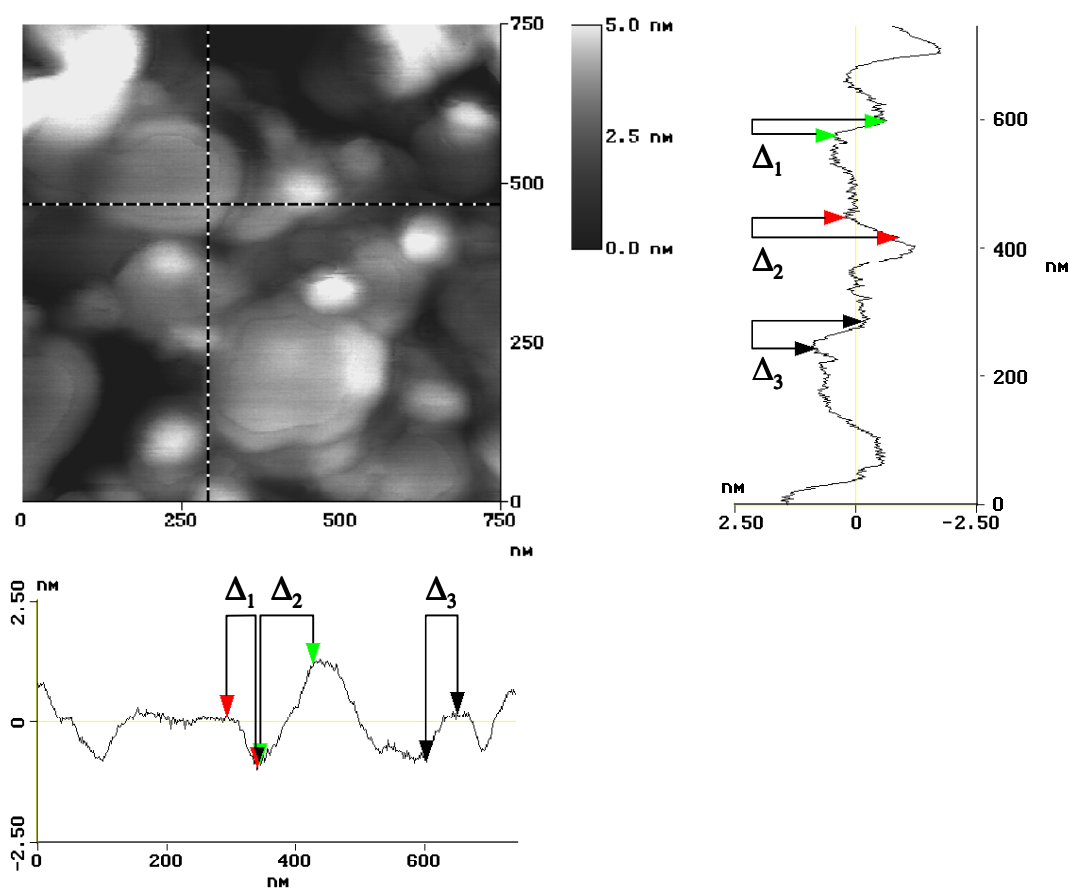
Figure 5.12: Details of SFM images in figure 5.11. Dashed lines in the image indicate the positions in the height profiles below or on the right hand side. The step heights in the profile to the right of the image (listed from top to bottom) are $\Delta_1 = 10.17$ Å, $\Delta_2 = 10.93$ Å, and $\Delta_3 = 10.02$ Å. The step heights in the profile at the bottom of the image (listed from the left to the right) are $\Delta_1 = 10.7$ Å, $\Delta_2 = 20.93$ Å, and $\Delta_3 = 10.01$ Å.

The observed step heights are of integral multiples of 10 Å, and in good agreement with the dimensions of the *tert*-butylcalix[4]arene molecule that were determined from a force field optimized molecular structure [28].

In order to verify the preferred orientation of the *tert*-butylcalix[4]arene molecules discovered for thick layers ($d = 200$ Å) on SiO_2, corresponding FT-IR measurements in ATR mode were performed. Figure 5.13 illustrates the absorption of the *TM* and *TE* wave by a *tert*-butylcalix[4]arene layer, $d = 200$ Å, on an ATR crystal made of silicon.
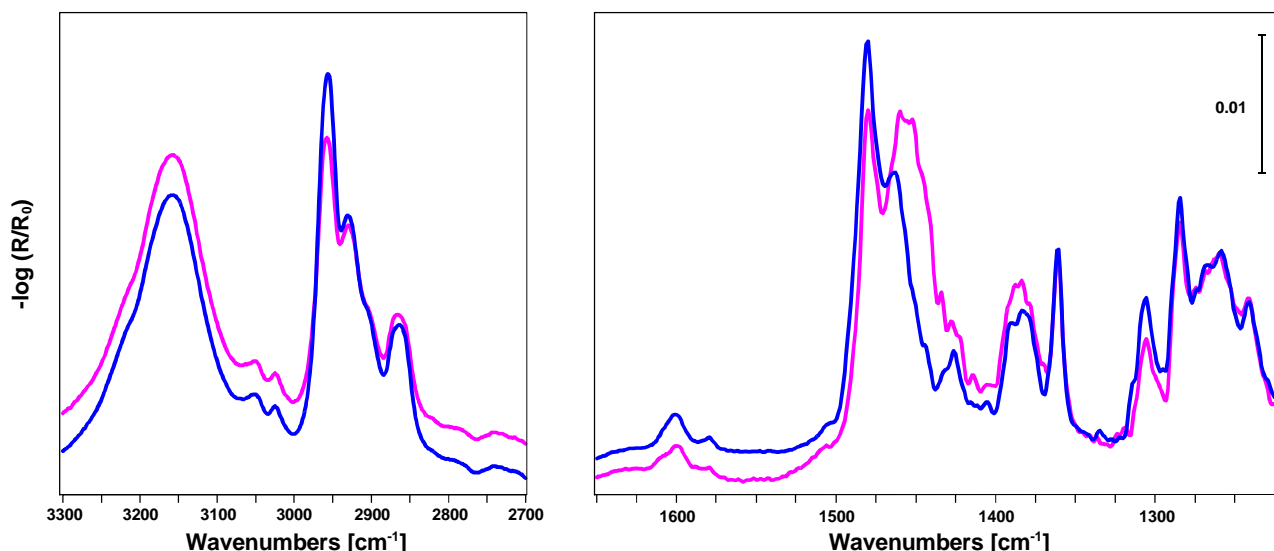
Figure 5.13:   TM (—) and TE spectra (—) of tert-butylcalix[4]arene (d = 200 Å) on Si.

Several vibration modes show different intensities of their absorption bands in the *TM* and *TE* wave of the ATR spectra. Since the light-transmitting spectral range of the silicon crystal is limited to wavenumbers $\tilde{\nu} \geq 1200$ cm^{-1}, however, the region 1150 - 500 cm^{-1} that provides most information about the orientation of the molecules is cut off. Therefore, the intensity inversions in the stretching vibration and the lower frequency region are the only clues for a preferred molecular orientation. Combined with the SFM results, however, an oriented growth of the *tert*-butylcalix[4]arene molecules on the SiO$_2$ substrate is concluded.

5.3.3   SFM Images of *tert*-Butylcalix[4]arene Layers

The *VOLMER-WEBER* growth model implies that the intermolecular attraction of the adsorbate molecules is stronger than the adsorbate-substrate interactions. This fact will be examined in the following for calixarene films with a nominal thickness of only a few layers. Figures 5.14a) and b) show contact mode SFM images of a *tert*-butylcalix[4]arene layer, $d = 20$ Å, on SiO$_2$ that were recorded within 6 h after evaporation.

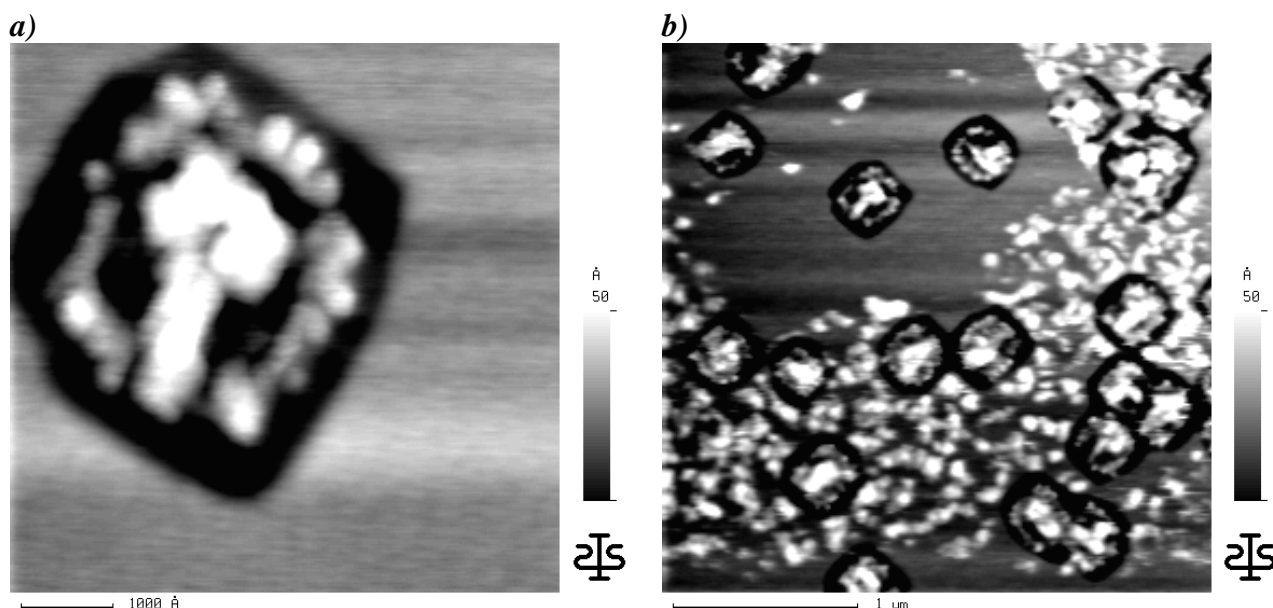*Figure 5.14:   Contact mode SFM images of a tert-butylcalix[4]arene layer, d = 20 Å, on a SiO₂ substrate immediately after evaporation. After the recording of image a) with a scanned area of (0.6 μm)², a bigger area of the sample, i. e. (3 μm)² was scanned, to generate image b).*

First an extremely small sector of the sample, i. e. $(0.6\,\mu m)^2$, was scanned yielding the image in figure 5.14a). A single cluster of *tert*-butylcalix[4]arene is shown on the SiO_2 surface. The latter is left absolutely flat by the cleaning procedure. Image 5.14b) was obtained by magnifying the scanned area to a sector of $(3\,\mu m)^2$ and by slightly changing the scanning position. Several interesting facts are seen in this image: In the region formerly left untouched by the scanning cantilever, molecular clusters of agglomerated *tert*-butylcalix[4]arenes are scattered on the surface while the remaining area is covered with smaller layers. Neither these small spots, nor the clusters are adsorbed strongly enough to withstand the lateral force exerted by the scanning cantilever, and, consequently, are wiped away after several SFM runs performed at the same position. Due to the fact that the small spots are nearly totally wiped away in the upper left part of the image while the number of clusters is not diminished that tremendously, the clusters seem to stick a little stronger to the substrate than the layers do. Unfortunately, the layers are not resistant enough towards the scanning process, so no height profile is available in order to determine their thickness.

Strong attraction among the adsorbate molecules may lead to a migration on an extremely flat surface, if sufficient energy is supplied. To prove this, the sample was stored for five days in a dry atmosphere at room temperature. The resulting SFM images are illustrated in figure 5.14c) and d).
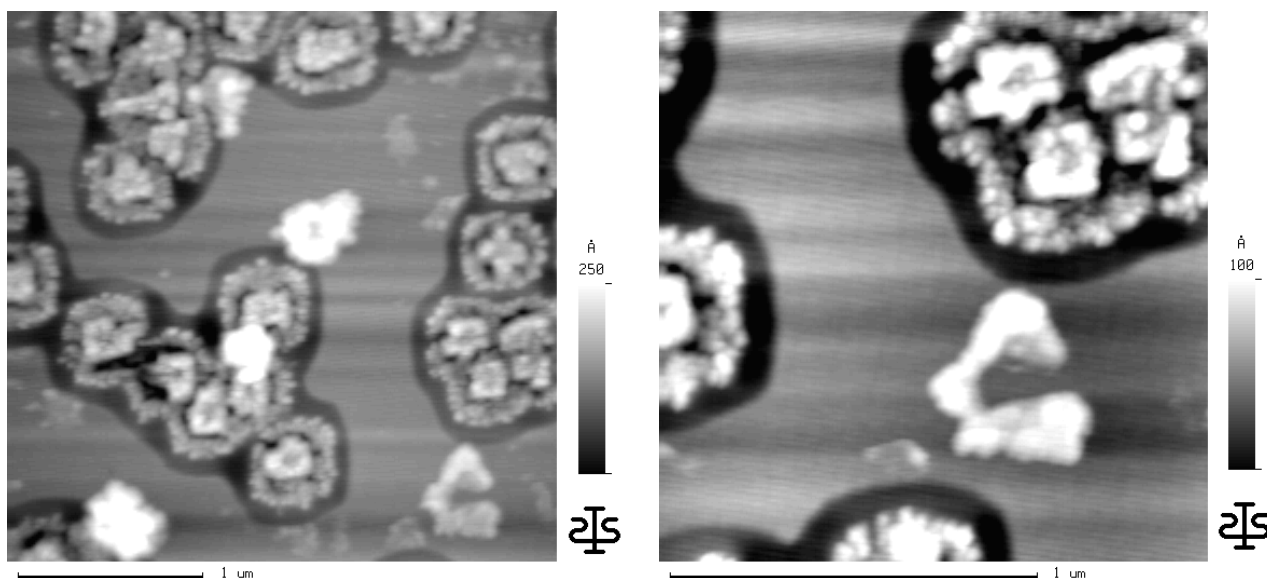
*Figure 5.14:   Contact mode SFM images of a tert-butylcalix[4]arene layer, d = 20 Å, on a SiO$_2$ substrate (continued).
The images c) and d) were recorded after storing the sample for five days at room temperature in an
atmosphere of dried argon. The scanned sectors are (3 μ)^2 and (1.5 μ)^2 in size, respectively.*

The scanned frame of image 5.14c) is of the same size as in figure 5.14b), i. e. (3 μm)^2. Most of the molecular spots described above have vanished, giving rise to *tert*-butylcalix[4]arene clusters that have grown significantly both in lateral direction and in height, as can be seen from a comparison of the gray scale bars to the right of the images b) and c). In contrast to image 5.14b) where nearly the entire substrate was covered with calixarene molecules, large regions of the free, uncovered SiO$_2$ appear in image 5.14c). The deposited *tert*-butylcalix[4]arene molecules seem to have migrated over the surface, to generate the observed clusters. In this case, room temperature provides sufficient energy to overcome the activation necessary for the interchange of sites on the flat substrate. Beside the numerous huge clusters, only one small spot of unclustered calixarene is left in figure 5.14d). Consequently, from the observed effect of agglomerating molecules, a high attraction between the calixarenes is concluded.

In order to analyze the cluster growth, SFM images of a *tert*-butylcalix[4]arene film with a nominal thickness of $d = 70$ Å on SiO$_2$ are displayed in figure 5.15.

a)

b)

c)
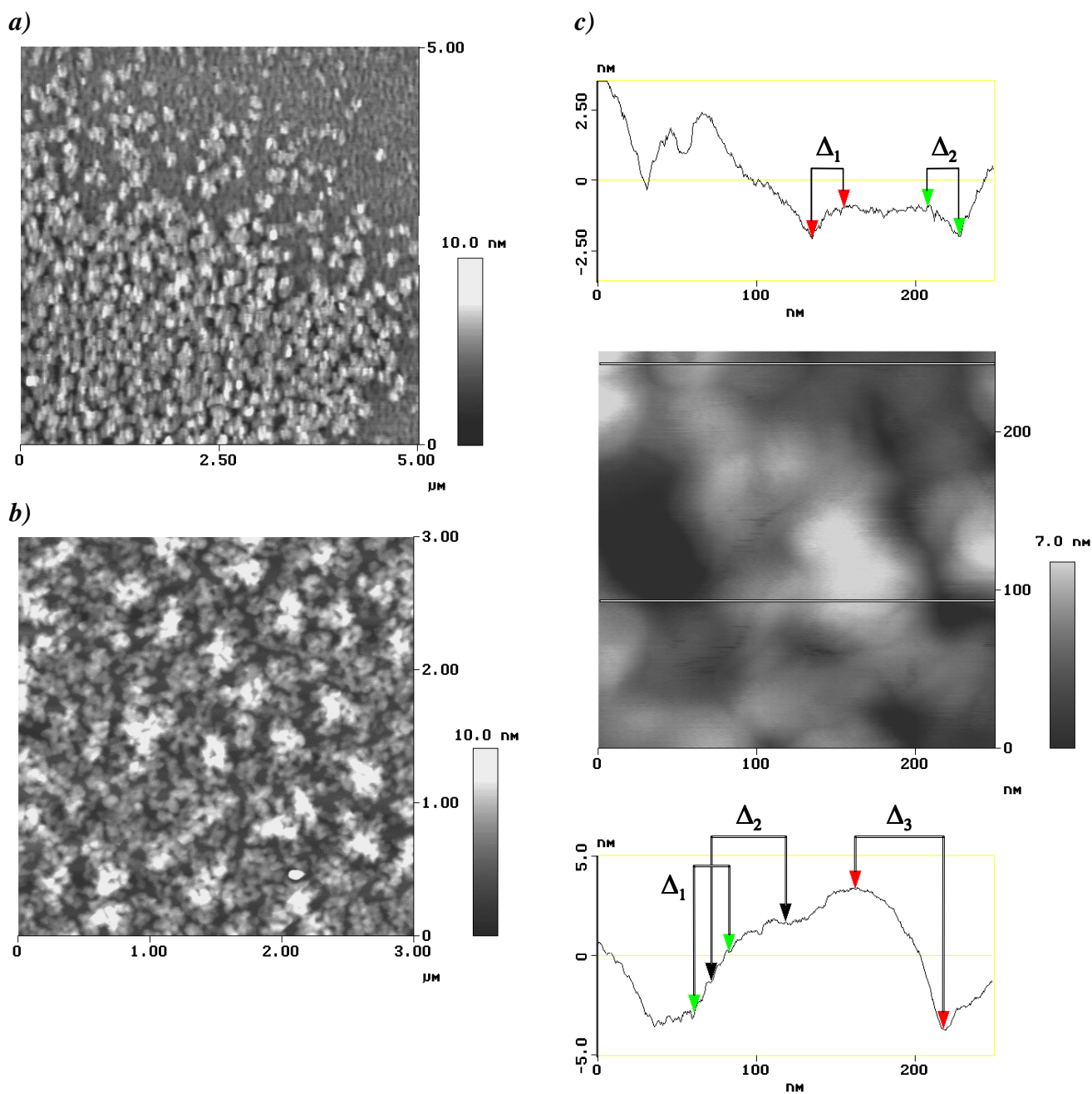
Figure 5.15: *SFM images of tert-butylcalix[4]arene, nominal thickness d = 70 Å, on SiO$_2$ in a) Contact Mode SFM or b) Tapping$^{®}$ Mode SFM. c) Detail of image b) with 2 height profiles, taken at the positions indicated by the horizontal lines. The step heights in the top profile (listed from left to right) are $\Delta_1 = 10.52$ Å, and $\Delta_2 = 10.13$ Å. The heights in the lower profile (listed from left to right) are $\Delta_1 = 30.77$ Å, $\Delta_2 = 30.00$ Å, and $\Delta_3 = 70.51$ Å, respectively.*

The contact mode SFM image 5.15a) illustrates a situation that has already occurred in figure 5.14b). The organic layer is bound too weakly to the substrate and is pushed aside by the scanning cantilever. By imaging the film in tapping mode SFM, shown in figure 5.15b) and c), the oscillating cantilever applies less mechanical stress to the *tert*-butylcalix[4]arene layer. This causes less changes of the film during the imaging process as results from a comparison of SFM images

that were taken before and after numerous SFM runs were performed at the same position of the sample.

The magnified area of $(250 \, nm)^2$, illustrated in figure 5.14c), generates two height profiles that describe the positions marked by the horizontal lines on top and in the lower part of the image. The upper profile depicts steps of monomolecular height in the organic overlayer, which are next to larger clusters. The lower height profile characterizes an area with marked difference in the layer topography. It shows one *tert*-butylcalix[4]arene cluster of approximately 1500 Å in lateral size and 70 Å in height, as indicated by the value of Δ_3. The latter perfectly coincides with the nominal layer thickness. Several particular height levels can be recognized on the left tailing flank of the profile. As denoted by Δ_1 and Δ_2 which correspond to the height of 3 monolayers of the *tert*-butylcalix[4]-arene molecules, the step heights are of integral multiples of 10 Å. Two small areas of the uncoated substrate appear to the left and to the right of the calixarene cluster.

These results confirm the *VOLMER-WEBER* growth mechanism without any doubt. Flat islands on top of the clusters are clearly indicated in the images, while steps of molecular height are found on the tailing flanks of the clusters.

5.3.4   Chemical Modification of the Silicon Surface with GOPTS

Since the thermal deposition of *tert*-butylcalix[4]arene molecules on pure SiO_2 surfaces generates physisorbed layers that are only rather weakly bound to the substrate, a pathway to chemisorbed calixarenes was explored in order to avoid the adsorbate being pushed away by a cantilever or any other similar mechanical stress.
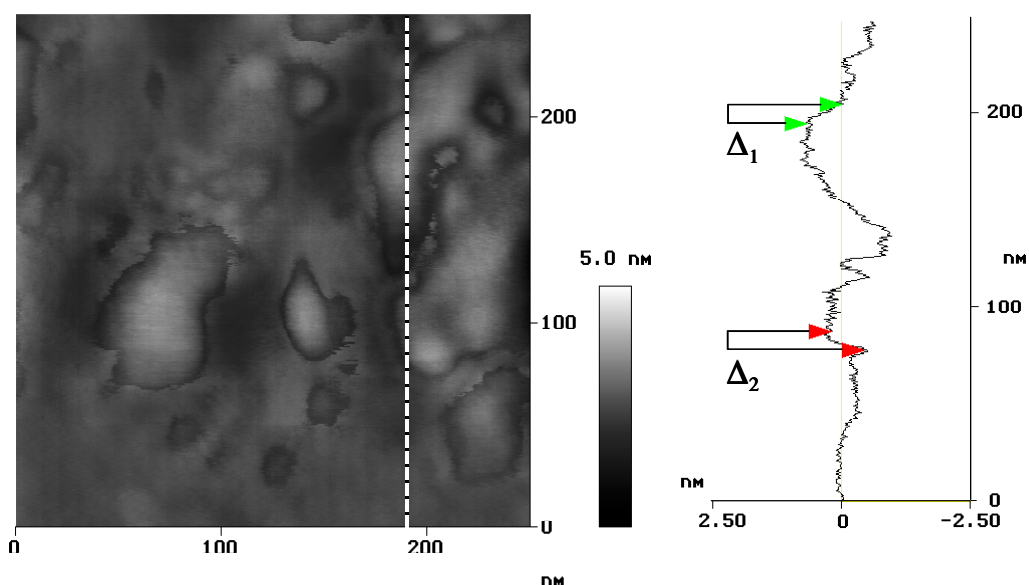

Figure 5.16:   a) Tapping mode SFM images of a GOPTS-modified SiO_2 surface, b) height profile taken along the dashed line in a). The step heights listed (from top to bottom) are $\Delta_1 = 7.01$ Å, and $\Delta_2 = 6.62$ Å.

By modifying a silicon surface with a SAM of the epoxide terminated alkylsilane, 'GOPTS', a highly reactive substrate is generated. After evaporation, the calixarenes bind to the substrate by reaction of at least one phenyl group with the epoxide moiety of GOPTS. Figure 5.16 illustrates the particular stages in the preparation of *tert*-butylcalix[4]arene layers on a epoxide terminated SiO_2 substrate. The reactive surface after modification with GOPTS and a height profile determined perpendicular to the scan direction are shown in figure 5.16a) and b). Beside large regions where the substrate is flat, several smooth areas of a little lighter gray scale appear, indicating some inhomogeneities that may be due to the formation of a second monolayer of GOPTS or to the SiO_2 being affected by the GOPTS preparation; $\Delta_1 = 7.01$ Å and $\Delta_2 = 6.62$ Å are in the range of the molecular dimensions. The profile consciously was determined for a rather hilly area of the sample to ensure that the biggest difference in topography are measured to be lower than 10 Å. Deposition of *tert*-butylcalix[4]arene ($d \approx 300$ Å) and subsequent rinsing of the molecules that are physisorbed on the sample generated the surface displayed in the images 5.16c)-f).
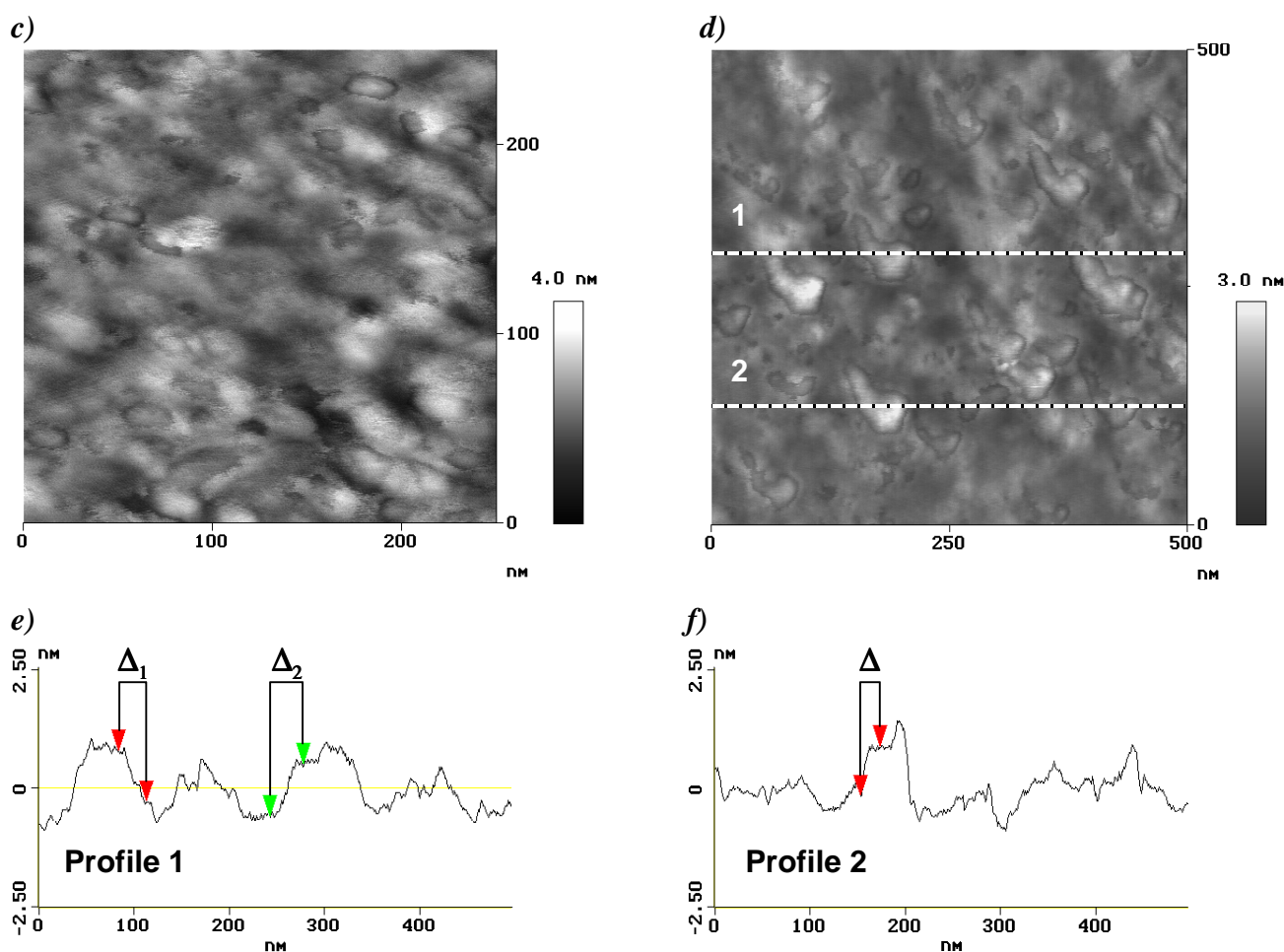

Figure 5.16   *c) Tapping mode SFM images of a tert-butylcalix[4]arene layers on GOPTS / SiO2 after rinsing of physisorbed molecules. d) -f) height profiles (#1 and #2) characterizing the layer at the positions marked by dashed lines in image d). The step heights in profile #1 are $\Delta_1 = 10.53$ Å, and $\Delta_2 = 10.92$ Å, and in profile #2, $\Delta = 10.36$ Å.*

The GOPTS / SiO$_2$ surfaces with and without *tert*-butylcalix[4]arene coating, differ in shape and size of the superior spots. The overall height in topography of less than 40 Å (cf. the gray scale bar), proves that no large calixarene clusters are left on the surface after rinsing. The profiles 5.16e) and f) correspond to the dashed horizontal lines marked with '1' and '2' and indicate terraces of approximately 10 Å in height. This indicates the presence of one monolayer of *tert*-butylcalix[4]-arene on large areas of the modified substrate.

5.4   *tert-Butylcalix[4]arene Layers on Modified Gold Surfaces*

The previous chapter dealt with the growth of *tert*-butylcalix[4]arene layers on silicon substrates that were either hydrophilic due to the cleaning process or chemically modified to posses a reactive terminal group capable of forming chemical bonds with the adsorbed molecules (layers). In this section, the influence of wettability properties on the orientation of the molecules in the layer will be examined in detail.

5.4.1   Characterization of Self-Assembled Thiol Monolayers (SAMs)

SAMs of alkane thiols HS-(CH$_2$)$_n$-X on gold are a suitable model system for the study of interfacial phenomena because of their ease of preparation, their high quality, and the wide range of surface properties achievable by using different chain-terminating groups X. Figure 5.17 shows the infrared reflection-absorption (RA) spectra of self-assembled monolayers of the alkane thiols used in this thesis. The terminal groups were chosen according to their hydrophilic (X = OH) or hydrophobic (X = CH$_3$) properties which match with the hydrophilicity of the hydroxyl groups at the lower rim of the calixarene or the hydrophobic cavity and the hydrophobic properties of the *tert*-butyl residues of the calixarene. The methyl terminated SAM also is predestinated for CH$_3$-π interactions with aromatic systems like the calixarene skeleton. A favoured inclusion of aromatic molecules, comparable with X = -O-CO-C$_6$H$_5$, into the cavity is known from literature [20]. The quality of the SAMs was confirmed by IRAS, ellipsometry and contact angle measurements.

An incubation time of more than 15 h for the self-assembly resulted in high ordering and a high density of the thiol layers. The *all-trans* configuration of the methylene groups in the aliphatic chain is identified by the position of the CH stretching vibrations, mainly of the asymmetric CH$_2$ stretching vibration. In transmission spectra of liquid alkane thiols, ν_{as}(CH$_2$) is centered at $\tilde{\nu} \approx 2925$ - 2927 cm^{-1} and is shifted toward lower in IRAS spectra of the SAM. Low $\tilde{\nu}$ is indicative of well established *all-trans* configuration within the SAM.
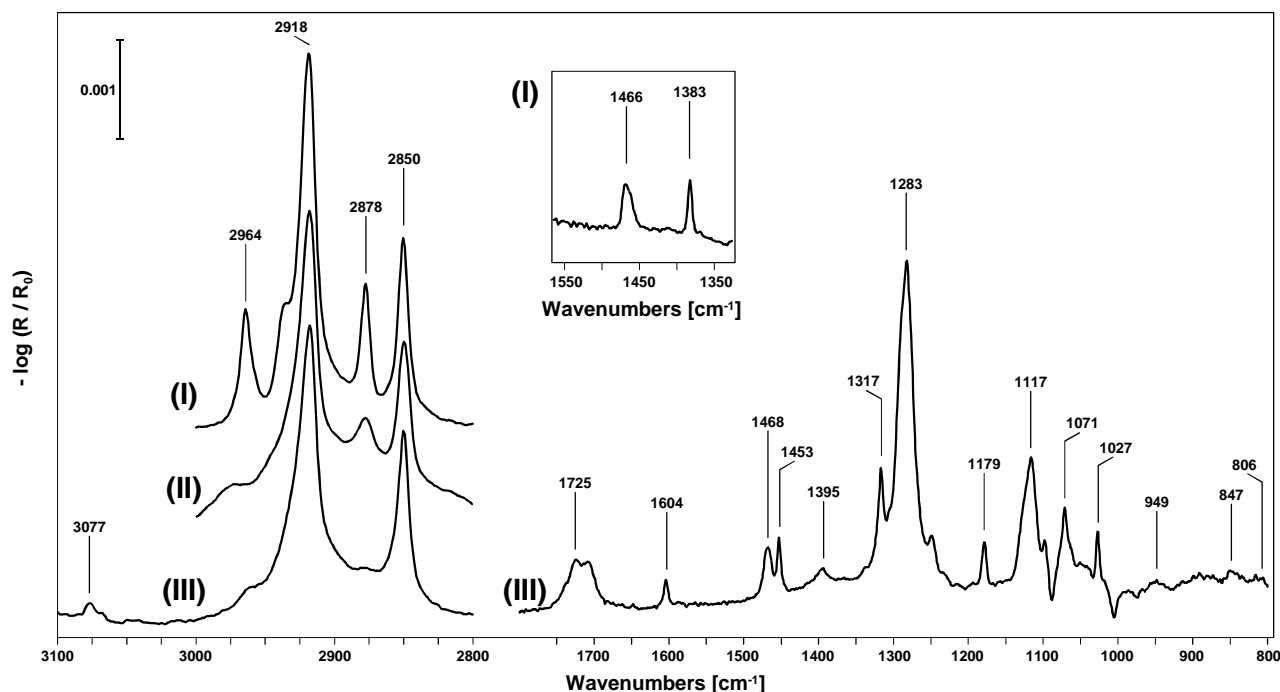
Figure 5.17: RA spectra of self assembled thiol monolayers of (I) Au / S-(CH$_2$)$_{17}$-CH$_3$ (II) Au / S-(CH$_2$)$_{18}$-OH and (III) Au / S-(CH$_2$)$_{18}$-O-CO-C$_6$H$_5$ at room temperature. p-polarized radiation at an incidence angle of 83° was used. The CH-stretching region is displayed to the left of the figure, and the low frequency region for Au / S-(CH$_2$)$_{18}$-O-CO-C$_6$H$_5$ to the right. The inset shows the scissoring mode deformation vibration modes of the Au / S-(CH$_2$)$_{17}$-CH$_3$ SAM, i. e. $\delta_{sc}(CH_2)$ at $\tilde{\nu}$ = 1466 cm^{-1} and $\delta_{sc}(CH_3)$ at $\tilde{\nu}$ = 1383 cm^{-1}.

The characteristic stretching vibration bands of the different thiols are summarized in the following.

Table 5.4:   Characteristic symmetric and asymmetric CH stretching vibrations (ν_s and ν_{as}) of alkane thiol SAMs on gold. In literature, the $\nu(CH_3)$ and $\nu(CH_2)$ modes often are referred to as [r] and [d] branches, [r$_{FR}^+$] denotes the Fermi resonance.

	expected peak position [71, 75]	Au / S-(CH$_2$)$_{17}$-CH$_3$	Au / S-(CH$_2$)$_{18}$-OH	Au / S-(CH$_2$)$_{18}$-O-CO-C$_6$H$_5$
$\nu_{as}(CH_3)$ [r$^-$]	2965 cm^{-1}	2964.2 cm^{-1}		
$\nu_{s,FR}(CH_3)$ [r$_{FR}^+$]	2937 cm^{-1}	2937.3 cm^{-1}		
$\nu_{as}(CH_2)$ [d$^-$]	2917.7 ... 2919.3 cm^{-1}	2918.7 cm^{-1}	2917.7 cm^{-1}	2917.9 cm^{-1}
$\nu_s(CH_3)$ [r$^+$]	2875 cm^{-1}	2877.7 cm^{-1}		
$\nu(CH_2)$ adjacent to OH	2876 cm^{-1}		2877.9 cm^{-1}	
$\nu_{as}(CH_3)$ [d$^+$]	2849.8 ... 2850.5 cm^{-1}	2850.5 cm^{-1}	2849.8 cm^{-1}	2850.2 cm^{-1}
$\nu(CH)$, aromatic	3074 cm^{-1}			3076.8 cm^{-1}

The absorption band observed for the Au / S-(CH$_2$)$_{18}$-OH SAM at $\tilde{\nu}$ = 2877.7 cm^{-1} results from the perturbed CH$_2$ stretching vibration that is associated with the outermost methylene group adjacent to

OH. An assignment for the observed absorption peaks of the phenyl terminated SAM, Au / S-$(CH_2)_{18}$-O-CO-C_6H_5, is given below in table 5.5 [104, 150].

Table 5.5:   Observed frequencies for the most prominent absorption bands of the Au / S-$(CH_2)_{18}$-O-CO-C_6H_5 SAM.

$\tilde{\nu} = 1725$ cm^{-1} ν (C=O) [a])	$\tilde{\nu} = 1604$ cm^{-1} ν_{ar} (CC), 8A & B	$\tilde{\nu} = 1468$ cm^{-1} δ_{sc} (CH$_2$)	$\tilde{\nu} = 1453$ cm^{-1} ν_{ar} (CC), 19B [b])	$\tilde{\nu} = 1317$ cm^{-1} β (CH), 3	$\tilde{\nu} = 1283$ cm^{-1} ν (C-O)
$\tilde{\nu} = 1179$ cm^{-1} β (CH), 9A & B	$\tilde{\nu} = 1117$ cm^{-1} ν (CH) or ν (O-CH$_2$)	$\tilde{\nu} = 1071$ cm^{-1} β (CH), 15	$\tilde{\nu} = 1027$ cm^{-1} γ (CH), 5	$\tilde{\nu} = 847$ cm^{-1} δ_{sc} (O=C-O)	$\tilde{\nu} = 806$ cm^{-1} ω (C=O)

[a]) $\nu_{(ar)}$: (aromatic) stretching vibration; δ_{sc}: scissoring mode deformation; β: in-plane bending, γ: out-of-plane bending, ω: wagging.

[b])   nomenclature of *WILSON* for the assignment of the C-H vibrations of the phenyl ring [150].

Table 5.6:   Ellipsometric thickness and contact angles of the produced thiol SAMs. The advancing and receding contact angle θ_a / θ_r were determined for water (H$_2$O) and hecadecane (HD).

	Au / S-(CH$_2$)$_{17}$-CH$_3$		**Au / S-(CH$_2$)$_{18}$-OH**		**Au / S-(CH$_2$)$_{18}$-O-CO-C$_6$H$_5$**	
ellipsometric thickness [Å]	22 ± 1		24 ± 1		27 ± 1	
contact angle with H$_2$O [°]	$\theta_a = 110 \pm 1$	$\theta_r = 105 \pm 1$	$\theta_a \leq 20$	$\theta_r \leq 10$	$\theta_a = 68 \pm 1$	$\theta_r = 59 \pm 1$
contact angle with HD [°]	$\theta_a = 47 \pm 1$	$\theta_r = 45 \pm 1$	$\theta_a \leq 10$	$\theta_r \leq 10$	$\theta_a \leq 10$	$\theta_r \leq 10$

The ellipsometric thicknesses and the contact angles of the SAMs are in good agreement with values reported in literature [75]. Enquist *et al.* [143] produced the phenyl terminated SAM with a shorter aliphatic chain, i. e. HS-$(CH_2)_{16}$-O-CO-C_6H_5, $d_E = 25 \pm 1$ Å. An increase in thickness of 2 Å due to two additional methylene groups is reasonable. The contact angles of the C_{18} phenyl SAM are rather similar to the reported values for the C_{16} phenyl, θ_a / θ_r (H$_2$O) = 68 ± 1° / 63 ± 1°. These results and the RA spectra confirm the quality of the prepared SAMs.

The behaviour of the methyl terminated, hydrophobic thiol SAM at low ($T = 82$ K) and high temperatures ($T = 398$ K) was investigated using IRAS, and the resulting RA spectra are displayed in figure 5.18.
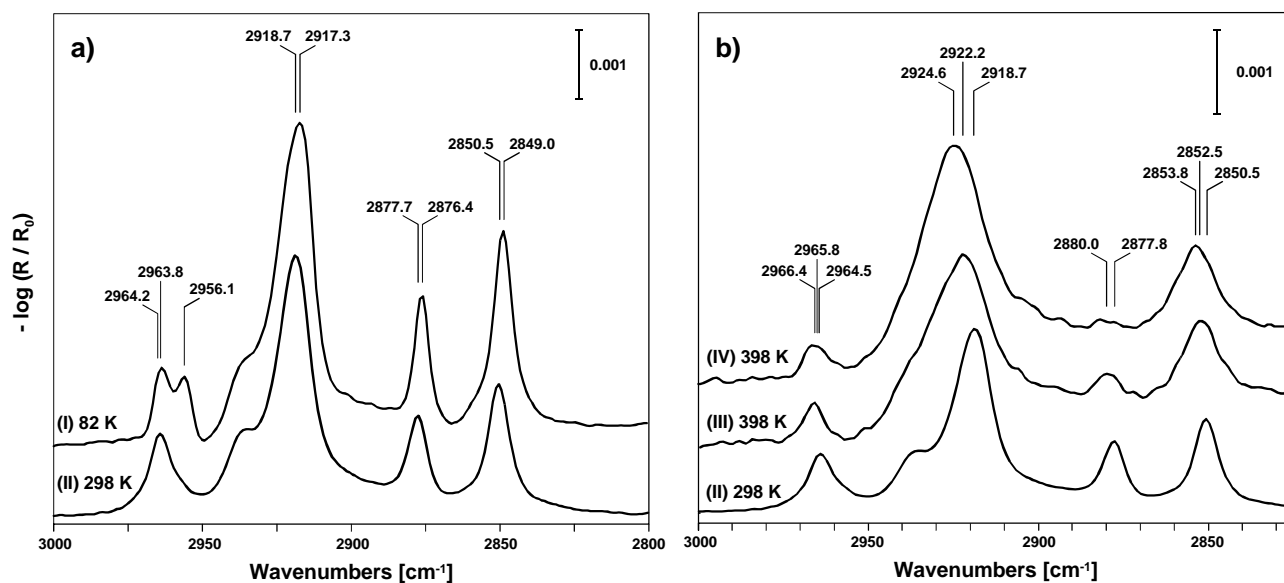
Figure 5.18: RA spectra of the CH₃-terminated SAM (CH-stretching region, measured in ultra high vacuum) at different temperatures. All peak frequencies differ slightly from room temperature values. a) RA spectra measured at T = 82 K (I) and at room temperature (II). The r⁻ branch [ν_{as}(CH₃)] splits into two modes assigned as r_a^- and r_b^-. b) RA spectra at room temperature (II), immediately after heating up to T_s = 398 K (III), and after 3 h of annealing at T_s = 398 K (IV). In all cases, a freshly sputtered and annealed gold substrate was taken as reference.

As a consequence of the decrease in molecular flexibility (i. e. rotation around the C_3 axis of the CH₃ group) at $T = 82$ K, the in-plane (r_a^-) and out-of-plane (r_b^-) modes of the asymmetric CH₃ stretching vibration, ν_{as}(CH₃), are resolved in the spectrum, and the r⁻ branch is split into two clearly resolved peaks at $\tilde{\nu} = 2964$ and 2956 cm⁻¹. The temperature effect leads to a higher intensity of the absorption bands and a smaller band width.

Annealing of the Au / S-(CH₂)₁₇-CH₃ SAM for 1 h at $T = 398$ K causes two effects, as illustrated in figure 5.18b). As generally expected for measurements performed at higher temperatures, the peaks in the RA spectra suffer from a broadening due to an increased flexibility of the aliphatic chains. The latter explains the vanishing intensity of the symmetric CH₃ stretching vibration centered at $\tilde{\nu} = 2878$ cm⁻¹ in the upper RA spectrum. The higher temperature also affects the ordering of the aliphatic chains as characterized by the stretching vibrations of the methylene groups. A significant shifting of the ν_{as}(CH₂) band from $\tilde{\nu}_{298K} = 2919$ cm⁻¹ to $\tilde{\nu}_{398K} = 2925$ cm⁻¹ corresponds to the loss of the *all-trans* configuration in the CH₂ chains of the thiol.

5.4.2 *tert*-Butylcalix[4]arene Layers on Gold Surfaces with Different Wettability Properties

The following results demonstrate in which way the growth, i. e. the orientation of the *tert*-butyl-calix[4]arene molecules, is affected by different terminal groups of the thiol SAMs on gold. A typical difference RA spectrum of a *tert*-butylcalix[4]arene layer ($d = 500$ Å) deposited on the modified hydrophilic gold surface Au / S-(CH₂)₁₈-OH is shown in figure 5.19. The term 'difference

spectrum' indicates that prior to the evaporation, a single channel spectrum of the thiol SAM was recorded and taken as reference R_0.
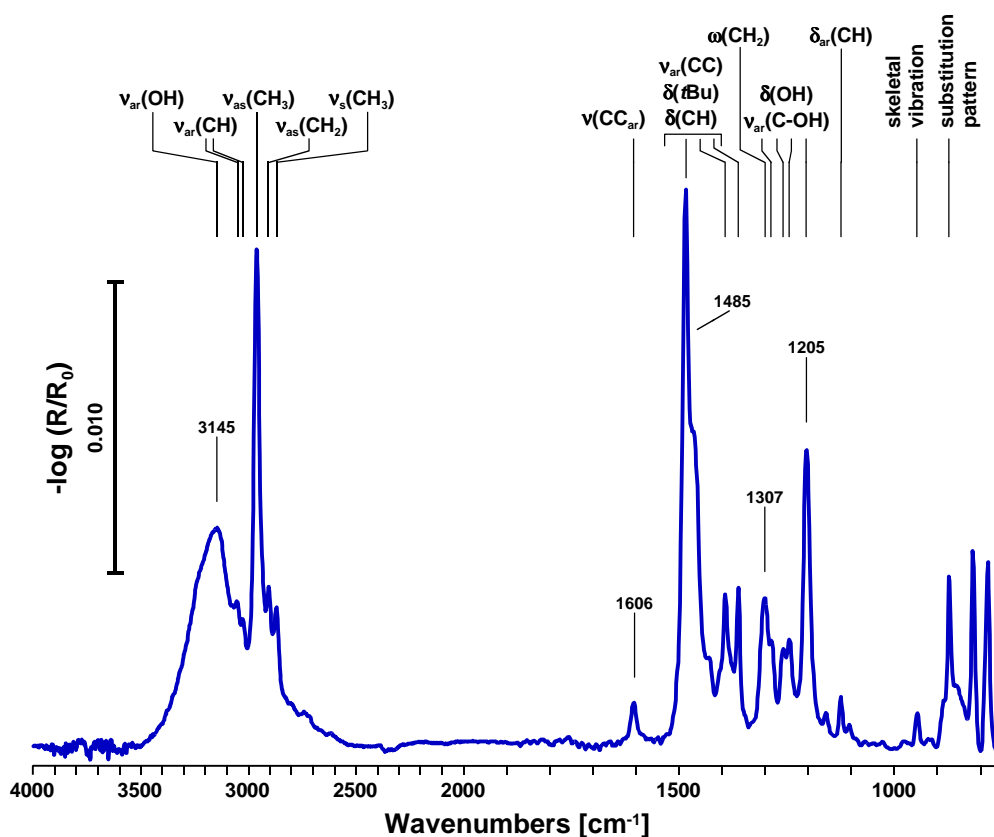

Figure 5.19:   RA difference spectrum of tert-butylcalix[4]arene (d = 500 Å) on Au / S-(CH$_2$)$_{18}$-OH with an assignment of the most prominent absorption bands.

An assignment of the marked vibration bands is given in table 5.1. The positions of most of the vibration modes in the spectrum resemble the values in the transmission spectra (figure 5.1). The aromatic stretching vibration, ν_{ar}(CC), at $\tilde{\nu} = 1606$ and 1485 cm^{-1}, the CH$_2$ wagging vibration at $\tilde{\nu} = 1305$ cm^{-1}, and the skeletal vibration of the *tert*-butyl group centered at $\tilde{\nu} = 1205$ cm^{-1} are shifted towards higher wavenumbers ($\Delta\tilde{\nu} = 2 ... 4$ cm^{-1}). This may be due to packing effects on the hydrophilic surface.

For a *tert*-butylcalix[4]arene layer ($d = 30$ Å) on the OH terminated SAM, the contact angles with water and hexadecane were measured. An advancing contact angle with water, θ_a(H$_2$O) $= 47 \pm 1°$, indicates that some amount of the molecules is oriented with the cavity towards the ambient phase, and the hydroxyl groups at the lower rim favorably point at the hydrophilic thiol SAM. The receding angle of θ_r(H$_2$O) $= 33 \pm 1°$ leads to a pronounced hysteresis, that is understood as the result of the disturbance of the physisorbed film due to the water droplet. The contact angles with hexadecane, θ_a(HD) $= 12 \pm 1°$ and θ_r(HD) $\leq 10°$, are in good agreement with values obtained both for the OH and the C$_6$H$_5$-terminated SAM, table 5.6.

Because of the surface selection rule, a preferred orientation of all the *tert*-butylcalix[4]arene molecules in the film should lead to a decrease (increase) in intensity of vibration modes that are polarized parallel (perpendicular) to the surface. Since no change in relative intensity is observed in the RA spectrum, figure 5.19, in relation to the transmission spectrum representing an isotropic sample, figure 5.1, the layer is assumed to grow isotropically without any long-range order.

The position of the OH stretching vibration, $\tilde{\nu}$ [$\nu_{ar}(OH)$] = 3145 cm^{-1}, corresponds to the frequency range indicated for an empty cavity. This result certifies a satisfactory thermal cleaning of the *tert*-butylcalix[4]arene molecules prior to deposition. It also indicates that no significant interaction between the phenolic hydroxyl group of the calixarene and the terminal OH group of the thiol SAM occurs, since the latter should cause a shifting of $\tilde{\nu}$.

In order to probe short-range ordering effects of the thiol SAMs, the growth of *tert*-butylcalix[4]-arene films with a nominal thickness in the range of monolayers on three different SAMs on gold is studied in detail by means of IRAS.

Figure 5.20 shows the difference RA spectra of thin *tert*-butylcalix[4]arene films on the modified hydrophilic gold surface, Au / S-$(CH_2)_{18}$-OH. The amount of calixarene on the hydrophilic substrate corresponds to a film thickness of ½, 1, ..., 2½ monolayers, from bottom to the top, respectively.
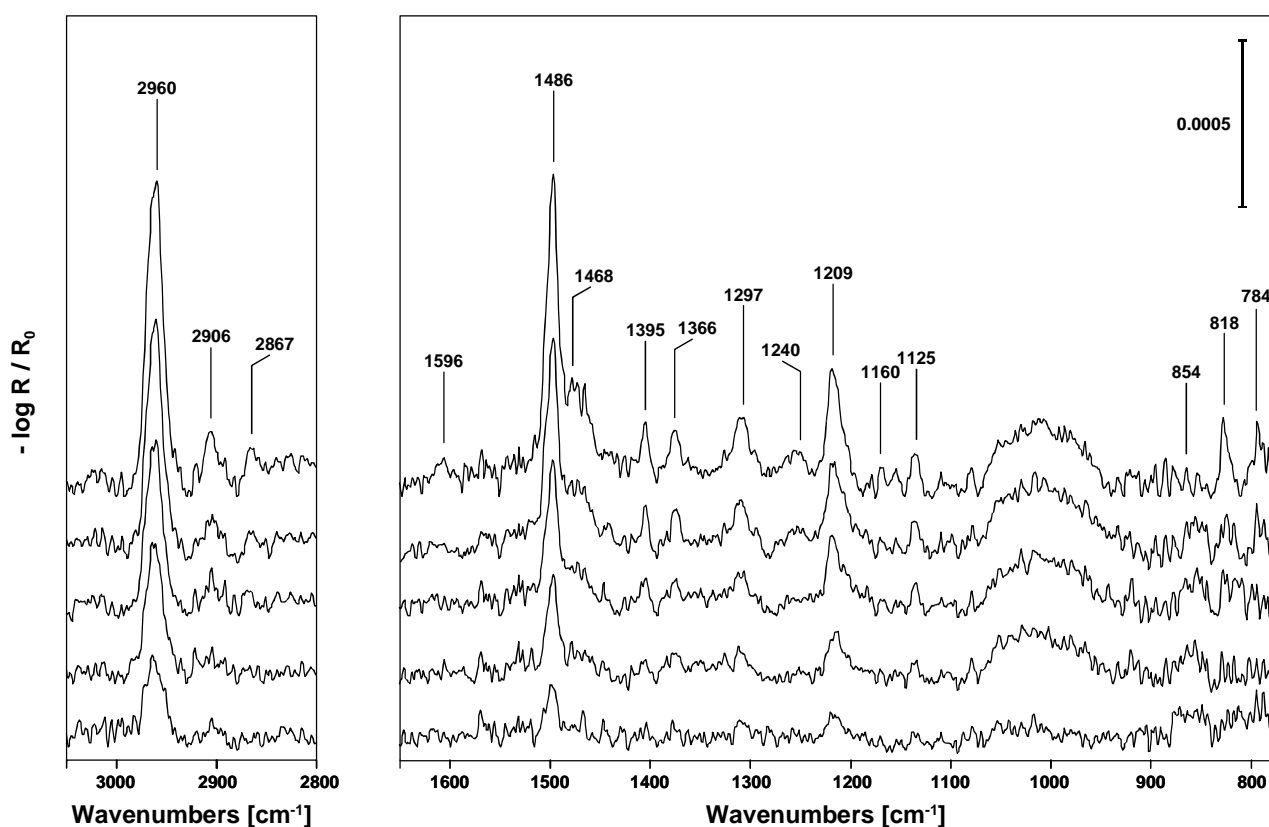

Figure 5.20: Difference RA spectra of a tert-butylcalix[4]arene with increasing thickness comparable to ½, 1, 1½, 2, and 2½ monolayers evaporated on the hydrophilic gold surface Au / S-(CH$_2$)$_{18}$-OH.

Even for a very low coverage of the substrate, the characteristic *tert*-butylcalix[4]arene vibration bands appear clearly above the noise level in the spectra. As has been noticed for the thick layer characterized in figure 5.19, the position of the peaks differs only slightly from the transmission spectrum. Some orientation effects, however, are indicated by the absence of infrared absorption at $\tilde{v} = 1428$ and 1257 cm^{-1}. The latter seems to be covered by the shoulder of the peak centered at $\tilde{v} = 1240$ cm^{-1}. The CH$_2$ wagging vibration ($\tilde{v} = 1305$ cm^{-1}) coalesces with one of the skeletal vibrations of the *tert*-butyl group ($\tilde{v} = 1285$ cm^{-1}), giving rise to an absorption at $\tilde{v} = 1297$ cm^{-1} with shoulders at $\tilde{v} = 1305$ and 1285 cm^{-1}.

Difference RA spectra of a *tert*-butylcalix[4]arene with a nominal thickness of $d = 5$, 10, and 80 Å (i. e. ½, 1, and 8 monolayers) on the modified hydrophobic gold surface, Au / S-(CH$_2$)$_{17}$-CH$_3$, are illustrated in figure 5.21.
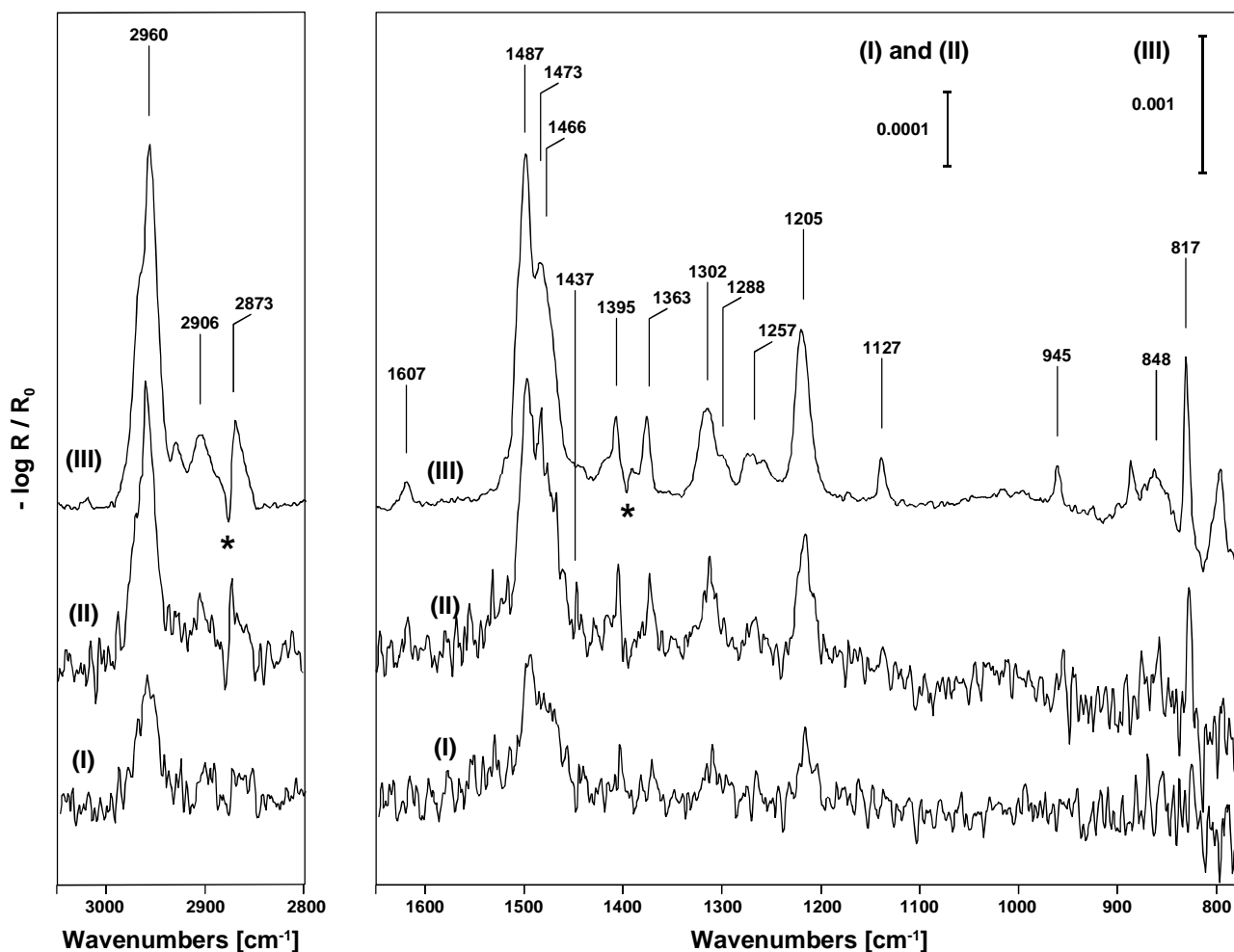
Figure 5.21: Growth of tert-butylcalix[4]arene films on Au / S-(CH$_2$)$_{17}$-CH$_3$: Difference RA spectra of nominally ½, 1, and 8 monolayers are denoted as (I), (II), and (III), respectively. A vanishing intensity of several vibration modes in (I) and (II), e. g. at $v = 1242$, 1159, and 1125 cm^{-1} indicates a preferred orientation of the molecules in the layer. Note the 'negative' peaks marked by '*' in the figure, and the different scale of the spectra.

Since the MCT detector is cooled with liquid nitrogen, the amount of condensed ice on the detector element increases with time. This gives rise to a broad absorption band with variable intensity in the OH stretching vibration region that overlaps with the ν(OH) of the calixarene. Therefore, the position of the ν(OH) absorption band is omitted in further discussions.

The comparison of the figures 5.20 and 5.21 reveals differences in the growth behaviour of *tert*-butylcalix[4]arene on the modified hydrophilic and hydrophobic gold surfaces. First, the stretching vibration band of the aromatic rings, ν_{ar}(CC), is significantly broadened on the methyl terminated SAM. Also, in the low frequency region and the fingerprint area of the spectra (I) and (II) in figure 5.21, several characteristic vibration modes of the *tert*-butylcalix[4]arene molecule are missing, i. e. at wavenumbers $\tilde{\nu} = 1242$, 1159, and 1125 cm^{-1}, no absorption of infrared radiation is observed.

This latter fact is explained in terms of the *surface selection rule* that was deduced in chapter 3. It states that, as a result of the phase shift upon reflection at metal surfaces, an amplification of vibration modes with a transition moment parallel to the surface normal occurs, whereas absorption bands vanish if their dipole moment changes perpendicular to the surface normal. In this context, the three missing absorption bands mentioned above indicate that their dipole moments are aligned perpendicular to the surface normal, not just for a couple of molecules, but for (nearly) all of the *tert*-butylcalix[4]arenes. This fact clearly proves a preferred orientation, i. e. an ordered growth, of the *tert*-butylcalix[4]arene molecules on the hydrophobic, methyl terminated thiol SAM.

In the region of the CH stretching vibrations, ν_{as}(CH$_3$) is shifted towards lower wavenumbers, giving rise to a 'negative' peak, i. e. a drop in intensity below the baseline, that appears at $\tilde{\nu} = 2879$ cm^{-1}, marked by '*'. The effect of 'negative' peaks, has already been reported by ENQUIST and LIEDBERG [151]. The authors interpret the significant loss of vibrational intensity, as compared to the clean SAM, to be due to overlayer-substrate interactions. The negative peaks occur due to the fact that for the *difference* spectra, the clean SAM substrate was taken as a reference, R_0, and the *tert*-butylcalix[4]arene layer deposited on the SAM as a sample, R. Decreasing intensities of the [r$^-$] and [r$^+$] vibration modes are observed for increasing thickness of the *tert*-butylcalix[4]arene film. Since these modes are associated with the chain-terminating methyl groups, obviously, an increasing number of methyl groups becomes involved in interactions between the *tert*-butyl-calix[4]arene and the thiol SAM. Also, the broadening of the ν_{ar}(CC) vibration band is concluded to be due to these overlayer-substrate interactions.

In order to understand the interactions on a molecular level, small molecules that mimic the different functional groups and building blocks of the calixarene were deposited on the methyl terminated SAM. If, for example, the interaction is due to an attractive interactions between the *tert*-butyl group of the calix[4]arene and the methyl group of the SAM, a spectrum of an aliphatic molecule with a *tert*-butyl moiety, e. g. dimethylbutane (H$_3$C)$_3$C-CH$_2$-CH$_3$, adsorbed on the SAM will show the same effect, i. e. induce negative absorption bands. Model compounds such as

alcohols or phenols, aliphatic molecules with a *tert*-butyl group or aromatic molecules, were taken into account, with toluene tested first. Figure 5.22 compares both absorbance and difference spectra of the Au / S-(CH$_2$)$_{17}$-CH$_3$ surface prior to and after the deposition of *tert*-butylcalix[4]arene films (d = 30, 50 Å) or a dosing of 15 L of deuterated toluene (d^8-toluene, C$_6$D$_5$-CD$_3$).
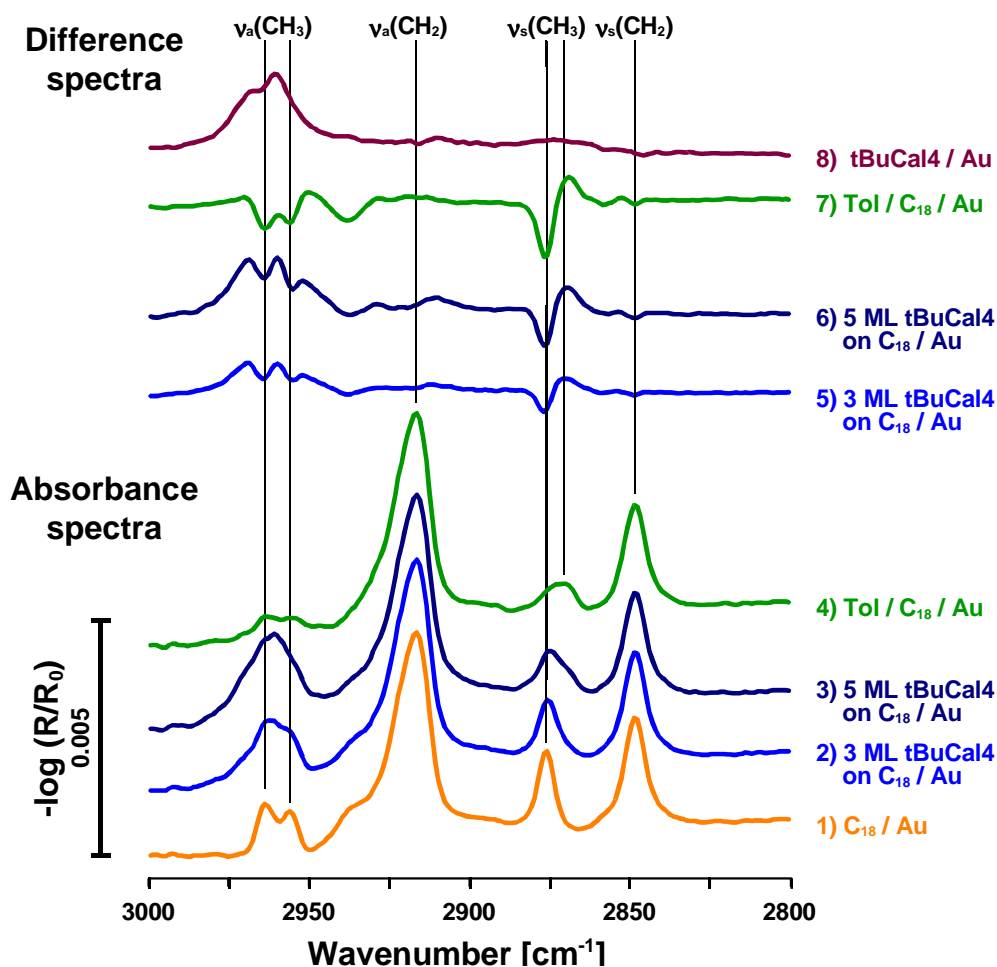
Figure 5.22: *RA spectra of the CH stretching vibration region indicating interactions of the methyl terminated thiol Au / S-(CH$_2$)$_{17}$-CH$_3$ with d^8-toluene and thin layers of tert-butylcalix[4]arene, d = 30 and 50 Å, respectively. The spectra #1 - #4 were measured with a freshly sputtered and annealed gold surface taken as reference. The RA spectra #5 - #7 were calculated to show the differences in the spectra #2 - #4 relative to the clean SAM (#1), e. g. the difference spectrum of #2 and #1 is depicted as #5. To the top, the RA spectrum of tert-butylcalix[4]arene deposited on a freshly sputtered and annealed gold surface is illustrated for comparison. Here no interactions with the substrate are indicated. The spectra are measured at a sample temperature of T$_s$ = 82 K.*

The CH stretching vibration region of a typical RA spectrum of the hydrophobic SAM is denoted as spectrum #1 in figure 5.22. Note the splitting of the asymmetric CH$_3$ stretching vibration giving rise to a r$_a^-$ and r$_b^-$ branch. The positions of the vibration bands are $\tilde{\nu}$ [ν_a(CH$_3$)] = 2963.8 and 2956.0 cm^{-1}, $\tilde{\nu}$ [ν_a(CH$_2$)] = 2916.7 cm^{-1}, $\tilde{\nu}$ [ν_s(CH$_3$)] = 2876.3 cm^{-1}, and $\tilde{\nu}$ [ν_s(CH$_2$)] = 2848.7 cm^{-1}.

An evaporation of nominally 3 and 5 monolayers of *tert*-butylcalix[4]arene generates the RA spectra #2 and #3. As a consequence of the interactions discussed above, the maximum of the CH$_3$

stretching vibration bands is shifted to $\tilde{\nu}\,[\nu_s(CH_3)] = 2875.3\ cm^{-1}$, with a shoulder on the low frequency flank. As a response to the growing thickness of the calixarene layer, the intensity of the $\nu_{as}(CH_3)$ vibration increases and the splitting diminishes. The $\nu(CH_2)$ vibrations are unaffected by the *tert*-butylcalix[4]arene layer and remain unchanged in shape and position. From this, it is concluded that the inner SAM structure remains unperturbed upon deposition and that the interaction with the calixarene molecules is limited to the tail groups of the SAM.

The effect of dosing 15 L d^8-toluene on the Au / S-$(CH_2)_{17}$-CH_3 SAM is shown in the absorption spectrum #4. Since $\tilde{\nu}\,(C\text{-}D) \approx 2100\ cm^{-1}$, none of the toluene bands appears in the spectrum. Again, the $\nu(CH_2)$ vibrations are unaffected by the dosing, whereas the $\nu_{as}(CH_3)$ band nearly disappears, r_{FR}^+ almost vanishes, and $\nu_s(CH_3)$ is shifted to $\tilde{\nu} = 2870.7\ cm^{-1}$.

The difference in absorption calculated between SAMs with or without *tert*-butylcalix[4]arene coating are depicted as spectra #5 and #6, and the difference resulting from the dosing of toluene is shown in #7. The unaffected behaviour of the $\nu(CH_2)$ vibrations generates a straight line around $\tilde{\nu} = 2917$ and $2850\ cm^{-1}$, while the $\nu_{as}(CH_3)$ peaks show two significant drops in intensity at $\tilde{\nu} = 2964.7$ and $2955.2\ cm^{-1}$ that correlate to a vanishing of the r_a^- and r_b^- band of the thiol SAM. In all three difference spectra, a negative peak at $\tilde{\nu} \approx 2937\ cm^{-1}$ indicates the decreasing intensity of the r_{FR}^+ vibration, strongly pronounced in #7 obtained after toluene dosing. Interactions with the organic overlayers lower the excitation frequency of the symmetric CH_3 and cause a pronounced negative peak at $\tilde{\nu} = 2877\ cm^{-1}$, i. e. the position of $\nu_s(CH_3)$ in the spectrum of the pure SAM, whereas a strong positive peak appears at the lower wavenumber of $\tilde{\nu} \approx 2870\ cm^{-1}$.

With respect to peak shifting and negative absorption bands, toluene and *tert*-butylcalix[4]arene demonstrate an identical behaviour on the CH_3-terminated thiol SAM. Therefore, an affinity of aromatic rings to enter into CH_3-π interactions with the SAM [56] is concluded to be the driving force that leads both to an interaction with the organic layer and to a preferred orientation of the *tert*-butylcalix[4]arene molecules in the film.

In the same way as described above for the CH_3 and OH terminated SAM, *tert*-butylcalix[4]arene films were deposited on the phenyl terminated surface, Au / S-$(CH_2)_{18}$-O-CO-C_6H_5. In analogy to the methyl terminated SAM, a preferred orientation of the molecules in the film was expected as a result of interactions between *tert*-butylcalix[4]arene and the phenyl groups of the SAM. The latter, however, was not observed. Perhaps due to the high density of the thiol layer, the C_6H_5 groups are too close to each other and, hence, an inclusion into the *tert*-butylcalix[4]arene cavity is sterically hindered. 'Spacer' molecules within the SAM might help to overcome this problem.

5.4.3   Temperature Programmed Desorption of Calixarenes and SAMs

The relative strength of the interactions that keep the layers on the surface can be estimated by temperature programmed desorption (TPD). The magnitude of the peak desorption temperature (desorption energy) can provide information about the mechanisms of adsorption, i.e. it can be used to distinguish between physisorption and chemisorption phenomena. By combining mass spectrometry (MS) and infrared reflection-absorption spectroscopy (IRAS), the macroscopic effect of the thermal desorption of an organic film is simultaneously monitored on the molecular level. Figure 5.23 shows the traces of the temperature programmed desorption of *tert*-butylcalix[4]arene layers deposited on the hydrophilic Au / S-$(CH_2)_{18}$-OH and the hydrophobic Au / S-$(CH_2)_{17}$-CH_3 SAMs on gold. For comparison, the TPD spectra of both the SAMs without organic overlayer are illustrated.
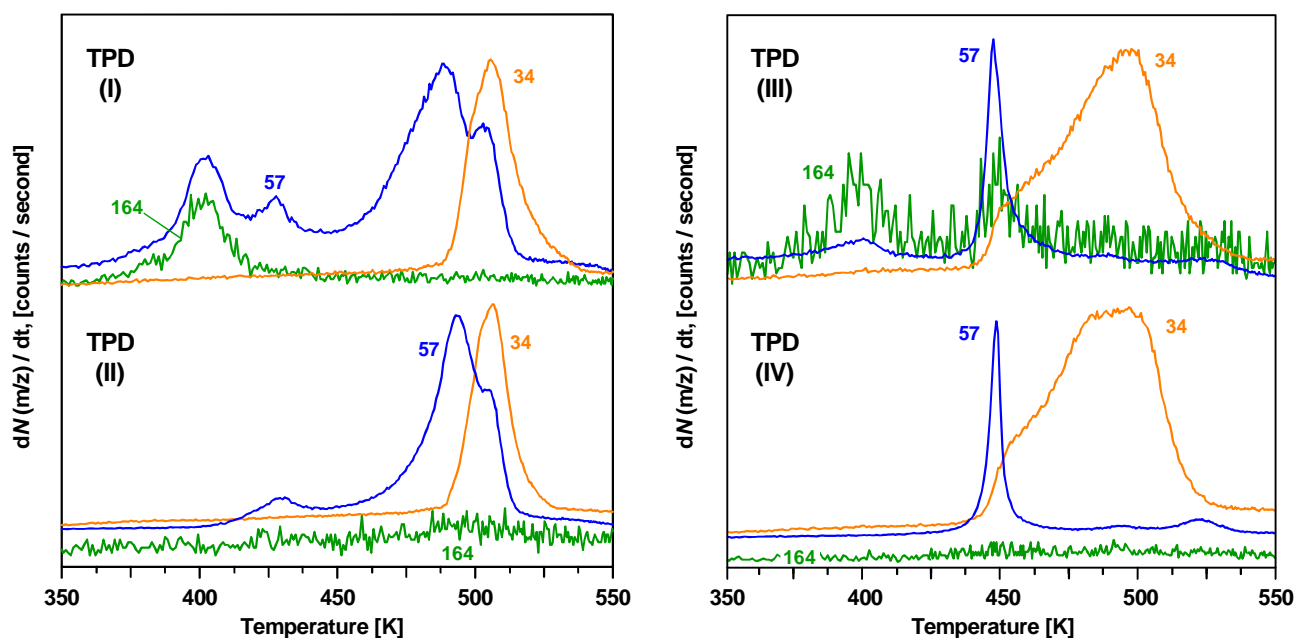
Figure 5.23:   TPD spectra of different organic layers on gold surfaces, heating rate $\beta = 0.33 \ Ks^{-1}$. TPD (I) tert-butyl-calix[4]arene on H_3C-$(CH_2)_{17}$-S / Au, (II) CH$_3$-terminated SAM on gold, (III) tert-butylcalix[4]arene on OH-terminated SAM on gold, and (IV) pure HS-$(CH_2)_{18}$-OH SAM on gold.

Assignment of the Detected Masses. The extremely stable *tert*-butylcalix[4]arene molecule generates only very few cracking products found in mass spectra. Since the [M$^+$] peak at m/z = 648 exceeded the measurement range of the used MS, only the fragments appearing at m/z = 57 and m/z = 164 are useful for a characterization of the desorption progress. Three fragments, i. e. m/z = 32, 33, and 34, contribute to the trace of the desorbing sulfur, and the latter showed the highest counting efficiency.

m/z = 57 C_4H_9, common fragment for many organic compounds and - due to a favored elimi-nation of the *tert*-butyl group - characteristic fragment of the *tert*-butylcalix[4]arene.

m/z = 164   Fragment consisting of a quarter of the *tert*-butylcalix[4]arene molecule.

m/z = 34   Sulfur, trace with highest intensity compared to other masses characteristic for sulfur.

The thermal desorption of *tert*-butylcalix[4]arene / H_3C-$(CH_2)_{17}$-S / Au (TPD trace *I*)occurs in the following steps: At a sample temperature of $T_s \approx 401$ K, the calixarene molecules desorb and generate peaks of m/z = 57 and 164. Different amounts of the aliphatic chains (m/z = 57) of the SAM desorb at $T_{peak,1} \approx 427$ K, $T_{peak,2} = 488$ K, and $T_{peak,3} = 505$ K. The second peak is dominating and contains most likely fragments from the thiol. The third one coincides with the desorption of the covalently bound sulfur fragments from the surface.

Without the calixarene adlayer, the peaks in the TPD traces (*II*) have roughly the same shape but are sharpened. Only a few desorbing thiol fragments give rise to a small peak at $T_s \approx 427$ K, while $T_{peak,2} = 493$ K is observed strongly. The latter indicates that the SAM is more stable and homogeneous if no perturbation by the calixarene layer has taken place.

The TPD spectra of the OH terminated SAM with or without *tert*-butylcalix[4]arene film, TPD (*III*) and (*IV*), show one major difference: One single sharp peak of m/z = 57 at $T_s \approx 450$ K indicates an immediate desorption of all the aliphatic chains of the Au / S-$(CH_2)_{18}$-OH SAM, whereas the detaching sulfur generates a broad trace reaching from $T_s \approx 460$ K to $T_s \approx 520$ K. The fragments of the OH SAM are virtually unaffected by the calixarene molecules, as concluded by comparison of (*III*) and (*IV*). The desorption of the calixarenes from the OH terminated SAM, however, gives rise to two peaks at $T_s \approx 401$ - 408 K and $T_s \approx 447$ K, as detected by an increase of the m/z = 57 and 164 traces in the spectra.

The desorption behaviour of *tert*-butylcalix[4]arene layers of different thickness deposited on freshly sputtered or SAM covered gold substrates is illustrated in figure 5.24. In all the spectra, only the shape of the m/z = 164 traces is considered.

a)

b)

Figure 5.24: TPD traces of tert-butylcalix[4]arene layers deposited in different thickness on gold or thiol SAMs on gold. a) Comparison of the desorption temperature, T_{des}, of the tert-butylcalix[4]arene on pure gold (I), on Au / S-(CH$_2$)$_{18}$-OH (II), and on Au / S-(CH$_2$)$_{17}$-CH$_3$ (III), respectively. b) TPD spectra of a series of tert-butylcalix[4]arene layers on the methyl terminated SAM. The layer thickness increases from d = 20 Å (I) to d = 100 Å (V).

Depending on the nature of the gold substrate, the main peak of the desorbing *tert*-butylcalix[4]-arene appears at temperatures of $T_{des} = 395$ K on a clean gold surface, $T_{des} = 401$ K on the hydrophobic thiol SAM terminated with methyl groups, and $T_{des} = 401$ - 408 K for the desorption from the hydrophilic Au / S-(CH$_2$)$_{18}$-OH, figure 5.24a).

With regard to the measuring accuracy, no variation of T_{des} with the increasing layer thickness was detected from the curves and the fittings in figure 5.24b). This indicates a 1st order kinetic for the desorption of *tert*-butylcalix[4]arene from the Au / S-(CH$_2$)$_{17}$-CH$_3$ substrate, as expected for a non-dissociated molecule. The significant broadening of the symmetric peaks may be due to the substrate-overlayer interactions that were discussed above.
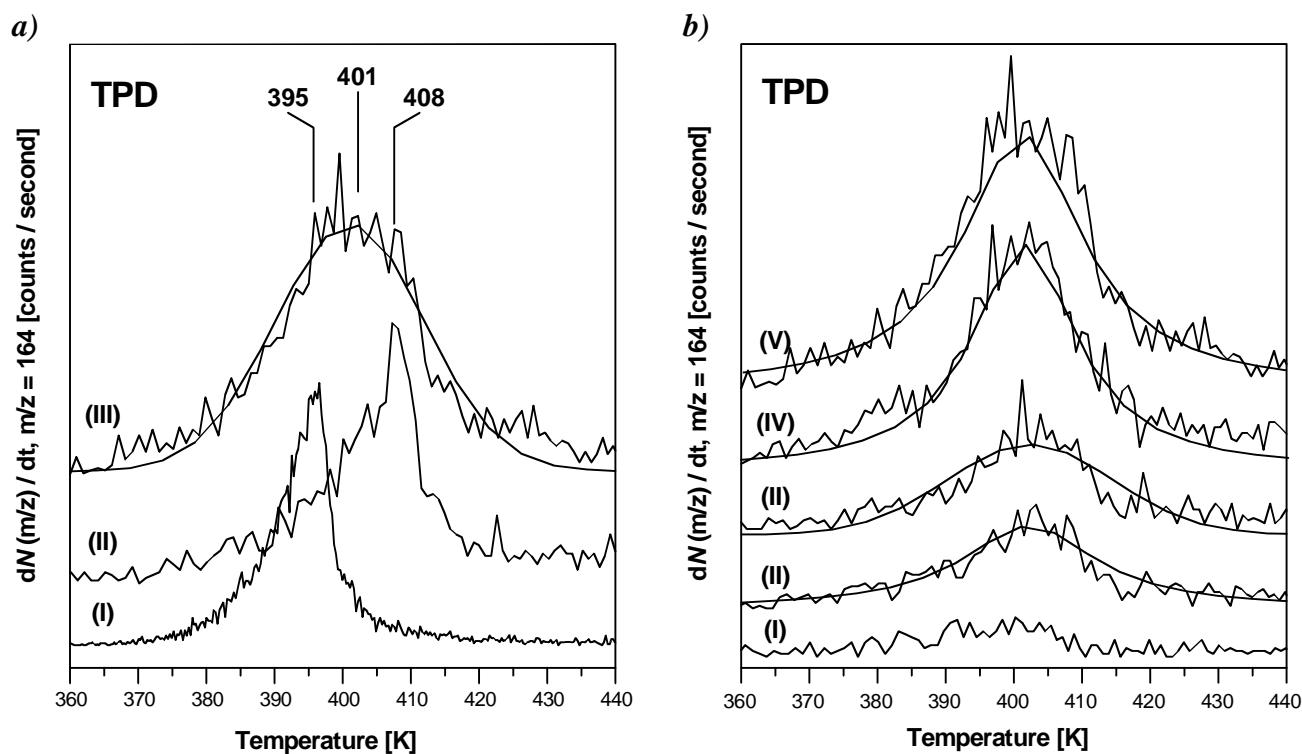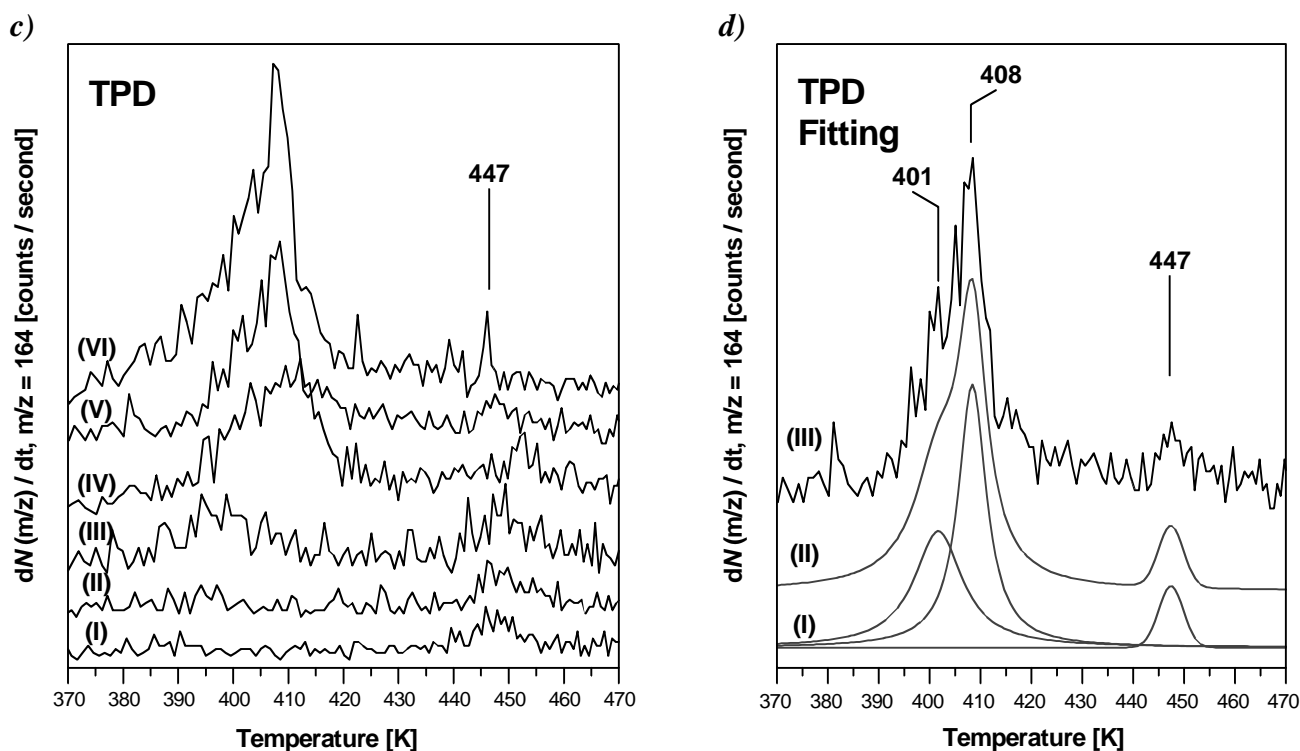
c)

d)

Figure 5.24: TPD traces of tert-butylcalix[4]arene layers deposited in different thickness on thiol SAMs on gold (continued). c) Desorption of tert-butylcalix[4]arene layers with a thickness reaching from d = 10 Å (I) to d = 120 Å (VI) from the OH terminated SAM generates three peaks in the spectra that are fitted in d)

The shape of the TPD traces in figure 5.24c) is described on the basis of the peak fitting performed for film V ($d = 80$ Å) in 5.24d). Three peaks contribute to the desorption, i. e. besides $T_{des,1} = 401$ K, known from the CH_3 terminated thiol, other species of calixarene molecules that are bound stronger to the OH terminated SAM gives rise to sharp peaks at $T_{des,2} = 408$ K and $T_{des,3} = 447$ K. The latter coincides with the removal of the methylene chains of the SAM and has roughly the same size for all coverages. For a more detailed analysis, the area of the desorption peaks at $T_{des,1} = 401 - 408$ K (contributes to A_{P1}) and at $T_{des,3} = 447$ K (A_{P3}) were estimated by peak fitting. The ratio of the peak areas, i. e. $R_{1/3} = A_{P1} / A_{P3}$, is approximately 1:1 for film II ($d = 20$ Å), 3:1 (III, $d = 40$ Å), 8:1 (V, $d = 80$ Å), and 11:1 (VI, $d = 120$ Å), respectively. Although the observed counting rate is rather low, these values seem to have sufficient accuracy to indicate that one monolayer of *tert*-butylcalix[4]-arene sticks stronger to the surface than the others, thus increasing the desorption temperature by about 40 K.

The TPD results have shown the following differences for the two surfaces. While only one desorption peak of the calixarene is observed for the CH_3 terminated SAM, an additional desorption peak (m/z = 164) appears in the TPD trace of the OH terminated substrate at $T_{des,3} = 447$ K. The peak at 400 K is most likely due to self associated (aggregated) calixarenes, i.e. to calixarenes that

bind to each other *via* some sort of $CH_3 \cdots CH_3$ or $CH_3 \cdots \pi$ interactions. The additional peak at $T_{des,3} = 447$ K might be due to hydrogen bonded calixarene molecules of the first monolayer.

Due to the interactions of the aromatic moieties, the calixarene film affects the methyl terminated thiol SAM and, hence, changes its desorption behaviour. The amount of weakly bound aliphatic fragments is increased, and $T_{peak,2}$ shifted by 5 K. In contrast to this, the general desorption of the hydroxyl terminated SAM does not change upon deposition of a calixarene overlayer.

The constant desorption temperature observed for different coverages as well as the shape of the TPD traces (cf. figure 3.18d) indicate a 1st order desorption kinetic for the *tert*-butylcalix[4]aren both on the OH and the CH_3 terminated surfaces. According to the Redhead method [123], the activation energy for the desorption can be calculated from equation 3.48. For the applied heating ramp of $\beta = 0.33$ K s^{-1}, and assuming first, $k_m^0 = 10^{13}$ s^{-1}, as commonly done in literature, an activation energy $E_{A,des,1} = 111.3$ kJ mol^{-1} results for $T_{des,1} = 401$ K, whereas for $T_{des,3} = 447$ K an energy of $E_{A,des,3} = 124.5$ kJ mol^{-1} is calculated. With respect to the large mass of the *tert*-butyl-calix[4]arene molecule, the vibration frequency is estimated to be $k_m^0 > 10^{11}$ s^{-1}. For this frequency value, the desorption energies calculated from equation 3.48 are $E_{A,des,1} = 96.0$ kJ mol^{-1} and $E_{A,des,3} = 107.4$ kJ mol^{-1}, respectively, as 'lower' limit of the evaluated energies. In any case, the activation energy for the desorption of the 'last' *tert*-butylcalix[4]arene layer on the OH terminated SAM, correlating to $T_{des,3}$, is increased by approximately 12 kJ mol^{-1} as compared to $T_{des,1}$.

For a better insight into the desorption process, figures 5.25 - 5.27 show the RA spectra recorded during the TPD of *tert*-butylcalix[4]arene on $H_3C-(CH_2)_{17}-S$ / Au.

The RA spectra of the pure Au / S-(CH$_2$)$_{17}$-CH$_3$ SAM and of a *tert*-butylcalix[4]arene layer ($d = 200$ Å) on the CH_3 terminated SAM on gold are shown for comparison and denoted as (I) and (II) in figure 5.25. The different stages during the desorption process are shown in spectra (III-XII), figure 5.25.
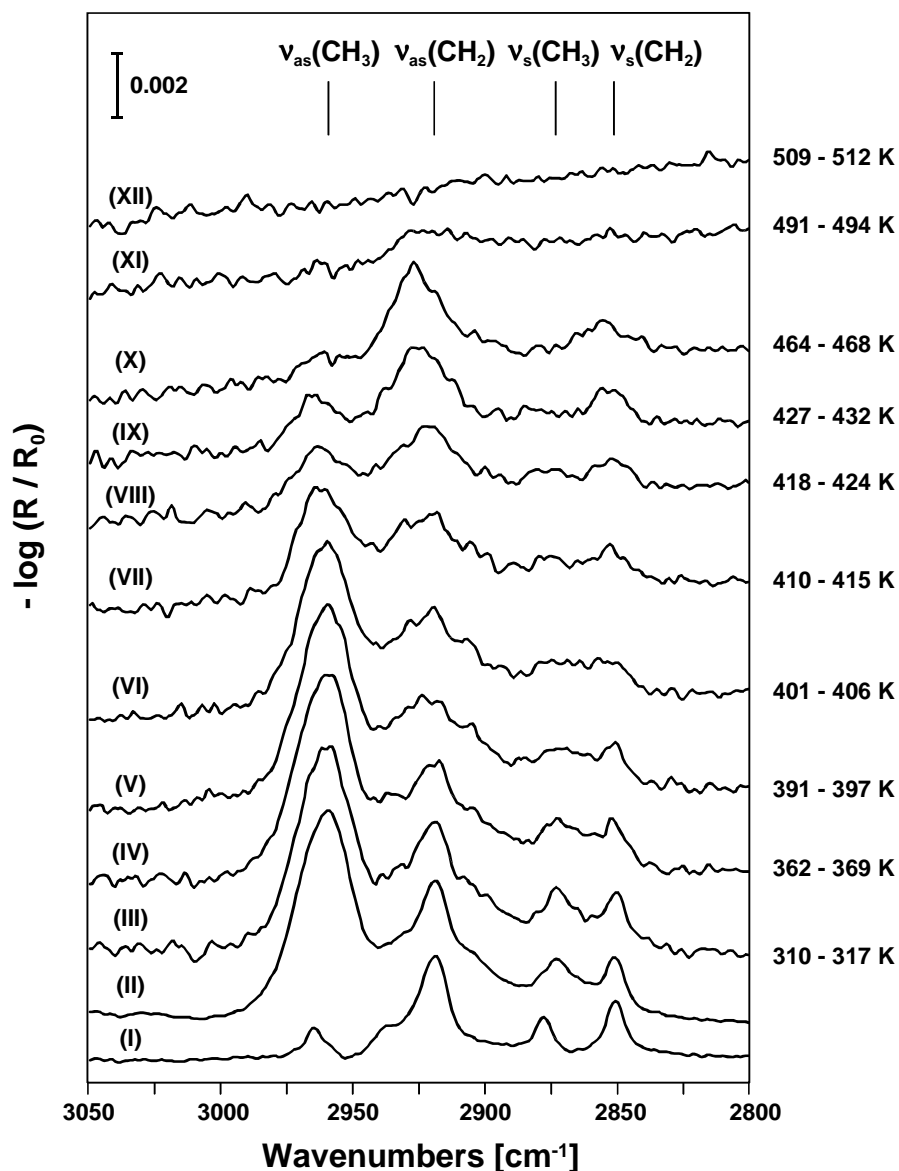
Figure 5.25: RA spectra of I) the Au / S-(CH₂)₁₇-CH₃ SAM, II) tert-butylcalix[4]arene layer (d = 200 Å) on H₃C-(CH₂)₁₇-S / Au, recorded in the UHV at room temperature and III) ... XII) particular stages of the TPD of tert-butylcalix[4]arene / CH₃-(CH₂)₁₇-S / Au at different temperatures of the sample, Tₛ. denoted to the right of the spectra.

Below $T_s \approx 397$ K, position, shape and intensity of the $\nu_a(CH_3)$ vibration remain unaffected by an increasing sample temperature, whereas the $\nu_a(CH_2)$ vibration band broadens in the spectra (II) - (V). This broadening is due to the displacement of the $\nu_a(CH_2)$ vibration mode towards higher wavenumbers (the intensity decreases at $\tilde{\nu} = 2918$ cm^{-1} and increases at $\tilde{\nu} = 2927$ cm^{-1}), and indicates a diminishing amount of *all-trans* configuration of the methylene groups that correlates with a decrease of order and density in the SAM, figure 5.25 and 5.26a).

a)

b)
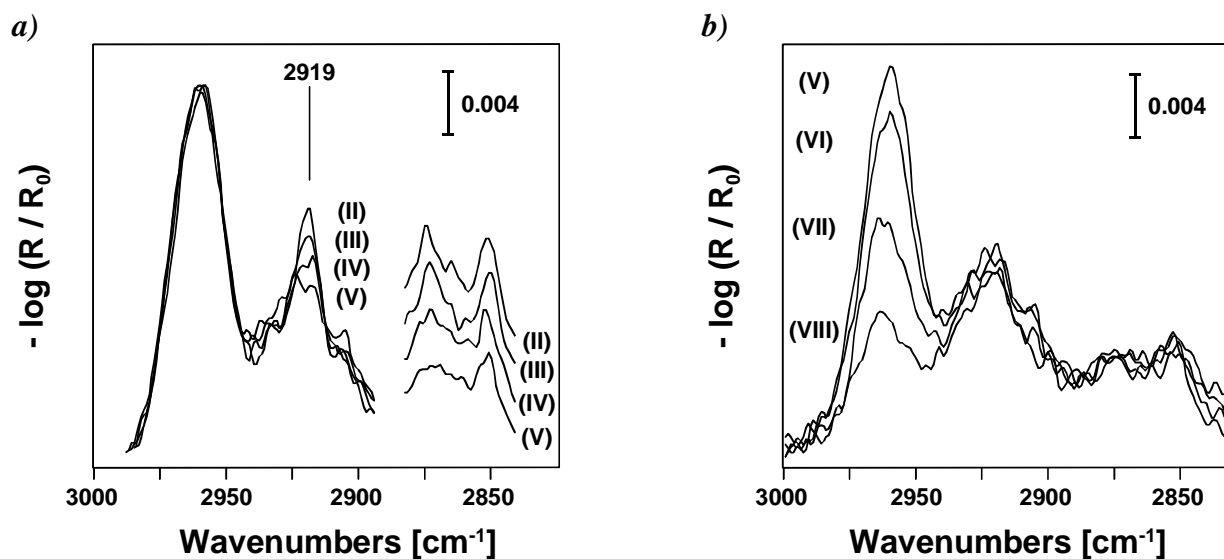
Figure 5.26: *RA spectra of tert-butylcalix[4]arene / CH_3-$(CH_2)_{17}$-S / Au. The RA spectra illustrate a) the disordering of the thiol SAM as characterized by a decrease of the band located at $v = 2919$ cm^{-1}, for $T_s = 300$ - 347 K, and b) the desorption of the tert-butylcalix[4]arene in the temperature range of $T_s = 391$ - 424 K. The numbering corresponds to the stages in figure 5.25.*

In the temperature range of $391\,K \leq T_s \leq 424\,K$, a declining intensity of the $v_{as}(CH_3)$ band demonstrates the desorption of the *tert*-butylcalix[4]arene molecules, while the thiol layer remains essentially unchanged, as confirmed by a constant position and shape of $\tilde{v}\,[v_{as}(CH_2)] \approx 2920$ cm^{-1} in the spectra (V) - (VIII), figure 5.25 and 5.26b).
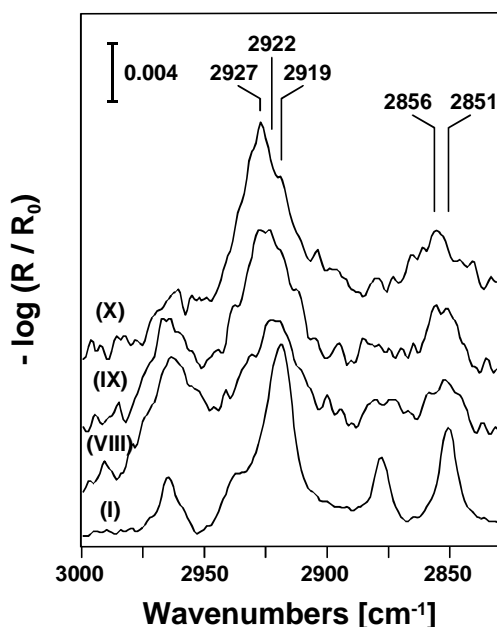
Figure 5.27: *RA spectra of CH_3-$(CH_2)_{17}$-S / Au. Three different phases of the desorption of the SAM (VIII-X) are compared to the RA spectrum of the freshly prepared CH_3-$(CH_2)_{17}$-S / Au surface (I). A shifting of the peak position with increasing temperature indicates a continuous disordering of the methylene groups in the thiol SAM.*

For temperatures $T_s \geq 424$ K, the thiol monolayer is affected and the CH_2 vibrations significantly shift towards higher wavenumbers, ending up at $\tilde{\nu}\,[\nu_a(CH_2)] = 2927$ cm^{-1}, and $\tilde{\nu}\,[\nu_s(CH_2)]$ $= 2856$ cm^{-1}. The SAM has mutated to a 'spaghetti-like' thiol adsorbed on the gold without any ordering of the molecules in (X) - (XII), figure 5.27, before it finally desorbs at temperatures $T_s \geq$ 494 K.

For the temperature programmed desorption of *tert*-butylcalix[4]arene on the HO-$(CH_2)_{18}$-S / Au SAM, no disordering of the thiol SAM is found before the desorption of the calixarene takes place.

In analogy to the experiment described in chapter 5.3.1, figure 5.9, annealing experiments of *tert*-butylcalix[4]arene layers ($d \approx 100$ Å) evaporated on the HS-$(CH_2)_{17}$-CH_3 and HS-$(CH_2)_{18}$-OH SAM were performed at sample temperatures of $T_s = 325$, 335, and 345 K, evidently below the desorption temperature, $T_{des,1}$, of the calixarene on these SAMs. In RA spectra recorded after 30 min, 1 h and 3 h of annealing, no clue for an ordering in the *tert*-butylcalix[4]arene film was detected in the shape of the spectra. The latter should be indicated by a vanishing of particular vibration modes while other bands remain unchanged in intensity. However, at $T_s < T_{des,1}$, small amounts of the *tert*-butylcalix[4]arene molecules desorb from the surface. This is shown by a decreasing intensity of all calixarene characteristic absorption bands with annealing time. Finally, in the TPD experiments performed after 'annealing', the m/z = 164 trace remains within the noise level for the entire temperature range, and none of the calixarene peaks appears in the m/z = 57 trace. This indicates that the calixarenes have desorbed prior to the TPD, and it is concluded that the supply of thermal energy causes a desorption rather than an orientation of the molecules in the film.

5.4.4   Interactions with Toluene and Chloroform

The ability of calixarenes to form supramolecular complexes with various organic molecules has been proven by several X-ray structure studies [20]. Calixarenes are also used as recognition layers for mass sensitive sensors like QMBs and SAWs [28]. To monitor the host-guest interactions, inclusion complexes of *tert*-butylcalix[4]arenes with a specific guest molecule in the cavity were compared to the pure host molecule by means of transmission FT-IR spectroscopy [145].

This paragraph deals with the inclusion behaviour of *tert*-butylcalix[4]arene films evaporated on gold surfaces towards organic solvents like toluene and chloroform, as determined by IRAS in UHV. Deuterated solvents were used in order to distinguish the absorption bands from the host and the guest molecules. Figure 5.28 shows the stretching vibration region of RA spectra of *tert*-butylcalix[4]arene layers on a clean gold surface with or without d^8-toluene, C_6D_5-CD_3, or chloroform, $CDCl_3$ overlayers at a temperature of $T_s = 82$ K.
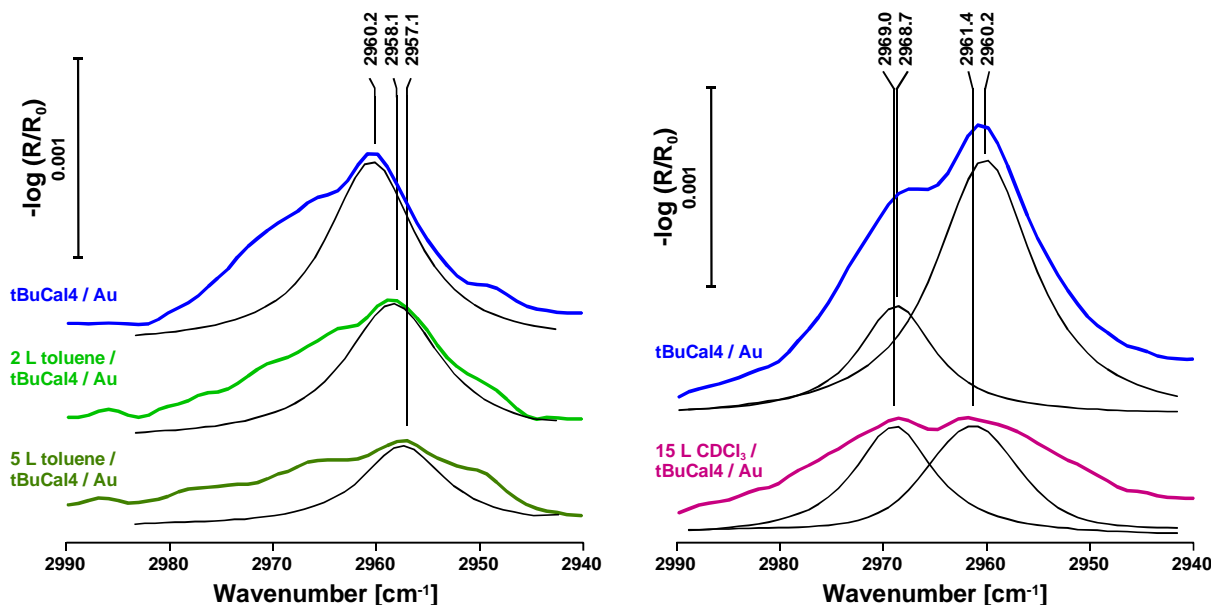
Figure 5.28: Dosing of deuterated organic guest molecules to tert-butylcalix[4]arene films deposited on pure gold surfaces. a) Dosing of d^8-toluene (2L and 5L) to a calixarene layer, d = 25 Å. For clarity, the other fitting curves were omitted b) 15 L of deuterated chloroform, $CDCl_3$, adsorbed on tert-butylcalix[4]arene, d = 50 Å at T_s = 82 K.

Upon adsorption of d^8-toluene (2L and 5L), the asymmetric CH_3 stretching mode vibration band of the *tert*-butylcalix[4]arene moves from $\tilde{v} = 2960.1$ cm^{-1} to $\tilde{v} = 2958.2$ and 2957.1 cm^{-1}, respectively, and also decreases in intensity. A lowered intensity is also observed for the aromatic stretching vibration, $v_{ar}(CC)$, centered at $\tilde{v} = 1488$ cm^{-1}, and for the in-plane bending vibration, $\beta(CC)$ at $\tilde{v} = 782$ cm^{-1}. The shifting towards lower wavenumbers, i. e. the decrease in binding strength, may be due to interactions between the *tert*-butyl groups of the calix[4]arene and the aromatic ring of toluene. The same effect, however to a larger extent, occurred in transmission mode for a *tert*-butylcalix[4]arene inclusion complex with toluene, where $v_{as}(CH_3)$ shifted $\tilde{v} = 2961.3$ cm^{-1} (for the pure host molecule) to $\tilde{v} = 2954.9$ cm^{-1} after complexation [145].

A similar phenomenon is observed for $v_{as}(CH_3)$ if 15 L of deuterated chloroform, $CDCl_3$, are dosed to *tert*-butylcalix[4]arene. Curve fitting reveals that two vibration modes centered at $\tilde{v} = 2969$ cm^{-1} and $\tilde{v} = 2960$ cm^{-1} with different intensity contribute to the absorption band of the pure calixarene film on gold. While the band at $\tilde{v} = 2969$ cm^{-1} is nearly unaffected by the chloroform adlayer, the mode of lower energy shifts by 1 cm^{-1} in position and significantly looses intensity. The former, again, is explained by changes of the binding strength due to inclusion. Because of the fact, that no calixarene molecule can disappear from the surface upon the dosing process, the decrease of intensity can be understood in terms of the surface selection rule. Obviously due to an inclusion of chloroform into the calixarene film, the transition dipole moment corresponding to the band at $\tilde{v} = 2960$ cm^{-1} changes its orientation with respect to the surface normal and, therefore, less interaction with the infrared radiation takes place. The same explanation holds for the decrease in intensity that was observed for the dosing of toluene.

5.5   bis(tert-Butylcalix[4]arene) Methionine Acylamide on Gold

The preparation of the bis(*tert*-butylcalix[4]arene) methionine acylamide (abbreviated by 'BC4MA' in the following) was described in chapter 4. This new type of calixarene derivative consists of a *tert*-butylcalix[4]arene platform and 2 chiral methionine acylamide residues at the lower rim, and is expected to form self-assembled monolayers on convenient substrates such as gold surfaces. The layer forming ability and the orientation of the cavity with respect to the surface were proved by means of IRAS, ellipsometry, contact angle measurements, SFM and XPS.

The synthesis of BC4MA is proved by ^{1}H-NMR, MS and IR spectroscopy (figure 5.31). The peaks found in the mass spectrum (FD desorption from a potassium target) are interpreted as follows: m/z = 1054 (100%) [M] $^+$, m/z = 851 (35%) [M-203] $^+$, monosubstituted calixarene fragment, m/z = 648 (35%) [M-406] $^+$, *tert*-butylcalix[4]arene fragment, m/z = 1093 (16%) [M+39] $^+$, BC4MA · K$^+$ adduct. ^{1}H-NMR (CDCl$_3$): $\delta = 9.5$ (s) OH, $\delta = 6.9$ (s) aromatic ring, $\delta = 4.6$ (s) peptide proton, $\delta = 3.7$ (s) methyl ester, $\delta = 2.6$ (s) and 2.4 (s) CH$_2$ groups in the methionine segment, $\delta \approx 2.0$ (s) terminal CH$_3$ group in the methionine segment, $\delta = 1.2$ (m) *tert*-butyl groups. A weaker hydrogen bonding interaction is the result of the substitution of two of the four hydroxyl groups at the lower rim, and leads to a shifting of the hydroxyl proton from $\delta_{OH} = 10.2$ ppm in the *tert*-butylcalix[4]-arene to $\delta_{OH} = 9.5$ ppm in BC4MA. Note that the *cone* conformation of the product is confirmed by a dublett centered at $\delta = 3.8$ ppm. The figures 5.29 and 5.30 illustrate XP spectra of a BC4MA layer on gold.
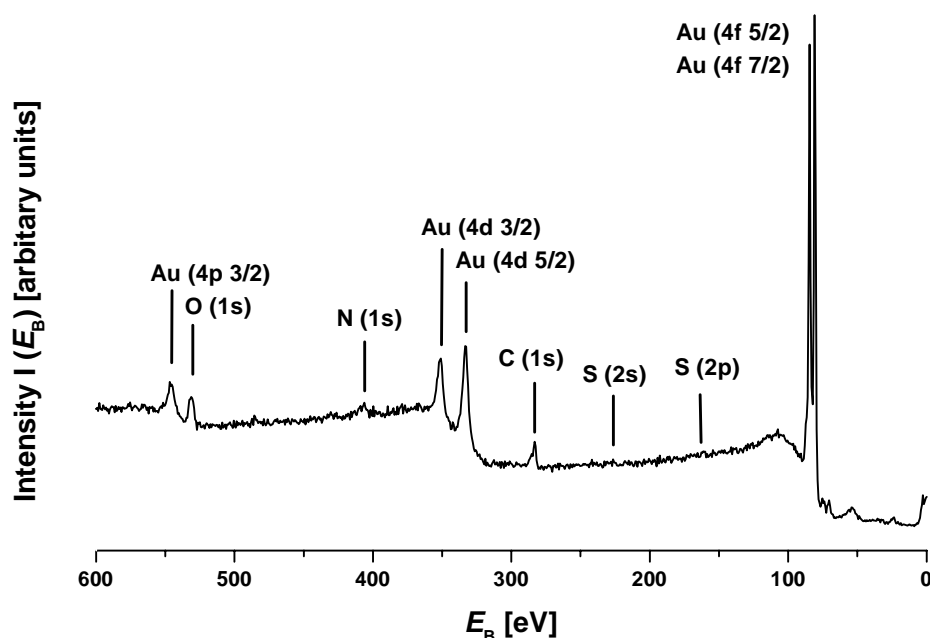
Figure 5.29:   X-Ray photoelectron spectrum of a self assembled BC4MA monolayer on gold. The core levels both of the substrate and the organic adlayer (marked in this survey spectrum) are shown in detail in figure 5.30. The assignment is taken from [90].

The observed XPS peaks are labeled and assigned as follows: Due to a sufficient mean free path of the electrons, both the SAM and the substrate appear in the spectra. The gold substrate is characterized by binding energies of $E_B = 546.2$ eV (4p 3/2), 351.5 eV (4d 3/2), 333.4 eV (4d 5/2), 85.4 eV (4f 5/2), and 81.8 eV (4f 7/2). The peaks that characterize the *tert*-butylcalix[4]arene methionine derivative are displayed in figure 5.30.
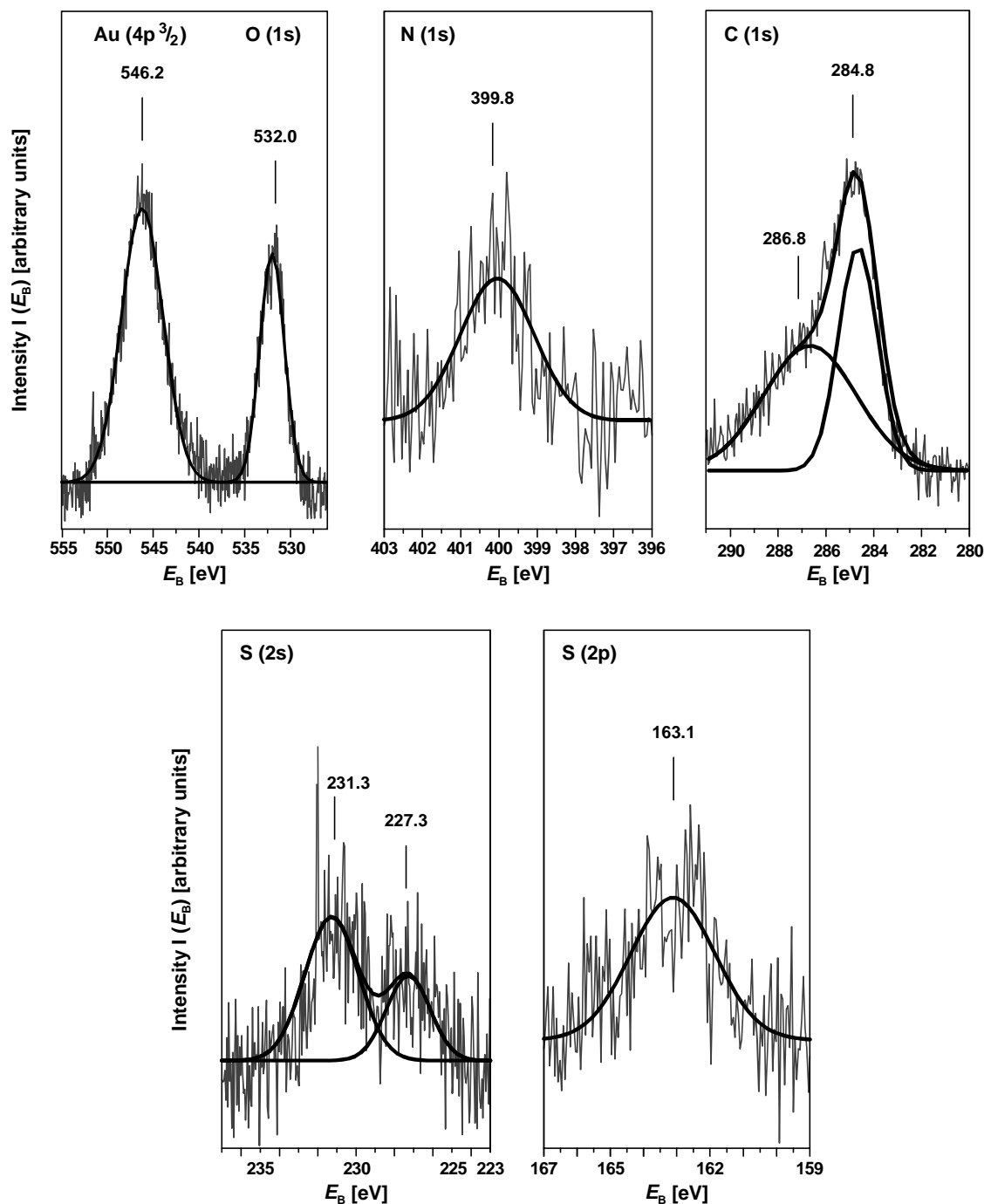
Figure 5.30: XP Spectra of the Au (4p 3/2), O (1s), N (1s), C (1s), S (2s), and S (2p) core level region. The peak positions result from the peak fittings indicated in the spectra.

The positions of O(1s), $E_B = 532.0$ eV, and C(1s), $E_B = 284.8$ eV perfectly agree with the values obtained for the *tert*-butylcalix[4]arene on silicon, chapter 5.3.1. The elements N, C, and S in the methionine residue give rise to additional peaks located at $E_B = 399.8$ eV for N(1s), 286.8 eV for C(1s), 227.3 eV for S(2s), and 163.1 eV for S(2p). These binding energies are in good agreement with the corresponding values in literature [154]. Due to a relatively huge X-ray spot, the Ta clamps that hold the sample give rise to a peak at $E_B = 231.3$ eV.

While XPS provides information about the elemental composition of the sample, infrared spectroscopy additionally characterizes the functional groups. In order to verify that the BC4MA molecule adsorbs without decomposition on the gold surface, the spectra of BC4MA measured as a KBr pellet in transmission and adsorbed on a clean gold surface in IRAS mode are compared in figure 5.31.
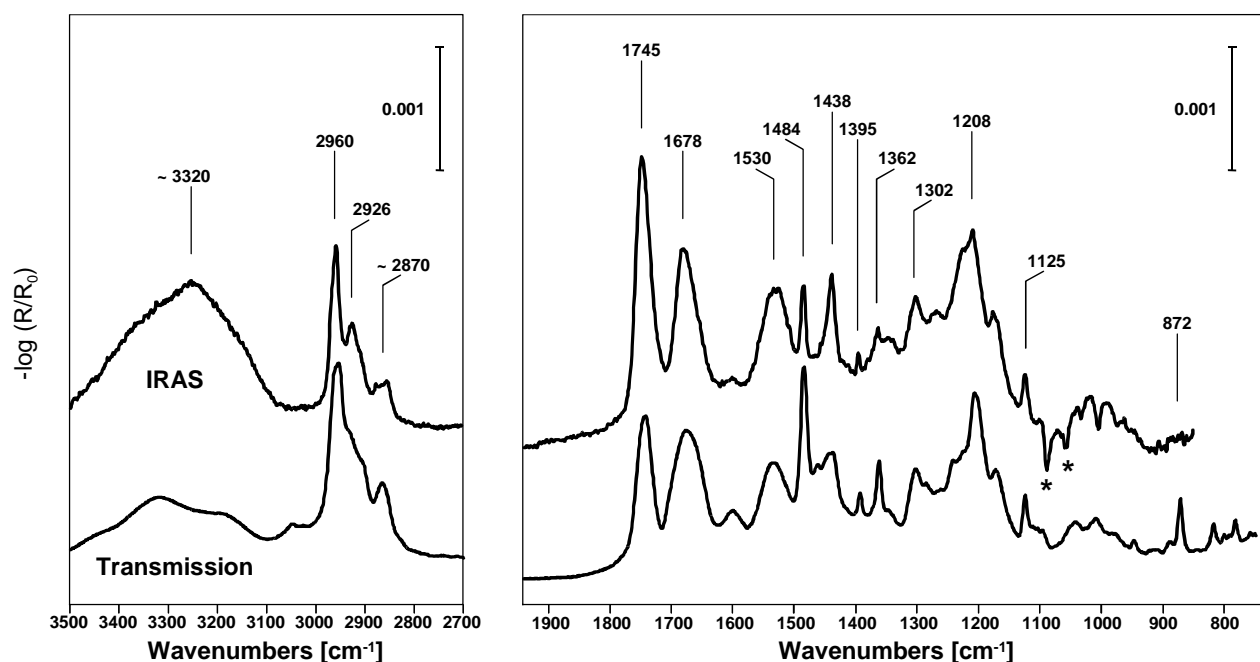
Figure 5.31: RA spectrum of a BC4MA SAM adsorbed on gold and transmission spectrum of BC4MA in KBr. The latter was scaled down by a factor of 0.009 to have comparable peak heights Negative peaks are due to a D_3C-$(CD_2)_{15}$-S / Au SAM on the reference plate (R_0), and marked with ''.*

Evidently, the absorption pattern of the BC4MA coincides in both spectra with respect to the peak positions. Due to the *surface selection rule* that is valid only for IRAS, the absorption bands may have different intensities in the spectra. The vibration modes of the *tert*-butylcalix[4]arene (table 5.1) and the ester and amid vibration modes that arise from the methionine segment contribute to the spectra. The CO stretching vibrations of the ester group and the amide are located at $\tilde{v}$ [v(CO)] = 1745 cm^{-1}, and $\tilde{v}$ [$v_{amide,I}$(CO)] = 1678 cm^{-1}, respectively, while at $\tilde{v}$ [$\beta_{amide,II}$(NH)] = 1530 cm^{-1}, the NH bending vibration is excited. The weak negative peaks seen in the RA spectrum in the range of 1100 - 1000 cm^{-1} are due to the deuterated Au / S-$(CD_2)_{15}$-CD_3 SAM on the reference plate (R_0), used as protection against organic contamination from the air.

The contact angle with water is rather sensitive to the wetting properties of the groups on top of the surface. Due to the amphiphilic behaviour of the different segments of the BC4MA, i. e. the hydrophobic cavity, the *tert*-butyl groups, and the hydrophilic amino acid residue at the lower rim, contact angle measurements provide useful information about the orientation of the molecules in the SAM. Figure 5.32 shows typical contact angles with water performed by the sessile drop method on various SAMs on gold. The BC4MA layer is compared to alkane thiols HS-$(CH_2)_n$-X with different wetting properties.

$\theta = 73 \pm 1°$ **OH** $\theta = 10 - 20°$

Ph $\theta = 60 - 70°$ **CH$_3$** $\theta = 110 - 112°$
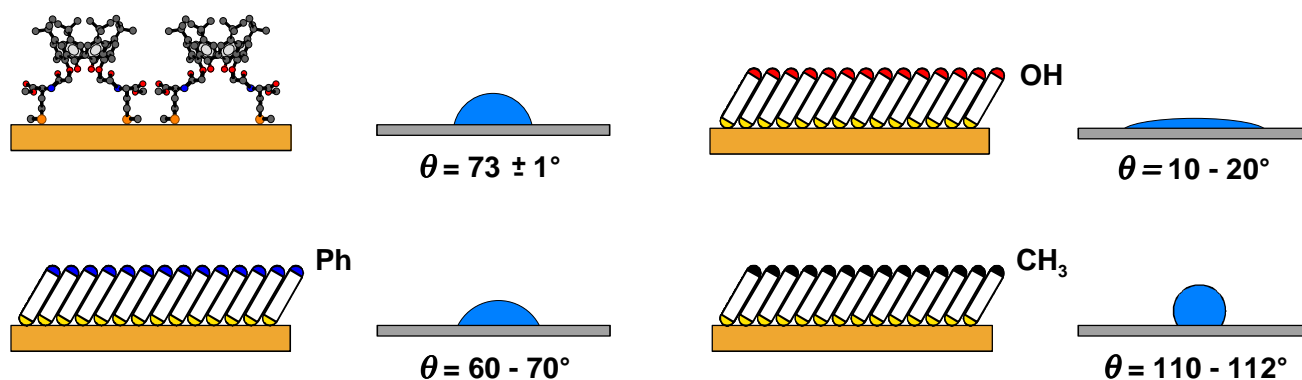
Figure 5.32: Contact angles, θ, of several self-assembled monolayers (SAMs on gold) measured by the sessile drop method with water.

The advancing contact angle of the BC4MA layer with water, $\theta_a(H_2O) = 73 \pm 1°$ is in perfect agreement with $\theta_a(H_2O) = 73°$ reported for the *tert*-butylcalix[4]arene tetrathiolate by GUTSCHE and ALLARA [80]. They lie between the values determined for the CH_3 and C_6H_5 terminated thiol SAM on gold. Since the contact angle for polar SAMs produced by amino acids or carboxylic acids is in the range of $\theta_a(H_2O) \approx 10 - 20°$, the observed value indicates only a small influence of the amino acid fragment on the wetting of the SAM. Consequently, the polar segment is closer to the gold film than the cavity and the *tert*-butyl groups are. It is therefore concluded that the open cavity of the *tert*-butylcalix[4]arene methionine derivative points at the ambient phase above the SAM, while the sulfur containing methionine is covalently linked to the gold surface.

The receding contact angle of the BC4MA layer with water, $\theta_r(H_2O) = 44 \pm 1°$, leads to a pronounced hysteresis that may be due to the flexibility of the BC4MA molecules in the SAM. The advancing droplet interacts with the cavity on top of the unperturbed SAM as confirmed by $\theta_a(H_2O) = 73°$. A few seconds later, when the water droplet is suck back into the syringe, the cavity may have slightly tilted, thus, enabling interactions with the polar methionine segment, and, consequently, leading to a significantly smaller value for the receding angle. The contact angles with hexadecane, $\theta_a(HD) = 12 \pm 1°$ and $\theta_r(HD) = 10 \pm 1°$, indicate that no CH_2 groups are present at the surface of the SAM.

In comparison with the size of the *tert*-butylcalix[4]arene molecule of approximately 10 Å in height, the ellipsometric thickness of the BC4MA monolayer, $d_E = 15 \pm 1$ Å, lies in good agreement with the expected values and molecular dimensions determined by means of *HYPERCHEM* (Hypercube Inc., Ontario, Canada, Version 5.0). The homogeneity of the self-assembled BC4MA monolayer was probed by tapping mode SFM, figure 5.33.
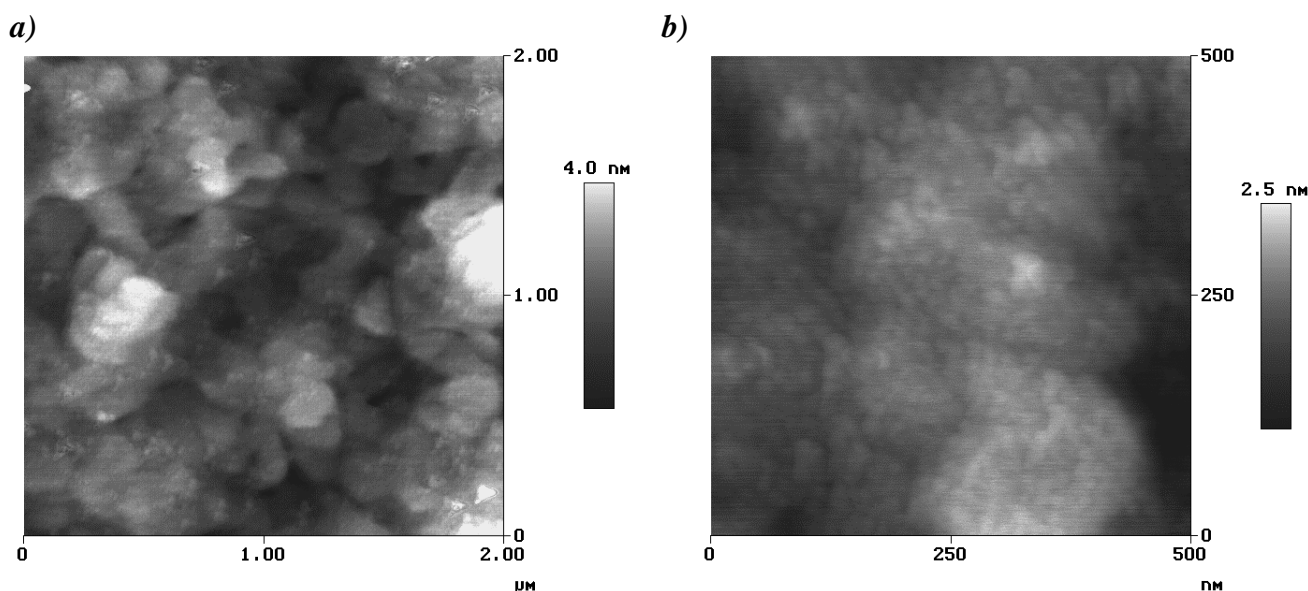
Figure 5.33: Tapping mode SFM images of a self-assembled BC4MA monolayer on a gold film (d = 2000 Å) evaporated on mica. Prior to incubation the gold layer was annealed for 1 h at 500 K.

The textures of the gold substrate with terraces at a size of roughly 200 Å dominate in the SFM images. The calixarene SAM can be recognized as spots of lighter gray scale on the surface, and the primary point is that no clusters of the calixarene molecule are detected on either of the images. Since the adlayer is stable over several SFM runs, a non-specific physisorption of BC4MA is ruled out. Due to the flexibility of the calixarene skeleton, the resolution of the images is reduced as compared to the uncovered gold substrate.

Because of the amphiphilic nature of the BC4MA molecule, interactions of organic molecules with the π-basic cavity and between polar groups and the amino acid fragment are expected as reported for similar caliarene derivatives [21, 53]. The inclusion behaviour was tested by dosing experiments with deuterated chloroform. Figure 5.34 shows the CD and CCl stretching vibrations in the RA spectra. The spectrum of 15 L of CDCl$_3$ on clean gold is depicted on top (I), as a reference for an isotropic orientation of the chloroform molecules in the adlayer. Starting at the bottom of the figure, the RA difference spectra that result from a dosing of 1.2 L (I) ... 20 L (IX) of CDCl$_3$ to the BC4MA monolayer indicate different intensities of the CD and CCl stretching vibrations.
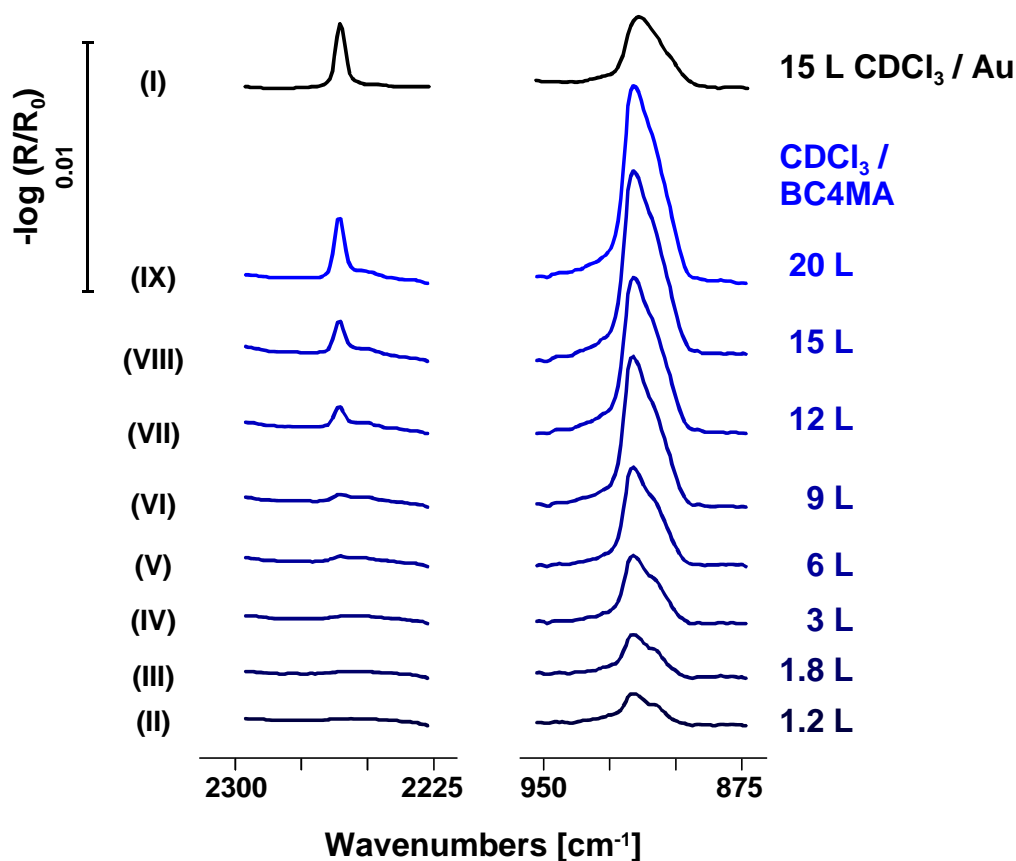
Figure 5.34: Dosing of various amounts of CDCl₃ to a BC4MA monolayer on gold gives rise to an increase of the C-D and C-Cl stretching vibration. On top, the RA spectrum of 15 L of CDCl₃ on a freshly cleaned, sputtered and annealed gold surface is shown as a comparison of the absorption intensities. During the dosing, a sample temperature of $T_s = 82$ K was maintained.

Deuterated chloroform (point group C_{3v}) is characterized by the stretching vibrations ν(CD), A_1-type, located at $\tilde{\nu} = 2260$ cm^{-1}, and the *E*-type stretching vibrations ν(CCl), at $\tilde{\nu} = 916$ cm^{-1}. The two peaks have roughly the same peak height in spectrum (I). In contrast to this, the intensities of the CD and CCl streching vibration bands do not increase simultaneously in the spectra (II) - (IX). With increasing CDCl₃ dosing to the BC4MA monolayer, only a weak absorption by the ν(CD) mode is observed for a coverage below 6 L, while the amount of infrared radiation absorbed by the CCl stretching vibration increases nearly linearly. The differences are displayed by the area of the absorption bands generated by 1.2 L, 1.8 L ... 20 L of CDCl₃ on the BC4MA SAM in table 5.7.

For comparison, the values of 15 L of CDCl₃ on a clean gold surface, spectrum (I), are given in the table. The peak area of the ν(CD) absorption band is determined to $A\,[\nu(\text{CD})] = 0.0125$ arbitrary area units (aau), while $A\,[\nu(\text{CCl})] = 0.0481$ aau is the determined peak area for the ν(CCl) absorption band. The ratio of the peak areas results in $R_{\text{CCl/CD}} = 3.84$.

Table 5.7 *Integrated Peak area and ratio of the CCl and CD stretching vibrations for different amounts of CDCl$_3$ deposited on a SAM of the tert-butylcalix[4]arene amino acid derivative and of 15 L CDCl$_3$ on a freshly sputtered and annealed gold surface for comparison.*

	pure gold	dosing of CDCl$_3$ on a BC4MA SAM on gold							
	15 L	1.2 L	1.8 L	3 L	6 L	9 L	12 L	15 L	20 L
A [ν(CCl)]	0.0125	2.014E-2	2.593E-2	4.253E-2	6.250E-2	9.588E-2	1.040E-1	1.239E-1	1.309E-1
A [ν(CD)]	0.0481	4.264E-4	5.462E-4	6.411E-4	1.385E-3	1.738E-3	4.382E-3	6.624E-3	1.188E-2
$R_{CCl/CD}$	3.84	47.23	47.47	66.23	45.11	55.27	23.73	18.70	11.01

The discrepancy between the intensity ratio of ν(CCl) and ν(CD) on the pure gold and the ratios arising from a low coverage on the calixarene SAM is the most pronounced for 3 L of CDCl$_3$. It decreases with an increasing amount of the guest molecule, but even for a 20 L layer, A[ν(CD)] is still too small compared to A[ν(CCl)] and to $R_{CCl/CD}$ = 3.84 observed for the chloroform dosing on the pure gold.

These differences are described in terms of the *surface selection rule* in the following. Assuming an isotropic orientation of the chloroform molecules condensed on the clean gold substrate, the dipole moments of both vibration modes are randomly orientated in the organic overlayer and, therefore, excited in the same degree by the infrared radiation polarized parallel to the surface normal, i. e. $E_\parallel$. This results in a similar peak height of both the stretching vibrations.

The deviation from the ratio $R_{CCl/CD}$ = 3.84, observed for the dosing of CDCl$_3$ on the calixarene SAM, is mainly due to the infinitesimal absorption of the ν(CD) vibration mode. The latter indicates that the majority of the chloroform molecules is oriented with their C_3 axis perpendicular to the surface normal since only in this case, the A_1-type vibration is not excited by IR radiation. Therefore, it is concluded that the CDCl$_3$ molecules condense in a certain spatial orientation on the BC4MA monolayer, and that this ordering is due to interactions with the *tert*-butylcalix[4]arene methionine derivative. For a dosing of more than 6 L, the ordering effect of the BC4MA on the CDCl$_3$ seems to have decreased and the appearance and an increasing intensity of the ν(CD) absorption band indicates a random orientation of supplementary CDCl$_3$ molecules in the condensed film.

6   Summary and Future Perspectives

tert-butylcalix[4]arene is a cyclic molecule with a hydrophobic cavity and a hydrophilic group at the lower rim. Intermolecular non-covalent binding interactions, e. g. *VAN DER WAALS* forces and hydrogen bonds, contribute to host-guest interactions that lead to the formation of supramolecular inclusion complexes with small organic molecules like toluene and chloroform in the solid state. The purpose of this thesis was to investigate the growth of *tert*-butylcalix[4]arene layers on pure and chemically modified gold and silicon surfaces with different wettability properties. The films were prepared by physical vapor deposition (PVD) and self-assembly (SAM) methods, and characterized by means of Fourier-transform infrared spectroscopy in attenuated total reflection mode (ATR) and infrared reflection-absorption spectroscopy (IRAS). Surface sensitive methods, like scanning force microscopy (SFM), UV and X-ray photoelectron spectroscopy (UPS, XPS), temperature programmed desorption (TPD), ellipsometry and contact angle measurements provide complementary information about the layer properties. With respect to the different substrates, the growing behaviour is mainly characterized by the following results.

- ATR measurements with plane-polarized infrared radiation demonstrate the influence of the surface properties of semiconducting substrates on the layer formation. *tert*-butylcalix[4]arene films ($d = 20$ ... 7500 Å) evaporated on a ZnSe crystal show significant differences in the absorption of *TM* and *TE* wave (dichroism). The selection rules for the *tert*-butylcalix[4]arene (C_{4v} symmetry) and the pronounced dichroism indicate an oriented growth and imply that the molecules are aligned with their principal axis (i. e. C_4) parallel to the surface normal, tilted by an angle of $\upsilon' \approx 21°$. In contrast to this, *tert*-butylcalix[4]arene layers grow isotropically on top of a KRS 5 crystal (consisting of TlBr and TlI). If guest molecules such as toluene are present during the deposition process, i. e. by evaporating crystalline inclusion complexes, again, the calixarene have a preferred orientation in the films, whereas the guest molecule is found in the cavity.

- The deposition of *tert*-butylcalix[4]arene layers ($d \approx 200$ Å) on the native SiO_2 / Si (001) surface gives rise to an island growth with a two-dimensional ordering of the molecules, as confirmed by SFM. The step height of approximately 10 Å agrees with the dimensions of the *tert*-butyl-calix[4]arene. SFM images of thin *tert*-butylcalix[4]arene layers ($d = 20$ ... 70 Å) on SiO_2

confirm a *VOLLMER-WEBER* growing mechanism. Strong intermolecular interactions of the physisorbed molecules lead to a migration and cluster formation of the calixarenes. The chemical binding of *tert*-butylcalix[4]arene to the SiO_2 substrate *via* an epoxide terminated silane was successful in generating monolayers.

- The molecular architecture and the amphiphilic properties of the *tert*-butylcalix[4]arene molecule affect the interactions between substrate and adsorbat, as displayed by the growing of *tert*-butyl-calix[4]arene films on modified gold surfaces with different terminal groups and wetting properties. Self assembled monolayers (SAMs) of alkane thiols, $HS-(CH_2)_n-X$, on gold are hydrophilic (X = OH, COOH), hydrophobic (X = CH_3) or show an aromatic character (X = O-$CO-C_6H_5$). IRAS spectra of *tert*-butylcalix[4]arene layers evaporated on the clean gold surface, on the hydrophilic or aromatic SAM suggest no preferred orientation of the molecules in the film. In contrast to this, a preferential orientation of the *tert*-butylcalix[4]arene molecules in the first monolayer on the hydrophobic, methyl terminated SAM (X = CH_3, n = 17) was found. The latter is due to interactions of the phenol units of the calixarene with the methyl groups of the SAM. Assays to anneal disordered *tert*-butylcalix[4]arene films at $T_s < T_{des}$ caused a desorption rather than a preferred orientation of the molecules in the film.

TPD experiments and IR spectroscopy in reflection-absorption (RA) mode probe the interactions of the *tert*-butylcalix[4]arene with the various substrates.

- Depending on the substrate, the *tert*-butylcalix[4]arene molecules desorb at temperatures of $T_S \approx 395$, 401-408 K from the clean gold surface and the hydrophilic or hydrophobic thiol SAM, respectively, following a first order desorption kinetic. Due to substrate-overlayer interactions, the desorption temperature of *tert*-butylcalix[4]arene on $HS-(CH_2)_{17}-CH_3$ is increased by 6 K compared to the pure gold surface.

- The combination of TPD and IRAS states a four step mechanism for the desorption of *tert*-butyl-calix[4]arene on $H_3C-(CH_2)_{17}-S$ / Au. Prior to the desorption of the calixarene at $T_S \approx 401$ K, the *all-trans* configuration of the aliphatic chains in the thiol SAM is thermally disrupted. This disordering process continues and causes the desorption of a small portion of thiol fragments at $T_S \approx 427$ K, while most of the aliphatic chains are desorbed of at $T_S \approx 488$ K, before, finally, the covalently bound sulfur fragments detach from the gold surface. In the desorption trace of *tert*-butylcalix[4]arene deposited on $HS-(CH_2)_{18}-OH$, an additional peak of constant area at $T_S \approx 447$ K indicates *one* monolayer of calix[4]arene that is stronger bound to the thiol SAM. The activation energies of the desorption were calculated according to the Redhead method.

Due to a covalent binding of sulfur to a gold surface, alkane thiols form self assembled monolayers (SAMs). This property has been applied to the *tert*-butylcalix[4]arene by substitution of two hydroxyl groups at the lower rim of by methionine derivatives.

- Bis(*tert*-butylcalix[4]arene) methionine acylamide was synthesized. It forms self-assembled monolayers on gold surfaces, as confirmed by IRAS, SFM, XPS, and ellipsometry. Contact angle measurements imply a "face up" orientation of the cavity, i. e. pointing at the ambient phase above the surface. Evidently due to interactions with the calixarene SAM, the dosing of deuterated chloroform, $CDCl_3$, generates an ordered overlayer for the first approximately 6 monolayers of $CDCl_3$, whereas no dichroism of the vibration bands is observed for the deposition of deuterated toluene, C_6D_5-CD_3.

This first member of a new type of calixarenes offers several perspectives for future efforts. Linked to QMBs (quartz micro balances) *via* S - Au bond, a detection of organic molecules both in liquid and gaseous phase is expected. Interactions may occur with the aromatic, π-basic and polar binding positions of the *tert*-butylcalix[4]arene methionine derivative, and, due to chirality in the amino acid residue, chiral selectivity - as observed in similar systems [155] - might be possible.

In analogy to the results of the *tert*-butylcalix[4]arene deposition on the CH_3 terminated SAM, ordering effects of the phenyl terminated HS-$(CH_2)_{18}$-O-CO-Ph have to be studied more carefully. Assuming a sterical hindering for the inclusion of the phenyl group into the calixarene cavity, a mixed monolayer with a shorter spacer, e. g. HS-$C_{12}H_{25}$, between the phenyl terminated thiol chains is expected to be a convenient substrate for ordered *tert*-butylcalix[4]arene layers. Due to the inclusion of the phenyl groups, the calixarene cavity is expected to be oriented 'face down', i. e. towards the surface.

7 References

[1] J. M. Lehn, *Angew. Chem.*, **100** (1988) 91-116.

[2] J. M. Lehn, *'Supramolecular Chemistry - Concepts and Perspectives'*, VCH, Weinheim, 1995, ISBN 3-527-29312-4.

[3] C. D. Gutsche and L. J. Bauer, *J. Am. Chem. Soc.*, **107** (1985) 6063-6069.

[4] P. Lhotak and S. Shinkai, *J. Phys. Org. Chem.*, **10** (1997) 273-285.

[5] D. J. Cram, *Angew. Chem.*, **100** (1988) 1041-1052.

[6] C. J. Pedersen, *Angew. Chem.*, **100** (1988) 1053-1059.

[7] P. Ehrlich, *'Studies on Immunity'*, Wiley, New York, 1906.

[8] E. Fischer, *Ber. Deutsch. Chem. Ges.*, **27** (1894) 2985.

[9] A. Werner, *Zeitschr. Anorg. Chem.*, **3** (1893) 267.

[10] D. E. Koshland, Jr., *Proc. Natl. Acad. USA*, **44** (1958) 98.

[11] W. Göpel and K. D. Schierbaum, *'Sensors - A Comprehensive Surveye'*, Vol. 2, Ed. W. Göpel, J. Hesse, and J. N. Zemel, VCH-Verlag, Weinheim, 1991, ISBN 3-527-26768-9, J. Gerblinger, K. H. Haerdtl, H. Meixner, and R. Aigner, *'Sensors - A Comprehensive Surveye'*, Vol. 8, Ed. W. Göpel, J. Hesse, and J. N. Zemel, VCH-Verlag, Weinheim, 1995, ISBN 3-527-26774-3 and references cited therein.

[12] J. Mitrovics, H. Ulmer, U. Weimar, and W. Göpel, *Acc. Chem. Res.*, **31** (1998) 307-316.

[13] C. D. Gutsche, *'Calixarenes - Monographs in Supramolecular Chemistry'*, Ed. J. F. Stoddard, The Royal Society of Chemistry, London, 1989, ISBN 0-85186-916-5, and C. D. Gutsche, *'Calixarenes Revisited - Monographs in Supramolecular Chemistry'*, Ed. J. F. Stoddard, Royal Society of Chemistry, Cambridge, 1998, ISBN 0-85404-502-3.

[14] J. Vicens and V. Böhmer, *'Calixarenes - A Versatile Class of Macrocyclic Compounds'*, Kluwer Academic Publishers, Dordrecht, 1991, ISBN 0-7923-0714-3.

[15]   A. Zinke and E. Ziegler, *Chem. Ber.*, **B 74** (1941) 1729, A. Zinke and E. Ziegler, *ibid.*, **77** (1944) 264-272, A. Zinke, G. Zigeuner, K. Hössinger, and G. Hoffmann, *Monatsh. Chem.*, **79** (1948) 438, A. Zinke, R. Krenz, E. Leggewie, and K. Hössinger, *ibid.*, **83** (1952) 1213-1227.

[16]   B. T. Hayes and R. F. Hunter, *Chem. Ind.*, (1956) 193-194. B. T. Hayes and R. F. Hunter, *J. Appl. Chem.*, **8** (1958) 743.

[17]   C. D. Gutsche and R. Muthukrishnan, *J. Org. Chem.*, **43** (1978) 4305-4306.

[18]   V. Böhmer and M. A. McKervey, *Chemie in unserer Zeit*, **25** (1991) 195-207. V. Böhmer, *Angew. Chem.*, **107** (1995) 785-818.

[19]   H. Kämmerer, G. Happel, and F. Caesar, *Die Makromolekulare Chemie*, **162** (1972) 179-197. G. Happel, B. Mathiasch, and H. Kämmerer, *ibid.*, **176** (1975) 3317-3334. H. Kämmerer and G. Happel, *Makromol. Chem.*, **179** (1978) 1199-1207. H. Kämmerer and G. Happel, *Monatshefte für Chemie*, **109** (1978), 767-773.

[20]   R. Ungaro, G. D. Andreetti, and A. Pochini, *J. Chem. Soc., Chem. Comm.*, (1979) 1005-1007.

[21]   G. D. Andreetti, A. Pochini, and R. Ungaro, *J. Chem. Soc., Perkin Trans. 2*, (1983) 1773-1779. C. Alfieri, E. Dradi, A. Poccini, G. D. Andreetti, and R. Ungaro, *J. Chem. Soc., Chem. Comm.*, (1983) 1075-1077. R. Ungaro, A. Pochini, G. D. Andreetti, and V. Sangermano, *ibid.*, (1984) 1979-1985. R. Ungaro, A. Pochini, G. D. Andreetti, and P. Domiano, *ibid.*, (1985) 197-201. G. Calestani, F. Ugozzoli, A. Arduini, E. Ghidini, and R. Ungaro, *ibid.*, (1987) 344-346. G. D. Andreetti, O. Ori, F. Ugozzoli, C. Alfieri, A. Pochini, and R. Ungaro, *Journal of Inclusion Phenomena*, **6** (1988) 523-536.

[22]   S. Shinkai, *Tetrahedron*, **49** (1993) 8933-8968, S. Shinkai, *Adv. Supramol. Chem.*, **3** (1993) 97-130.

[23]   P. Linnane and S. Shinkai, *Chem. & Ind.*, (1994) 811-814, D. R. Smith, *ibid.*, (1994) 14-17, R. Perrin, R. Lamartine, and M. Perrin, *Pure Appl. Chem.*, **65** (1993) 1549-1559.

[24]   A. Ulman, *'An Introduction to Ultrathin Organic Films: From Langmuir-Blodgett to Self-Assembly'*, Academic Press, Boston, 1991, ISBN 0-12-708230-1.

[25]   L. Dei, A. Casnati, P. L. Nostro, and P. Baglioni, *Langmuir*, **11** (1995) 1266-1272.

[26]   F. Davis, L. O'Toole, R. Short, and C. J. M. Stirling, *Langmuir*, **12** (1996), 1892-1894.

[27]   J. C. Thyson, J. L. Moore, K. D. Hughes, and D. M. Collard, *Langmuir*, **13** (1997) 2068-2073.

[28]   A. Dominik, H. J. Roth, K. D. Schierbaum, and W. Göpel, *Supramolecular Science*, **1** (1994) 11-19, K. D. Schierbaum, A. Gerlach, W. Göpel, W. M. Müller, F. Vögtle, A. Dominik, and H. J. Roth, *Fresenius J. Anal. Chem.*, **394** (1994), 372-379, A. Dominik: *'Molecular Docking an Calix[4]arenen'* Diploma Thesis, University of Tübingen, 1994, A. Gerlach: *'Die Wechselwirkung organischer Moleküle mit supramolekularen Verbindungen'*, Dissertation, University of Tübingen, 1993.

[29]   K. Bodenhöfer: *'Chirale Erkennung mit Schwingquarzsensoren'*, Dissertation, University of Tübingen, 1997, ISBN 3-932694-15-5.

[30]   N. P. Franks and W. R. Lieb, *Science*, **254** (1991) 427. N. P. Franks and W. R. Lieb, *Nature*, **367** (1994) 607.

[31]   E. J. Ariëns, *Eur. J. Clin. Pharmacol.*, **26** (1984) 663.

[32]   H. Beyer and W. Walter, *'Lehrbuch der organischen Chemie'*, 23rd ed., Hirzel, Stuttgart, Leipzig, 1998, ISBN 3-7776-0808-4.

[33]   P. Lhotak and S. Shinkai, *J. Synth. Org. Chem., Jap.*, **53** (1995), 963-974.

[34]   A. Ikeda and S. Shinkai, *Chem. Rev.*, **97** (1997) 1713-1734.

[35]   C. D. Gutsche, M. Iqbal, and D. Stewart, *J. Org. Chem.*, **51** (1986) 742-745. C. D. Gutsche and L.-G. Lin, *Tetrahedron*, **42** (1986) 1633-1640. C. D. Gutsche and M. Iqbal, *Org. Synth.*, **68** (1990) 234-237.

[36]   V. Böhmer, H. Goldmann, W.Vogt, and E. Paulus, *J. Am .Chem. Soc.*, **110** (1988) 6811-6817. V. Böhmer, H. Goldmann, W. Vogt, E. F. Paulus, F. L. Tobiason, and M. J. Thielman, *J. Chem. Soc., Perkin Trans. 2*, (1990) 1769-1775.

[37]   T. Sone, Y. Ohba, K. Moriya, H. Kumada, and K. Ito, *Tetrahedron*, **53** (1997) 10689-10698.

[38]   H. Kumagai, M. Hasegawa, S. Miyanari, Y. Sugawa, Y. Sato, T. Hori, S. Ueda, H. Kamiyama, and S. Miyano, *Tetrahedron Lett.*, **38** (1997) 3971-3972.

[39]   J. W. Cornworth, P. D'Arcy Hart, G. A. Nicholls, R. J. W. Rees, and J. A. Stock, *Br. J. Pharmacol.*, **10** (1955) 73. J. W. Cornworth, E. D. Morgan, K. T. Potts, and R. J. W. Rees, *Tetrahedron*, **29** (1973) 1659.

[40]   T. Harada, J. M. Rudzinski, E. Osawa, and S. Shinkai, *Tetrahedron*, **49** (1993) 5941-5954. A. Ikeda, H. Tsuzuk, and S. Shinkai, *J. Chem. Soc. Perkin Trans 2*, (1994) 2073-2080.

[41]   W. P. van Hoorn, *'Conformational and Dynamical Properties of Calixarenes'*, Dissertation, University of Twente, 1997, ISBN 90-3650909-2.

[42]   P. D. J. Groothenhuis, P. Kollman, L. C. Groenen, D. N. Reinhoudt, G. J. van Hummel, F. Ugozzoli, and G. D. Andreetti, *J. Am. Chem. Soc.*, **112** (1990) 4165-4176.

[43]   T. Harada, F. Ohseto, and S. Shinkai, *Tetrahedron*, **50** (1994) 13377-13394.

[44]   J. de Mendoza, P. Prados, N. Campillo, P. M. Nieto, C. Sáchez, J.-P. Fayet, M. C. Vertut, C. Jaime, and J. Elguero, *Recl. Trav. Chim. Pays-Bas*, **112** (1993) 367-369.

[45]   K. B. Lipkowitz and G. Pear, *J. Org. Chem.*, **58** (1993) 6729-6736.

[46]   J. Blixt and C. Detellier, *J. Am. Chem. Soc.*, **116** (1994) 11957-11960.

[47]   L. C. Groen, E. Steinwender, B. T. G. Lutz, J. H. van der Maas, and D. N. Reinhoudt, *J. Chem. Soc., Perkin Trans 2*, (1992) 1893-1898. J. A. Kanters, A. Schouten, E. Steinwender,

J. H. van der Maas, L. C. Groenen, and D. N. Reinhoudt, *J. Mol. Struct.*, **269** (1992) 49-64. B. T. G. Lutz, G. Astarloa, J. H. van der Maas, R. G. Janssen, W. Verboom, and D. N. Reinhoudt, *Vibrational Spectroscopy*, **10** (1995) 29-40. R. G. Janssen, W. Verboom, B. T. G. Lutz, J. H. van der Maas, M. Maczka, J. P. M. van Duynhoven, and D. N. Reinhoudt, *J. Chem. Soc., Perkin Trans. 2*, (1996) 1869-1876.

[48]   B. Brzezinski, F. Bartl, and G. Zundel, *J. Phys. Chem. B*, **101** (1997) 5611-5613.

[49]   K. Araki, K. Iwamoto, S. Shinkai, and T. Matsuda, *Bull. Chem. Soc. Jpn.*, **63** (1990) 3480-3485.

[50]   S. W. Keller, G. M. Schuster, and F. L. Tobiason, *Polym. Mater. Sci. Eng.*, **57** (1987) 906-910.

[51]   J. Schreeder, R. H. Vreekamp, J. F. J. Engbersen, W. Verboom, J. P. M. van Duynhoven, and D. N. Reinhoudt, *J. Org. Chem.*, **61** (1996) 3476-3481. W. Verboom, R. H. Vreekamp, P. J. Bodewes, S. Harkema, and D. N. Reinhoudt, *Rec. Trav. Chim. Pays-Bas*, **119** (1996) 402-405. O. Struck, W. Verboom, W. J. J. Smeets, A. L. Spek, and D. N. Reinhoudt, *J. Chem. Soc., Perkin Trans. 2*, (1977) 223-227.

[52]   C. D. Gutsche, B. Dhawan, K. H. No, and R. Muthukrishnan, *J. Am. Chem. Soc.*, **103** (1981) 3782-3792. C. D. Gutsche and L. J. Bauer, *J. Am. Chem. Soc.*, **107** (1985) 6052-6059. C. D. Gutsche, *Top. Curr. Chem.*, **123** (1984) 1-47.

[53]   S. G. Bott, A. W. Coleman, and J. L. Atwood, *J. Am. Chem. Soc.*, **108** (1986) 1709-1710.

[54]   H. J. Schneider, F. Werner, and T. Blatter, *J. Phys. Org. Chem.*, **6** (1993) 590-594.

[55]   H. H. Minn, S.-K. Chang, and K. T. No, *Theor. Chim. Acta*, **75** (1989) 233-245.

[56]   J. Uzawa, S. Zushi, Y. Fukuda, Y. Kodama, K. Nishihata, K. Umemura, M. Nishio, and M. Hirota, *Bull. Chem. Soc. Jpn.*, **53** (1980) 3623-3630.

[57]   A. Ikeda, H. Tsuzuki, and S. Shinkai, *Terahedron Letters*, **35** (1994) 8417-8420.

[58]   F. Inokuchi, K. Araki, and S. Shinkai, *Chem. Lett.*, (1994) 1383-1386.

[59]   K. K. Laali and T. M. Liang, *J. Chem. Res. (S)*, (1995) 240-241.

[60]   M. Vincenti, *J. Mass. Spec.*, **30** (1995) 925-939.

[61]   P. S. H. Wong, X. Y. Yu, and D. V. Dearden, *Inorg. Chim. Acta*, **246** (1966) 259-265.

[62]   R. B. Chaâbane, M. Gamoudi, G. Guillaud, C. Ouve, F. Gaillard, and R. Lamartine, *Synth. Met.*, **66** (1994) 49-54.

[63]   Y. Ishikawa, T. Kunitake, T. Matsuda, T. Otsuka, and S. Shinkai, *J. Chem. Soc., Chem. Comm.*, (1989) 736-738. K. Yagi, S. B. Khoo, M. Sugawara, T. Sakaki, S. Shinkai, K. Odashima, and Y. Umezawa, *J. Electroanalyt. Chem.*, **401** (1996) 65-79.

[64]   L. Dei, A. Canati, P. Lo Nostro, A. Pochini, R. Ungaro, and P. Baglioni, *Langmuir*, **12** (1996) 1589-1593.

[65] M. D. Conner, I. Kudelka, and S. L. Regen, *Langmuir*, **7** (1991) 982-987.

[66] M. D. Conner, V. Janout, I. Kudelka, P. Dedek, J. Zhu, and S. L. Regen, *Langmuir*, **9** (1993) 2389-2397. W. Lee, R. A. Hendel, P. Dedek, V. Janout, and S. L. Regen, *J. Am. Chem. Soc*, **117** (1995) 6793-6794. R. A. Hendel, E. Nomura, V. Janout, and S. L. Regen, *J. Am. Chem. Soc.*, **119** (1997) 6909-6918.

[67] T. Richardson, M. B. Greenwood, F. Davis, and C. J. M. Stirling, *Langmuir*, **11** (1995) 4623-4625.

[68] M. Namba, M. Sugawara, P. Bühlmann, and Y. Umezawa, *Langmuir*, **11** (1995) 635-638.

[69] H. Kawabata and S. Shinkai, *Chem. Express*, **8** (1993) 765-768. Y. Ishikawa, T. Kunitake, T. Matsuda, T. Otsuka, and S. Shinkai, *J. Chem. Soc., Chem. Comm.*, (1989) 736-738. M. Brake, V. Böhmer, P. Kramer, W. Vogt, R. Wortmann, *Supramol. Chem.*, **2** (1993) 65-70. Y. Nakamoto, G. Kallinowski, V. Böhmer, and W. Vogt, *Langmuir*, **5** (1989) 1116-1117.

[70] R. G. Nuzzo and D. L. Allara, *J. Am. Chem. Soc.*, **105** (1983) 4481-4483.

[71] J. D. Swalen, D. L. Allara, J. D. Andrade, E. A. Chandross, S. Garoff, J. Israelachvili, T. J. McCarthy, R. Murray, R. F. Pease, J. F. Rabolt, K. J. Wynne, and H. Yu, *Langmuir*, **3** (1987) 932. C. D. Bain, E. B. Troughton, Y.-T. Tao, J. Evall, G. M. Whitesides, and R. G. Nuzzo , *J. Am. Chem. Soc.*, **111** (1989) 321. L. H. Dubois and R. G. Nuzzo, *Annu. Rev. Phys. Chem.*, **43** (1992) 437.

[72] L. Bertilsson and B. Liedberg, *Langmuir*, **9** (1993) 141. R. V. Duevel and R. M. Corn, *Anal. Chem.*, **64** (1992) 337. A. N. Parikh, B. Liedberg, S. V. Atre, M. Ho, and D. L. Allara, *J. Phys. Chem.*, **99** (1995) 9996-10008.

[73] B. Liedberg and P. Tengvall, *Langmuir*, **11** (1995) 3821.

[74] A. Ulman, *Chem. Rev.*, **96** (1996) 1533-1554.

[75] L. H. Dubois and D. L. Allara, *J. Am. Chem. Soc.*, **112** (1990) 558-569. L. H. Dubois, B. R. Zegarski, and R. G. Nuzzo, *ibid.*, **112** (1990) 570-579. S. V. Atre, B. Liedberg, and D. L. Allara, *Langmuir*, **11** (1995) 3882-3893. J. B. Schlenoff, M. Li, and H. Ly, *J. Am.Chem. Soc.*, **117** (1995) 12528-12536. C. D. Bain, J. Evall, and G. M. Whitesides, *J. Am. Chem. Soc.*, **111** (1989) 7155-7164. A. N. Parikh and D. L. Allara, *J. Chem. Phys.*, **96** (1992) 927-945. I. Enquist, I. Lundström, and B. Liedberg, *J. Phys. Chem.*, **99** (1995) 12257-12267. I. Enquist, M. Lestelius, and B. Liedberg, *ibid.*, **99** (1995) 14198-14200.

[76] K. D. Schierbaum, T. Weiss, E. U. Thoden van Velzen, J. F. J. Engbersen, D. N. Reinhoudt, and W. Göpel, *Science*, **265** (1994) 1413-1415. K. D. Schierbaum, *Ber. Bunsenges. Phys. Chem.*, **99** (1995) 1230-1242. F. Davis and C. J. M. Stirling, *Langmuir*, **12** (1996) 5365-5374. H. Schönherr, G. J. Vansco, B.-H. Huisman, F. C. J. M. van Veggel, and D. N. Reinhoudt, *Langmuir*, **13** (1997) 1567-1570. E. U. T. van Velzen, J. F. J. Engbertsen, and D. N. Reinhoudt, *J. Am. Chem. Soc.*, **116** (1994) 3597-3598.

[77] D. L. Dermody, R. M. Crooks, and T. Kim, *J. Am. Chem. Soc.*, **118** (1996) 11912-11917.

[78] X. Yang, D. McBranch, B. Swanson, and D. Li, *Angew. Chem.*, **108** (1996) 572-575.

[79] M. W. J. Beulen, B.-H. Huisman, P. A. van der Heijden, F. C. J. M. van Veggel, M. G. Simons, E. M. E. F. Biemond, P. J. de Lange, and D. N. Reinhoudt, *Langmuir*, **12** (1996) 6170-6172. B.-H. Huisman, E. U. T. van Velzen, F. C. J. M. van Veggel, J. F. J. Engbersen, and D. N. Reinhoudt, *Tetrahedron Lett.*, **36** (1995) 3273-3276. H. Schönherr, G. J. Vancso, B. H. Huisman, F. C. J. M. van Veggel, and D. N. Reinhoudt, *Langmuir*, **15** (1999) 5541-5546.

[80] C. G. Gibbs and C. D. Gutsche, *J. Am. Chem. Soc.*, **115** (1993) 5338-5339. C. G. Gibbs, P. K. Sujeeth, J. S. Rogers, G. G. Stanley, M. Krawiec, W. H. Watson, and C. D. Gutsche, *J. Org. Chem.*, **60** (1995) 8394-8402. W. Hill, B. Wehling, C. G. Gibbs, C. D. Gutsche, and D. Klockow, *Anal. Chem.*, **67** (1995) 3187-3192. M. T. Cygan, G. E. Collins, T. D. Dunbar, D. L. Allara, C. G. Gibbs, and C. D. Gutsche, *Anal. Chem.*, **71** (1999) 142-148.

[81] X. Delaigue, J. M. Harrowfield, M. W. Hosseini, A. De Cian, J. Fischer, and N. Kyritsakas, *J. Chem. Soc., Chem. Comm.*, (1994) 1579-1580. X. Delaigue, M. W. Hosseini, N. Kyritsakas, A. De Cian, and J. Fischer, *J. Chem. Soc., Chem. Comm.*, (1995) 609-610.

[82] K. D. Schierbaum and W. Göpel, *Synth. Met.*, **61** (1993) 37-45.

[83] G. D. Andreetti, V. Böhmer, J. G. Jordon, M. Tabatabai, F. Ugozzoli, W. Vogt, and A. Wolff, *J. Org. Chem.*, **58** (1993) 4023-4032 and references cited therein.

[84] H. Günzler and H. M. Heise, *'IR-Spektroskopie'*, 3rd edition, VCH, Weinheim, 1996, ISBN 3-527-28759-0.

[85] N. C. Colthup, L. H. Daly, and S. E. Wiberley, *'Introduction to Infrared and Raman Spectroscopy'*, 3rd edition, Academic Press, San Diego, 1990, ISBN 0-12-182554-X.

[86] G. M. Barrow, *'Introduction to Molecular Spectroscopy'*, MacGraw-Hil, New York, 1962, ISBN 0-07-Y85904-3.

[87] P. R. Griffith and J. A. deHaseth, *'Fourier Transform Infrared Spectrosmetry (Chemical Analysis Vol. 83)'*, Wiley, New York, 1986, ISBN 0-471-09902-3.

[88] G. Herzberg, *'Molecular Spectra and Molecular Structure, Vol. I, Spectra of Diatomic Molecules'*, 2nd edition, Van Nostrand Reinhold Company, Princetown, New Jersey, New York, 1950, ISBN 0-442-03385-0, G. Herzberg, *'Molecular Spectra and Molecular Structure, Vol. II, Infrared and Raman Spectra of Polyatomic Molecules'*, Van Nostrand Reinhold Company, Princetown, New Jersey, New York, 1962, ISBN 0-442-03386-9.

[89] J. T. Yates and T. M. Madey, *'Vibrational Spectroscopy of Molecules on Surfaces (Methods of Surface Characterization, Vol. 1)'*, Plenum Press, New York, 1987, ISBN 0-306-42505-X.

[90] W. Göpel and C. Ziegler, *'Struktur der Materie: Grundlagen, Mikroskopie und Spektroskopie'*, B. G. Teubner, Stuttgart, 1994, ISBN 3-8154-2110-1.

[91] L. J. Bellamy, *'Ultrarot-Spektrum und chemische Konstitution'*, 2nd edition, Steinkopff, Darmstadt 1966.

[92]   D. Brune, R. Hellborg, H. J. Whitlow, and O. Hunderi, *‘Surface Characterization: A User’s Handbook’*, Scandinavian Science Publications, Wiley-VCH, Weinheim, 1997, ISBN 3-527-28843-0.

[93]   M. Hesse, H. Meier, and B. Zeeh, *‘Spektroskopische Methoden in der organischen Chemie’*, 5th edition, G. Thieme, Stuttgart, 1995, ISBN 3-13-576105-3.

[94]   Bergmann - Schäfer, *‘Lehrbuch der Experimentalphysik, Band 3 - Optik’*, editor H. Niedrig, 9th edition, Walter de Gruyter, Berlin, 1993, ISBN 3-11-012973-6.

[95]   I. P. Lorenz, *‘Gruppentheorie und Molekülschwingung’*, Attempto, Tübingen, 1992, ISBN 3-89308-159-3.

[96]   N. J. Harrick, *‘Internal Reflection Spectroscopy’*, 3rd edition, Harrick Scientific Corporation, New York, 1979, ISBN 0-933946-13-9. F. M. Mirabella, Jr. and N. J. Harrick, *‘Internal Reflection Spectroscopy: Review and Supplement’*, Harrick Scientific Corporation, New York, 1985, ISBN 0-933946-14-7. F. M. Mirabella, Jr., *‘Internal Reflection Spectroscopy - Theory and Applications’*, Marcel Dekker Inc., New York, 1993, ISBN 0-8247-8730-7.

[97]   R. G. Greenler, *J. Chem. Phys.*, **44** (1966) 310.

[98]   R. Zbinden, *‘Infrared Spectroscopy of High Polymers’*, Academic Press, New York, London, 1964.

[99]   F. M. Mirabella, *J. Polym. Sci, Polym. Phys. Ed.,* **20** (1982) 2309, *ibid.*, **21** (1983) 2403, *ibid.*, **22** (1984) 1283.

[100]   P. A. Flournoy and W. J. Schaffers, *Spectrochimica Acta*, **22** (1966) 5, P. A. Flournoy, *ibid.* **22** (1966) 13.

[101]   S. A. Francis and A. H. Ellison, *J. Opt. Soc. Am.*, **49** (1959) 131.

[102]   R. G. Greenler, *J. Chem. Phys.*, **50** (1969) 1963.

[103]   J. Pritchard in *‘Vibrations in Adsorbed Layers’*, Conference Record Series of KFA, H. Ibach and S. Lehwald, editors, Jülich, 1978, 114, P. Hollins and J. Pritchard, *Prog. Surf. Sci*, **19** (1985) 275-350.

[104]   Linköping Studies in Science and Technology: *a)* I. Enquist, *‘Microscopic Wetting’*, Dissertation No. 453, Linköping, 1996, ISBN 91-7871-828-7. *b)* M. Lestelius, *‘Taylor-Made Monolayer Assemblies for In Vitro Studies of Blood Protein - Surface Interactions’*, Dissertation No. 455, Linköping, 1996, ISBN 91-7871-834-1. *c)* H. Kariis, *‘Adsorption of Organic Phosphines and Thiols On Metal Surfaces’*, Dissertation No. 523, Linköping, 1998, ISBN 91-7219-117-5.

[105]   P. Drude, *Ann. Phys. Chem.*, **36** (1889), 532, 865.

[106]   R. M. A. Azzam and N. M. Bashara, *‘Ellipsometry and Polarized Light’*, 3rd impression of the paperback edition, Elsevier Science B. V., Amsterdam, 1996, ISBN 0-444-87016-4.

[107]   F. L. McCrackin, E. Passaglia, R. R. Stromberg, and H. L. Steinberg, *J. Res. Natl. Bur. Std.*, **67A** (1963) 363.

[108] W. Göpel and C. Ziegler, *'Einführung in die Materialwissenschaften'*, B. G. Teubner, Stuttgart, Leipzig, 1996, ISBN 3-8154-2111-X.

[109] J. Israelachvili, *'Intermolecular and Surface Forces'*, 6th reprint of the 2nd edition, Academic Press, London, San Diego, 1997, ISBN 0-12-375181-0.

[110] A. W. Adamson and A. P. Gast, *'Physical Chemistry of Surfaces'*, 6th edition, John Wiley & Sons, Inc., New York, 1997, ISBN 0-471-14873-3.

[111] *'Contact Angle, Wettability and Adhesion: Festschrift in Honor of Professor Robert J. Good'*, editor: K. L. Mittal, VSP BV, Utrecht, 1993, ISBN 90-6764-157-X.

[112] J. M. Howe, *'Interfaces in Materials: Atomic Structure, Thermodynamics and Kinetics'*, John Wiley & Sons, Inc. New York, 1997, ISBN 0-471-13830-4.

[113] H. J. Paus, *'Physik in Experimenten und Beispielen'*, Carl Hanser, München, 1995, ISBN 3-446-17371-4.

[114] A. B. D. Cassei, *Faraday Disc. Chem. Soc.*, **3** (1948) 11.

[115] M. A. Herman and H.Sitter, *'Molecular Beam Epitaxy - Fundamentals and Current Status'*, Springer, Berlin, Heidelberg, New York, 1989, ISBN 3-540-19075-9.

[116] E. Bauer, *Z. Kristallogr.*, **110** (1958) 372-394.

[117] Andrew Zangwill, *'Physics at Surfaces'*, Cambridge University Press, Cambridge, 1988, ISBN 0-521-34752-1.

[118] L. C. Feldman and J. W. Mayer, *'Fundamentals of Surface and Thin Film Analysis'*, North-Holland, New York, Amstedam, 1986, ISBN 0-444-00989-2.

[119] F. Urbach, *Sitzber. Akad. Wiss. Wien, Math.-Naturw. Kl. Abt. IIa*, **139** (1930) 363.

[120] J. B. Taylor and I. Langmuir, *Phys. Ref.*, **44** (1933) 423.

[121] L. R. Apker, *Industrial and Engineering Chemistry*, **40** (1948) 846.

[122] G. J. Ehrlich, *Phys. Chem.*, **60** (1956) 1388. G. J. Ehrlich, *Adv. Catal.*, **14** (1963) 255.

[123] P. A. Redhead, *Trans. Faraday Soc.*, **57** (1961) 641, P. A. Redhead, *Vacuum*, **12** (1962) 203-211.

[124] J. L. Falconer and R. J. Madix, *Surf. Sci.*, **48** (1975) 393.

[125] J. L. Falconer and J. A. Schwarz, *Catal. Rev. - Sci. Eng.*, **24** (1983) 141-227.

[126] D. A. King, *Surf. Sci.*, **47** (1975) 384-402.

[127] J. T. Jates, Jr., *'Methods of Experimental Physics'*, Vol. 22, 425, Academic Press, Orlando, Florida, 1985, ISBN 0-12-475964-5.

[128] A. M. deJong and J. W. Niemantsverdriet, *Surf. Sci.*, **233** (1990) 355-365.

[129] M. Smutek, C. Cerny, and F. Buzek, *Adv. Catal.*, **24** (1975) 343.

[130] W. Göpel, M. Henzler, and C. Ziegler, *'Oberflächenphysik des Festkörpers'*, 2nd edition, B. G. Teubner, Stuttgart, 1994, ISBN 3-519-13047-5.

[131] H. Lüth, *'Surfaces and Interfaces of Solids (Springer Series in Surface Science, Vol. 15)'*, Springer, Berlin, Heidelberg, New York, 1993, ISBN 3-540-52681-1.

[132] H. Ibach, W. Erley, and H. Wagner, *Surf. Sci.*, **92** (1980) 29.

[133] T. Weiß, *'Präparation und Charakterisierung von Högbergaren-Monoschichten auf Goldoberflächen'*, Diploma Thesis, University of Tübingen 1994, T. Weiß, *'Organische Monoschichten zur molekularen Erkennung'*, Dissertation, University of Tübingen, 1998, ISBN 3-932694-47-3.

[134] N. H. Turner and J. A. Schreifels, *Anal. Chem.*, **70** (1998) 229R-250R.

[135] G. Binnig, C. F. Quade, and C. Gerber, *Phys. Rev. Lett.*, **56** (1986) 930.

[136] G. Binnig, H. Rohrer, C. Gerber, and E. Weibel, *Phys. Rev. Lett.*, **49** (1982), 57.

[137] S. N. Magonov and M.-H. Whangbo, *'Surface Analysis with STM and AFM: Experimental and Theoretical Aspects of Image Analysis'*, VCH, Weinheim, New York, 1996, ISBN 3-527-29313-2.

[138] R. Howland and L. Benatar, *'A Practical Guide To Scanning Probe Microscopy (Manual)'*, Park Scientific Instruments, 1993-1996. *'Scanning Probe Microscopy (Manual)'*, Digital Intruments, 1997, and www.di.com.

[139] H. C. Hamaker, *Physica*, **4** (1937) 1058.

[140] O. Böhme, *'Rasterkraftmikroskopische, photoelektronenspektroskopische und massen-spektrometrische Untersuchungen geordneter Quinquethiophen-Aufdampfschichten auf oxidischen Substraten'*, Dissertation, Universiy of Tübingen, 1996. B. Reusch, *'Spektroskopische und rastersondenmikroskopische Grenzflächenuntersuchungen zum Korrosionsverhalten von Werkstoffen der Dentalmedizin'*, Dissertation, Universiy of Tübingen, 1998.

[141] S.-I. Prak, J. Nogami, and C. F. Quate, *Phys. Rev.*, **B 36** (1987), 2863.

[142] David Parker, *'Macrocycle Synthesis, A Practical Approach'*, Oxford University Press, Oxford, New York, 1996, ISBN 0-19-855841-4.

[143] I. Enquist, M. Lestelius, and B. Liedberg, *Langmuir*, **13** (1997), 4003-4012.

[144] I. Enquist, I. Lundström, and B. Liedberg, *J. Phys. Chem.*, **99** (1995) 12257-12267.

[145] O. Maute, *'FTIR-ATR spektroskopische Untersuchungen an geordneten tert-butylcalix[4]-arene Schichten'*, Diploma Thesis, University of Tübingen, 1994.

[146] A. Pfau, *'Defekte und elektronische Oberflächen-Struktur von Re/CeO$_{2-x}$: Modell Studien für Abgaskatalysatoren'*, Dissertation, Universiy of Tübingen, 1995, ISBN 3-8264-1179-4.

[147]   G. Socrates, *'Infrared Characteristic Group Frequencies'*, John Wiley & Sons, Chichester, 1980, ISBN 0-471-27592-1.

[148]   N. B. Colthup, L. H. Daly, and S. E. Wiberley, *'Introduction to Infrared and Raman Spectroscopy'*, 3rd edition, Academic Press, San Diego, 1990, ISBN 0-12-182554-X.

[149]   R. Soda, *Bull Chem. Soc. Jap.*, **34** (1961) 1482-1491. R. Soda, *ibid.,* **35** (1962) 152-158.

[150]   E. B. Wilson, *Phys. Rev.*, **45** (1934) 706-714. K. S. Pfitzer and D. W. Scott, *J. Am. Chem. Soc.*, **65** (1943) 803-824.

[151]   I. Enquist and B. Liedberg, *J. Phys. Chem.*, **99** (1995).

[152]   C. d'Anterroches, *J. Microsc. Spectros. Electron.*, **9** (1984) 147.

[153]   G. Ertl and J. Küppers, *'Low Energy Electrons and Surface Chemistry'*, VCH, Weinheim, 1985, ISBN 3-527-26056-0.

[154]   C. D. Wagner, W. M. Riggs, L. E. Davis, J. F. Moulder, and G. E. Mullenberg, *'Handbook of X-Ray Photoelectron Spectroscopy'*, Perkin-Elmer Corporation, Eden Prairie, Minnesota, 1978.

[155]   J. Pfeiffer, *'Calixresorcinarene als neue chirale Stationärphasen in GC und LC, Synthese und Anwendung von Chirasil-Calix und Chirasil-Calix-Dex zur Enantiomerentrennung und Aminosäureanalytik'*, Dissertation, University of Tübingen, 1999.

8 Appendix: Abbreviations and Acknowledgement

8.1 Abbreviations

Å	Ångström, 10^{-10}m
$\underline{\alpha}$	polarizability
a,b,c	molecular coordinate system
A_1, A_2, B_1, B_2, E	symmetry types (or species)
ATR	Attenuated Total Reflection
C_4, σ_v	symmetry operations
d	thickness
d_e, d_p	effective thickness, depth of penetration in ATR
$D_{TM/TE}, D_{x/z}$	dichroic ratio of *TM* and *TE* wave, radiation in *x*- and *z*-direction
$\underline{E}, E_\perp, E_\parallel$	electric field, perpendicular or parallel with respect to the plane of incidence
FT-IR	Fourier-Transform infrared spectroscopy
GOPTS	3-Glycidyloxypropyl-trimethylsilane
κ	attenuation coefficient
IRAS	Infrared Reflection Absorption Spectroscopy
LB film	Langmuir Blodgett film
$\underline{\mu}, \underline{M}$	dipole moment of the individual molecule and the entire film
MS	Mass spectrometry
$n_i, n_t\ n_f,$	refractive index of the incident or transmitting medium or the film
R_{ads}, R_{des}	rate of adsorption and desorption
R_{TM}, R_{TE}	reflectivities of the TM and TE waves
SAM	Self-Assembled Monolayer
SFM	Scanning Force Microscopy
$\theta, \theta_a, \theta_r$	contact angle, advancing and receding contact angle
θ_i, θ_t	angle of incidence and transmission
TM TE	transverse electric and transverse magnetic waves in ATR
TPD / TDS	Temperature Programmed Desorption / Thermal Desorption Spectroscopy
UHV	Ultrahigh vacuum
$\nu, \delta, \beta, , \omega, \tau$	vibration modes: ν stretching, δ: deformation, β: bending, ρ: rocking, ω: wagging, τ: twisting
XPS / UPS	X-Ray and Ultraviolet Photoelectron Spectroscopy
x,y,z	coordinate system of the spectrometer (space)
$\tilde{\nu}$	wavenumber in infrared spectra
φ	surface coverage

8.2   List Of Publications

- O. Maute, V. Hoffmann and K.D. Schierbaum: The Growth of Oriented *tert*-Butylcalix[4]arene Multilayers: an Internal Reflection Spectroscopy Study, submitted to Langmuir

- O. Maute, O. Böhme, B. Reusch, I. Stemmler, K. D. Schierbaum: Ordered *tert*-Butylcalix[4]-arene Films on Silicon Surfaces, in preparation

- O. Maute, K. D. Schierbaum, W. Göpel, H. Kariis, and B. Liedberg: Thin *tert*-Butylcalix[4]arene Layers on Gold Surfaces with Different Wettability Properties: A Combined IRAS- and TPD-Study, in preparation

- O. Maute, J. Pfeiffer, V. Schurig, B. Liedberg, and K. D. Schierbaum: A New Type of Monolayer Forming Calix[4]arenes: Comprehensive Studies of bis (*tert*-Butylcalix[4]arene) Methinoine Methyl Ester Acylamid on Gold, in preparation.

- O. Maute, V. Hoffmann and K.D. Schierbaum: Detection of Host-Guest Interactions of the *tert*-Butylcalix[4]arene Molecule by Infrared and Raman Spectroscopy, in preparation.

- O. Maute, H. Kariis, B. Liedberg, and K. D. Schierbaum: Dünne *tert*-Butylcalix[4]aren-Schichten auf modifizierten Goldoberflächen: Kombinierte IRAS- und TDS-Untersuchungen, Poster at the spring meeting of the Deutsche Physikalische Gesellschaft, Regensburg, 1998.

- O. Maute, K. D. Schierbaum, W. Göpel, H. Kariis, and B. Liedberg: Thin *tert*-Butylcalix[4]arene Layers on Gold Surfaces with Different Wettability Properties: A Combined IRAS- and TPD-Study. Poster at the ESF (European Science Foundation) -Artificial Biosensing Interfaces (ABI) meeting, Pisa, 1998

Meine akademischen Lehrer waren:

8.3   Danksagung

Herrn Prof. Wolfgang Göpel (1943-1999) verdanke ich ein interessantes wissenschaftliches Umfeld und hervorragende Arbeitsbedingungen, die das Forschen an seinem Institut sehr angenehm machten. Auch für die Förderung meiner Auslandsaufenthalte bin ich ihm sehr dankbar. In ihm lernte ich einen charismatischen Wissenschafter mit Genie und Weitblick kennen, dessen Andenken mich stets begleiten wird.

Herrn Prof. Klaus Schierbaum möchte ich sehr für die Anregung dieses interessanten Themas, die zuverlässige Betreuung, seine Kollegialität und sein Vertrauen in meine Arbeit danken.

Herrn Prof. Volker Hoffmann danke ich für die freundliche Übernahme des Koreferats und viele hilfreichen Diskussionen und Ratschläge.

Herrn Prof. Bo Liedberg danke ich sehr herzlich für die gute und fruchtbare Zusammenarbeit, anregende Diskussionen und viele richtungsweisende Ideen, vor allem aber dafür, daß er mir stets mit Rat und Tat zur Seite stand.

Besonders herzlich danke ich Götz Reinhardt für viele Gespräche und seine Kameradschaft.

Unserem Großgerätelaborleiter und Ansprechpartner für Problemlösungen aller Art, Tilo Weiß, danke ich für seine vielfältige Unterstützung. Insidertips im Umgang mit dem SFM erhielt ich von Oliver Böhme, Berthold Reusch, Lars Ohlson und Hartmut Stadler. An den UHV-Systemen konnte ich mich stets auf die Kompetenz und Hilfe von Wolfgang Neu, Peter Hebo und Peter Lönn verlassen. Daß im IPC- und IFM-Netzwerk alles gut wurde, lag an Andreas Haug, Michael Kuch, und Per Lossenberg. Besonders hervorzuheben ist die Energie, mit der Michael Wandel meine Computerprobleme stets optimal löste. Dafür möchte ich ihnen allen herzlich danken.

Nur in einem angenehmen Umfeld läßt es sich gut arbeiten, und das verdanke ich meinen Zimmer-kolleg/innen Günter Appel, Volker Baitinger, Marc Beck, Stefanie Jung, Diana Loyek, Martin Rösch und Ralf Mayer, dem harten Kern im Kaffeeraum Elke Nadler, Simone Hahn, Michael „Mic" Kaspar, Reiner Krapf und Egon Merz sowie Markus Schweizer-Berberich, Ralph-Michael Rummel, Stefan Fischer, Andreas Pfau, Aleksander Vidic und allen anderen Mitarbeitern des Arbeitskreises.

Die Zusammenarbeit und die Gemeinschaft mit meinen schwedischen Kollegen Magnus Lestelius, Mattias Östblum, Ramunas Valiokas, Veronika und Thomas Kugler, Sofia Svedhem, Kajsa Uvdal, Trine Vikinge-Platou und Isak Enquist, werden mir immer eine schöne Erinnerung an meine Zeit am IFM sein. Ein besonderer Dank gebührt, Hans Kariis, der mir stets hilfreich zur Seite stand.

Jens Pfeiffer danke ich sehr für unsere erfolgreiche Kooperation, Matthias Kramer und Frauke Palmer für einen umfangreichen Erfahrungsaustausch und Ivo Stemmler für die Idee mit 'GOPTS'.

Zum Schluß ist es mir wichtig, meiner Frau Marion und unserer Tochter Annkathrin Vanessa für ihr Durchhaltevermögen, die vielen Stunden der Entspannung und unsere schöne Zeit in Schweden zu danken. Tanja Schneider, Oliver Rau und Iris Schwarz danke ich für die langjährige und krisenfeste Freundschaft. Und ein großer Dank gebührt meinen Eltern, die mir mein Studium ermöglicht und mich in meinem Handeln stets unterstützt haben.

8.4   Curriculum Vitae

Oliver Maute

geboren   am 01. Februar 1967 in Reutlingen.

Familienstand: verheiratet, ein Kind

Schule:

09 / 1973 – 06 / 1977	Römerschanz-Grundschule, Reutlingen.
08 / 1977 – 06 / 1986	Friedrich-List Gymnasium, Reutlingen.

Wehrdienst:

07 / 1986 – 04 / 1987	Allgemeiner Grundwehrdienst bei der Luftwaffe in Roth und Meßstetten. Ausbildung zum Fernmelder.

Studium:

04 / 1987	Immatrikulation an der Eberhard-Karls Universität, Tübingen im Studiengang Chemie (Diplom).
10 / 1989	Vordiplom-Prüfung
08 / 1994	Diplom-Hauptprüfung.
09 / 1994 – 03 / 1995	Diplomarbeit am Institut für Physikalische und Theoretische Chemie der Universität Tübingen „FTIR / ATR-spektroskopische Untersuchungen geordneter *tert*-Butylcalix[4]aren-Schichten", unter Anleitung von Prof. W. Göpel und K. D. Schierbaum.

Promotion:

09 / 1995 – 12/1999	Doktorarbeit am Institut für Physikalische und Theoretische Chemie der Universität Tübingen in Kooperation mit dem Institut für Physik und Meßtechnik (*IFM*) der Universität Linköping, Schweden.
	"Preparation of Ordered *tert*-Butylcalix[4]arene Layers on Modified Surfaces: Comparative FTIR, SFM, TPD, and Contact Angle Studies" unter Anleitung von Prof. W. Göpel, Prof. K. D. Schierbaum und Prof. B. Liedberg.
12 / 1996 – 09 / 1998	Mehrere Forschungsaufenthalte am Institut für Physik und Meßtechnik (*IFM*) an der Universität von Linköping, Schweden.